Influence of radiation damage on fracture toughness of aluminum alloys in nuclear research reactors

Zacharie Shokeir

PSL UNIVERSITÉ PARIS

THÈSE DE DOCTORAT
DE L'UNIVERSITÉ PSL

Préparée à MINES ParisTech

Influence of radiation damage on fracture toughness of aluminum alloys in nuclear research reactors

Modélisation de l'effet de l'irradiation sur la ténacité des alliages d'aluminium dans les réacteurs nucléaires expérimentaux

Soutenue par

Zacharie Shokeir

Le 7 octobre 2022

École doctorale n°621

Ingéniérie des Systèmes, Matériaux, Mécanique, Énergétique

Spécialité

Mécanique

Composition du jury :

Amine BENZERGA Professor, Texas AM University	*Président*
Jonas FALESKOG Professor, KTH	*Rapporteur*
Damien FABREGUE Professeur des universités, INSA Lyon	*Rapporteur*
Florent HANNARD Chargé de recherche, FNRS	*Examinateur*
Tom PETIT Ingénieur de recherche, CEA Saclay	*Examinateur*
Jérôme GARNIER Ingénieur de recherche, CEA Saclay	*Examinateur*
Yazid MADI Chargé de Recherche, Centre des Matériaux MINES Paris	*Examinateur*
Jacques BESSON Directeur de recherche, CNRS	*Directeur de thèse*

MINES PARIS | PSL

ABSTRACT

The 6061-T6 aluminum alloy is used for the fabrication of pressure vessels in nuclear research reactor. Neutron radiation causes microstructural changes that harden the material (45 and 60% increase in the yield and mechanical strengths respectively) and deteriorate its ductility (drop from 9 to 15% in the total elongation). Despite these changes in the elastic–plastic behavior, there is no evidence in the literature that the toughness of the irradiated alloy decreases, and some results even show that toughness is not affected. Therefore, investigating the influence of neutron radiation on the ductile failure of the alloy is necessary. The main objective of this thesis is to develop a physics-based model to predict the toughness of irradiated 6061-T6 aluminum alloy. The ductile damage mechanisms are investigated via a coupled experimental–numerical approach: (i) Void nucleation is studied via polished sections and in situ tensile tests performed on notched specimens; (ii) Finite element simulations of unit cells allow to quantify void growth; (iii) By considering two void populations, these simulations also allow to analyze void coalescence. In parallel, strain hardening drop is studied on a model 6061 aluminum having undergone different heat treatments, in order to be able to decorrelate its effect on toughness: by applying the previously developed model, crack propagations in CT specimens are correctly reproduced. Assuming that irradiation does not affect the particles responsible for the damage, the developed model is then applied to the irradiated material, by coupling it to an irradiated elastic–plastic phenomenological model, developed thanks to the database collected in the literature. Irradiated tensile and toughness specimens are tested in hot cells in order to definitively validate the PhD model. In addition to the various contributions brought to the topic of the modeling of the ductile failure, the main conclusion is that the toughness of the 6061-T6 aluminum alloy remains constant as a function of the irradiation dose.

RÉSUMÉ

L'alliage d'aluminium 6061-T6 est utilisé pour la fabrication de la cuve de réacteurs nucléaires de recherche. L'irradiation provoque des modifications microstructurales qui durcissent le matériau (augmentations de 45 et 60% de la limite d'élasticité et de la résistance mécanique) et détériorent sa ductilité (diminution de 9 à 15% de l'allongement à rupture). Malgré ces évolutions du comportement élastoplastique, il n'est pas prouvé dans la littérature que la ténacité de l'alliage irradié diminue, et quelques résultats montrent même qu'elle n'est pas affectée. Des investigations concernant l'influence de l'irradiation sur la rupture ductile de l'alliage sont donc nécessaires. L'objectif principal de cette thèse est ainsi de développer un modèle physique permettant de prédire la ténacité de l'alliage d'aluminium 6061-T6 irradié. Les mécanismes d'endommagement ductile sont investigués par une approche couplée expérimental – numérique : (i) La germination est étudiée via des coupes polies et des essais de traction in situ réalisés sur éprouvettes entaillés ; (ii) Des simulations par éléments finis de cellules unitaires permettent de quantifier la croissance ; (iii) En considérant deux populations de vides, ces simulations permettent également d'analyser la coalescence. Parallèlement, le durcissement et la chute d'écrouissage sont étudiés sur un aluminium 6061 modèle ayant subi différents traitements thermiques, afin de pouvoir décorréler leurs effets sur la ténacité : en appliquant le modèle précédemment développé, les propagations de fissure dans des éprouvettes CT sont correctement reproduites. En supposant que l'irradiation n'affecte pas les particules responsables de l'endommagement, le modèle non irradié est ensuite appliqué à l'état irradié, en le couplant à un modèle phénoménologique élastoplastique irradié, développé grâce à la base de données collectée dans la littérature. Des éprouvettes de traction et de ténacité irradiées sont testées dans des cellules blindées afin de valider définitivement le modèle de la thèse. Outre les différentes contributions apportées à la thématique de la modélisation de la rupture ductile, la principale conclusion est que la ténacité de l'alliage d'aluminium 6061-T6 reste constante en fonction de la dose d'irradiation.

PUBLICATIONS

The following publications are included in this thesis:

Shokeir, Z. et al. (2022a). 'Analytical formula for optimum GTN q_1 and q_2 parameters.' In: *Int. J. Frac.*

Shokeir, Z. et al. (2022b). 'Edge tracing technique to study post–necking behavior and failure in Al–alloys and anisotropic plasticity in line pipe steels.' In: *Fatigue and Fract. Engng Mater. Struct.*, pages 1–16. DOI: 10.1111/ffe.13754.

ACKNOWLEDGMENTS

First of all, I would like to thank the members of the jury. Thank you **Amine Benzerga** for coming all the way from Texas to give me valuable insights regarding my work. It was an honor to have such an expert in Failure Mechanics. Thank you **Jonas Faleskog** and **Daminen Fabrègue** for reviewing my manuscript and giving me your detailed feedback. I really appreciated our discussion during the defense. Thank you **Florent Hannard** for coming from Belgium to discuss my work. I really enjoyed reading your PhD work when I first started my PhD in 2019. I found it outstanding.

Secondly, I would like to thank my PhD supervisors. Thank you **Claire Ritter** for welcoming me at the CEA and helping me out during my first days at work. I wish you all the best in your career. Thank you **Jérôme Garnier** for all what you taught me regarding Aluminum Alloys and the Radiation Damage. I hope to see you acheive all what you wish at the CEA. Thank you **Tom Petit** for the tremendous amount of support you gave me during these three years (on a professional and personal level). You are very passionate about Research and Mechanics of Materials. I hope to see you managing big European and International projects in the coming future. Thank you **Yazid Madi** for the enormous support you gave me. I remember you staying till 10pm to help me carry out my experiments in the lab. What is even more suprising is that you give the same amount of support to all your PhD students. You did an excellent work in innovating in the experimental techniques used to test materials. You have great ideas that are driven by your passion. Thank you **Jacques Besson** for the time and effort you put in my PhD. You have a lot of ongoing projects and PhD students, which made me worried when I started my PhD. But, I was surprised by the amount of time you dedicated to my PhD to help me get the best out of it. We spent so much time together discussing results, coding and writing articles. I cannot summarize all what I learned by working with an intelligent person as you. I wish you all the best in the coming years.

Thirdly, I would like to thank someone who was not officialy my supervisor but who helped me a lot during the past three years. Thank you **Jean-Michel Scherer** for all what you taught me. We spent so much time together analyzing the results and technical problems I faced during my work. During that time, I discovered your unbelievable problem solving skills. The latter will help you to be an excellent researcher.

Fourthly, I would like to thank the friends and colleagues I worked with. Thank you **Geoffrey Celeste** and **Nathan Odou** for the amazing time we spent together. Alhtough I am extremely happy to finish my PhD, I am unhappy that we are not going to share what we had during the past three years: rock climbing together, having

drinks after work, discussing our mysterious work results and especially laughing our lungs out. Thank you **Abderrahman Guelzim** for all what we shared together. We started as colleagues and now you are family. I cannot wait to see you defend your thesis which will be outstanding. Thank you **Nicolas Leost** and **Axel Aublet** for the excellent presentations you shared with us during the past years. Your both work on impressive and crucial topics. I wish you all the best in your careers. Thank you **Lili Wan** and **Boualem Rais** for all the activities/after works we did together in a group because you proposed them. Thank you **Juan Deyo Maeztu-Redin**, **Clément Ribart**, **Clément Cadet**, **David Siedel** and **Jorge artinez Dosal** for your pleasant humour which is very needed when working on a PhD thesis.

Fifthly, I would like to thank the people I worked with at Centre des Matériaux. Thank you **Fabrice** for the amount of experiments we carried out together. Some of them took more than 10 hours and I was surprised by how much you were patient and willing to help. Thank you **René**, **Vasco**, **Fred** for the high quality machining you provided me. Thank you **Abdenour** and **Régis** for the lab work we carried out together. Thank you **Maria**, **Antoine** and **Kevin** for the sample preparation work. Thank you **Laurent** and **Basile** for solving all my technical issues and teaching me valuable IT tricks.

Sixly, I would like to thank the people I worked with at CEA. Thank you **Bruno Maugard**, **Benoît Tanguy**, **David Leboulch**, **Jérémy Hure**, **Thomas Helfer**, **Guillaume**, **Hiep**, **Stéphan**, **Philippe Grange**, **Rachma**, **Kamila**, **Pierrick**, **Louis Ziolek**, **Eric Leroy**, **Damien Schildknecht**, **Johann Pegaitazi**.

Finally, I would like to thank the closest people to my heart. You are my endless support system, during the PhD, but also since I was a child: Zeina, my father, my mother, my brothers and my grandmother.

CONTENTS

LIST OF FIGURES

JHR	Jules Horowitz Reactor
NRR	Nuclear Research Reactor
NPR	Nuclear Power Reactor
HFIR	High Flux Isotope Reactor
HFBR	High Flux Beam Reactor
$\dot{\Phi}_f$	Fast neutron flux, n/cm^2s
$\dot{\Phi}_{th}$	Thermal neutron flux, n/cm^2s
Φ_f	Fast neutron fluence, n/cm^2
Φ_{th}	Thermal neutron fluence, n/cm^2
R_Φ	Thermal to fast neutron fluence ratio

1

INTRODUCTION

RÉSUMÉ

Dans ce chapitre, une introduction des enjeux de la thèse est présentée. Le chapitre s'articule autour de trois volets principaux. Le premier volet est consacré au contexte industriel. Le deuxième volet est dédié aux objectifs scientifiques de la thèse. Enfin, le troisième volet porte sur le plan du mémoire.

As perceived by the majority of us, Nuclear Reactors are destined to generate electricity. In fact, there are two main types of Nuclear Reactors: Nuclear Power Reactor (NPR) which are used for electricity production or maritime propulsion and NRR. NRR are a neutron source that serve primarily for material testing and radioisotope production for nuclear medicine (e. g. scans of the heart, lung or thyroid). There are four material testing NRR in Europe among which some of them are no longer operating (e. g. the French NRR (called OSIRIS) shutdown in 2015). The latter is to be replaced by the material testing Jules Horowitz Reactor (JHR) (shown in fig. 1.1 (a)). The JHR is under construction at Cadarache in the South of France. Nowadays, the nuclear industry is moving towards reactors that aim for a considerable reduction of nuclear waste and an enhanced utilization of uranium resources. In order to reduce nuclear waste, the classic "thermal" NPR are to be replaced with the new generation "fast" neutron reactors. In a fast neutron reactor, the fission reaction is sustained by highly energetic neutrons (unlike classic thermal-neutron reactors). However, enough scientific data is mandatory for designing and operating the new generation fast-neutron reactors. This is where the NRR come into use.

The JHR is a material testing NRR destined to fulfill several technological and scientific challenges concerning testing nuclear fuel and material behavior under high radiation doses in order to provide information to the actually running NPR (Gen II III) and future ones (Gen IV). Moreover, the JHR will also produce up to 25% of the needed radio-elements for nuclear medicine in the European Union. The JHR is mainly financed by The French Alternative Energies and Atomic Energy Commission (CEA). The JHR is identified as a research infrastructure of pan-European interest by the European Strategic Forum on Research Infrastructure (ESFRI). 20% of the JHR project running costs are provided by European and International partners: CIEMAT (Spain), UJV-NRI (Czech Republic), SCK-CEN (Belgium), VTT (Finland), as well as

other Indian, Israeli, Swedish, British and Japanese research institutes. The partnership allows partners to have a long term access to an up-to-date high performance research infrastructure.

As mentioned earlier, the JHR produces high radiation doses for the purpose of material testing. Radiation can be expressed in terms of neutron flux which can be decomposed into: fast neutron and thermal neutron flux. Fast neutrons can be defined as neutrons with an energy (E) higher than a certain threshold. The fast neutron flux ($\dot{\Phi}_f$) in the JHR reaches up to 5×10^{14} n/cm^{2}s ($E > 0.907$ MeV) in the reactor's core on the circumference around the fuel rods. Water is used as a neutron moderator in the JHR reactor's core (fig. 1.1 (b)). The neutron flux is highly energetic in the core in order to irradiate the specimens used for material testing. These specimens are presented by blue, yellow and pink dots in fig. 1.1 (c). The same figure displays the fuel rods in white circles. The whole pack of fuel rods is submerged in the vessel-rack assembly filled with water (shown by the large yellow filled circle in fig. 1.1 (c)). The testing specimens maintained outside of the vessel (e. g. blue circles in fig. 1.1 (c)) should receive a high radiation dose. If the vessel material has a high neutron capture cross section, less neutrons will pass through and a lower flux will irradiate the outside test specimens. Therefore, the vessel material must have a high "neutron transparency". The vessel material is chosen based on this main criterion as well as other criteria:

- Corrosion resistance to withstand the $\sim$ 16 bars water cooling system inside the assembly.
- High thermal conductivity and low nuclear gamma-ray heating to cope with the cooling system.
- Good mechanical properties in the range of operating temperatures (35-70°C).
- Good weldability for joining several parts of the vessel by welding.

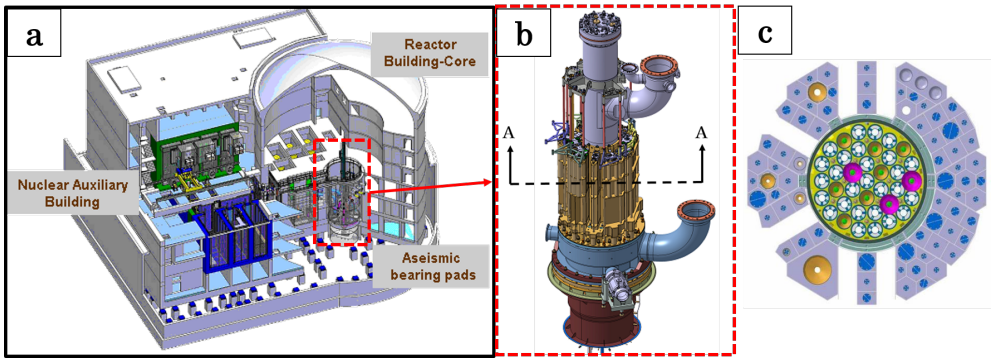

Figure 1.1: (a) Maquette of the JHR, (b) reactor's core, (c) cross section of the vessel-rack assembly in the reactor's core (fuel rods (white circles) and test specimens (yellow, pink and blue circles) are displayed)

The 6061-T6 aluminum alloy is chosen for fabricating the vessel since it has the required properties mentioned above. Moreover, aluminum alloys are widely used in NRR due to their high capacity of heat removal which is crucial in NRR [Farrell, 2012]. About 80% of the heat produced by nuclear fission is dissipated in fissile materials in American NRR [Farrell, 2012]. 5-20% of the remaining heat is generated in the surrounding core structural materials being bombarded by fission produced particles. While heat is essential in PNR to produce electrical energy, heat is inconvenient in NRR and must be exhausted. Aluminum alloys are outstanding when it comes to this issue. Nevertheless, irradiation causes microstructural changes that induce material hardening and decrease the ductility of metals [Alexander, 1999; Farrell, 2012; Kolluri, 2016; Weeks et al., 1993]. Irradiation damage in aluminum is divided into two families: transmutation damage (associated to the thermal flux) and displacement cascade damage (associated to the fast flux).

Thermal neutrons produce extra Si in aluminum by the following transmutation process [Farrell, 2012]:

$$^{27}Al + n_{th} \rightarrow {}^{28}Al + \gamma\,;\ {}^{28}Al \rightarrow {}^{28}Si + e^{-} + \bar{\nu} \tag{1.1}$$

The higher the thermal fluence (fluence $\rightarrow$ flux integrated in time, Φ_{th}), the more created Si in the Al matrix. The extra Si can create Si amorphous particles in pure aluminum alloys or Mg_xSi_y particles in AlMg and AlMgSi alloys (e. g. 5xxx and 6xxx aluminum alloys). In 6061 aluminum alloys, a Mg_xSi_y phase already exists in an unirradiated alloy by the means of a heat treatment (age hardening). Both phases, radiation-induced and age hardening Mg_xSi_y, increase the material's strength and lower its fracture toughness [Alexander, 1993; Farrell et al., 1979]. The age hardening Mg_xSi_y phase is unstable under ion and neutron irradiation. Recent work observed the dissolution of age hardening Mg_xSi_y nano-particles under ion radiation [Flament, 2015]. Other authors also claimed the dissolution of original strengthening Mg_xSi_y phase under neutron radiation in the 6061-T6 alloy [Farrel, 2011; Weeks et al., 1993]. Therefore, thermal neutrons strengthen the 6xxx aluminum alloys via precipitation of a radiation-induced phase.

Fast neutrons resulting from the nuclear fission reaction collide with atoms in the metallic crystalline structure. A fast neutron transfers its high energy to the first atom it strikes and ejects it from its initial site. This atom, also called a Primary Knock-on Atom (PKAs), travels in the crystalline structure and creates an atomic disorder. This phenomenon is known as an atomic displacement cascade. The latter creates material defects such as lattice vacancies and self-interstitial atoms [Kolluri, 2016]. Such atomic defects diffuse rapidly over time and give rise to an increase in the dislocation density and cavities. This results in a significant strengthening effect [Was, 2017]. The induced strengthening due to atomic displacement cascades occurs independently from the transmutation damage explained above. So far, the effect of each, neutron and thermal flux, is explained without considering the relation between both flux.

To fully understand the radiation damage, one must note that atomic displacement cascade and transmutation damages can be correlated by the ratio of thermal to fast fluences $R_\Phi = \frac{\Phi_{th}}{\Phi_f}$. In other words, two irradiated 6xxx alloys can have different microstructures and mechanical properties if the Φ_{th} is identical but the R_Φ is different [Farrel, 2011]. The physical explanation behind the R_Φ effect on mechanical properties is to be elaborated in this thesis. Since the R_Φ is a ratio of thermal to fast neutrons, one must define the energy thresholds used to distinguish thermal and fast neutrons. Conventional thermal and fast fluences are defined to compare results in this work. Φ_{th} hereby refers to neutrons with an energy $E = 0.025$ eV while Φ_f refers to neutrons an energy $E > 0.1$ MeV.

Few experimental data regarding the behavior of aluminum 6061-T6 under irradiation is available in the literature and are published by:

- The American Oak Ridge National Laboratory which owns the High Flux Isotope Reactor (High Flux Isotope Reactor (HFIR)) that contains aluminum 6061-T6 parts in the reactor core.
- The American Brookhaven National Laboratory which built and operates the High Flux Beam Reactor (High Flux Beam Reactor (HFBR)). The HFBR's vessel is fabricated from aluminum 6061.

Aluminum 6061-T6 samples irradiated at high doses ($\Phi_{th} = 341 \times 10^{21} n/cm^2$) in the HFIR are characterized at 328 K in the work of Farrell et al., 1979. Microstructural defects such as dislocation loops and cavities are observed as long as precipitates produced by extra Si from the transmutation damage (up to 7% wt. Si increase). The 0.2% flow stress and ultimate tensile strength increase by 45 and 60% respectively, while the elongation % at failure drops from 15 to 9%. Similar results are observed in other research conducted on the same irradiated alloy and are regrouped by Yahr, 1997.

The fracture toughness of the irradiated 6061-T6 alloy is tested in the work of Alexander, 1999 (HFIR related) and Weeks et al., 1993 (HFBR related). Alexander, 1999 observes an overall stability in fracture toughness when compared to the unirradiated alloy. However, the trends of the fracture toughness—irradiation dose are not as clear as for the strength and elongation percentage—irradiation dose. This is due to the competition between the radiation-induced hardening (which enhances the fracture toughness) and the ductility drop (which deteriorates the fracture toughness). This matter highlights one of the major research problems of this thesis: *How does the competition between radiation-induced strengthening and ductility drop affect the overall fracture toughness of the irradiated 6061-T6 alloy?*

The whole vessel-rack is composed of multiple welded aluminum parts. This thesis focuses on the middle shaft of the vessel-rack (1.4 m high) which is an *ESPN*. Such vessels are rigorously designed to fulfill the specifications defined by the French

ESPN stands for Équipement Sous Pression Nucléaire in French & Nuclear pressure vessels in English

Nuclear Safety Authority (*ASN*, Autorité de Sûreté Nucléaire). Furthermore, the 6061-T6 alloy is approved for service in the American nuclear reactors as a class 1 nuclear components material, see the Boiler and Pressure Vessel Code of the American Society of Mechanical Engineers, Case N-519 [ASME, 1994]. That being said, one of the CEA's key focus points in the JHR project is to ensure good ductility and fracture toughness of the vessel-rack shown in fig. 1.2 (b) at high radiation doses. This matter highlights the industrial objective of the research conducted in this thesis.

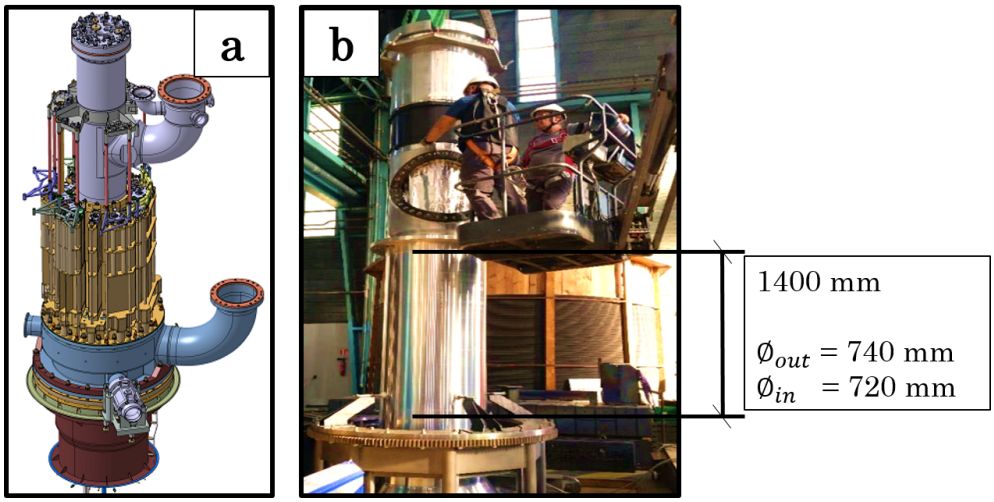

Figure 1.2: (a) Reactor's core, (b) vessel rack assembly holding the fuel rods inside, dimensions of the central shaft are noted

PhD thesis objectives As mentioned above, CEA must guarantee the fracture toughness of the vessel-rack assembly after radiation embrittlement. The most straightforward method is to test the fracture toughness of highly irradiated 6061-T6 samples using the facilities in the CEA laboratories. However, CEA does not possess highly irradiated 6061-T6 samples. The latter can only be obtained by irradiating them for several years in a NRR (as it is the case for other materials that are to be irradiated the JHR for material testing in the future). In addition, very few results are available in the literature regarding the fracture toughness of the irradiated 6061-T6 samples in the HFIR and HFBR. Therefore, the CEA carries tremendous amount of research in order to understand the physical and mechanical behavior of the irradiated 6061-T6 alloy. This thesis is driven by results of its predecessors:

- Flament, 2015; Garric, 2019 are focused on the microstructural changes during irradiation. The cited authors shows that the unirradiated alloy contains: micron-sized fragilizing Mg_2Si and Fe-rich particles, submicron Cr and Mn-rich dispersoids and need-like nano Mg_xSi_y precipitates. The latter are obtained via a heat treatment to enhance the alloy's strengthening and are dissolved under ion-irradiation as observed in the work of Flament et al., 2017. After the dissolution of the age hardening nano Mg_xSi_y precipitates, free Mg and Si

atoms create new Mg_xSi_y precipitates with a different morphology. However, the constituent micron-sized fragilizing particles are not affected by irradiation. Therefore, these theses ([Flament, 2015; Garric, 2019]) allow to understand the nature of submicron Cr and Mn-rich dispersoids as well as the evolution of nano precipitates during irradiation. Nonetheless, the effect of the studied precipitates on the fracture toughness is not covered in these theses.

- Petit, 2018; Rekik, 2017; Shen, 2012 are focused on the mechanical behavior of the unirradiated and mildly irradiated 6061-T6 alloys. Shen, 2012 observes damage mechanisms under tensile loading at the microscopic level. Mg_2Si and Fe-rich particles break and give birth to voids in the aluminum matrix. The nucleated voids grow under plastic strain and create microscopic cracks that lead to complete structure failure. Therefore, the work of Shen, 2012 allows to understand the role of constituent micron-sized fragilizing particles during damage at the microscopic scale. Furthermore, Shen, 2012 investigates the effect of anisotropic plasticity on the observed damage micromechanisms which is out of scope regarding the current study. Petit, 2018 studies the effect of age hardening nano Mg_xSi_y precipitates on the fracture toughness of the unirradiated alloy. Besides, Petit, 2018 carries out an experimental investigation on a mildly irradiated 6061-T6 alloy. The yield and tensile strengths increase due to neutron radiation while the fracture toughness remains constant. Having said that, the fracture toughness of the irradiated alloy is still not stimulated in the mentioned theses.

The above cited theses provide a better comprehension regarding the damage mechanisms in the unirradiated alloy as well as the microstructural changes under irradiation. There is still an unfilled gap regarding the modeling of the irradiated alloy's behavior. The main objective of the current *PhD* is to fill this gap by simulating the fracture toughness observed in the literature review, graph shown in fig. 1.3. In order to develop a physics-based model that can predict the fracture toughness of the irradiated 6061-T6 alloys, the following research hypotheses are made:

1. Hypothesis 1: Ductile damage in the 6061-T6 alloy is initiated by failure of the macroscopic fragilizing Mg_2Si and Fe-rich particles that create voids in the aluminum matrix (i. e. void nucleation). This is followed by void growth and coalescence. The Mg_2Si and Fe-rich particles are not impacted by radiation. Therefore, it is supposed in this thesis that the damage micro-mechanisms (void nucleation, growth and coalescence) of the unirradiated alloy are not altered after irradiation.

2. Hypothesis 2: The strengthening nano Mg_xSi_y precipitates obtained during age hardening are dissolved under irradiation. A new fine Mg_xSi_y phase is created due to the transmutation of aluminum to silicon. The fine irradiation-induced precipitates lead to a significant increase in strength and drop in ductility.

Therefore, it is supposed in this thesis that the irradiation-induced Mg_xSi_y phase affects the elastic-plastic behavior of the alloy.

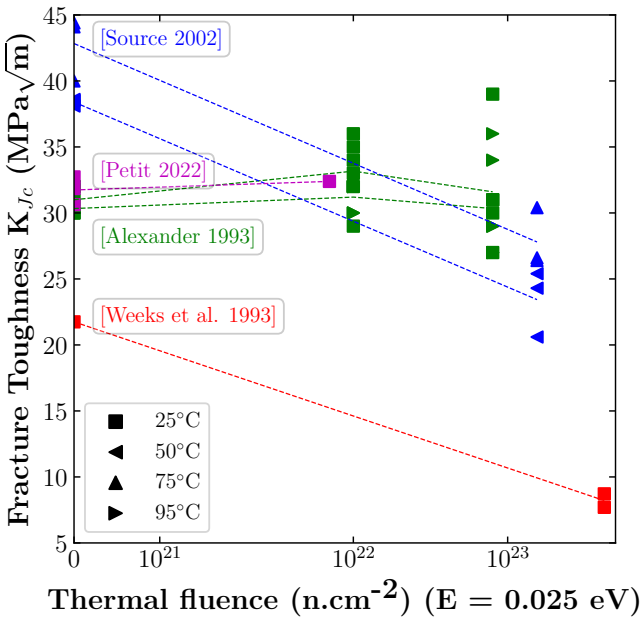

Figure 1.3: Fracture toughness results of irradiated 6061-T6 samples tested at different temperatures. Samples are irradiated in the HFIR [Alexander, 1993] and HFBR [Weeks et al., 1993]. [Source 2002] is unpublished research.

The above made hypotheses allow to divide the physical model into two parts: a damage model (independent from the radiation dose) and an elastic-plastic hardening model that varies as a function of the radiation dose. Consequently, the damage mechanisms can be investigated on the unirradiated alloy for economic and safety reasons. The *PhD* thesis objectives are divided as follows:

1. Objective 1: Understand the void nucleation, growth and coalescence mechanisms via investigations on the unirradiated 6061-T6 alloy. The damage model is to be calibrated based on experimental evidence. However, damage strongly depends on the stress triaxiality. The latter accelerates damage. Therefore, the experimental investigations on the unirradiated 6061-T6 alloy must be carried out on a pertinent range of stress triaxiality.

2. Objective 2: Develop a phenomenological elastic-plastic hardening model that is based on the available tensile results (irradiated alloy) in the literature. An appropriate range of Φ_{th} and R_Φ must be considered to model the alloy's behavior at different stages in the JHR's lifespan.

3. Objective 3: Decorrelate the effect of strengthening and strain hardening drop on the overall fracture toughness. The radiation damage discussed earlier lead to a rapid increase in the yield strength and a significant decrease in strain hardening

capacity. This investigation does not necessarily require irradiated materials. The study can be carried out on heat treated 6061 alloys with different yield strength and strain hardening levels.

The above mentioned objectives can allow to validate or disprove the research hypotheses. Once the two parts of the physical model are developed, the irradiated material can be simulated to see if it can predict results in fig. 1.3.

PhD manuscript outline The following outline gives an overview of the manuscript plan:

Chapter 2: *Literature review:* This chapter offers a literature review over the principal scientific topics: aluminum alloys 6061, ductile failure in the 6061 aluminum alloy and radiation damage in the 6061 aluminum alloy.

Chapter 3: *Analytical formula for optimum GTN q_1 and q_2 parameters:* This chapter gives an overview regarding the tensile experimental technique used to calibrate the elastic-plastic behavior beyond necking. The experimental techniques illustrated in this chapter are used as is in chapters 5 and 6.

Chapter 4: *Edge tracing technique to study post–necking behavior and failure in Al–alloys and anisotropic plasticity in line pipe steels:* The chosen damage model aims to predict void nucleation, growth and coalescence in ductile alloys. This chapter elaborates the calibration process of **void growth** parameters.

Chapter 5: *Ductile failure in aluminum alloys at low, intermediate and high stress triaxiality:* This chapter explains the calibration process of **void nucleation and coalescence** parameters in the unirradiated alloy: 6061-T6-BE. In order to challenge to calibrated damage model, a wide range of stress triaxialites ($0.33 - - - 3$) is simulated: simple and notched tension tensile samples presented in chapter 3 as well as compact-tension samples presented in the current chapter. This chapter along with the previous chapters (3, 4 and 5) fulfill objective 1.

Chapter 6: *Strain hardening and strength effect on the fracture behavior of the 6061 aluminum alloys:* The aim of this chapter is to fulfill objective 3. A different 6061 alloy is used in this chapter (see table 1.1 for a list of the studied alloys in this *PhD* thesis). The yield strength and hardening capacity of the 6061 alloy can be modified by an age hardening heat treatment. At a constant heat treatment temperature, the treatment time results in different strengths. Therefore, alloys in this chapter are called T6+HT+$x$hr as shown in table 1.1, where x refers to the age hardening time. The fracture behavior of the 5 tested materials is modeled using the calibrated model in chapter 5.

Chapter 7: *Phenomenological approach for modeling the radiation–induced hardening in 6061 aluminum alloys:* This chapter illustrates the methodology for developing the

phenomenological elastic-plastic model used to express the plastic flow as a function of the thermal fluence and R_Φ. This chapter fulfills objective 2.

Chapter 8: *Neutron radiation effect on the fracture behavior of the 6061 aluminum alloy:* This chapter is the final outcome of the above chapters. The calibrated damage model is coupled with the phenomenological elastic-plastic flow law to simulate the fracture toughness in the irradiated 6061-T6 alloy.

Figure 1.4 recaps the *PhD* manuscript plan detailed above.

Table 1.1: Nomenclature of studied materials in this *PhD* thesis

	CHAPTERS	STUDIED MATERIAL
Objective 1	4, 5	6061-T6-BE
Objective 3	6	T6 AR & T6+HT+$x$hr

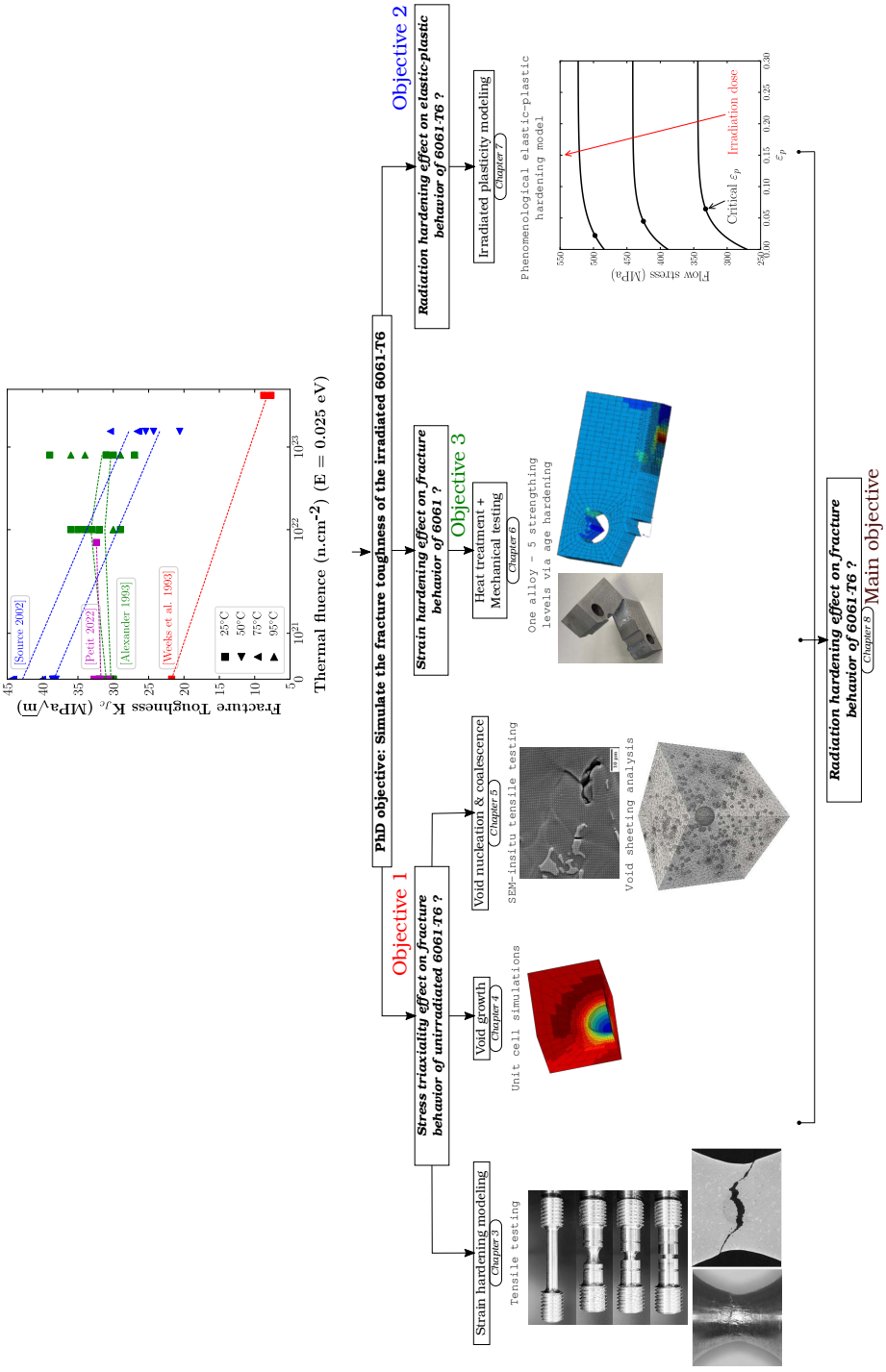

Figure 1.4: Recap over the *PhD* manuscript plan detailed above. PhD principal objective: Model the fracture toughess of the irradiated 6061-T6 alloy.

BIBLIOGRAPHY

ASME (1994). *Use of 6061-T6 and 6061-T651 Aluminum for Class 1 Nuclear Components, Section III, Division 1, Cases of Boiler and Pressure Vessel Code, Supplement 10-NC*. Technical report. American Society of Mechanical Engineers: New York (see p. 5).

Alexander, D. (1993). 'The Effect of Irradiation on the Mechanical Properties of 6061-T651 Aluminum.' In: *Effects of Radiation on Mater.*, pages 1151–1167. DOI: 10.2172/10162906 (see pp. 3, 7).

Alexander, D. (1999). 'The Effect of Irradiation on the Mechanical Properties of 6061-T651 Aluminum Base Metal and Weldments.' In: *Effects of Radiation on Mater.*, pages 1027–1044. DOI: 10.1520/STP13918S (see pp. 3, 4).

Farrel, K. (2011). 'A Spectral Effect on Phase Evolution in Neutron-Irradiated Aluminum?' In: *MRS Proceedings*. Volume 373. DOI: 10.1557/PROC-373-165 (see pp. 3, 4).

Farrell, K. (2012). 'Performance of Aluminum in Research Reactors.' In: *Comprehensive Nuclear Materials*, 147–175. DOI: 10.1016/B978-0-08-056033-5.00113-0 (see p. 3).

Farrell, K. and R. King (1979). 'Tensile Properties of Neutron-Irradiated 6061 Aluminum Alloy in Annealed and Precipitation-Hardened Conditions.' In: *Effects of Radiation on Mater.*, pages 440–449. DOI: 10.1520/STP38180S (see pp. 3, 4).

Flament, C. (2015). 'Etude des évolutions microstructurales sous irradiation de l'alliage d'aluminium 6061-T6.' PhD thesis. Université Grenoble Alpes (see pp. 3, 5, 6).

Flament, C. et al. (2017). 'Stability of β'' nano-phases in Al-Mg-Si(-Cu) alloy under high dose ion irradiation.' In: *Acta Mater.* 128, pages 64–76. ISSN: 1359-6454. DOI: 10.1016/j.actamat.2017.01.044 (see p. 5).

Garric, V. (2019). 'Etude du gonflement par cavités d'un alliage d'aluminium irradié sous faisceau d'ions.' PhD thesis. Université Grenoble Alpes (see pp. 5, 6).

Kolluri, M. (2016). 'Neutron Irradiation Effects in 5xxx and 6xxx Series Aluminum Alloys: A Literature Review.' In: *Radiation Effects in Mat.*, pages 393–411. DOI: 10.5772/63294 (see p. 3).

Petit, T. (2018). 'Compréhension et modélisation d'essais de ténacité avec pop-in: application á l'aluminium 6061-T6 et influence de l'irradiation neutronique.' PhD thesis. Ecole Nationale Supérieure des Mines de Paris (see p. 6).

Rekik, W. (2017). 'Etude de la ténacité d'une soudure en undermatch: Application á la tenue mécanique de la jonction soudé FE en Al6061-T6.' PhD thesis. Ecole National de Mécanique et d'Aéronautique (see p. 6).

Shen, Y. (Dec. 2012). 'Comportement et endommagement des alliages d'aluminium 6061-T6: approche micromécanique.' PhD thesis. Ecole Nationale Supérieure des Mines de Paris (see p. 6).

Was, G. (2017). 'Fundamentals of Radiation Materials Science.' In: Springer-Verlag New York. Chapter 2, pages 3–76. DOI: 10.1007/978-1-4939-3438-6 (see p. 3).

Weeks, J. et al. (1993). 'Effects of High Thermal Neutron Fluences on Type 6061 Aluminum.' In: *Effects of Radiation on Mater.*, pages 1168–1182 (see pp. 3, 4, 7).

Yahr, G. T. (1997). 'Prevention of Nonductile Fracture in 6061-T6 Aluminum Nuclear Pressure Vessels.' In: *J. Pressure Vessel Technol.* 119 (2), pages 150–156. DOI: 10.1115/1.2842276 (see p. 4).

2

LITERATURE REVIEW

RÉSUMÉ

Dans ce chapitre, une large revue est présentée pour couvrir les principaux sujets scientifiques rappelés dans l'introduction de la thèse. Le chapitre est divisé en trois sections principales. Chaque section commence par une question à laquelle il est répondu à la fin de la section.

Preamble In this chapter, a wide review is presented to cover the main scientific subjects recalled in the thesis introduction. The chapter is divided into three main sections. Each section starts with a question that is answered at the end of the section.

2.1 ALUMINUM ALLOY 6061-T6

Inquiry Given the chemical composition and fabrication process of a 6061 aluminum alloy, how can the yield strength and strain hardening capacity be changed via a heat treatment process to obtain different strengthening levels for objective 3?

2.1.1 *General nomenclature of aluminum alloys*

Aluminum alloys are unique when it comes to combining several properties needed in today's engineering applications that require ecological, economical, and attractive versatile metallic materials. Good thermal and electrical conductivity, ease of manufacturing, low density (2.7 g/cm^3 compared to 7.8 g/cm^3 in steels), and corrosion resistivity are among the several properties that distinguish aluminum alloys. Consequently, the latter are the most used structural metals after steels [Davis, 2001].

Aluminum alloys are firstly classified according to their shaping process: wrought and cast alloys. They are then divided into heat treatable and work hardened alloys, fig. 2.1. The alloy is heat treatable if it responds to thermal treatments based on phase solubility as quenching, age/precipitation hardening [Develay, 1992]. On the contrary, a work hardened alloy gains its final properties by mechanical reduction combined

with annealing process(es) [Garat, 2012]. Nomenclatures have been developed for wrought and cast alloys. The latter are presented by 3 digits followed by a decimal value while wrought alloys are presented by 4 digits as shown in table 2.1. The first digit indicates the principal alloying element(s). The second digit designates the variation with respect to the original alloy (i. e. 0 for the original composition, 1 for the first variation, etc.) The last two digits indicate the additional elements.

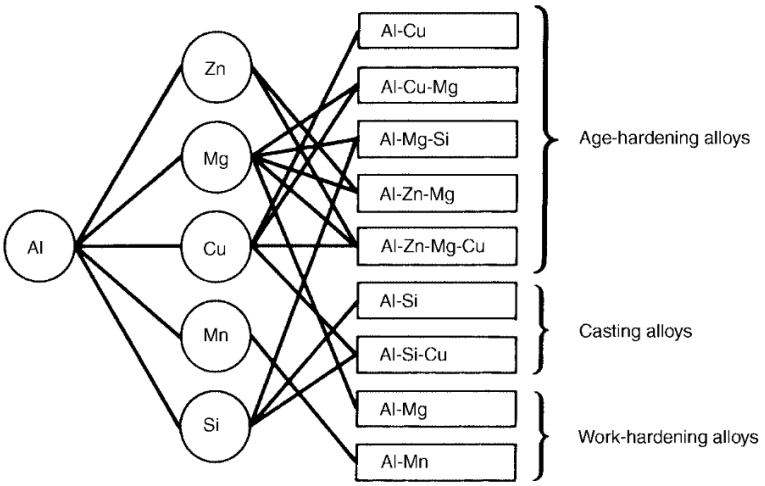

Figure 2.1: Principal aluminum alloys (courtesy of Davis, 2001)

Table 2.1: Classification of wrought aluminum alloys according to their main alloying element(s) and strengthening mechanism [Develay, 1992]

	ALUMINUM SERIES	ALLOY SYSTEM
Work hardening alloys	*1xxx*	*(>99%wt. Al)*
	3xxx	*Mn*
	4xxx	*Si*
	5xxx	*Mg*
Heat treatable alloys	*2xxx*	*Cu*
	6xxx	*Mg-Si*
	7xxx	*Zn*

The 6xxx series is an age hardening AlMgSi alloy widely used in modern technology requiring metals with a high strength-to-weight ratios. The strength of heat treatable alloys (2xxx, 6xxx and 7xxx) is enhanced via the precipitation of secondary phases during a heat treatment process which involves three basic steps: homogenization, reheat and age hardening. An alloy is heat treatable if it has a terminal solid solution that has a decreasing solid solubility as the temperature decreases [Prasad et al., 2017]. The nomenclature of age hardening alloys is usually longer as the temper state is added to the alloy's series (e. g. 6061-T6). The temper letter following the 4-digit code specifies the thermo-mechanical treatments applied to the alloy in order to achieve

the desired properties [Develay, 1992]. For illustration, the AlMgSi alloy is usually tempered to a "T" state. This means that the alloy reached a stable temper state via a heat treatment [Kaufman, 2000]. The temper letter is always followed by a digit indicating the combination of age hardening heat treatment procedures. The temper letter does not refer to the reheat and temper which can be carried out regardless of the temper state. The different heat treatments regarding the 6xxx alloy in a temper state are [Develay, 1992; Kaufman, 2000]:

- **T4:** Precipitation hardening is obtained by natural hardening (i. e. without extra heat treatment after quenching) to obtain a high ratio of tensile to yield strength (work hardening capacity) and high fracture toughness. This temper is also called "under-aged".
- **T6:** Quenching is followed by an age hardening treatment for a given time at a constant temperature to obtain fine precipitates and the highest strength level. The fracture toughness is lower than the T4 temper. This temper is also called "peak-aged".
- **T7:** The age hardening time or temperature are higher than the treatment of the T6 temper. The strength is lower than the T6 temper. The strength is sacrificed to enhance other properties as the reduction of warpage or distortion during machining. This temper is also called "over-aged".

2.1.2 *Microstructure of the 6061-T6 aluminum alloy*

The 6061-T6 is a multi phase alloy of which the mechanical properties are determined by the microstructure resulting from the fabrication process and the heat treatment. The phases present in the α-Al matrix are formed during the solidification process and evolve during the T6 heat treatment. The list below categorizes the major precipitates found in an 6061-T6 alloy in the descending order of size:

- **Large constituent particles (1 μm < particle size < 10 μm):** They are formed due to the interaction between alloying elements (Mg and Si that result in the two-component phase β-Mg_2Si) and between elements that are difficult to remove in the course of metallurgical process (Fe that results in AlFeSi intermetallic phases) [Totten et al., 2018]. The heat treatment following the solidification (homogenization, reheat and age hardening) have an influence on the chemical composition and morphology of microstructure phase constituents. Figure 2.2 shows a typical complete heat treatment process of a 6xxx alloy from the as cast till the age hardening phase. The homogenization process (performed at temperatures between 530 and 600°C) lead to a homogeneous distribution of alloy components in the α-Al matrix and the partial dissolution of β-Mg_2Si

particles in solid solution α-Al [Totten et al., 2018]. The dissolution of β-Mg_2Si is depends mainly on the temperature and not the homogenization time. The dissolution of β-Mg_2Si is intensive during the first hours of homogenization and then tends to saturate [Totten et al., 2018]. The β-Al_5FeSi plate-like phase formed during solidification is transformed during homogenization to a spherical α-$Al_{12}(Fe_xMn_{(1-x)})_3Si$ phase [Belov et al., 2005; Kuijpers et al., 2003]. The β-Al_5FeSi phase reduces the plastic workability of 6xxx alloys as it cracks easily. The three above mentioned phases (β-Mg_2Si, β-Al_5FeSi and α-$Al_12(Fe_xMn_{(1-x)})_3Si$) are damage initiators in the 6061 alloy. They tend to fail and create voids in the aluminum matrix [Lassance et al., 2007].

- **Dispersoids (50 nm < particle diameter < 500 nm):** Dispersoid particles are beneficial for wrought alloys during the thermomechanical processing. They control recrystallization and grain growth [Totten et al., 2018]. However, their precipitation must be controlled to obtain finely distributed particles ($< 0.3\ \mu$m) that are mainly composed of Cr and Mn. The maximum solubility of Cr and Mn in solid solution is 0.35 and 0.6% respectively [Massalski et al., 1986]. This means that the amount of Cr and Mn that can be retained in solid solution is very limited. Therefore, the maximum volume fraction of dispersoids that can be precipitated is small ($< 1\%$) [Totten et al., 2018]. The dispersoids' size explains why they do not contribute to the material strengthening. Apart from strengthening, dispersoids may have a harmful influence during fracture [Fabrègue et al., 2008; Hannard et al., 2018]. They might lead to a second population of void nucleation (primary population: large constituent particles discussed above). This depends on their size and distribution in the matrix.

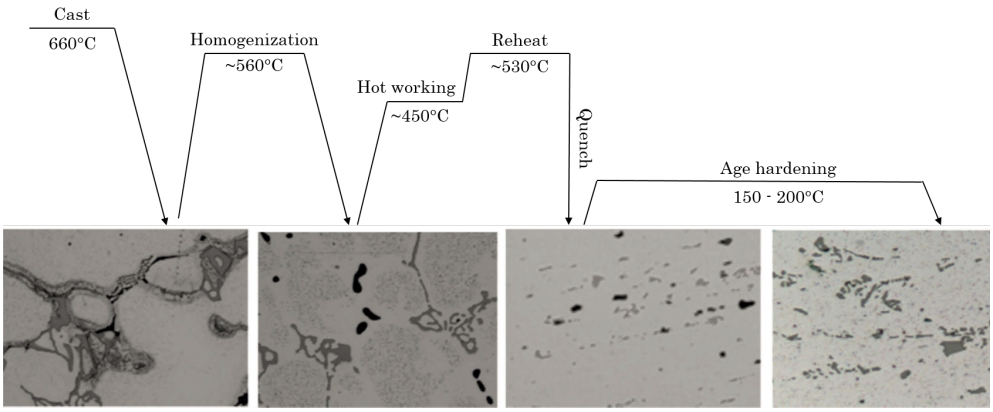

Figure 2.2: Microstructural evolution during the T6 heat treatment process: homogenization, reheat and age hardening [Totten et al., 2018]

- **Strengthening particles (10 nm < particle length < 50 nm):** During the reheat process, shown in fig. 2.2, $\beta - Mg_2Si$ dissolve in solid solution α-Al. The latter is in a thermodynamic disequilibrium. During the age hardening treatment

shown in fig. 2.2, the strengthening phase precipitates according to the following sequence [Edwards et al., 1998; Lars et al., 2000]:

$$\alpha-\text{Al} \rightarrow GP \rightarrow \beta'' \rightarrow \beta' \rightarrow \beta(Mg_xSi_y) \tag{2.1}$$

where α-Al is the solutionized solid solution, GP are the Guinier-Preston zones, β'' are β' are the strengthening nano-sized metastable phases, and $\beta(Mg_xSi_y)$ is the stable equilibrium phase.

At an early stage during age hardening, Mg and Si atoms in the α-Al solutionized solid solution form spherical GP zones that are coherent with the matrix and that have a diameter ranging from 1-3 nm [Totten et al., 2018]. The GP zones increase the alloy's yield strength while maintaining a good strain hardening capacity. Later during the age hardening treatment, a highly dispersed needle-like coherent β'' phase is formed. The β'' phase gives the maximum strengthening (peak-aged alloy) due to their high density [Dubost et al., 1991]. Afterwards, the metastable semi coherent β' forms as lamellae or rods parallel to the direction $< 100 >$. At the final stage of age hardening, the stable non coherent $\beta(Mg_2Si)$ forms as lamellae and have the least strengthening effect. The precipitation process of the strengthening phases in the 6061 alloy is more complicated than it is noted in eq. (2.1) and is extensively illustrated in the literature by using highly advanced techniques of microscopic observations [Edwards et al., 1998; Flament, 2015; Matsuda et al., 2000; Totten et al., 2018].

Inquiry answer It is now clear how the age hardening process can lead to different morphology and size of nano strengthening particles. This leads to different yield strengths and hardening capacities for objective 3. The lowest yield strength and highest hardening capacity require the least precipitation hardening time/temperature. The highest yield strength requires a combination of time and temperature that result in a peak-aged alloy. This relationship between the strengthening level and the nano strengthening phases is explained in chapter 6. Therefore, several strengthening levels can be obtained using a 6061 aluminum alloy. This should allow decorrelating the effect of strengthening and ductility drop on the overall fracture toughness.

2.2 DUCTILE FAILURE IN THE 6061 ALUMINUM ALLOY

Inquiry What are the microscopic damage phenomena in the 6061 aluminum alloy during the process of ductile failure?

2.2.1 *General introduction to ductile failure*

The failure of structural metals is widely investigated over the past decades. Understanding the damage mechanisms is of a great importance to predict the lifetime of mechanical components and design materials with higher performances. Engineering components fabricated from ductile metals tend to fail by tearing, which is the observed macroscopic evidence. However, prior this macroscopic observation, failure takes place at the microscopic level of the material. The most commonly observed microscopic damage mechanisms in ductile metals are: void nucleation, void growth and void coalescence [Garrison et al., 1987; Petch, 1954; Puttick, 1959]. The different failure mechanisms covered by the term "ductile failure" are summarized in the work of Tekoğlu et al., 2015 as illustrated in fig. 2.3 (a similar theoretical representation of the failure mechanisms is presented in the work of Noell et al., 2018). This schematic presentation is a theoretical point of view regarding the existing ductile failure mechanisms. There is no sharp transition between the shown mechanisms:

1. Mechanism 1: occurs in pure metals and single crystal metals which fail without damage due to the absence of void nucleation sites.
2. Mechanism 2: takes place when the plastic strain is localized in shear bands. As a result, void nucleation, growth and coalescence take place in the localization shear bands. Morgeneyer et al., 2014 show that plastic localization takes place in front of a crack in an aluminum alloy before void nucleation.
3. Mechanism 3: corresponds to void nucleation in the material before the macroscopic localization. The accumulated porosity has a significant material softening effect that takes over the strain hardening. This leads to plastic localization in a shear band. The Gurson constitutive model [Gurson, 1977] incorporates the porosity as a variable to account for material softening prior localization.
4. Mechanism 4: void coalescence takes place without prior localization. The onset of void coalescence dictates the onset of macroscopic localization. Tekoğlu et al., 2015 investigates cases where mechanisms 3 and 4 occur separately or simultaneously.
5. Mechanism 5: is a sub-category of mechanism 4 with a single difference: void coalescence takes place in a localized manner over a few voids (versus macroscopic localization over many voids, i. e. mechanism 4).

2.2.2 *Experimental evidence of void nucleation, growth and coalescence in the 6061 aluminum alloy*

The documented observations in the literature regarding the damage of the 6061-T6 alloy are as follows:

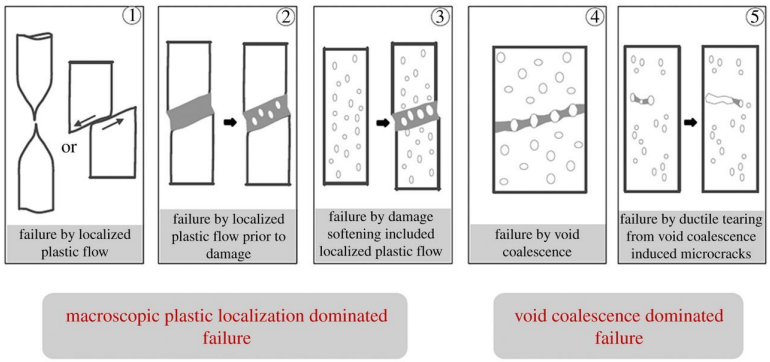

Figure 2.3: Different failure mechanisms covered by the term "ductile failure" as summarized in the work of Tekoğlu et al., 2015

1. **Void nucleation:** is an instantaneous event taking place when particles in the metallic matrix fracture or get detached by interphase–interface decohesion [Argon et al., 1975; Tanaka et al., 1970]. These secondary phases act like "seeds" for nucleating voids. Void nucleation can be classified into two categories: void nucleation by particle fragmentation and void nucleation by particle–interface decohesion [Caceres et al., 1996; Chu et al., 1980; Le Roy et al., 1981]. Both types of void nucleation can take place simultaneously in the 6061 alloy as shown in the 5182 aluminum alloy studied in the work of Butcher et al., 2011. For a given alloy with its secondary phases, the factors that favor one mode of nucleation over the other are: matrix elastic-plastic properties (yield strength and hardening capacity), particle shape and orientation with respect to the loading direction [Benzerga et al., 2010].

   Under plastic strain, the differences in stiffness between secondary phases and the metallic matrix lead to void nucleation at the particle–matrix interface. This is referred to as nucleation by particle decohesion [Babout et al., 2004]. Secondary phases can also fracture and create voids.

   Figure 2.4 illustrates the void nucleation mechanisms in a 6061-T6 alloy. The micron-sized particles: Mg_2Si (diameter $\sim 5\ \mu m$) and intermetallics Al(FeMn)Si (length $1 - 10\ \mu m$) fracture during loading as displayed in fig. 2.4. Void nucleation by particle decohesion takes place at the Mg_2Si–matrix interface. Moreover, the Mg_2Si particles fail at an early stage (during the elastic phase) as it observed in the work of Maire et al., 2005; Petit et al., 2019; Shen et al., 2013. The Mg_2Si particles can be considered as pre-existing voids when modeling damage in 6xxx alloys. However, intermetallic particles are stronger and fail under plastic strain. The volume fraction of intermetallic particles in 6061 alloys is around 1% [Ghahremaninezhad et al., 2012; Lassance et al., 2007] and can reach 2% in some cases [Petit et al., 2019]. This leads to the fact that damage in 6xxx

alloys is “nucleation controlled”. This term refers to alloys that mainly fail due to nucleated voids.

The above presented void nucleation mechanisms are focused on the 6061 aluminum alloy. Other void nucleation mechanisms can be observed in other metals. Void nucleation can also be triggered by submicron particles [Chan et al., 1981; Querin et al., 2007]. Voids can nucleate at grain boundaries, triple junctions or twin intersections in pure metals [Garrison et al., 1987; Noell et al., 2017]. However, this is out of scope for the 6061 alloy which has micron-sized particles that activate void nucleation. Besides, there are pre-existing voids in some metals that are taken into account when modeling the material’s behavior but are not considered as nucleated voids [Zhang et al., 2000].

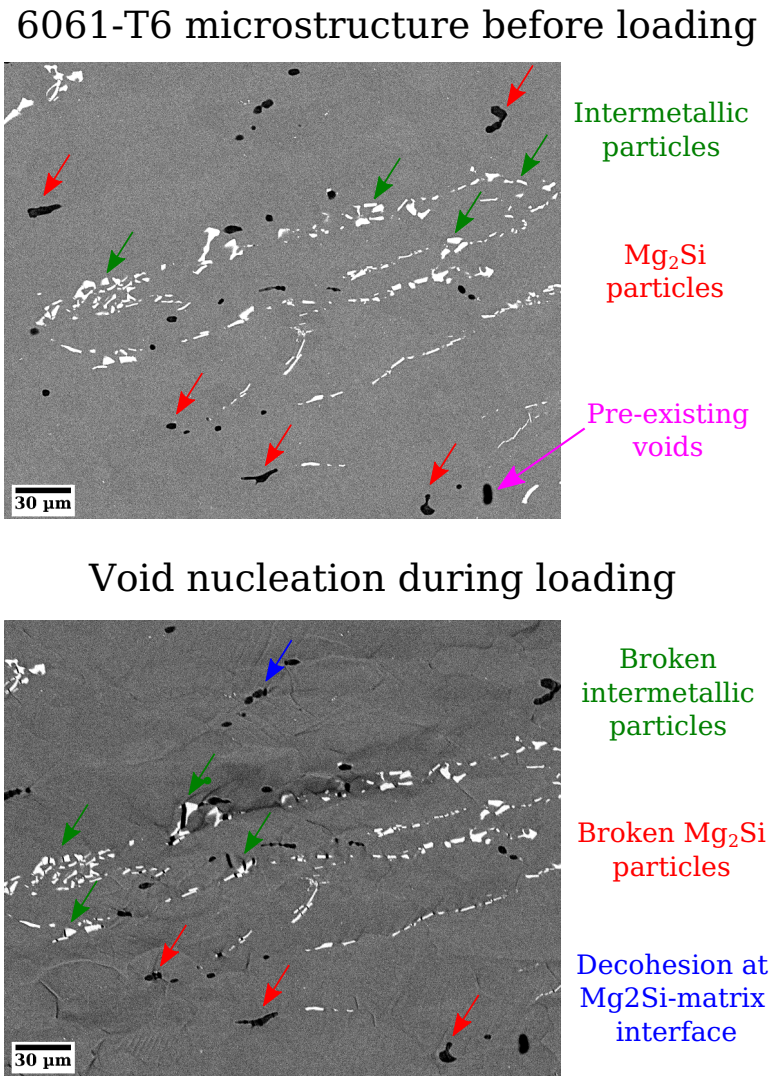

Figure 2.4: Void nucleation mechanisms in a 6061-T6 aluminum alloy. Mg_2Si and intermetallic particles fail and create voids in the metallic matrix.

2. **Void growth:** nucleated and pre-existing voids grow in shape and volume under plastic strain. A seminal observation is made during an experimental study carried out on uniaxial tensile steel samples tested under hydrostatic pressure [Bridgman, 1945]. The specimens tested under higher pressure support larger strains and more necking prior to rupture. Liu et al., 1993 carried out the same tensile tests under superimposed hydrostatic pressure on 6061 aluminum samples. The conclusions are in agreement with Bridgman, 1945. As a result, early developed ductile damage models [Mc Clintock, 1968; Rice et al., 1969] assume that void growth in an elastic-plastic matrix depends on the far-field hydrostatic stress. However, void growth in the 6061-T6 alloy is subdued when compared to void growth in steels [Ghahremaninezhad et al., 2013]. This is explained by the above mentioned fact that damage in the 6061-T6 alloy is "nucleation controlled". Once damage is initiated in the form of fractured intermetallic particles, subsequent failure takes place with a low increase in the overall strain.

3. **Void coalescence:** voids link together by one of the three known mechanisms [Benzerga et al., 2010; Pineau et al., 2016]: internal necking, void sheeting mechanism and necklace coalescence (less common). Internal necking is the most common void-linking mechanism occurring in the intervoid ligament. An example of void coalescence by internal necking in a 6061-T6 alloy is illustrated on the left in fig. 2.5. The void sheeting mechanism (also known as coalescence in a micro-shear band) takes place in materials with two populations of particles that are different in size [Cox et al., 1974; Prince et al., 1979; Walsh et al., 1989]. A secondary population of voids nucleate in a finely dispersed manner over the disperoid particles [Fabrègue et al., 2008; Hahn et al., 1975]. Despite the fact that the secondary population of voids are smaller in size than the voids resulting from fracture of intermetallic particles, they still lead to a decrease in the global ductility since void growth is suddenly interrupted while the voids are still apart [Benzerga et al., 2010; Hannard et al., 2018; Liu et al., 2011; Trejo-Navas et al., 2018]. An example of void coalescence by void sheeting in a 6061-T6 alloy is displayed on the right in fig. 2.5. Nonetheless, it is claimed that void coalescence by internal necking is the predominating mechanism in the mid-thickness of tested 6061-T6 samples where the stress triaxiality is at its highest level [Shen et al., 2013].

2.2.3 *Damage modeling in the 6061 aluminum alloy*

Damage modeling is an old problem that dates from 1500 when Léonard de Vinci attempts to explain failure via mechanics. Years later, failure theories are developed by linking the deformation and stress in a representative elementary volume (e. g. Hosford [Hosford, 1972], Tresca, von-Mises, Hill [Hill, 1965]). However, it is not until

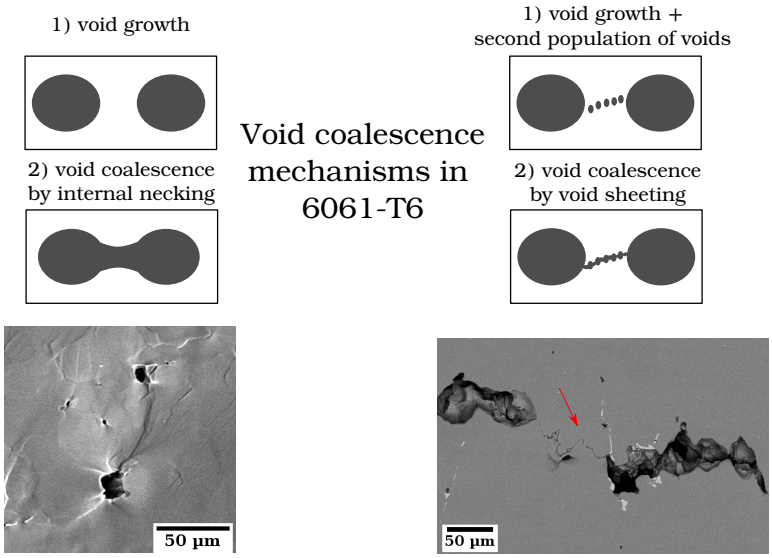

Figure 2.5: Left: void coalescence by internal necking, right: void coalescence by void sheeting in a 6061-T6 alloy

1958 that Kachanov [Kachanov, 1958] introduces the concept of effective stress. This concept is based on considering a fictitious undamaged material and comparing it with the actual damaged material. Kachanov's idea is revisted by other researchers to develop other models as: Lemaitre (France) [Lemaitre, 1985], Hult (Sweden), Leckie (England), Murakami (Japan). Lemaitre model is used by Hanssen et al., 2002 to model damage in 6061 alloys. The effective stress $\underline{\tilde{\sigma}}$ in the Lemaitre damage theory is defined as follows:

$$\underline{\tilde{\sigma}} = \frac{\underline{\sigma}}{1 - D} \tag{2.2}$$

where $\underline{\sigma}$ is the Cauchy stress tensor, D is a damage variable (i. e. $D = 0$ corresponds to the undamaged state, $0 < D < 1$ characterizes the damage state and finally $D = 1$ corresponds to the rupture of the material). The difficulty when using the Lemaitre damage theory is the parameters identification process. All parameters in Lemaitre model must be identified via experimental methods and cannot be fitted [Mkaddem et al., 2004]. Therefore, the Lemaitre damage theory is considered as a phenomenological approach.

There are other models that describe void growth in an infinite perfectly plastic matrix using constitutive equations. Mc Clintock, 1968 and Rice et al., 1969 develop the early micromechanical models describing the growth of isolated voids. The Rice and Tracey model is used to describe void growth in a 6061 alloy in the work of Shen, 2012 and Hannard et al., 2016. The drawback of both models is that they consider isolated voids that do not interact and do not affect the material's overall behavior (i. e. no material softening).

Later, Gurson [Gurson, 1977] establishes a constitutive formulation that describes void growth in a finite matrix by incorporating the porosity (f) as a damage variable

in the model. The Gurson model is then improved in the work of Chu et al., 1980; Tvergaard, 1981, 1982 to account for the strain hardening effect as well as the void nucleation and coalescence phases. The improved model is referred to as the GTN model. Several authors modified the Gurson constitutive equations to take into account different factors as: kinematic hardening [Besson et al., 2003; Leblond et al., 1995; Mear et al., 1985], plastic anisotropy [Benzerga et al., 2001; Doege et al., 1995; Grange et al., 2000; Liao et al., 1997; Rivalin et al., 2000], void shape effect [Gologanu et al., 1993, 1994, 1997; Pardoen et al., 2000], viscoplasticity [Klocker et al., 2003; Leblond et al., 1994; Moran et al., 1990; Tvergaard, 1990], two void populations [Perrin et al., 2000], void size effect [Wen et al., 2005], void coalescence criteria [Pardoen et al., 2000; Thomason, 1968; Tvergaard et al., 1984; Zhang et al., 1995]. The several extensions are detailed in the work of Lassance et al., 2007. Moreover, Besson, 2010 and Benzerga et al., 2016 offer extensive reviews regarding the Gurson model and its extensions.

Authors in the literature that use the Gurson equations and its extensions to model damage in the 6061 alloy are numerous. Table 2.2 recapitulates the published work in which the Gurson model is applied to the 6061 alloy. The nucleation and coalescence models of each published work are listed in table 2.2 to emphasize the fact that several nucleation and coalescence criteria can be used. This is to be discussed below. Moreover, the modeled samples in each work are listed in table 2.2 to highlight the fact that the model parameters are usually calibrated over a given range of stress triaxiality.

Table 2.2: Authors that model void nucleation, growth and coalescence in 6xxx alloys using the Gurson or Rice and Tracey models

Author(s)	Aluminum alloy	Damage model	Nucleation model	Coalescence model	Modeled sample(s)
He et al., 2021	6061	Gurson extension for shear	Strain-based exponential law [Chu et al., 1980]	f_*	Flat simple, notched and shear tensile
Petit et al., 2019	6061	GTN	Stress-based power law	f_*	Compact-tension (CT)
Nguyen et al., 2018	6061-T6	Gurson extension for shear	Strain-based exponential law [Chu et al., 1980]	f_*	Flat simple, notched and shear tensile + Axisymmetric notched tensile
Safdarian, 2018	6061-T6	GTN	Strain-based exponential law [Chu et al., 1980]	f_*	Flat punch test samples
Hannard et al., 2016	6061	Rice and Tracey [Rice et al., 1969]	Stress-based Weibull law	Thomason [Thomason, 1990]	Cellular automaton
Yu et al., 2014	6061	Gurson extension for shear	Strain-based exponential law [Chu et al., 1980]	f_*	Flat tensile
Shen et al., 2013	6061	GTN	Strain-based exponential law [Chu et al., 1980]	f_*	Compact-tension (CT)

Author(s)	Aluminum alloy	Damage model	Nucleation model	Coalescence model	Modeled sample(s)
Simar et al., 2010	6005	Gurson extension [Gologanu et al., 1997]	Stress-based exponential law [Chu et al., 1980]	f_* + f_c given by Thomason criterion	Simple tensile bars
Lassance et al., 2007	6060	Gurson extension [Gologanu et al., 1997]	Stress-based Beremin model [Beremin, 1981]	Thomason [Thomason, 1990]	Simple and notched axisymmetric tensile
Huber et al., 2005	Al-Si11-Mg0.3	Gurson extension [Gologanu et al., 1997]	Stress threshold + strain-based polynomial	Thomason [Thomason, 1990]	Axisymmetric notched tensile

The constitutive equations as well as the derivatives of the Gurson model are fully detailed in A.1.1. The work of Broggiato et al., 2007; Faleskog et al., 1997; Kami et al., 2015; Kim et al., 2004; Li et al., 1994; Nguyen et al., 2018; Springmann et al., 2006; Zhang, 1996 propose experimental and numerical methods to calibrate the different GTN parameters. Unlike the Lemaitre model, some of the Gurson parameters can be adjusted via numerical fitting [Mkaddem et al., 2004]. The different nucleation and coalescence equations coupled with the Gurson model for modeling damage in the 6061 alloy are discussed below:

1. **Void nucleation:** can be divided into three categories: strain-based, stress-based and energy-based nucleation models. Energy-based nucleation models are adapted to small particles (< 25 nm in [Tanaka et al., 1970] and < 100 nm in [Benzerga et al., 2010]). The critical nucleation strain can be attained by the energy-based criterion for small particles. However, void nucleation in 6061 alloys takes place on micron-sized particles as discussed in section 2.2.2[1].

   Usually strain-based nucleation models are preferred as they are easy to implement in the finite element code. This explains why most of the cited authors in table 2.2 use the strain-based exponential nucleation law proposed by Chu et al., 1980 and shown in eq. (A.14). However, strain-based nucleation models do not account for the dependence of void nucleation on stress triaxiality [Benzerga et al., 2010]. A comparison between stress and strain-based nucleation models is carried out in the work of Needleman, 1987. The stress and strain-based nucleation models lead to quite different results. This is explained by the fact that the stress-based nucleation model leads to earlier plastic localization as nucleation depends on the hydrostatic tension. Another comparison between stress and strain-based nucleation models is carried out in a 5182 aluminum alloy in the work of Butcher et al., 2011. The cited authors conclude that the stress-based model is to be preferred for this main reason: the nucleation threshold strain depends on the loading condition and the stress state. To illustrate, the nucleation threshold strain determined on uniaxial tensile samples is not adapted to other stress states and loading conditions. Conversely, the nucleation stress threshold is less sensitive to the loading condition and transferable to other stress states. A comparison between a stress-and-strain-based nucleation and the Gaussian nucleation law proposed by Chu et al., 1980 is explained in the work of Petit et al., 2019. The cited authors model crack propagation in 6061 alloys. It is shown that the nucleation stress threshold depends on the hardening level of the material. Therefore, Petit et al., 2019 could not model 6061 alloys with different hardening levels using a strain-based nucleation model. However, the

1 Thomason, 1990 gives a general point of view regarding the role of stress and strain in void nucleation by stating: *"It is generally believed that large particles nucleate voids according to stress (particle cracking) while small particles (radius less than* 1 μm*) nucleate according to strain (particle debonding)"*

cited authors achieve good results over the different hardening levels by using a stress-and-strain-based nucleation model. Therefore, the different comparisons mentioned above highlight the fact that the stress-based nucleation model are adapted to model different stress triaxiality and hardening levels.

The early model proposed by Ashby, 1966 accounts for the particle decohesion from the matrix. The normal stress at the particle–matrix interface increases due to the accumulation of plastic strain. Void nucleation occurs when this normal stress exceeds a critical stress (model parameter). Argon, 1976 proposed a definition of the critical stress for void nucleation by particle decohesion:

$$\sigma_{inh} + \sigma_m = \sigma_c \tag{2.3}$$

where σ_{inh} is the interfacial tensile stress from the strain inhomogeneity, σ_m the mean stress and σ_c the critical stress for void nucleation. σ_{inh} is then defined as follows [Argon, 1976]:

$$\sigma_{inh} = k_A \, \sigma_{\text{eq}} \tag{2.4}$$

where k_A is a geometrical factor to account for different particle shapes: slender rods, platelets and spherical. The principal stress inside the particle is taken equal to σ_{inh}. The way σ_{inh} is expressed in the work of Argon, 1976 does not take into account the interaction between nucleated voids, especially when the particles' volume fraction is high ($> 1\%$) and the inter-particle distance is low ($\leq$ particle diameter). Argon et al., 1975 explains that the displacement incompatibility at the particle–matrix interface results in a "secondary plastic zone" around the particle. When the particles' volume fraction is small, the secondary plastic zones do not touch. Therefore, the σ_{inh} in eq. (2.4) is well adapted as the interfacial tensile stress is independent of the particle size and depends only on the local flow stress. However, Argon et al., 1975 propose another expression for σ_{inh} while considering a larger particle size which leads to the interaction between "secondary plastic zones". This results in added parameters in the expression of σ_{inh}:

$$\sigma_{inh} = k_A \, \sigma_{\text{eq}} + C_1 \frac{L_p}{R_p} + C_2 \left(\frac{R_p}{L_p} \varepsilon_p \right)^n \tag{2.5}$$

where L_p is the inter-particle distance, R_p the particle radius, C_1 and C_2 are material coefficients, n the strain hardening exponent and ε_p the macroscopic plastic strain. Even though Argon et al., 1975 assume that eq. (2.4) is adapted to low particle volume fraction ($< 1\%$), a heterogeneous distribution of particles can lead to a small inter-particle distance (in the particle-rich zone) and an interaction between secondary plastic zones.

The Beremin model [Beremin, 1981] defines the stress inside the particle as the sum of the stress in the matrix and an additional stress transfer arising from the deformation mismatch between the particle and the matrix. Particles are considered as brittle solids that fracture when the maximum principal stress in the particle reaches the nucleation critical stress:

$$\sigma_I^{\text{particle}} = \sigma_c \tag{2.6}$$

The maximum principal stress in the particle ($\sigma_I^{\text{particle}}$) can be given by using the Eshelby's theory [Eshelby, 1957] and the secant elastic-plastic modulus extension proposed by Berveiller and Zaoui [Berveiller et al., 1978] for the deforming matrix:

$$\sigma_I^{\text{particle}} = \sigma_I + k_b \, E_p \, \varepsilon_{\text{eq}} \tag{2.7}$$

where σ_I is the maximum principal stress in the matrix, k_b is a stress concentration factor that depends on the particle shape and orientation and E_p is the matrix secant modulus. The cited authors assume that E_p is much smaller than the particle's Youngs modulus. The elastic strain in the particle is neglected. Given the secant modulus $E_p = \sigma_{\text{eq}}/\varepsilon_{\text{eq}}$, eq. (2.7) can be written as follows:

$$\sigma_I^{\text{particle}} = \sigma_I + k_b \, \sigma_{\text{eq}} \tag{2.8}$$

Beremin, 1981 notice a strong temperature dependence in σ_c when comparing experimental results with the simulation carried out using eq. (2.8). Therefore, the cited authors recommend replacing the secant modulus (E_p) with the tangent modulus ($E_t = (\sigma_{\text{eq}} - \sigma_0)/\varepsilon_{\text{eq}}$) since since the strain inhomogeneity effect must not include the yield stress σ_0. Equation (2.8) can be rewritten as follows:

$$\sigma_I^{\text{particle}} = \sigma_I + k_b(\sigma_{\text{eq}} - \sigma_0) \tag{2.9}$$

The geometrical factor k_b is equal to 1 for a perfect spherical particles. However, k_b increases with increasing the particle aspect ratio (W) for a prolate particle ($W \gg 1$). More details concerning the evolution of k_b as a function of W are given in the work of Hannard, 2017.

2. **Void growth:** is driven by the q-parameters in the GTN model. The q_1 and q_2 are material parameters that are introduced to the Gurson model in the work of Tvergaard, 1981, 1982. The cited authors introduced the q-parameters to obtain good agreement between experimental and simulated stress—strain curves. The q-parameters have an effect on the material softening (i. e. increasing q_1 and/or q_2 leads to an increase in void growth which results in material softening). Equation (A.6) shows the GTN constitutive equation in which q_1 is directly linked to the porosity evolution, while q_2 is linked to both: porosity evolution and the stress state. Faleskog et al., 1998 highlight the effect of the q-parameters

on the material stress—strain behavior in a unit cell. The unit cell model is an adequate tool for studying void growth and coalescence as presented in the early work of Becker et al., 1994; Kuna et al., 1996; Needleman, 1972; Worswick et al., 1990. The voids distributed in a solid material can be represented using a 3D periodic array of unit cells with a single void in the center of each cell. The boundary conditions on the unit cell allow to represent the solid material containing several voids. The unit cell model is used to investigate void growth in the work of Borg et al., 2008; Chien et al., 2000; Hosseini et al., 2022; Ling et al., 2016; Steglich et al., 2010; Wen et al., 2005. The work of Faleskog et al., 1997 is more oriented to the calibration of q_1 and q_2 parameters using the unit cell model. The calibration methodology developed by the cited authors consists of three steps. Firstly, finite element unit cell simulations are carried out over a given range of stress triaxiality. The void in the unit cell corresponds to the initial void volume fraction in the studied material. The unit cell matrix has an elastic-plastic behavior that is defined using a Ramberg-Osgood flow law [Ramberg et al., 1943]. Secondly, finite element simulations are carried out over the same range of stress triaxiality using a homogenized model. The latter has no void in its center but has a GTN behavior with the porosity as a variable. Finally, the q_1 and q_2 parameters used in the homogenized model are optimized in order to minimize the error between the stress—strain and void growth—strain curves of the unit and homogenized cells.

3. **Void coalescence:** by internal necking can be modeled using different approaches. The commonly used void coalescence models for the 6061 alloy are the f_* and the Thomason model as shown in table 2.2. The f_* approach is introduced to the Gurson model by Tvergaard et al., 1984. The idea is to replace the porosity f in the Gurson yield criteria by an effective porosity f_*. The latter is equal to f as long as the critical porosity f_c is not reached. Beyond f_c, the f_* is multiplied by a factor to abruptly accelerate void growth till material failure. The f_* coalescence approach adds two new parameters: f_c and f_r (porosity at failure). The latter do not have a physical signification [Benzerga et al., 2016] and can be determined using a cell model as presented in the work of Pardoen et al., 2000. By far, the f_* approach is the most commonly used coalescence criterion to model the 6061 alloy.

   The Thomason [Thomason, 1968] coalescence model predicts the onset of coalescence by internal necking by attainment of some plastic limit load in the inter-void ligament. Benzerga et al., 1999 improves the Thomason model as it was not solved in a close form. A generic way of expressing the Thomason coalescence criteria is shown in eq. (A.10) and eq. (A.11). Zhang et al., 1994 and Besson, 2009 illustrate the use of the Thomason model with the Gurson model. Other authors use the Thomason model to detect the onset of coalescence

(activation of the Thomason yield criterion) and then use the critical porosity at the onset of coalescence in the f_* equation. This mixed method is presented in the work of Simar et al., 2010 (6005 aluminum) and Butcher et al., 2011 (5182 aluminum).

Void coalescence by void sheeting is less investigated in the literature. To begin, some authors [Bandstra et al., 2001; Brocks et al., 1995; Fabrègue et al., 2008; Faleskog et al., 1997; Tvergaard, 1998] study the effect of a second population of voids on the overall ductility in a cell model. [Bandstra et al., 2001; Faleskog et al., 1997; Tvergaard, 1998] incorporate the secondary voids in the cell mesh while [Brocks et al., 1995; Fabrègue et al., 2008] use a unit cell with a Gurson behavior for the matrix to represent the secondary voids. It is shown that the secondary void population has a significant effect on the onset of coalescence. Now that secondary void population role in damage is clear, it is still not easy to integrate in the existing models. Small voids nucleate continuously during the ductile failure process on disperoids in 6xxx aluminum alloys. One can implement a secondary void nucleation model to take into account the small nucleated voids. This should not cause any numerical difficulties since the implementation can be done in the same manner as for the nucleation of primary voids. However, the main issue is the experimental difficulty in determining the nucleation rate of secondary voids. It might even be difficult to determine the second population porosity regardless of its origin (i. e. void nucleation or growth) [Perrin et al., 2000].

Enakoutsa et al., 2009; Perrin et al., 2000 propose an extension to the Gurson model to take into account the second population of voids in the Gurson yield criteria. The primary and secondary voids are noted f_1 and $\hat{f}_2$ respectively. However, the drawback of the proposed Gurson extension is that it assumes that f_1 and $\hat{f}_2$ are of the same size.

Inquiry answer The microstructure of the 6061 alloy dictates the microscopic damage phenomena. The alloy contains micron-sized Mg_2Si and intermetallic particles that break during loading. This results in nucleated voids that grow under plastic strain. Void growth is sensible to the strain hardening capacity of the material. Therefore, the age hardening treatment that determines the 6061 alloy's nano precipitation morphology and size has an effect on void growth. Thereafter, small voids nucleate over dispersoids that are rich in Cr and Mn. The small voids can lead to abrupt void coalescence in shear bands before the primary voids link together.

2.3 IRRADIATION EFFECTS ON THE AA6061-T6

Inquiry Given that the radiation damage alters the microstructure at the atomic scale, how does these atomic changes reflect on overall macroscopic material's mechanical properties and especially the material's fracture toughness ?

2.3.1 *Nuclear fission & neutron flux*

Human is able to produce energy by nuclear fission of a naturally occurring element: Uranium. U-235 is one of the unstable isotopes used to create a controlled steady chain process of nuclear fission, fig. 2.6. When U-235 is bombarded with neutrons, it instantly breaks because it is unstable. This collision results in nucleus of smaller atoms plus two or three neutrons. These two or three neutrons can create another fission reaction by colliding with other U-235 atoms. Neutrons pointing to "non-fission event" as shown in fig. 2.6 cause material damage which is explained in the following section.

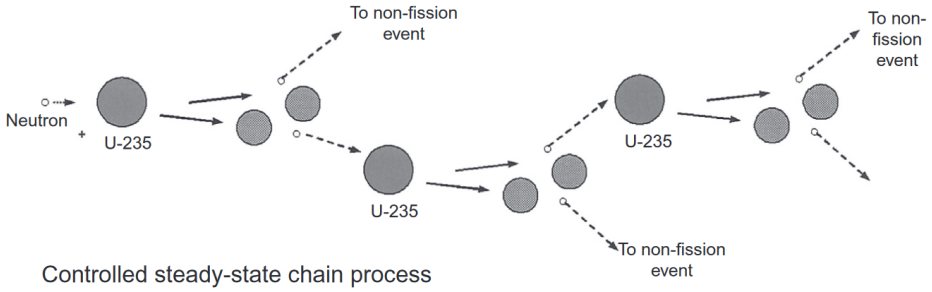

Figure 2.6: Controlled steady chain of a nuclear fission reaction as in nuclear reactors [Suppes et al., 2016]

The core structural components of a nuclear reactor are bombarded by neutrons produced from the nuclear fission reaction. As a result, the core structural components undergo radiation damage. The latter depends on the irradiation dose which can be expressed in terms of neutron fluence (i. e. neutron flux integrated in time, Φ). Neutron flux are classified according to the neutrons' energy. Neutrons with high energy (0.1-10 MeV) are referred to as fast neutrons while neutrons with low energy ($\sim$ 0.025 eV at 20°C) are referred to as thermal neutrons [Azevedo, 2011; Gittus, 1978; Little, 1976]. Section 2.3.2 is dedicated to the microstructural changes in aluminum alloys caused by the thermal neutron flux. Section 2.3.3 gives a detailed explanation of the microstructure evolution under a fast neutron flux. Section 2.3.4 combines the knowledge from the precedent sections to illustrate the irradiation-induced hardening in the 6061 aluminum alloy.

2.3.2 *Microstructural changes in aluminum alloys due to thermal neutron flux*

Thermal neutron flux (E $\sim$ 0.025 eV) is responsible for (n, γ) reactions that transmute aluminum atoms into silicon atoms as follows:

$$^{27}Al + n_{th} \rightarrow {}^{28}Al + \gamma\,;\, {}^{28}Al \rightarrow {}^{28}Si + e^{-} + \bar{\nu} \tag{2.10}$$

Si is insoluble in Al below 350°C [Farrell, 2012; Farrell et al., 1970]. However, dissolved Mg in the Al matrix reacts with the produced Si to create Mg_2Si particles as explained by Kolluri, 2016. As a result, the Al-Mg (5xxx) aluminum alloys are converted to Al-Mg-Si (6xxx) under radiation-induced solidus transmutation. In the absence of Mg, the Al-Si system is a simple eutectic system without compounds. Figure 2.7a shows large rounded voids coated with Si in a heavily irradiated carbon extraction replica from a 1100-O alloy. At the same irradiation dose, fig. 2.7b shows the Si particles around the Mg_xSi_y precipitates in a 6061-T6 alloy.

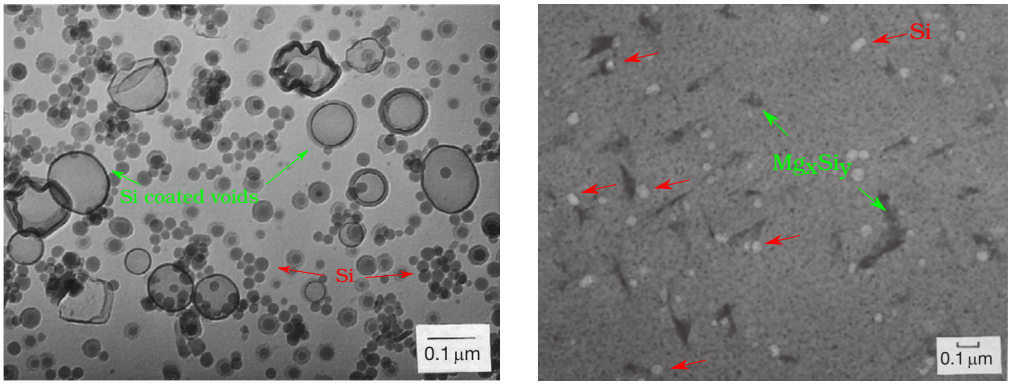

(a) 1100-OAl (b) 6061-T6

Figure 2.7: Observed samples irradiated to $\sim 140 \times 10^{21}\ n/cm^2$ (E > 0.1 MeV) and $\sim 230 \times 10^{21}\ n/cm^2$ (E = 0.025 eV) at $\sim 55°$ showing: (a) large rounded voids coated with Si and random Si particles in the matrix of a carbon extraction replica from 1100-OAl (the larger features with the dark rims are the coated voids, four of them partially collapsed without breaking, indicating a highly ductile coating), (b) Si transmuted particles around the Mg_xSi_y precipitates in a 6061-T6. [Farrell, 2012]

In order to illustrate, transmutation damage causes an increase of 7 wt.% of Si in a 5052-O alloy irradiated at a thermal fluence of $\sim 310 \times 10^{21}\ n/cm^2$ [Farrell, 1981]. Another study reports an increase of 7 wt.% Si in a 6061 aluminum alloy irradiated at a thermal fluence ($E = 0.025$ eV) of $341 \times 10^{21}\ n/cm^2$ [Farrell et al., 1979]. This solidus transmutation has a significant impact on the alloy's mechanical properties. Gaseous transmutation is not considered as an issue in Al alloys [Farrell, 1981, 2012; Kolluri, 2016]. All aluminum alloys shown in figure fig. 2.8 have one thing in common: the same rate of swelling due to Si production. Swelling in irradiated materials is defined as the increase in volume due to the accumulation of irradiation defects and foreign

atoms [2]. However, their resistance to swelling differs. The resistance is estimated by the onset of fluence at which swelling starts increasing. The 6061-T6 alloy has a higher resistance than pure Al due to the presence of the $\beta - Mg_2Si$ phase that reduces void nucleation at the atomic scale [Farrell, 2012].

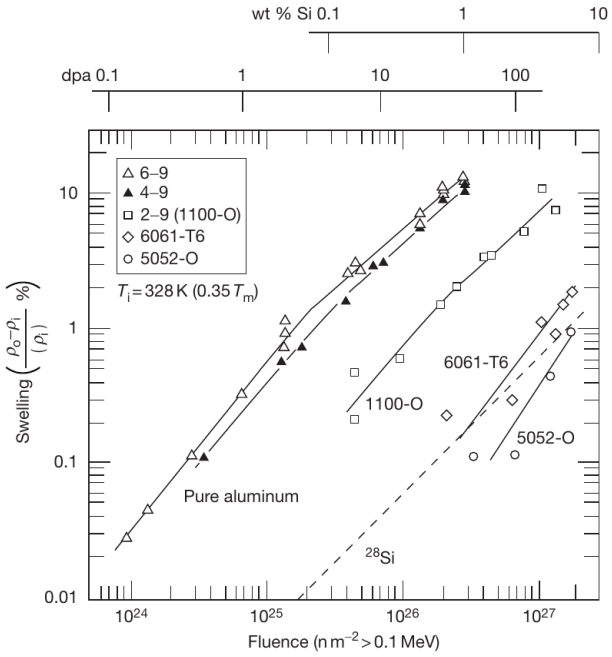

Figure 2.8: Radiation-induced swelling in aluminum alloys as a function of the fast fluence Φ_f. Dotted line shows swelling due to transmutation produced Si. [Farrell, 2012]

In 6061 alloys, the irradiation-induced Mg_xSi_y phase should not be confused with the age hardening Mg_xSi_y phase. The latter is nucleated during the age hardening treatment. On the other hand, the irradiation-induced Mg_xSi_y phase is nucleated in the presence of Si produced by transmutation. The age hardening phase is unstable under neutron and ion irradiation. Recent research showed that the original Mg_xSi_y nano-particles are unstable under ion radiation [Flament, 2015]. Similarly, neutron radiation dissolves the original Mg_xSi_y phase according to Farrel, 2011; Weeks et al., 1993. It is worth noting that the same cited authors [Farrell, 2012; Farrell et al., 1975; King et al., 1972] observed, under diffraction contrast conditions, the original Mg_xSi_y phase unaffected after neutron radiation. Table 2.4 is an inventory of all available

2 Swelling could be caused by bubble formation (gaseous transmutation) or precipitate formation due to solidus transmutation explained above. Bubbles of insoluble gases can be formed by the fast neutron–atom interaction. The insoluble gases are produced by transmutation of certain elements in metals. Helium is usually produced by transmutation in most of the core structural materials of fission reactors. Mg based aluminum alloys (e. g.6061 and 5052) have an excellent resistance to swelling, by bubble formation, with an incubation dose for gas cavity formation of $\sim 50 \times 10^{21}\ n/cm^2$ [Farrell, 1981]. This is 1000 times greater than the incubation dose for gas cavity formation in pure Al alloys. For illustration, swelling due to gaseous transmutation is estimated to be only 1% in a 5xxx alloy [Farrell, 1981] versus 7% of produced Si due to solidus transmutation.

articles in the literature and the different opinions regarding the stability of the original age hardening Mg_xSi_y phase under neutron radiation.

2.3.3 *Microstructral changes in metals due to fast neutron flux*

Fast neutrons are a main source of damage in metals since the elastic interactions between neutrons and atoms in the lattice structure displace atoms from their lattice positions. The atomic displacement takes place if the transferred energy from the elastic interaction exceeds the threshold known as the displacement energy (E_d). The maximum transferred energy to the lattice structure (E_m) is defined as follows:

$$E_m = \frac{4\ M\ m\ E}{(M+m)^2} \tag{2.11}$$

where M is the atomic mass of the material, m the mass of a neutron and E the neutron energy. Given that the transferred energy is inversely proportional to the atomic mass, the transferred energy from a 2 MeV fast neutron flux varies as follows: H = 2.0 MeV, C = 0.57 MeV, Al = 0.28 MeV, Fe-α = 0.14 MeV, Ni = 0.13 MeV, Cu = 0.12 MeV, Zr = 0.09 MeV [Little, 1976].

From a theoretical point of view, the neutron–atom collision event (also called the ballistic phase) is an event that takes about 10^{-11} seconds and can be summarized as follows [Was, 2017]:

1. The atom–neutron elastic interaction ejects the atom from its initial site. The ejected atom is referred to as a Primary Knock-on Atom (PKA). The PKA has an energy defined as E_{PKA} which is the difference between the transferred energy (E_m) and the displacement energy (E_d) [Azevedo, 2011].

2. The PKA travels in the crystalline structure and displaces more atoms from their initial sites by an elastic interaction. This creates an atomic disorder. This domino-like effect is known as the displacement cascade.

3. The PKA terminates as an interstitial atom that already created Frenkel defects (self-interstitial atoms and vacancy pairs) along its passage in the lattice structure, fig. 2.9. The atomic displacement ends when the atom's energy drops below $2E_d$.

The number of created Frenkel defects N_d can be estimated by the ratio between the excess energy and the displacement energy as follows [Little, 1976]:

$$N_d = \frac{0.8\ E_{PKA}}{2\ E_d} \tag{2.12}$$

The number of atomic displacements per unit time (N_{PKA}) is directly proportional to the number of Frenkel defects produced by a single PKA (N_d) and the number of generated PKAs :

$$N_{PKA} = \dot{\phi}\sigma_{EO} \tag{2.13}$$

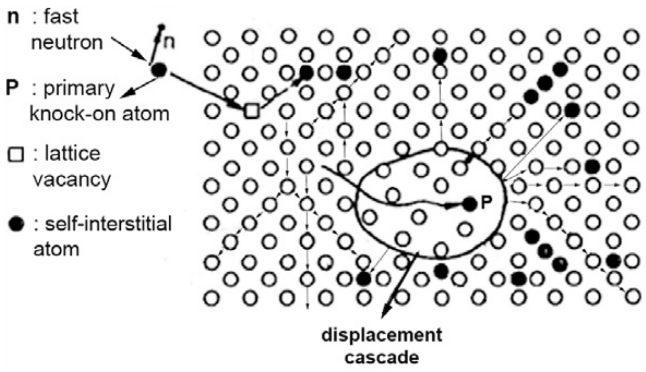

Figure 2.9: Schematic representation of a displacement cascade occurring in a lattice structure [Azevedo, 2011]

where $\dot{\phi}$ is the neutron flux and σ_{EO} the neutron elastic scattering cross-section of the material.

After the ballistic phase, there is a thermal spike (local temperature increase) due to the propagation of the PKA's kinetic energy in the distorted area. The temperature calculated at this thermal spike is higher than the material's melting temperature [Azevedo, 2011; Nordlund et al., 2018]. However, since this stage of high-kinetic-energy lasts only a few picoseconds, the calculated temperature is not considered as a normal equilibrium temperature. Later, self-interstitial atoms and vacancies can easily migrate which leads to the formation of vacancy or self-interstitial clusters and mutual annihilation. Grains and dislocation boundaries act as sinks to irradiation induced-defects [Nordlund et al., 2018].

Taking into account all phenomena discussed above, the irradiation-induced point defects formation depends on intrinsic variables (material, initial microstructure) and extrinsic variables (irradiation temperature, neutron radiation characteristics, total irradiation time). The process is summarized in table 2.3.

Once the point defects are created in the material, they tend to evolve in different manners. Figure 2.10 illustrates the possible events taking place in a lattice structure after the creation of point defects. The main events are: annihilation and recombination of SIA and vacancies, dissociation (emission of small defects resulting from bigger ones) and migration of defects. Surviving defects result in 2D and 3D material defects as shown in fig. 2.10: dislocation loops, vacancy clusters, solute clusters, interstitial clusters and vacancy solute clusters. The growth of the defect clusters depends on the irradiation temperature since it is a thermally activated process. Below 0.4 of the homologous temperature (service range for metallic components in neutron thermal reactors) defect clusters' growth takes place till the density of irradiation-induced defects saturates. Beyond this temperature range, created defects might completely recover by thermal diffusion [Azevedo, 2011; Little, 1976].

Table 2.3: Average timescale for the production of irradiation damage in a metallic material [Was, 2017]

TIME	EVENT	RESULT
$10^{-18}s$	Energy transfer due to the atom-neutron elastic interaction	Creation of a PKA
$10^{-13}s$	Lattice atoms displacement due to collision with the PKA	Displacement cascade (fig. 2.9)
$10^{-11}s$	Energy dissipation, spontaneous recombination, and clustering	Frenkel defects (vacancy and pairs of self-interstitial atoms (SIA))
$> 10^{-8}s$	Defect interactions due to thermal migration	SIA and vacancy recombination, clustering, trapping, defect emission

As a summary, the irradiation-induced defects at the atomic scale are categorized into four types: point defects (interstitials and vacancies), one-dimensional defects (dislocations), two-dimensional defects (dislocation loops), and three-dimensional defects (voids and solute rich clusters, precipitates). These defects produced by fast neutron-atom collisions (except for the point defects) are assumed to impede the dislocation gliding [Azevedo, 2011; Becquart et al., 2010; Little, 1976; Lucas, 1994; Nordlund et al., 2018].

2.3.4 *Irradiation-induced hardening mechanisms in the 6061 aluminum alloy*

The radiation damage explained above causes changes in the 6061 aluminum alloy's microstructure which lead to an irradiation-induced hardening effect. Figure 2.11 illustrates the radiation damage effect on the tensile properties of irradiated aluminum alloys. The tensile and ultimate tensile strengths increase as the fluence increases while the uniform elongation % and the hardening capacity (ratio of ultimate to yield strength) decrease. This is true for all the presented aluminum alloys in fig. 2.11. The strengths of the 5052-O alloy increase at a higher rate with respect to other aluminum alloys. This can be explained by the fact that the added Si by transmutation result in a new strengthening Mg_xSi_y phase [Kolluri, 2016]. The 6061-T6 alloy has an age hardening Mg_xSi_y phase that is dissolved and replaced by the irradiation-induced Mg_xSi_y phase. However, the 5052-O alloy is an AlMg alloy with no age hardening phase prior irradiation. The introduction of the irradiation-induced Mg_xSi_y phase to the 5052-O alloy leads to the dramatic increase in strength beyond a fluence of $\sim 1 \times 10^{25}\ n/m^2$.

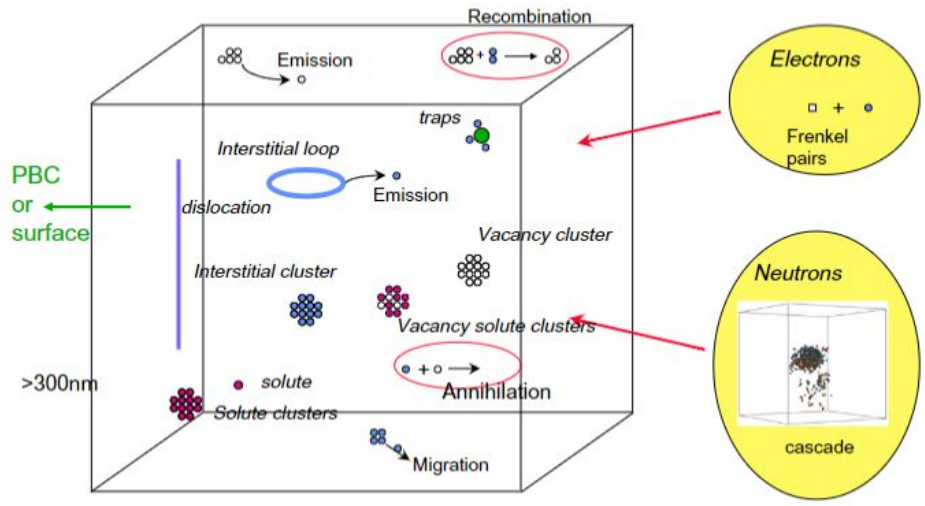

Figure 2.10: Possible events taking place in a lattice structure after the ballistic phase: migration, dissociation (emission of small defects resulting from bigger ones), aggregation of like defects, and annihilation between opposite defects [Becquart et al., 2010]

The irradiation-induced hardening in the 6061-T6 alloy is well explained in the literature review [Kolluri, 2016]:

1. Hardening caused by Φ_f: the fast neutrons resulting in an increase in dislocation density and voids have an instant effect on strengthening. At an early stage in irradiation, a sudden increase in strength is associated to the fast neutrons as the transmutation damage effect becomes more significant at high irradiation doses that lead to more transmuted Si. However, the rate of increase in strengthening due to Φ_f tends to saturate. The saturation fluence Φ_f is about $\sim 2 \times 10^{26}\ n/m^2$ for steels irradiated at 603 K ($\sim$ 0.35 T_m) [Was, 2017]. Strengthening due to Φ_f in aluminum alloys is expected to saturate at lower fluences due to the low effective displacement energy of Al ($\sim$ 25 eV) compared to Fe ($\sim$ 40 eV) [Farrell, 2012].

2. Hardening caused by Φ_{th}: is associated to the radiation-induced precipitation of the Mg_xSi_y phase in 5xxx and 6xxx alloys. The precipitation of this new phase depends implicitly on the fast neutron flux. This matter is to be explained below. However, it is important to note that the radiation-induced Mg_xSi_y phase is the major source of strengthening at high Φ_{th}. Si particles do not produce as much strengthening as dislocations. Conversely, Si can be beneficial as shearing of soft Si amorphous particles produces low amounts of strain hardening [Kolluri, 2016]. Although Si does not cause remarkable strengthening, the Si precipitates at grain boundaries at extremely high thermal fluences ($\Phi_{th} > 200 \times 10^{21}\ n/cm^2$) are believed to cause a dramatic drop in fracture toughness [Alexander, 1999; Weeks et al., 1993]. Figure 2.7b (b) displays ripening of age hardening Mg_xSi_y particles in 6xxx alloys by added Si. This does not result in high strengthening either. For

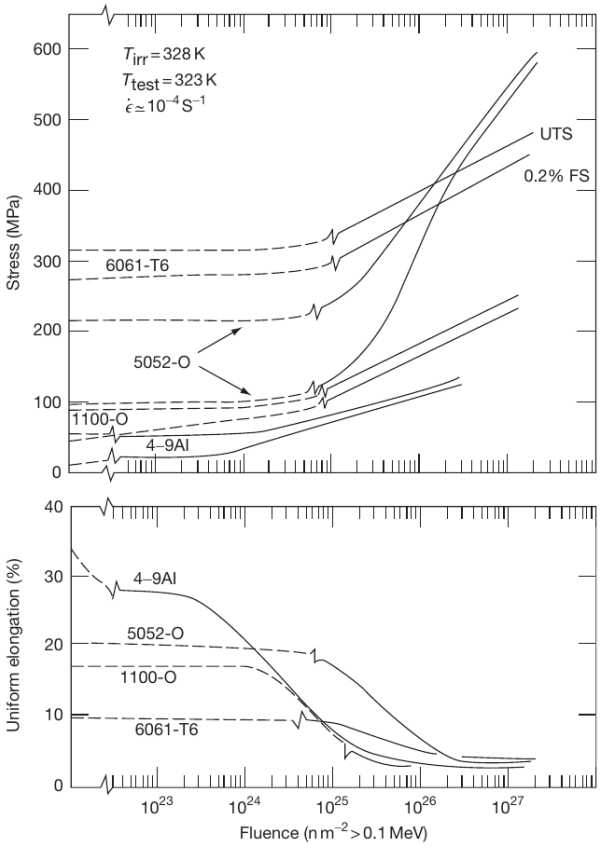

Figure 2.11: Changes in tensile properties of irradiated aluminum alloys tested at room temperature [Farrell, 2012; Farrell et al., 1979]

a given age hardening Mg_xSi_y particle density, an increase in precipitate size (r) countered by a decrease in planar spacing (λ) of the precipitates leads to minimal or no increase in the yield shear stress.

The hardening features explained above assume no coupling between fast and thermal neutrons. The spectrum or the ratio of thermal to fast fluence R_Φ can be highlighted when the results of tensile tests are discriminated by thermal and fast fluences as shown in fig. 2.12. This figure shows plotted results from the HFIR reactor [Alexander, 1993, 1999; Farrell et al., 1979] and the HFBR reactor [Weeks et al., 1990, 1993]. The R_Φ of HFIR samples is about 1.7-2.3 against 0.5-21 for HFBR samples. When results of both reactors are mixed and plotted against the thermal fluence, no special tendency is observed. The same results plotted as a function of fast fluence show different levels of strengthening. On the same plot, lines connecting samples irradiated under the same R_Φ mark out the tendency related to the spectrum. For $\Phi_f = 1 \times 10^{26}\ n/m^2$, the tensile strength is higher for samples of $R_\Phi = 21$ than those of $R_\Phi = 1.3$.

For a better comprehension, fig. 2.13 compares microstructures of two 6061-T6 samples with two different R_Φ. The left sample, taken from HFBR with $R_\Phi = 21$, shows

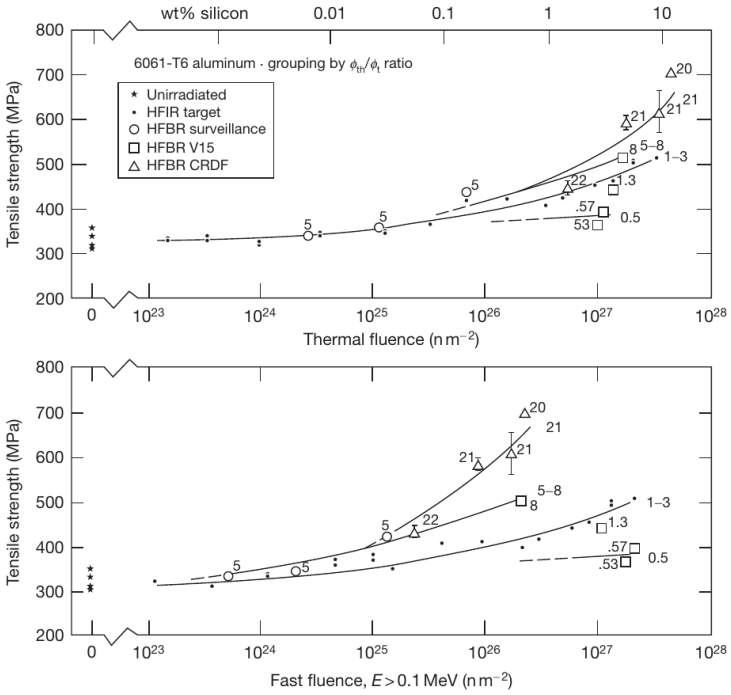

Figure 2.12: Tensile properties of irradiated 6061-T6 Al alloy discriminated by thermal and fast fluence. Samples were irradiated in the HFIR (High Flux Irradiaton Reactor) and HFBR (High Flux Beam Reactor). Connecting lines represent the spectrum $R_\Phi = \frac{\Phi_{th}}{\Phi_f}$ [Farrell, 2012]

fine dispersed Mg_xSi_y precipitates. The right sample from HFIR with $R_\Phi = 1.7$ shows coarser Mg_xSi_y precipitates for the same thermal fluence. In fact, the thermal fluence controls the Si production while the fast fluence controls the ripening and sputtering of newly produced precipitates [Farrel, 2011]. Therefore, at $\Phi_f = 1 \times 10^{27}\ n/m^2$ and a given increase in wt% Si, one can conclude that [Farrel, 2011]:

- The HFIR sample (right micrograph in fig. 2.13) with $R_\Phi = 1.7$ received a higher dose of fast neutrons. This promoted more transport of sputtered Si atoms to ripen existing precipitates. The resulting precipitates are coarse and the strengthening level is relatively lower than the HFBR sample.
- The HFBR sample (left micrograph in fig. 2.13) with $R_\Phi = 21$ received a lower dose of fast neutrons. This resulted in finely dispersed particles and higher strengthening.

All in all, the available data in the literature review on irradiated 6061-T6 alloys is very limited. The HFIR and HFBR are the two American research reactors that provide a great amount of publicly published information. The related articles are summarized in table 2.4. This study also includes unpublished data on irradiated 6061-T6. The data is a courtesy of CEA (The French Alternative Energies and Atomic Energy

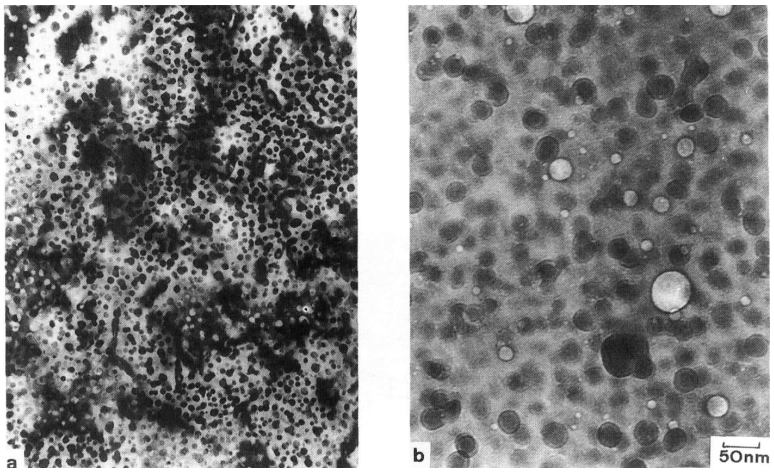

Figure 2.13: Microstructures of irradiated 6061-T6 Al alloy at a spectrum R_Φ of 21 (left) in the HFBR reactor and R_Φ of 1.7 (right) in the HFIR reactor [Farrel, 2011]. Both microstructures are observed at the same thermal fluence Φ_{th}. The higher the spectrum R_Φ, the higher the fast fluence Φ_f.

Commission). The specimens are irradiated in the French reactor named OSIRIS and the Belgian reactor known as BR2. Table 2.4 summarizes the main literature results regarding the tensile behavior of the irradiated 6061-T6 alloy. The fracture toughness evolution of the irradiated 6061-T6 alloy remains an unanswered question that is discussed in the following section.

Table 2.4: Summary of available data in the literature review on irradiated 6061-T6 alloys

Research reactor	Reference	Irradiation conditions	Microstructural changes	Mechanical properties
HFIR	King et al., 1972	$\Phi_{th}^{max.} = 120 \times 10^{21}\ n/cm^2$ R_Φ = 1.3 60°C	Age hardening Mg_xSi_y not affected [3]	Significant increase in strength; decrease in ductility
	Farrell et al., 1975	$\Phi_{th}^{max.} = 301 \times 10^{21}\ n/cm^2$ R_Φ = 2.4 50°C	6% wt. produced Si; age hardening Mg_xSi_y not affected [4]	50-80% increase in yield and ultimate strengths; total elongation dropped from 10-15% to 3-5%
	Farrell et al., 1979	$\Phi_{th}^{max.} = 300 \times 10^{21}\ n/cm^2$ R_Φ = 1.6 50°C	7% wt. produced Si; same microstructural changes cited above [5]	45% increase in yield stress; 60% increase in ultimate tensile stress; total elongation dropped from 15 to 9%
	Alexander, 1993	$\Phi_{th}^{max.} = 10 \times 10^{21}\ n/cm^2$ R_Φ = 2 95°C	Not discussed	Significant increase in strength; decrease in ductility; fracture toughness not affected

3 Quoted: "... suggesting that no major irradiation-induced changes occurred in the morphology of the coherent precipitate.
4 Quoted: "Apparently, irradiation did not significantly affect Mg_2Si precipitates..."
5 Quoted: "The microstructural features introduced by irradiation are essentially the same as those reported earlier in 6061 aluminum [King et al., 1972]"

Research reactor	Reference	Irradiation conditions	Microstructural changes	Mechanical properties
	Alexander, 1999	$\Phi_{th}^{max.} = 80 \times 10^{21}\ n/cm^2$ $R_\Phi = 2$ 95°C		
	Farrel, 2011	Comparing [Farrell et al., 1979] & [Weeks et al., 1993]	Age hardening Mg_xSi_y re-solution [6]	Higher $R_\Phi \rightarrow$ higher irradiation hardening
	Farrell, 2012	Review article	Age hardening Mg_xSi_y not affected [7]	Reciting the above results
HFBR	Weeks et al., 1990	$\Phi_{th}^{max.} = 320 \times 10^{21}\ n/cm^2$ $R_\Phi = 21$ 60°	Age hardening Mg_xSi_y re-solution [8]	Significant increase in strength; decrease in ductility; fracture toughness decreased by $14\text{MPa}\sqrt{\text{m}}$
	Weeks et al., 1993	$\Phi_{th}^{max.} = 400 \times 10^{21}\ n/cm^2$ $R_\Phi = 21$ 60°		
OSIRIS (France)[9]	CEA		Unpublished	
BR2 (Belgium)[10]	SCK·CEN		Unpublished	

6 Quoted: "Other microstructural changes involved the nearly-complete re-solution of the original, fine, acicular precipitate of Mg_2Si phase in both cases."
7 Quoted: "The conclusion Mg_2Si precipitates are unstable in a neutron flux is at odds with the .. fact that the precipitates persist to very high fluences in 6061-T6 ..."
8 Quoted: "TEM photographs of irradiated material are shown ... The original, acicular Mg_2Si precipitate was destroyed by the irradiation and was replaced by a high concentration of spherical particles about 8 nm diameter consisting primarily of silicon"
9 URL: https://www.cea.fr/multimedia/Pages/richmedias/visites-virtuelles/reacteur-de-recherche-osiris.aspx
10 URL: https://www.sckcen.be/fr/qui-sommes-nous/informations-sur-lorganisation/infrastructure

2.3.5 *Evolution of the fracture toughness in the 6061-T6 aluminum alloy during neutron irradiation*

Results from the literature regarding the fracture toughness after irradiation are plotted in fig. 2.14. In fact, these few results are the only existing data that propel this research work. Therefore, one must note the degree of confidence in the available data regarding the fracture toughness of the irradiated alloy. Figure 2.14 (a) and (b) show the fracture toughness as a function of the thermal and fast fluence respectively. Comparing fig. 2.14 (a) and fig. 2.14 (b) illustrates the R_Φ for each set of irradiated toughness tests. For instance, samples in the work of Weeks et al., 1993 are irradiated at a high $R_\Phi = 21$ which leads to a significantly lower Φ_f in fig. 2.14 (b) when compared to the Φ_{th} in fig. 2.14 (a).

Alexander, 1993, 1999 study 6061-T651 Compact-Tension (CT) samples (28.6 $\times$ 27.4 $\times$ 11.4 mm thick) fabricated from the middle of the thickness of a 199 mm plate. The CT samples are machined in the T-L orientation so that the crack propagates in the rolling direction (i. e. toughness in the T-L direction is lower than the L-T direction [Alexander, 1999]). The CT samples are pre-cracked at room temperature to a crack length-to-width (a/W) value of about 0.5 and then side grooved 10% of their thickness on each side prior irradiation. The CT samples are irradiated in HFIR at Oak Ridge National Laboratory (ORNL), USA. The thermal fluence is estimated to be $\Phi_{th}(E < 0.4 \text{ eV}) = 10$ and $80 \times 10^{21}\ n/cm^2$ and the fast fluence to be $\Phi_f = 5$ and $40 \times 10^{21}\ n/cm^2$ ($E > 0.1$ MeV) respectively. The aim of this irradiation program is to test the material's fracture toughness for the Advanced Neutron Source to be built at ORNL. 16 CT samples are inserted in a capsule which holds them end-to-end. Narrow channels in each capsule allow the reactor's cooling water to pass over the samples to maintain the required temperature (95°C). The flux gradient in the capsule is calculated over the length.

Petit et al., 2022 study a CT12.5 sample that is machined prior irradiation. A single CT sample is irradiated in the CEA (Osiris Reactor, France). The sample is pre-cracked prior irradiation and tested at room temperature after irradiation. The thermal fluence is estimated to be $\Phi_{th}(E = 0.25 \text{ eV}) = 6.9 \times 10^{21}\ n/cm^2$ and the fast fluence to be $\Phi_f = 1.4\ \times 10^{21}\ n/cm^2$ ($E > 0.1$ MeV) respectively.

Weeks et al., 1990, 1993 study 6061-T6 miniature 3 mm thick notched impact specimens machined from irradiated CRDF tubes (i. e. control rod drive follower tubes) found in the HFBR at Brookhaven National Laboratory, USA. The CRDF tube of interest (irradiation temperature = 50°C) has an outer diameter of 3.25 cm and a thickness of 4.06 mm. Samples are cut from areas of the tube where the thermal fluence is estimated to be $\Phi_{th} = 420 \times 10^{21}\ n/cm^2$ and the fast fluence to be $\Phi_f = 20 \times 10^{21}\ n/cm^2$ ($E > 0.1$ MeV). Impact testing is carried out in a hot cell (a chamber dedicated for irradiated material testing) using the ASTM E23 standards and

a Tinius Olsen impact tester (designed for testing plastics and adapted for aluminum alloys).

"Source 2002" is unpublished results that are the courtesy of CEA. Fracture toughness tests are carried out on bending samples that are machined from an neutron-irradiated tube.

Table 2.5 recapitulates the plotted values in fig. 2.14. Table 2.5 also elaborates the degree of confidence in the above presented work of Alexander, 1993, 1999; Weeks et al., 1990, 1993 regarding the fracture toughness of the irradiated 6061-T6 alloy. These literature results must be carefully analyzed since they are insufficient.

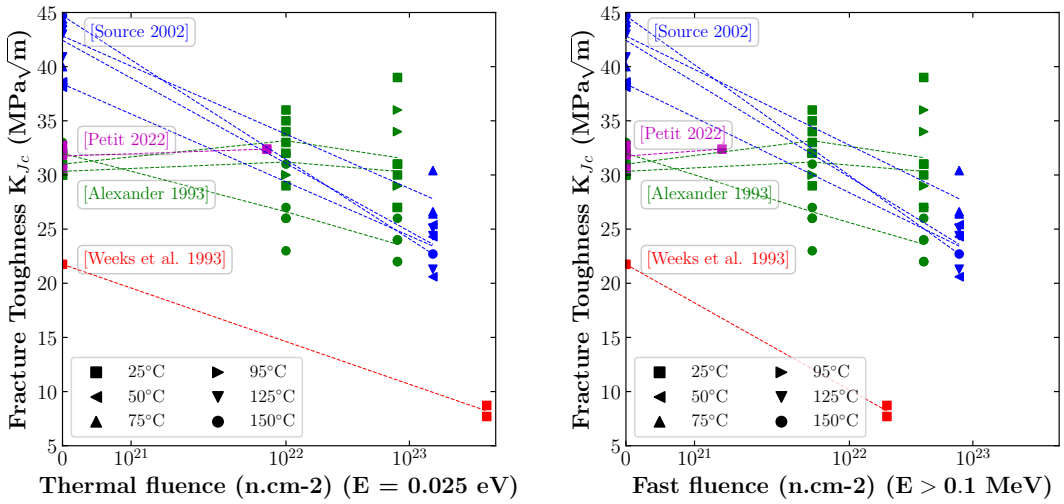

(a) Toughness vs. Φ_{th}

(b) Toughness vs. Φ_f

Figure 2.14: Fracture toughness as a function of the (a) thermal fluence and (b) fast fluence. Data collected from the literature.

Inquiry answer At the moment, results in the literature regarding the fracture toughness are insufficient. No conclusions can be drawn at this point to confirm if the fracture toughness increases or decreases as a function of the thermal fluence. Figure 2.14 show different tendencies regarding fracture toughness versus thermal fluence. Results from the work of Alexander, 1993 show a slight increase in fracture toughness at a testing temperature of 25°C. Results from the work of Weeks et al., 1993 show a significant decrease in fracture toughness at a high spectrum $R_\Phi = 21$. However, as mentioned in table 2.5, Weeks et al., 1993 evaluate the fracture toughness of the irradiated material using impact testing techniques on samples fabricated from irradiated tubes. The results tend to be less reliable when compared to the work of Alexander, 1993 where CT samples are machined before irradiation then irradiated in a nuclear research reactor. The radiation dose in the CT samples is well monitored

during the irradiation period. In addition impact tests carried out in the work of Weeks et al., 1993 give the material's resilience and not its toughness. It is not clear in the work of Weeks et al., 1993 how the resilience values are converted to toughness. This PhD thesis aims to understand the observed fracture toughness evolution in fig. 2.14.

Table 2.5: Plotted data in Figure 2.14 and the required conversion for the sake of comparison

REFERENCE	Φ_{th} (n.cm^{-2})	TEST TEMP.(°C)	K_{Jc} (MPa$\sqrt{m}$)
[Alexander, 1993][1,2]	0	26	33.0, 33.8, 33.6, 32.1
	0	95	29.9, 30.8, 30.2
	0	150	32.3, 31.3, 32.6
	1×10^{22}	26	33.9, 34.8, 35.6
	1×10^{22}	95	31.7, 32.2
	1×10^{22}	150	30.5, 27.3
[Alexander, 1999][1,2]	0	26	32
	1×10^{22}	26	33, 32, 29
	1×10^{22}	95	32, 30, 30
	1×10^{22}	150	26, 23, 26
	8×10^{22}	26	31, 39, 30, 31, 27
	8×10^{22}	95	36, 27, 29, 34, 29, 27
	8×10^{22}	150	24, 22, 24, 22, 26
[Petit et al., 2022]	0	26	32.7, 30.6, 31.9
	6.91×10^{21}	26	32.4
[Weeks et al., 1993][3]	0	26	21.75
	4.23×10^{23}	26	8.7 ± 0.8 [a]
	4.23×10^{23}	26	7.7 to 8.8 [b]

[1] Quoted: *"Based on J-integral formulation from ASTM E 1152-87 with conversion to K by $K^2 = JE$ (E = elastic modulus)"*

[2] Authors define thermal neutrons as neutrons with an energy: $E < 0.625$ eV. In order to place the data on the x-axis of fig. 2.14, the thermal fluence must be converted to the conventional fluence used in this work ($E = 0.025$ eV). Unfortunately, no conversion could be done, since the %wt. of transmuted Si is not published.

[3] Authors do not define the considered energy for thermal neutrons. However, they published the %wt. of transmuted Si as a function of the thermal fluence. This allows to calculate the conventional thermal fluence ($E = 0.025$ eV) given the below equation:

$$\Phi_{th}\,(E = 0.025\ eV) = \frac{\Delta Si_{\%wt.}}{m_{\%Al}} \frac{M_{Al}}{M_{Si}} \frac{1}{\sigma} \tag{2.14}$$

where $\Delta Si_{\%mass}$ is the %wt. of transmuted Si, the remaining %wt. of Al (%wt. Al before irradiation - $\Delta Si_{\%mass}$), M_{Al}, M_{Si} are the atomic masses of Al and Si respectively and finally σ is the neutron cross section ($\sigma = 2.344 \times 10^{-27}$ cm^2 for the given neutron energy).

[a] K_{IC} values from impact testing data carried on miniature 3 mm thick notched impact specimens.

[b] K_{IC} values from notch tensile testing data carried out on the same miniature 3 mm thick notched impact specimens mentioned above.

BIBLIOGRAPHY

Alexander, D. (1993). 'The Effect of Irradiation on the Mechanical Properties of 6061-T651 Aluminum.' In: *Effects of Radiation on Mater.*, pages 1151–1167. DOI: 10.2172/10162906 (see pp. 38, 41, 43, 44, 46).

Alexander, D. (1999). 'The Effect of Irradiation on the Mechanical Properties of 6061-T651 Aluminum Base Metal and Weldments.' In: *Effects of Radiation on Mater.*, pages 1027–1044. DOI: 10.1520/STP13918S (see pp. 37, 38, 42–44, 46).

Argon, A. S. (1976). 'Formation of Cavities From Nondeformable Second-Phase Particles in Low Temperature Ductile Fracture.' In: *J. Engng Mater. Technol.* 98.1, pages 60–68. DOI: 10.1115/1.3443338 (see p. 27).

Argon, A. et al. (1975). 'Cavity formation from inclusions in ductile fracture.' In: *Met. Trans.* 6A, pages 825–837 (see pp. 19, 27).

Ashby, M. (1966). 'Work hardening of dispersion-hardened crystals.' In: *The Philosophical Magazine: A Journal of Theoretical Experimental and Applied Physics* 14.132, pages 1157–1178. DOI: 10.1080/14786436608224282 (see p. 27).

Azevedo, C. (2011). 'A review on neutron-irradiation-induced hardening of metallic components.' In: *Eng. Fail. Anal.* 18.8, pages 1921 –1942. ISSN: 1350-6307. DOI: 10.1016/j.engfailanal.2011.06.008 (see pp. 31, 34–36).

Babout, L. et al. (2004). 'Damage initiation in model metallic materials: X-ray tomography and modelling.' In: *Acta Mater.* 52.8, 2475–2487 (see p. 19).

Bandstra, J. P. and D. A. Koss (2001). 'Modeling the ductile fracture process of void coalescence by void-sheet formation.' In: *Mater. Sci. Engng A* 319–321, pages 490–495 (see p. 30).

Becker, R. and R. Smelser (1994). 'Simulation of strain localization and fracture between holes in an aluminum sheet.' In: *J. Mech. Phys. Solids* 42.5, pages 777–796. DOI: 10.1016/0022-5096(94)90042-6 (see p. 29).

Becquart, C. et al. (2010). 'Modeling the long-term evolution of the primary damage in ferritic alloys using coarse-grained methods.' In: *Journal of Nuclear Materials* 406.1, pages 39 –54. DOI: 10.1016/j.jnucmat.2010.05.019 (see pp. 36, 37).

Belov, N. et al. (Oct. 2005). 'Constituent phase diagrams of the Al–Cu–Fe–Mg–Ni–Si system and their application to the analysis of aluminium piston alloys.' In: *Acta Mater.* 53, pages 4709–4722. DOI: 10.1016/j.actamat.2005.07.003 (see p. 16).

Benzerga, A. et al. (1999). 'Coalescence–controlled anisotropic ductile fracture.' In: *J. Engng Mater. Technol.* 121, pages 121–129 (see p. 29).

Benzerga, A. and J. Besson (2001). 'Plastic potentials for anisotropic porous solids.' In: *Eur. J. Mech./A* 20A.3, pages 397–434 (see p. 23).

Benzerga, A. and J.-B. Leblond (2010). 'Ductile Fracture by Void Growth to Coalescence.' In: *Advances in Applied Mechanics* 44, 169–305 (see pp. 19, 21, 26).

Benzerga, A. et al. (2016). 'Ductile Failure Modeling.' In: *Int. J. Frac.* 201, pages 29–80. DOI: 10.1007/s10704-016-0142-6 (see pp. 23, 29).

Beremin, F. M. (1981). 'Cavity formation from inclusions in ductile fracture of A508 steel.' In: *Met. Trans.* 12A, pages 723–731 (see pp. 25, 28).

Berveiller, M. and A. Zaoui (1978). 'An extension of the self–consistent scheme to plastically flowing polycrystals.' In: *J. Mech. Phys. Solids* 26, pages 325–344 (see p. 28).

Besson, J. (2009). 'Damage of ductile materials deforming under multiple plastic or viscoplastic mechanisms.' In: *Int. J. Plasticity* 25, pages 2204–2221 (see p. 29).

Besson, J. (2010). 'Continuum models of ductile fracture: a review.' In: *Int. J. Damage Mech.* 19, pages 3–52 (see p. 23).

Besson, J. and C. Guillemer-Neel (2003). 'An extension of the Green and Gurson models to kinematic hardening.' In: *Mech. Mater.* 35, pages 1–18 (see p. 23).

Borg, U. et al. (2008). 'Size effects on void growth in single crystals with distributed voids.' In: *Int. J. Plasticity* 24.4, pages 688–701. ISSN: 0749-6419. DOI: 10.1016/j.ijplas.2007.07.015 (see p. 29).

Bridgman, P. W. (1945). 'Effects of High Hydrostatic Pressure on the Plastic Properties of Metals.' In: *Rev. Mod. Phys.* 17 (1), pages 3–14. DOI: 10.1103/RevModPhys.17.3 (see p. 21).

Brocks, W. et al. (1995). 'Verification of the transferability of micromechanical parameters by cell model calculations with visco-plastic materials.' In: *Int. J. Plasticity* 11, pages 971–989 (see p. 30).

Broggiato, G. et al. (2007). 'Identification of Material Damage Model Parameters: an Inverse Approach Using Digital Image Processing.' In: *Meccanica* 42, pages 9–17. DOI: 10.1007/s11012-006-9019-5 (see p. 26).

Butcher, C. and Z. Chen (Apr. 2011). 'Characterizing void nucleation in a damage-based constitutive model using notched tensile sheet specimens.' In: *Theor. Appl. Fract. Mech.* 55, pages 140–147. DOI: 10.1016/j.tafmec.2011.04.004 (see pp. 19, 26, 30).

Caceres, C. and J. Griffiths (1996). 'Damage by the cracking of silicon particles in an Al-7Si-0.4Mg casting alloy.' In: *Acta Mater.* 44.1, pages 25–33. ISSN: 1359-6454. DOI: 10.1016/1359-6454(95)00172-8 (see p. 19).

Chan, I. and H. Wilsdorf (1981). 'The ductile fracture of precipitation-hardened Al-1.79wt.%Cu alloys containing θ' and θ precipitates.' In: *Mat. Sci. and Eng.* 49.3, pages 229–240. ISSN: 0025-5416. DOI: 10.1016/0025-5416(81)90117-8 (see p. 20).

Chien, W. et al. (July 2000). 'Modified Anisotropic Gurson Yield Criterion for Porous Ductile Sheet Metals.' In: *J. Engng Mater. Technol.* 123.4, pages 409–416. ISSN: 0094-4289. DOI: 10.1115/1.1395023 (see p. 29).

Chu, C. and A. Needleman (1980). 'Void nucleation effects in biaxially stretched sheets.' In: *J. Engng Mater. Technol.* 102, pages 249–256 (see pp. 19, 23–26).

Cox, T. and J. Low (1974). 'An investigation of the plastic fracture of AISI 4340 and 18 nickel-200 grade maraging steels.' In: *Met. Trans.* 5, pages 1457–1470 (see p. 21).

Davis, J. (2001). 'Aluminum andAluminum Alloys.' In: *Alloying: Understanding the Basics B-ASM-001*. ASM International, pages 351–416. ISBN: 0-87170-744-6 (see pp. 13, 14).

Develay, R. (1992). 'Propriétés de l'aluminium et des alliages d'aluminium corroyés.' In: *Techniques de l'ingénieur Métaux et alliages non ferreux* TIB357DUO.m440 (see pp. 13–15).

Doege, E. et al. (1995). 'Prediction of necking and wrinkling in sheet–metal forming.' In: *J. Mat. Proc. Tech.* 50, pages 197–206 (see p. 23).

Dubost, B. and P. Sainfort (1991). 'Durcissement par précipitation des alliages d'aluminium.' In: *Techniques de l'ingénieur Méthodes de caractérisation et d'analyse des métaux et alliages* TIB532DUO.m240 (see p. 17).

Edwards, G. et al. (1998). 'The precipitation sequence in AlMgSi alloys.' In: *Acta Mater.* 46.11, pages 3893 –3904. DOI: 10.1016/S1359-6454(98)00059-7 (see p. 17).

Enakoutsa, K. and J.-B. Leblond (2009). 'Numerical implementation and assessment of the GLPD micromorphic model of ductile rupture.' In: *Eur. J. Mech./A* 28, pages 445–460 (see p. 30).

Eshelby, J. (1957). 'The determination of the elastic field of an ellipsoidal inclusion, and related problems.' In: *Proc. Roy. Soc* A241, pages 357–396 (see p. 28).

Fabrègue, D. and T. Pardoen (2008). 'A constitutive model for elastoplastic solids containing primary and secondary voids.' In: *J. Mech. Phys. Solids* 56, pages 719–741 (see pp. 16, 21, 30).

Faleskog, J. and C. Shih (1997). 'Micromechanics of coalescence — I. Synergistic effects of elasticity, plastic yielding and multi–size–scale voids.' In: *J. Mech. Phys. Solids* 45.1, pages 21–50 (see pp. 26, 29, 30).

Faleskog, J. et al. (1998). 'Cell model for nonlinear fracture analysis — I. Micromechanics calibration.' In: *Int. J. Frac.* 89, pages 355–373 (see p. 28).

Farrel, K. (2011). 'A Spectral Effect on Phase Evolution in Neutron-Irradiated Aluminum?' In: *MRS Proceedings*. Volume 373. DOI: 10.1557/PROC-373-165 (see pp. 33, 39, 40, 42).

Farrell, K. (1981). 'Microstructure and tensile properties of heavily irradiated 5052-0 aluminum alloy.' In: *J. Nuclear Materials* 97.1, pages 33 –43. DOI: 10.1016/0022-3115(81)90415-3 (see pp. 32, 33).

Farrell, K. (2012). 'Performance of Aluminum in Research Reactors.' In: *Comprehensive Nuclear Materials*, 147–175. DOI: 10.1016/B978-0-08-056033-5.00113-0 (see pp. 32, 33, 37–39, 42).

Farrell, K. and R. King (1979). 'Tensile Properties of Neutron-Irradiated 6061 Aluminum Alloy in Annealed and Precipitation-Hardened Conditions.' In: *Effects of Radiation on Mater.*, pages 440–449. DOI: 10.1520/STP38180S (see pp. 32, 38, 41, 42).

Farrell, K. and A. Richt (1975). 'Postirradiation properties of the 6061-T6 aluminum High Flux Isotope Reactor hydraulic tube.' In: *American Society for Testing and Materials, Special Technical Publication*, pages 311–325. DOI: 10.1520/STP33695S (see pp. 33, 41).

Farrell, K. et al. (1970). 'Transmutation-produced silicon precipitates in irradiated aluminum.' In: *Metallography* 3.3, pages 275 –284. DOI: 10.1016/0026-0800(70)90015-7 (see p. 32).

Flament, C. (2015). 'Etude des évolutions microstructurales sous irradiation de l'alliage d'aluminium 6061-T6.' PhD thesis. Université Grenoble Alpes (see pp. 17, 33).

Garat, M. (2012). 'Propriét'es des alliages d'aluminium de fonderie.' In: *Techniques de l'ingénieur Métaux et alliages non ferreux* TIB357DUO.m4675 (see p. 14).

Garrison, W. M. and N. R. Moody (1987). 'Ductile Fracture.' In: *J. Phys. Chem. Solids* 48.11, pages 1035–1074 (see pp. 18, 20).

Ghahremaninezhad, A. and K. Ravi-Chandar (2012). 'Ductile failure behavior of polycrystalline Al 6061-T6.' In: *Int. J. Frac.* 174.2, 177–202 (see p. 19).

Ghahremaninezhad, A. and K. Ravi-Chandar (2013). 'Ductile Failure Behavior of Polycrys-talline Al 6061-T6 Under Shear Dominant Loading.' In: *Int. J. Frac.* 180, 23–29. DOI: 10.1007/s10704-012-9793-0 (see p. 21).

Gittus, J. (1978). *Irradiation effects in crystalline solids*. United Kingdom: Applied Science Publishers. ISBN: 0 85334 778 6 (see p. 31).

Gologanu, M. et al. (1993). 'Approximate models for ductile metals containing non–spherical voids — Case of axisymmetric prolate ellipsoidal cavities.' In: *J. Mech. Phys. Solids* 41.11, pages 1723–1754 (see p. 23).

Gologanu, M. et al. (1994). 'Approximate models for ductile metals containing non–spherical voids — case of axisymmetric oblate ellipsoidal cavities.' In: *J. Engng Mater. Technol.* 116, pages 290–297 (see p. 23).

Gologanu, M. et al. (1997). 'Recent extensions of Gurson's model for porous ductile metals.' In: *Continuum micromechanics, CISM Lectures series*. Edited by P. Suquet. Springer, New York, pages 61–130 (see pp. 23, 25).

Grange, M. et al. (2000). 'An anisotropic Gurson model to represent the ductile rupture of hydrided Zircaloy–4 sheets.' In: *Int. J. Frac.* 105.3, pages 273–293 (see p. 23).

Gurson, A. L. (1977). 'Continuum theory of ductile rupture by void nucleation and growth: Part I— Yield criteria and flow rules for porous ductile media.' In: *J. Engng Mater. Technol.* 99, pages 2–15 (see pp. 18, 22).

Hahn, G. and A. Rosenfield (1975). 'Metallurgical factors affecting fracture toughness of aluminum alloys.' In: *Met. Trans.* 6A.4, pages 653–668 (see p. 21).

Hannard, F. (2017). '3D characterization, modelling and tailoring of microstructure heterogeneity effects on damage and fracture of 6xxx aluminium alloys.' PhD thesis. Ecole Polytechnique de Louvain (see p. 28).

Hannard, F. et al. (2016). 'Characterization and micromechanical modelling of microstructural heterogeneity effects on ductile fracture of 6xxx aluminium alloys.' In:

Acta Mater. 103, pages 558–572. DOI: 10.1016/j.actamat.2015.10.008 (see pp. 22, 24).

Hannard, F. et al. (2018). 'Quantitative assessment of the impact of second phase particle arrangement on damage and fracture anisotropy.' In: *Acta Mater.* 148.15, pages 456–466 (see pp. 16, 21).

Hanssen, A. et al. (2002). 'Validation of constitutive models applicable to aluminium foams.' In: *Int. J. Mech. Sci.* 44.2, pages 359–406. DOI: 10.1016/S0020-7403(01)00091-1 (see p. 22).

He, Z. et al. (2021). 'An improved shear modified GTN model for ductile fracture of aluminium alloys under different stress states and its parameters identification.' In: *Int. J. Mech. Sci.* 192, page 106081. ISSN: 0020-7403. DOI: 10.1016/j.ijmecsci.2020.106081 (see p. 24).

Hill, R. (1965). 'Continuum Micro–Mechanisms of Elastoplastic Polycrystals.' In: *J. Mech. Phys. Solids* 13, pages 89–101 (see p. 21).

Hosford, W. (1972). 'Generalized isotropic yield criterion.' In: *J. Applied Mech.* 39.2, 607–609 (see p. 21).

Hosseini, N. et al. (2022). 'The effect of material orientation on void growth.' In: *Int. J. Plasticity* 148, page 103149. ISSN: 0749-6419. DOI: 10.1016/j.ijplas.2021.103149 (see p. 29).

Huber, G. et al. (2005). 'Predictive model for void nucleation and void growth controlled ductility in quasi-eutectic cast aluminium alloys.' In: *Acta Mater.* 53.9, pages 2739–2749. ISSN: 1359-6454. DOI: 10.1016/j.actamat.2005.02.037 (see p. 25).

Kachanov, L. (1958). 'Time of the rupture process under creep conditions.' In: *Isv. Akad. Nauk. SSR. Otd Tekh. Nauk.* 8, pages 26–31 (see p. 22).

Kami, A. et al. (2015). 'Numerical determination of the forming limit curves of anisotropic sheet metals using GTN damage model.' In: *J. of Materials Processing Tech.* 216, pages 472–483. DOI: 10.1016/j.jmatprotec.2014.10.017 (see p. 26).

Kaufman, J. (2000). 'Introduction to Aluminum Alloys and Tempers.' In: ASM International. Chapter Understanding the Aluminum Temper Designation System, pages 39–67. ISBN: 9780871706898 (see p. 15).

Kim, J. et al. (2004). 'Modeling of void growth in ductile solids: effects of stress triaxiality and initial porosity.' In: *Eng. Fract. Mech.* 71.3 (see p. 26).

King, R. et al. (1972). 'Neutron irradiation damage in a precipitation-hardened aluminum alloy.' In: *Symposium on the effects of radiation on structural materials*. Volume 14 (see pp. 33, 41).

Klocker, H. and V. Tvergaard (2003). 'Growth and coalescence of non-spherical voids in metals deformed at elevated temperature.' In: *Int. J. Mech. Sci.* 45, pages 1283–1308 (see p. 23).

Kolluri, M. (2016). 'Neutron Irradiation Effects in 5xxx and 6xxx Series Aluminum Alloys: A Literature Review.' In: *Radiation Effects in Mat.*, pages 393–411. DOI: 10.5772/63294 (see pp. 32, 36, 37).

Kuijpers, N. et al. (July 2003). 'A model of the β-AlFeSi to α-Al(FeMn)Si transformation in Al-Mg-Si alloys.' In: *Metall. Mater. Trans.* 44, pages 1448–1456. DOI: 10.2320/matertrans.44.1448 (see p. 16).

Kuna, M. and D. Sun (1996). 'Three-dimensional cell model analyses of void growth in ductile materials.' In: *Int. J. Frac.* 81, pages 235–258 (see p. 29).

Lars, L. and R. Nils (2000). 'Precipitation of dispersoids containing Mn and/or Cr in AlMgSi alloys.' In: *MSEA* 283, pages 144–152. DOI: 10.1016/S0921-5093(00)00734-6 (see p. 17).

Lassance, D. et al. (Jan. 2007). 'Micromechanics of room and high temperature fracture in 6xxx Al alloys.' In: *Progress in Materials Science* 52, pages 62–129. DOI: 10.1016/j.pmatsci.2006.06.001 (see pp. 16, 19, 23, 25).

Le Roy, G. et al. (1981). 'A model of ductile fracture based on the nucleation and growth of voids.' In: *Acta Metall.* 29.8, pages 1509–1522. DOI: 10.1016/0001-6160(81)90185-1 (see p. 19).

Leblond, J. et al. (1994). 'Exact results and approximate models for porous viscoplastic solids.' In: *Int. J. Plasticity* 10.3, pages 213–235 (see p. 23).

Leblond, J. et al. (1995). 'An improved Gurson–type model for hardenable ductile metals.' In: *Eur. J. Mech./A* 14A.4, pages 499–527 (see p. 23).

Lemaitre, J. (1985). 'A continuous damage mechanics model for ductile fracture.' In: *J. Engng Mater. Technol.* 107, pages 83–89 (see p. 22).

Li, Z. et al. (1994). 'A study of the internal parameters of ductile damage theory.' In: *Fatigue and Fract. Engng Mater. Struct.* 17.9, pages 1075–1087 (see p. 26).

Liao, K. et al. (1997). 'Approximate criteria for anisotropic porous ductile sheet metals.' In: *Mech. Mater.* 26, pages 213–226 (see p. 23).

Ling, C. et al. (2016). 'An elastoviscoplastic model for porous single crystals at finite strains and its assessment based on unit cell simulations.' In: *Int. J. Plasticity* 84, pages 58–87. DOI: 10.1016/j.ijplas.2016.05.001 (see p. 29).

Little, E. A. (1976). 'Neutron-irradiation hardening in irons and ferritic steels.' In: *Int. Mater. Rev.* 21.1, pages 25–60. DOI: 10.1179/imtr.1976.21.1.25 (see pp. 31, 34–36).

Liu, D. and L. J.J. (1993). 'The effects of superimposed hydrostatic pressure on deformation and fracture: Part I. Monolithic 6061 aluminum.' In: *Metall. Mater. Trans. A* 24, pages 601–608 (see p. 21).

Liu, G. et al. (2011). 'Coupling effect of primary voids and secondary voids on the ductile fracture of heat-treatable aluminum alloys.' In: *Mech. Mater.* 43, pages 556–566. DOI: 10.1016/J.MECHMAT.2011.06.014 (see p. 21).

Lucas, G. (1994). 'Effects of radiation on the mechanical properties of structural materials.' In: *J. Nuclear Materials* 216, pages 322 –325. DOI: 10.1016/0022-3115(94)90018-3 (see p. 36).

Maire, E. et al. (2005). 'Damage initiation and growth in metals. Comparison between modelling and tomography experiments.' In: *J. Mech. Phys. Solids* 53, pages 2411–2434 (see p. 19).

Massalski, T. and H. Okamoto (1986). *Binary Alloy Phase Diagrams*. Volume 1. American Society for Metals (see p. 16).

Matsuda, K. et al. (2000). 'Precipitation sequence of various kinds of metastable phases in Al1.0mass% Mg2Si0.4mass% Si alloy.' In: *J. Mater. Sci.* 35, pages 179–189. DOI: 10.1023/A:1004769305736 (see p. 17).

Mc Clintock, F. A. (1968). 'A criterion for ductile fracture by the growth of holes.' In: *J. App. Mech.* 35, pages 363–371 (see pp. 21, 22).

Mear, M. and J. Hutchinson (1985). 'Influence of yield surface curvature on flow localization in dilatant plasticity.' In: *Mech. Mater.* 4, pages 395–407 (see p. 23).

Mkaddem, A. et al. (Jan. 2004). 'Comparison between Gurson and Lemaitre damage models in wiping die bending processes.' In: *International Journal of Advanced Manufacturing Technology* 23, pages 451–461. DOI: 10.1007/s00170-003-1701-3 (see pp. 22, 26).

Moran, B. et al. (1990). 'Formulation of implicit finite element methods for multiplicative finite deformation plasticity.' In: *Int. J. Numer. Meth. Engng* 29, pages 483–514 (see p. 23).

Morgeneyer, T. et al. (2014). 'In situ 3-D observation of early strain localization during failure of thin Al alloy (2198) sheet.' In: *Acta Mater.* 69, pages 78–91 (see p. 18).

Needleman, A. (1972). 'Void growth in an elastic-plastic medium.' In: *J. Applied Mech.* 39, pages 964–970 (see p. 29).

Needleman, A. (1987). 'A continuum model for void nucleation by inclusion debonding.' In: *J. Applied Mech.* 54, pages 525–531 (see p. 26).

Nguyen, H. et al. (2018). 'Ductile fracture prediction and forming assessment of AA6061-T6 aluminum alloy sheets.' In: *Int. J. Frac.* 209, pages 143–162. DOI: 10.1007/s10704-017-0249-4 (see pp. 24, 26).

Noell, P. et al. (2017). 'Do voids nucleate at grain boundaries during ductile rupture?' In: *Acta Mater.* 137, pages 103–114. ISSN: 1359-6454. DOI: 10.1016/j.actamat.2017.07.004 (see p. 20).

Noell, P. et al. (2018). 'The mechanisms of ductile rupture.' In: *Acta Mater.* 161, pages 83–98. DOI: 10.1016/j.actamat.2018.09.006 (see p. 18).

Nordlund, K. et al. (2018). 'Primary radiation damage: A review of current understanding and models.' In: *J. Nuclear Materials* 512, pages 450 –479. DOI: 10.1016/j.jnucmat.2018.10.027 (see pp. 35, 36).

Pardoen, T. and J. Hutchinson (2000). 'An extended model for void growth and coalescence.' In: *J. Mech. Phys. Solids* 48.12, pages 2467–2512 (see pp. 23, 29).

Perrin, G. and J.-B. Leblond (2000). 'Accelerated void growth in porous ductile solids containing two populations of cavities.' In: *Int. J. Plasticity* 16.1, pages 91–120 (see pp. 23, 30).

Petch, N. J. (1954). 'The fracture of metals.' In: *Progress in Metal Physics* 5, pages 1–52. DOI: 10.1016/0502-8205(54)90003-9 (see p. 18).

Petit, T. et al. (2019). 'Effect of hardening on toughness captured by stress-based damage nucleation in 6061 aluminum alloy.' In: *Acta Mater.* 180, 349–365. DOI: 10.1016/j.actamat.2019.08.055 (see pp. 19, 24, 26).

Petit, T. et al. (2022). 'Neutron irradiation and heat treatment effects on pop-in crack propagation instabilities in a 6061 aluminium alloy.' In: *J. Nuclear Materials*, page 153909. DOI: 10.1016/j.jnucmat.2022.153909 (see pp. 43, 46).

Pineau, A. et al. (2016). 'Failure of metals I: Brittle and ductile fracture.' In: *Acta Mater.* 107, 424–483 (see p. 21).

Prasad, N. and R. Wanhill (2017). 'Aerospace Materials and Material Technologies.' In: Springer, Singapore. Chapter 2, pages 29–52. DOI: 10.1007/978-981-10-2134-3 (see p. 14).

Prince, K. and J. Martin (1979). 'The effects of dispersoids upon the micromechanisms of crack propagation in Al-Mg-Si alloys.' In: *Acta Mater.* 27.8, pages 1401–1408. DOI: 10.1016/0001-6160(79)90209-8 (see p. 21).

Puttick, K. E. (1959). 'Ductile fracture in metals.' In: *The Philosophical Magazine: A Journal of Theoretical Experimental and Applied Physics* 4.44, pages 964–969. DOI: 10.1080/14786435908238272 (see p. 18).

Querin, J. et al. (2007). 'Analysis of micro void formation at grain boundary triple points in monotonically strained AA6022-T43 sheet metal.' In: *Mater. Sci. Engng A* 463.1, pages 101–106. ISSN: 0921-5093. DOI: 10.1016/j.msea.2006.10.167 (see p. 20).

Ramberg, W. and W. Osgood (1943). *Description of stress-strain curves by three parameters*. Technical report (see p. 29).

Rice, J. R. and D. M. Tracey (1969). 'On the ductile enlargement of voids in triaxial stress fields.' In: *J. Mech. Phys. Solids* 17, pages 201–217 (see pp. 21, 22, 24).

Rivalin, F. et al. (2000). 'Ductile tearing of pipeline-steel wide plates — I. Dynamic and quasi-static experiments.' In: *Eng. Fract. Mech.* 68.3, pages 329–345 (see p. 23).

Safdarian, R. (2018). 'Forming limit diagram prediction of 6061 aluminum by GTN damage model.' In: *Mechanics & Industry* 19.2, page 202. DOI: 10.1051/meca/2018006 (see p. 24).

Shen, Y. (Dec. 2012). 'Comportement et endommagement des alliages d'aluminium 6061-T6: approche micromécanique.' PhD thesis. Ecole Nationale Supérieure des Mines de Paris (see p. 22).

Shen, Y. et al. (2013). 'Three-dimensional quantitative in situ study of crack initiation and propagation in AA6061 aluminum alloy sheets via synchrotron laminography and finite-element simulations.' In: *Acta Mater.* 61, pages 2571–2582. DOI: 10.1016/j.actamat.2013.01.035 (see pp. 19, 21, 24).

Simar, A. et al. (2010). 'Micro-mechanical modelling of ductile failure in 6005A aluminium using a physics based strain hardening law including stage IV.' In: *Eng. Fract. Mech.* 77.13, pages 2491–2503. ISSN: 0013-7944. DOI: 10.1016/j.engfracmech.2010.06.008 (see pp. 25, 30).

Springmann, M. and M. Kuna (2006). 'Determination of Ductile Damage Parameters by Local Deformation Fields: Measurement and Simulation.' In: *Arch. of Appl. Mech.* DOI: 10.1007/s00419-006-0033-9 (see p. 26).

Steglich, D. et al. (2010). 'Interaction between anisotropic plastic deformation and damage evolution in Al 2198 sheet metal.' In: *Eng. Fract. Mech.* 77.17, 3501–3518 (see p. 29).

Suppes, G. and T. Storvick (Sept. 2016). 'Sustainable Power Technologies and Infrastructure.' In: Academic Press. Chapter 2, pages 29–74. DOI: 10.1016/C2014-0-04843-5 (see p. 31).

Tanaka, K. et al. (1970). 'Cavity formation at the interface of a spherical inclusion in a plastically deformed matrix.' In: *The Philosophical Magazine: A Journal of Theoretical Experimental and Applied Physics* 21.170, pages 267–279. DOI: 10.1080/14786437008238415 (see pp. 19, 26).

Tekoğlu, C. et al. (2015). 'On localization and void coalescence as a precursor to ductile fracture.' In: *Philosophical transactions of the Royal Society of London. A* 373. DOI: 10.1098/rsta.2014.0121 (see pp. 18, 19).

Thomason, P. F. (1968). 'A theory for ductile fracture by internal necking of cavities.' In: *J. Ins. Metals* 96, pages 360–365 (see pp. 23, 29).

Thomason, P. (1990). *Ductile Fracture of Metals*. Pergamon Press, Oxford (see pp. 24–26).

Totten, G. et al. (2018). 'Encyclopedia of Aluminum and Its Alloys, Two-Volume Set (Print).' In: 1st edition. Metals and Alloys Encyclopedia Collection. CRC Press. Chapter 6XXX Alloys: Chemical Composition and Heat Treatment, pages 1–15. ISBN: 1466510803, 9781466510807 (see pp. 15–17).

Trejo-Navas, V. et al. (2018). 'Void growth and coalescence in a three-dimensional non-periodic void cluster.' In: *Int. J. Solids Structures* 139–140, pages 65–78. DOI: 10.1016/j.ijsolstr.2018.01.024 (see p. 21).

Tvergaard, V. (1981). 'Influence of voids on shear band instabilities under plane strain condition.' In: *Int. J. Frac.* 17.4, pages 389–407 (see pp. 23, 28).

Tvergaard, V. (1982). 'On the localization in ductile materials containing spherical voids.' In: *Int. J. Frac.* 18.4, pages 237–252 (see pp. 23, 28).

Tvergaard, V. (1990). 'Material failure by void growth to coalescence.' In: *Advances in Applied Mechanics* 27, pages 83–151 (see p. 23).

Tvergaard, V. (1998). 'Interaction of very small voids with larger voids.' In: *Int. J. Solids Structures* 30, pages 3989–4000. DOI: 10.1016/S0020-7683(97)00254-0 (see p. 30).

Tvergaard, V. and A. Needleman (1984). 'Analysis of the cup–cone fracture in a round tensile bar.' In: *Acta Metall.* 32, pages 157–169 (see pp. 23, 29).

Walsh, J. et al. (1989). 'The influence of Mn dispersoid content and stress state on ductile fracture of 2134 type Al alloys.' In: *Acta Mater.* 37.11, pages 2861–2871. DOI: 10.1016/S0001-6160(89)80001-X (see p. 21).

Was, G. (2017). 'Fundamentals of Radiation Materials Science.' In: Springer-Verlag New York. Chapter 2, pages 3–76. DOI: 10.1007/978-1-4939-3438-6 (see pp. 34, 36, 37).

Weeks, J. et al. (1990). 'Effects of High Thermal and High Fast Fluences on the Mechanical Properties of Type 6061 Aluminum on the HFBR.' In: *Effects of Radiation on Mater.* 2, pages 441–452 (see pp. 38, 42–44).

Weeks, J. et al. (1993). 'Effects of High Thermal Neutron Fluences on Type 6061 Aluminum.' In: *Effects of Radiation on Mater.*, pages 1168–1182 (see pp. 33, 37, 38, 42–46).

Wen, J. et al. (2005). 'The modified Gurson model accounting for the void size effect.' In: *Int. J. Plasticity* 21.2, pages 381–395. ISSN: 0749-6419. DOI: 10.1016/j.ijplas.2004.01.004 (see pp. 23, 29).

Worswick, M. and R. Pick (1990). 'Void growth and constitutive softening in a periodically voided solid.' In: *J. Mech. Phys. Solids* 38, pages 601–625 (see p. 29).

Yu, H. et al. (2014). 'Tensile fracture of ultrafine grained aluminum 6061 sheets by asymmetric cryorolling for microforming.' In: *Int. J. Damage Mech.* 23.8, pages 1077–1095. DOI: 10.1177/1056789514538083 (see p. 24).

Zhang, Z. (1996). 'A Sensitivity Analysis of Material Parameters for the Gurson Constitutive Model.' In: *Fatigue and Fract. Engng Mater. Struct.* 19, pages 561 –570. DOI: 10.1111/j.1460-2695.1996.tb00992.x (see p. 26).

Zhang, Z. and E. Niemi (1994). 'Analyzing ductile fracture using dual dilational constitutive equations.' In: *Fatigue and Fract. Engng Mater. Struct.* 17, pages 695–707 (see p. 29).

Zhang, Z. and E. Niemi (1995). 'A new failure criterion for the Gurson–Tvergaard dilational constitutive model.' In: *Int. J. Frac.* 70, pages 321–334 (see p. 23).

Zhang, Z. et al. (2000). 'A complete Gurson model approach for ductile fracture.' In: *Eng. Fract. Mech.* 67.2, pages 155–168 (see p. 20).

3

ANALYTICAL FORMULA FOR OPTIMUM GTN q_1 AND q_2 PARAMETERS

PREAMBLE

This chapter is submitted for publication in the International Journal of Fracture as follows:

Shokeir Z, Garnier J, Petit T, Madi Y, Besson J. Analytical formula for optimum GTN q1 and q2 parameters. Int. J. Frac. 2022;

RÉSUMÉ

Le processus d'optimisation des paramètres GTN est complexe à cause de la multitude des paramètres. Les paramètres de croissance de cavités sont généralement fixés aux valeurs recommandées dans la littérature $q_1 = 1.5$ et $q_2 = 1$, tandis que l'optimisation des paramètres de nucléation de cavités et de coalescence est effectué de manière rigoureuse. Le modèle de cellule unitaire peut être utilisé pour calibrer les paramètres q sous une seule condition : effectuer un nombre important de simulations pour couvrir une large gamme de triaxialité des contraintes et de fraction volumique initiale des vides. Ce processus est coûteux lorsqu'il s'agit d'étudier plusieurs matériaux ayant des comportements élasto-plastiques différents. L'objectif de ce travail est de proposer une formule analytique permettant de trouver les paramètres q optimaux sans aucune simulations. Pour cela, la relation entre les caractéristiques du matériau (limite d'élasticité, module d'Young, écrouissage) et la croissance de cavités dans une cellule unitaire est étudiée. Ensuite, la formule analytique q est exprimée comme une fonction du comportement élastique-plastique. Le résultat principal est que la formule analytique prédit bien la croissance de cavités dans des matériaux élastiques-plastiques très différents. Une étude de cas réelle est présentée pour montrer comment la formule analytique peut être utilisée pour modéliser la ténacité des matériaux ayant des comportements élasto-plastiques différents.

3.1 INTRODUCTION

The *void nucleation, growth, coalescence* is a dominant failure mechanism in most ductile metallic materials [Garrison et al., 1987; Petch, 1954; Puttick, 1959]. In structural materials, voids may either preexist in the matrix (due to the fabrication process) or nucleate on secondary phases by fracture or decohesion (at the particle–matrix interface). Thereafter, void growth takes place due to the plastic strain in the matrix [Needleman, 1987]. Modeling these damage mechanisms is of a great importance to predict the lifetime of mechanical components and design materials with higher performances. The early models found in the literature accounted only for void growth by modeling a single spherical [Rice et al., 1969] or cylindrical [Mc Clintock, 1968] void in an infinite elastic–plastic matrix. Both models highlighted the fact that the void growth rate increases exponentially with respect to the hydro-static stress (σ_{kk}). Nonetheless, the drawback of both models is that they consider isolated voids that do not interact and do not affect the material's overall behavior (i. e. no material softening). Later, Gurson, 1977 establishes a constitutive formulation that describes void growth in a finite matrix by incorporating the porosity (f) as a damage variable in the model. The Gurson model is then improved in the work of [Chu et al., 1980; Tvergaard, 1981, 1982] to account for the strain hardening effect as well as the void nucleation and coalescence phases. The improved model (referred to as GTN) is one the most commonly used models to study failure in elastic–plastic porous materials [1].

The use of the GTN porous plastic model requires a set of parameters to predict void nucleation, growth and coalescence. Void nucleation criteria are chosen based on the material. Experimental evidence regarding void nucleation are inevitable in order to identify the required nucleation criterion and parameters [Argon et al., 1975; Goods et al., 1979; Tang et al., 2021]. Void growth and coalescence models are more "universal". Void coalescence can be modeled by the f_* approach [Tvergaard et al., 1984] which is based on replacing the actual porosity (f) by an effective porosity (f_*) to accelerate void growth beyond the critical porosity f_c [2]. Void coalescence parameters can be calibrated via homogenized models to estimate the critical porosity leading to void coalescence [Benzerga et al., 1999; Pardoen et al., 2000]. The GTN void growth parameters (q_1, q_2) are usually fixed to 1.5 and 1 respectively as recommended by Tvergaard, 1981. This is a common practice in the literature [Broggiato et al., 2007; Lemaitre et al., 2005; Springmann et al., 2006]. The GTN parameters optimization process is highly challenging due to the non-uniqueness of the solution [Li et al., 1994; Zhang, 1996]. Therefore, fixing q_1, q_2 to 1.5 and 1 respectively while calibrating the remaining parameters might be a tempting approach. However, this methodology is criticized by Xia et al., 1995 who did attempts trying to reproduce the J-resistance

1 Benzerga et al., 2016; Besson, 2010 offer comprehensive reviews regarding the GTN and other related porous plastic models

2 See [Benzerga et al., 2010; Besson, 2009; Pardoen et al., 1998; Zhang et al., 2000] for other void coalescence criteria.

curves of a high hardening material presented in the work of Koplik et al., 1988. These attempts are unsuccessful and conclusions are made that the $q_1 = 1.25$ and $q_2 = 1$ from the work of Koplik et al., 1988 are not suitable for lower strain hardening-level materials. There is a lack of information regarding the effect of the q-parameters on the material's softening behavior.

The unit cell model is an adequate tool for studying void growth and coalescence as presented in the early work of Becker et al., 1994; Kuna et al., 1996; Needleman, 1972; Worswick et al., 1990. The regularly distributed voids in a solid material can be represented by a 3D periodic array of unit cells with a single spherical void in the center of each cell. Appropriate boundary conditions on the unit cell allow to represent the solid material containing several voids. Several authors study void growth in different materials [Borg et al., 2008; Chien et al., 2000; Hosseini et al., 2022; Ling et al., 2016; Steglich et al., 2010; Wen et al., 2005] and void coalescence [Fabrègue et al., 2008; Pardoen et al., 2000; Zhang et al., 2001] using the unit cell model. The latter can also be utilized to calibrate the q-parameters as explained by Faleskog et al., 1998. The cited authors developed a calibration methodology based on a unit cell model with a Ramberg-Osgood [Ramberg et al., 1943] elastic–plastic flow. Firstly, FE unit cell simulations are carried out over a given range of stress triaxialites. Then, FE simulations are carried out over the same range of stress triaxialites using a homogenized cell model with a GTN behavior [3]. Finally, the q_1 and q_2 parameters used in the homogenized model are optimized by minimizing the error between stress—strain curves of the unit and homogenized cells. Later, Kim et al., 2004 utilize the same q-parameters calibration process developed Faleskog et al., 1998 by to study the effect of stress triaxiality on void growth. Both, Faleskog et al., 1998 and Kim et al., 2004, agree that the q_1 and q_2 parameters are strong functions of the yield strength and hardening characteristics of the material. The cited authors add that the q-parameters cannot be treated as universal constants.

The q-parameters calibration methodology presented by Faleskog et al., 1998 requires a considerable quantity of 3D unit cell simulations to cover a wide range of stress triaxiality and initial void volume fraction (f_0). Even though this process results in optimum q_1 and q_2 values, it may often seem costly and time consuming when one needs to model several materials with different elastic–plastic behaviors. Besides, can one use the same q_1 and q_2 values calibrated for an undeformed material to model void growth in the same pre-deformed material?

The above statements call attention to the purpose of this paper: is it possible to propose an analytical formula to find the optimum q-parameters without any FE simulations? This analytical formula only exists if the relationship between q-parameters and the material characteristics (elastic–plastic behavior and void volume

3 The homogenized model referred to here is a 3D cell with no void in its center. The void is added via the GTN behavior of the homogenized cell. The latter's behavior can then be compared to the unit cell's behavior while assuring the same initial void volume fraction in both models.

fraction) is straightforward. Therefore, this paper is divided into five main sections that have the following objectives:

- Section 3.2: Present the unit cell model and the studied materials' behavior.
- Section 3.3: Investigate the effect of the yield strength, Young's modulus and strain hardening capacity on void growth in the unit cell model.
- Section 3.4 In accordance with the results of the previous section, the material characteristics that affect void growth in the unit cell model are sorted out to study their effect on the q-parameters. The objective of this section is to show how q_1 and q_2 change as a function of each material characteristic (e. g. q_1 as a function of the yield strength).
- Section 3.5: According to the tendencies observed in the previous section, an analytical formula is proposed to identify the optimum q_1 and q_2 values. The analytical formula should be able to give optimum q_1 and q_2 values for any chosen material behavior.
- Section 3.6: The analytical formula is applied to a real-life case study: modeling the fracture toughness of irradiated aluminum alloys using Compact-Tension samples. In nuclear reactors, the radiation dose increases the yield strength and decreases the strain hardening capacity of the core components. Therefore, the chosen case study is well adapted to the use of the analytical formula on materials with different elastic–plastic behaviors.

3.2 NUMERICAL METHODS

3.2.1 *Unit cell model*

The studied cells are cubic with a side length (L) and a spherical void at the center with a radius r that is deduced from the void volume fraction f as follows: $f = 4\pi \left(r/L\right)^3 /3$. 20-node 3D hexahedral elements with 8 integration points (reduced integration to limit volume locking) are used to mesh only one-eighth of the whole cell thanks to the symmetries.

The boundary and loading conditions are detailed in the work of Han et al., 2013. Normal displacements on the cell faces are maintained homogeneous so that the cell keeps a parallelipedic shape. This condition allows to perform displacement controlled FE simulations. The cell is loaded in the x-direction. The macroscopic Cauchy stress (σ_{xx}) and macroscopic plastic deformation (ε^p_{xx}) are calculated in the loading direction. The stress triaxiality is maintained constant over the cell as explained in the work of Brocks et al., 1995 (see fig. 1 in [Han et al., 2013]). The stress σ_{xx} is measured in the loading direction and a portion of this stress is applied on the two other directions

($\sigma_{yy} = \sigma_{zz} = \eta\sigma_{xx}$, where $\eta = (3T-1)/(3T+2)$ given T the stress triaxiality). The porosity (f) is calculated as follows:

$$f = 1 - \frac{V_0(1-f_0)}{V(1-\alpha_{\text{elastic}})} \tag{3.1}$$

where V_0 the initial cube total volume ($V_0 = 1$), f_0 the initial void volume fraction and α_{elastic} the elastic dilatation arising from the imposed mean stress given as follows:

$$\alpha_{\text{elastic}} = \frac{\sigma_m}{K_f} \tag{3.2}$$

where K_f is an effective bulk modulus taking into account the porosity effect as follows:

$$K_f = K_0 \frac{1-f}{1-f_0} \tag{3.3}$$

where K_0 is estimated at the very beginning of the simulation based on the increase in volume at the first time step (while the cell remains in the elastic regime) and ΔP as the difference in pressure:

$$K_0 = V_0 \frac{\Delta P}{\Delta V} = V_0 \frac{\sigma_m}{\Delta V} \tag{3.4}$$

The mesh size is optimized based on a convergence check over the macroscopic quantities of interest: σ_{xx}, ε^p_{xx} and the porosity. Section 3.7 explains the mesh size convergence check. All FE simulations in this work are carried out using Zset software [Besson et al., 1997]. The used finite–strain formalism is a generic formulation based on a reference frame which assures maintaining the standard small strain formulation while using an additive strain rate decomposition (i. e. $\underline{\dot{\varepsilon}}^{\text{to}} = \underline{\dot{\varepsilon}}^{\text{el}} + \underline{\dot{\varepsilon}}^{\text{p}}$ where $\underline{\dot{\varepsilon}}^{\text{to}}$ is the strain rate tensor and $\underline{\dot{\varepsilon}}^{\text{el}}$ the elastic strain rate tensor) [Sidoroff et al., 2001].

Table 3.1 recapitulates the studied f_0 and stress triaxialities. Each studied material in this work is simulated over the whole range of f_0 and $\sigma_m/\sigma_{\text{eq}}$. The range of f_0 is representative of real initial void volume fractions in industrial aluminum alloys [Needleman et al., 1990; Thomson et al., 2003].

3.2.2 *Elastic–plastic behavior*

Two hardening laws are used to model the unit cell's isotropic plastic behavior. Equation (3.5) shows the Voce flow stress law with σ_0, A, b as parameters and p the accumulated plastic strain:

$$\sigma_{\text{Voce law}}(p) = \sigma_0 + A\ (1 - e^{-b\,p}) \tag{3.5}$$

Table 3.1: Unit cell simulation matrix. Three different meshes with varying f_0. For each mesh, all stress triaxiality levels are modeled.

Initial void volume fraction (f_0)	Stress triaxiality (σ_m/σ_{eq})	Number of simulations
0.35%	1.0, 1.6, 2.2, 2.8	3 meshes × 4 stress triaxialities
1.00%		
2.15%		

Equation (3.6) describes the stress flow using a power hardening law with σ_0, p_0 as parameters, n the strain hardening exponent and p the accumulated plastic strain:

$$\sigma_{\text{Power law}}(p) = \sigma_0 \left(1 + \frac{p}{p_0}\right)^n \tag{3.6}$$

The reason why two hardening laws are chosen for this study is based on conclusions from the work of Lecarme et al., 2011. The cited authors emphasize the importance of the exponential strain hardening law introduced by Voce, 1995 since the power laws do not account for stages III and IV of hardening (see [Kocks et al., 2003] for a complete review on strain hardening). Figure 1 in the work of Lecarme et al., 2011 elaborates stage III where an increase in stress leads to a linear decrease in hardening due to the competition between dislocation interaction, accumulation, and recovery. The flow stress tends to saturate due to the linear decrease of hardening (commencement of stage IV). However, failure under high stress triaxiality usually takes place before stage IV is reached. Lecarme et al., 2011 conclude that the use of power hardening laws leads to underestimating void growth and overestimating the strain at failure by a factor of two. Nevertheless, the purpose of this study is to propose an analytical formula to find optimum q-values. The analytical formula should not be biased towards the Voce or power law. Therefore, both hardening laws are well-advised for this study.

In order to study the effect of the Voce versus power hardening laws on void growth, the elastic–plastic behavior given by both laws must be comparable. One way to do this is to assure that both laws result in the same plastic deformation at the maximum engineering stress given by an instability criterion. The Considère instability criterion can be used to estimate a critical plastic deformation ($p_{\text{Considère}}$) by solving the following equality [Considère, 1885]:

$$\frac{d\sigma_F(p_{\text{Considère}})}{dp} = \sigma_F(p_{\text{Considère}}) \tag{3.7}$$

At a given σ_0, the strain hardening exponent n is chosen and the p_0 parameter is fixed to 0.005 for the power law. Then, the $p_{\text{Considère}}$ of the power law can be determined by

eq. (3.7). The remaining Voce parameters A, b are determined by making sure that the $p_{\text{Considère}}$ and flow stress at $p_{\text{Considère}}$ is identical for both laws usging the following equalities:

$$(p_{\text{Considère}})_{\text{Power law}} = (p_{\text{Considère}})_{\text{Voce law}} \tag{3.8}$$

$$\sigma_{\text{Power law}}(p_{\text{Considère}}) = \sigma_{\text{Voce law}}(p_{\text{Considère}}) \tag{3.9}$$

3.3 RELATION BETWEEN THE ELASTIC–PLASTIC BEHAVIOR AND VOID GROWTH IN THE UNIT CELL MODEL

In this section, void growth is analyzed in a unit cell model. The objective is to study the effect of the Young's modulus (E), yield strength (σ_0) and strain hardening capacity on void growth. The effect of the hardening law on void growth is also investigated.

3.3.1 *Effect of the Young's modulus (E) on void growth*

In order to investigate the Young's modulus effect, the power law in eq. (3.6) is used with $\sigma_0 = 300$ MPa, $p_0 = 0.005$ and $n = 0.1$ to model the elastic–plastic behavior. The Young's modulus is varied from 35 to 210 GPa. Stress—plastic strain and porosity—plastic strain curves for different moduli are shown in fig. 3.1. The E has a modest influence on void growth that is observed between 35 and 70 GPa. However, the E effect on void growth saturates at high moduli (> 70 GPa).

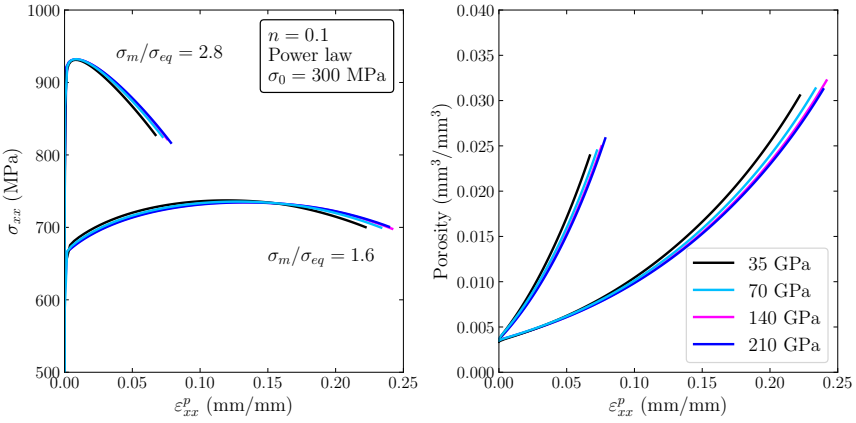

Figure 3.1: Cauchy stress—plastic strain and porosity—plastic strain curves given the same strain hardening exponent n and 3 different Young's moduli. The plastic flow is modeled by the power law in eq. (3.6) with $\sigma_0 = 300$ MPa, $p_0 = 0.005$ and $n = 0.1$.

3.3.2 *Effect of the yield strength (σ_0) on void growth*

In the following, the influence of yield strength and strain hardening on void growth is illustrated. Three yield strengths are chosen: 300, 500 and 700 MPa, and the strain hardening exponent n is varied from 0.015 to 0.21 for each of the chosen yield strengths. A wide range of yield strengths and hardening is chosen to consider real mechanical properties of different industrial alloys as: steels, aluminum and zirconium alloys. Table 3.2 lists the Voce and power law parameters of the studied materials. Each line in table 3.2 gives Voce and power law parameters for an equivalent $p_{\text{Considère}}$. The latter can be directly determined as follows: $p_{\text{Considère}} = n - p_0$. The Young's modulus and Poisson ratio are chosen as 70 GPa and 0.33 respectively.

Table 3.2: Plastic flow parameters of the studied materials. Each line gives a hardening behavior that can be modeled by the Voce or power laws. For a given material, both laws have the same $p_{\text{Considère}}$ and flow stress at $p_{\text{Considère}}$ as explained in the section 5.3.1.

	Voce law parameters		Power law parameters		
σ_0 (MPa)	A (MPa)	b (-)	n (-)	p_0 (-)	$p_{\text{Considère}}$
300	8.3	91.4	0.015	0.005	$n - p_0$
	46.3	34.8	0.050		
	126.7	18.5	0.100		
	268.2	11.4	0.160		
	436.4	8.4	0.210		
500	13.9	91.4	0.015		
	77.1	34.8	0.050		
	211.2	18.5	0.100		
	446.9	11.4	0.160		
	727.3	8.4	0.210		
700	19.4	91.4	0.015		
	108.0	34.8	0.050		
	295.6	18.5	0.100		
	625.7	11.4	0.160		
	1018.2	8.4	0.210		

Figure 3.2 shows the porosity—plastic strain curves of three materials having the same strain hardening exponent $n = 0.21$, same Young's modulus $E = 70$ GPa and three different yield strengths. The σ_0 effect is noticeable at high plastic strain. At low (1.0) and intermediate (1.6) stress triaxiality levels, the higher the yield strength, the higher the void growth at high strain levels. Void growth at low plastic strain levels

($\varepsilon^p_{xx} < 0.4$ for $\sigma_m/\sigma_{eq} = 1.0$) is identical between $\sigma_0 = 300, 500$ and 700 MPa. At high (2.8) stress triaxiality, σ_0 does not influence the void growth rate since coalescence is reached at lower plastic strain levels.

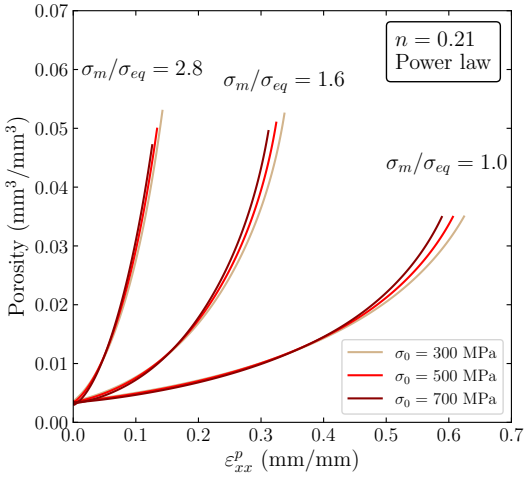

Figure 3.2: Effect of σ_0 on the void growth in a unit cell at low (1.0), intermediate (1.6) and high (2.8) stress triaxiality levels

Results in fig. 3.1 and fig. 3.2 affirm that decreasing E or increasing σ_0 increases the void growth rate. Since the E and σ_0 effects are antagonistic, increasing or decreasing σ_0 at a constant σ_0/E ratio should not affect the void growth rate. This hypothesis is validated in fig. 3.3 which shows stress—plastic strain and porosity—plastic strain curves of three materials having the same strain hardening exponent $n = 0.1$ and σ_0/E ratio. It is clear that the void growth rate remains unchanged at a constant σ_0/E ratio.

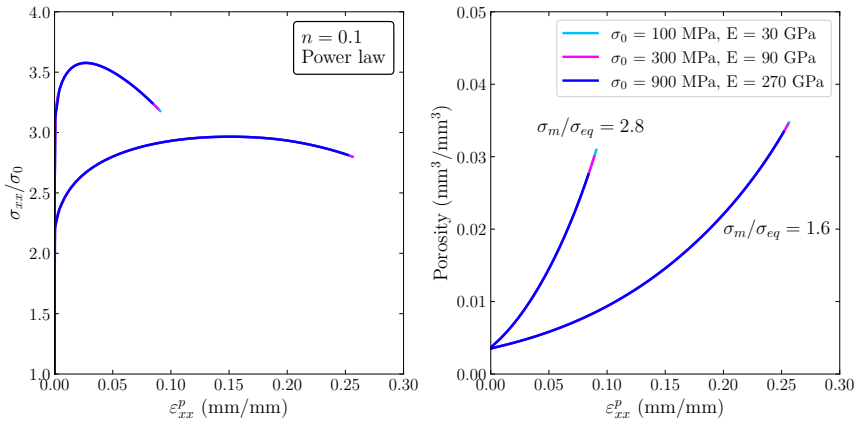

Figure 3.3: Cauchy stress—plastic strain and porosity—plastic strain curves for the same strain hardening exponent n and same σ_0/E ratio

3.3.3 *Effect of the strain hardening capacity on void growth*

The strain hardening effect on void growth is widely discussed in the literature since void growth depends on the plastic strain. Figure 3.4 displays the porosity—plastic strain curves of five materials having the same yield strength $\sigma_0 = 500$ MPa, same Young's modulus $E = 70$ GPa and five different strain hardening exponents n. The latter varies from 0.015 to 0.21 as shown in table 3.2. Figure 3.4 shows that at low stress triaxiality (1.0), the strain hardening exponent n has a high impact on void growth. However, the dependency of void growth on strain hardening is subdued at high stress triaxiality (2.8).

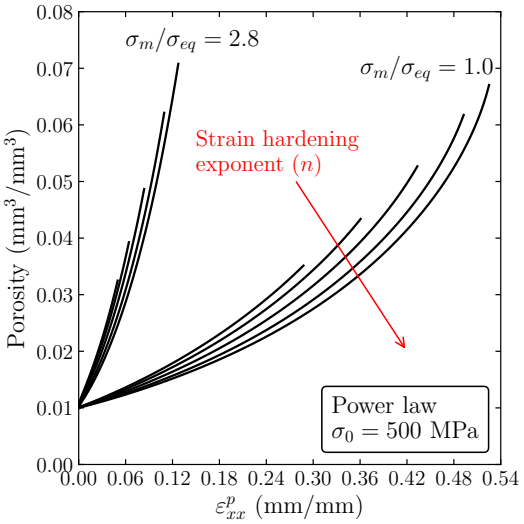

Figure 3.4: Porosity—strain curves with a varying strain hardening exponent $n = \{0.015, 0.05, 0.1, 0.16, 0.21\}$ at low (1.0) and high (2.8) stress triaxialities

3.3.4 *Effect of the strain hardening flow law on void growth*

The choice of the plastic flow law has an effect on void growth as discussed in section 3.2. This matter is made clear in fig. 3.5 as one can see that the power law results in lower void growth and higher deformation at coalescence (maximum ε^p_{xx} value in fig. 3.5). One must note that the Voce and power laws are compared at an equivalent $p_{\text{Considère}}$.

Another important fact to highlight is the sensibility of void growth to stress triaxiality when using the Voce and power laws at low stress triaxiality. As concluded by Faleskog et al., 1998, at high stress triaxialities (> 2), strain hardening weakens the dependency of void growth rate on stress triaxiality. This statement is true as it can be observed for high stress triaxiality (2.8) in fig. 3.6. The reason why void growth curves between Voce and power laws are almost identical at high stress triaxiality (2.8) is the

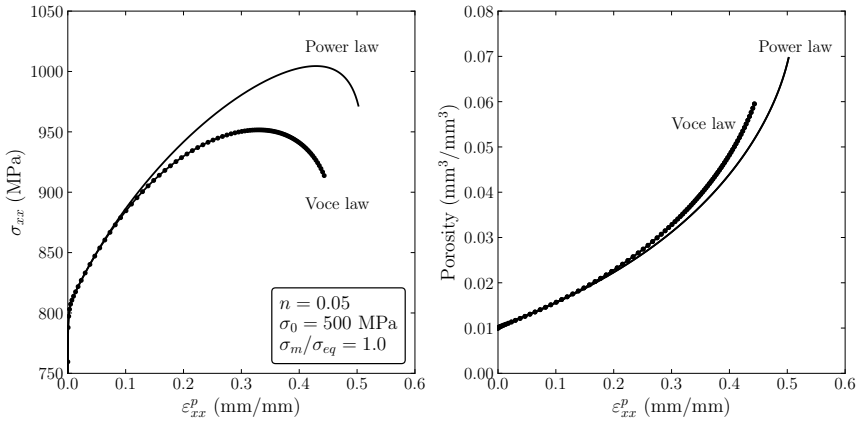

Figure 3.5: Effect of the strain hardening law (Voce vs. Power) on stress—strain curves and void growth at low stress triaxiality (1.0)

fact that both laws result in a quite similar flow stress (σ_F) till $p_{\text{Considère}}$ is reached. Moreover, at high stress triaxiality, the macroscopic plastic deformation in the unit cell does not reach $p_{\text{Considère}}$. Usually void coalescence in unit cell simulations under high stress triaxiality takes place prior $p_{\text{Considère}}$. This explains the good agreement between Voce and power laws at high stress triaxiality (2.8) in fig. 3.6. On the contrary, at low stress triaxiality, void coalescence takes place at deformation levels beyond $p_{\text{Considère}}$. Beyond $p_{\text{Considère}}$, only the Voce law accounts for stage III of hardening. The hardening saturation in the Voce law leads to higher void growth at high strain levels as seen at low stress triaxiality (1.0) in fig. 3.6. Consequently, this results in the differences observed between Voce and power laws at low stress triaxiality (1.0) in fig. 3.6. These results are in good agreement with the conclusions made by Lecarme et al., 2011 regarding the underestimation of void growth when using a power law. Furthermore, these results highlight the importance of characterizing the elastic–plastic behavior beyond the instability phase (i. e. beyond $p_{\text{Considère}}$). The characterization of the elastic–plastic behavior beyond the necking phase in tensile samples is discussed in other work [Shokeir et al., 2022].

Results from this section demonstrate the following facts:

- The Young's modulus E has a weak (but not negligible) effect on void growth at low moduli ($E \leq 70$ GPa and $\sigma_0/E = 0.0043$). No difference is observed between the high studied moduli ($E = 140$ and 210 GPa).
- At a fixed E, increasing the yield strength σ_0 increases void growth at high plastic strains. At low plastic strain, the three studied $\sigma_0 = 300, 500$ and 700 MPa displayed a similar void growth rate. However, at high plastic strains, the $\sigma_0 = 700$ MPa has a superior void growth rate.
- The strain hardening capacity has a blatant influence on void growth. The effect of hardening is by far the dominating material characteristic regarding void growth.

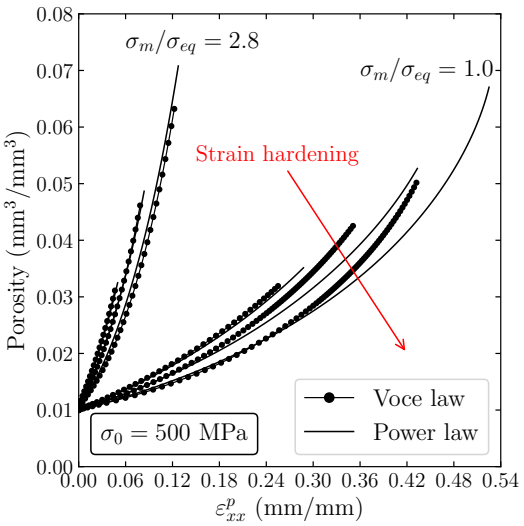

Figure 3.6: Comparison between the strain hardening law (Voce vs. Power) effect on void growth at low (1.0) and high (2.8) stress triaxiality for $n = \{0.015, 0.100, 0.210\}$. Voce and power laws are compared at the same $p_{\text{Considère}}$.

- The power flow law underestimates void growth as it does not account for the hardening saturation. The Voce law accounts for the hardening saturation, and therefore, results in a higher void growth rate at low and intermediate stress triaxiality < 1.6.

3.4 INFLUENCE OF THE ELASTIC–PLASTIC BEHAVIOR ON THE CALIBRATED q_1 AND q_2 VALUES

In this section, the q-parameters calibration process is applied on the studied materials in table 3.2. The effect of yield strength and strain hardening on the optimum q-values is investigated.

3.4.1 *Homogenized model*

The homogenized model is compared with the unit cell model in order to find the optimum q_1 and q_2 values. Unlike the unit cell model, the homogenized model does not contain a void in its center. However, the homogenized cell material behavior is modeled by the GTN model which incorporates the void volume fraction (f) as a damage variable. The homogenized model is explained below.

A 8-node 3D hexahedral element with a single integration point and side length (L) is used to compare with the unit cell model. The initial void in the homogenized cell is introduced via the GTN model parameter: f_0. The porosity is expressed as the increase in volume fraction due to void growth (f_g) [Tvergaard et al., 1984]. The model relies

on the definition of an effective stress ($\sigma_\star$) used to define the yield criterion as follows [Besson et al., 2001]:

$$S = \sigma_\star - \sigma_F(p) \tag{3.10}$$

where σ_F is the flow stress of the undamaged material. The plastic strain rate tensor is obtained using the normality rule as follows:

$$\underline{\dot{\varepsilon}}^{\mathrm{p}} = (1-f)\,\dot{p}\,\frac{\partial S}{\partial \underline{\sigma}} \tag{3.11}$$

where $\underline{\sigma}$ is the Cauchy stress tensor. The plastic multiplicator $\dot{p}$ is given such that $\underline{\dot{\varepsilon}}^{\mathrm{p}} : \underline{\sigma} = (1-f)\dot{p}\sigma_\star$. Furthermore, $\dot{p}$ is obtained either using the consistency condition (rate independent case) or a visco–plastic flow rule (rate dependent case). The effective stress of the GTN model is implicitly defined as a function of the stress tensor and the porosity as shown below:

$$\left(\frac{\sigma_{\mathrm{eq}}}{\sigma_\star}\right)^2 + 2q_1 f_* \cosh\left(\frac{3}{2}q_2\frac{\sigma_m}{\sigma_\star}\right) - 1 - {q_1}^2 f_*^2 \equiv 0 \tag{3.12}$$

where σ_{eq} is the von Mises equivalent stress, and σ_m the mean stress. f_* is defined such that:

$$f_* = \begin{cases} f & \text{if } f < f_c \\ f_c + \delta(f - f_c) & \text{otherwise} \end{cases} \tag{3.13}$$

where the "acceleration" factor $\delta \geq 1$ is expressed as:

$$\delta = \frac{1/q_1 - f_c}{f_r - f_c} \tag{3.14}$$

Coalescence is triggered when f reaches the critical value f_c. The porosity at failure is noted f_r. Finally, void growth is directly obtained from the plastic flow (mass conservation) as follows:

$$\dot{f}_g = (1-f)\mathrm{tr}(\underline{\dot{\varepsilon}}^{\mathrm{p}}) \tag{3.15}$$

Unit cell simulations do not account for void nucleation and coalescence. Therefore, both are not taken into account in the homogenized cell.

For each unit cell simulation, a corresponding homogenized cell simulation is carried using the same f_0, stress triaxiality and the elastic–plastic behavior. In order to

compare results of the homogenized and unit cell simulations, the same boundary conditions are applied on both the homogenized and unit cell.

The aim of the homogenized cell simulations is to assess the q_1 and q_2 parameters. The latter are fit by minimizing the error between the homogenized and unit cell curves regarding the evolution the σ_{xx} and the porosity (f) with respect to ε^p_{xx}. Errors on stresses and porosity are normalized for the sake of comparison. For each *unit vs. homogenized cell* comparison, the errors R_σ and R_f are calculated over the range of ($\varepsilon_{min} \rightarrow \varepsilon_{max}$) as follows:

$$R_\sigma = \frac{1}{2\left(\varepsilon_{max} - \varepsilon_{min}\right)} \int_{\varepsilon_{min}}^{\varepsilon_{max}} \left(\frac{\sigma_{\text{unit cell}}(\varepsilon) - \sigma_{\text{GTN}}(\varepsilon)}{\sigma_{\text{unit cell}}(\varepsilon)} \right)^2 d\varepsilon$$

$$R_f = \frac{1}{2\left(\varepsilon_{max} - \varepsilon_{min}\right)} \int_{\varepsilon_{min}}^{\varepsilon_{max}} \left(\frac{f_{\text{unit cell}}(\varepsilon) - f_{\text{GTN}}(\varepsilon)}{f_{\text{unit cell}}(\varepsilon)} \right)^2 d\varepsilon$$

where ε_{min} and ε_{max} are expressed as shown below:

$$\varepsilon_{min} = 0 \quad \text{and} \quad \varepsilon_{max} = \varepsilon_{\text{unit cell}} = \varepsilon_{\text{coalescence onset}} \tag{3.16}$$

The nondimensionalized objective function shown below is then minimized on k simulations:

$$F_{\text{obj}} = \frac{1}{k} \sum_{i=1}^{k} \left(R_\sigma + R_f \right) \tag{3.17}$$

3.4.2 *q_1 and q_2 calibration results*

The optimum q_1 and q_2 values for each of the materials in table 3.2 are displayed in fig. 3.7. The first general observation is that q_2 decreases as the strain hardening increases. This is true regardless of the chosen hardening law (Voce or power law). The q_2 parameter is included in the cosh(...) term and multiplied by $\sigma_m/\sigma_\star$ as shown in eq. (3.12). The $\sigma_m/\sigma_\star$ term is analogue to the stress triaxiality. As stated in the previous section, strain hardening weakens the dependency of void growth on stress triaxiality. This explains the lower q_2 at high strain hardening exponent n. Besides, the difference between the maximum and minimum q_2 corresponding to the lowest and highest n respectively is higher in the case of Voce law. This is explained by the highlighted result at the end of the previous section: the Voce law results in a higher void growth rate at low and intermediate stress triaxiality < 1.6.

The second general observation is that when q_1 increases, q_2 decreases. The highest q_1 is associated with the lowest q_2 for both Voce and power laws and vice versa. The q_1 parameter does not increase much as a function of n in the case of the power law.

This reflects the fact the power law does not account for the hardening saturation. The absence of hardening saturation leads to a weaker dependency of void growth on strain hardening which leads to a lower increase in q_1 as a function of n in the case of power law.

The last general observation is that at a constant n, an increase in σ_0 leads to a decrease in q_1 and an increase in q_2. The increase in q_2 as a function of σ_0 allows to comply with the results in fig. 3.2.

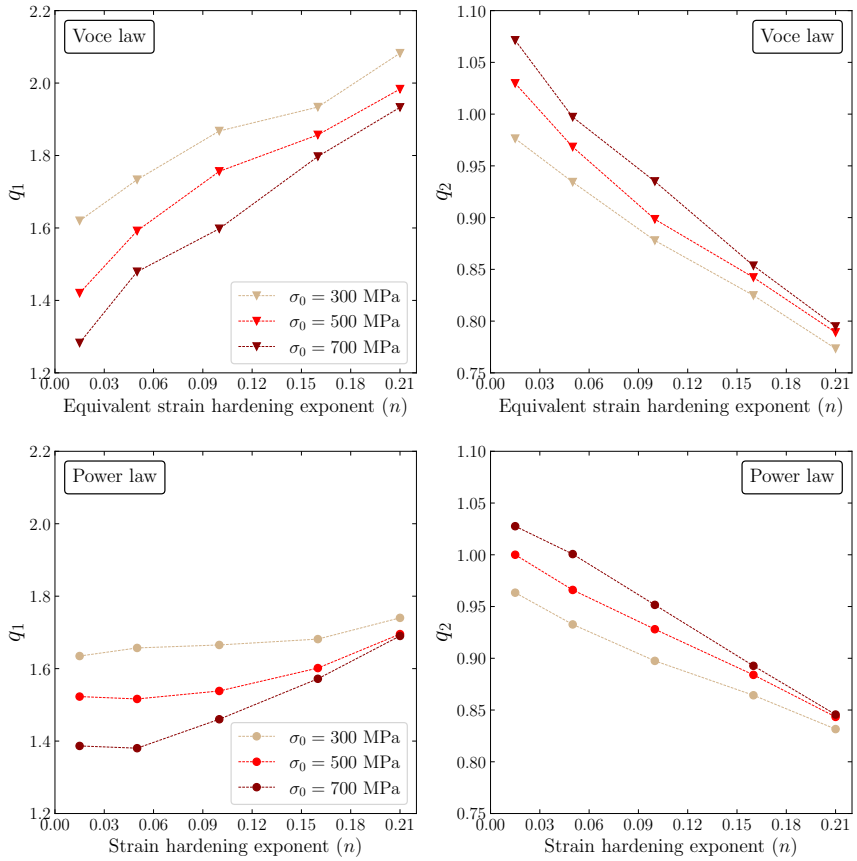

Figure 3.7: Calibrated q_1 and q_2 parameters as a function of the strain hardening exponent n using a Voce and power strain hardening laws at $\sigma_0 = 300$, 500 and 700 MPa

It is important to underline the fact that the initial void volume fraction does not affect void growth over a finite domain. This matter is discussed in section 3.7. Furthermore, Faleskog et al., 1998 studied $f_0 = 0.1$ and 1%. During the q-calibration process, the cited authors take into account both studied f_0 in the objective function.

Results from this section reveal the fact that a linear relation exists between the q-values and hardening, as well as, q-values and σ_0. This result constitutes the motivation for proposing an analytical formula for optimum q-values in the following section.

3.5 UNIVERSAL ANALYTICAL FORMULA FOR OPTIMUM q-VALUES

The objective of this section is to propose an analytical q-formula to find the optimum q-values of different materials without carrying out FE simulations per material. The analytical q-formula should only depend on the elastic–plastic behavior of the material (more precisely, yield strength, Young's modulus and strain hardening capacity). The following open ended questions are to keep in mind when proposing the analytical q-formula:

- A single optimum q_1, q_2 couple in fig. 3.7 requires a minimum of 12 unit cell FE simulations followed by an optimization process using the homogenized model. Is it possible to find the optimum q-values for several materials without carrying out plenty of FE simulations?
- Are the optimum q-values for an undeformed structure adapted for modeling void growth in the same predeformed structure? For instance, Shinohara et al., 2016 used different q-values to model a predeformed line pipe steel. This reveals the fact that same material can have a different void growth rate if it undergoes preliminary deformation.

3.5.1 *Development of the universal analytical q-formula*

In order to make the analytical q-formula independent from the used hardening law, the chosen approach is to relate the q-values to the instantaneous hardening level. The latter can be expressed as follows:

$$N(p) = \frac{\partial \log\left(\sigma_F(p)\right)}{\partial p} \tag{3.18}$$

In the same manner, an instantaneous strength to Young's modulus ratio can be expressed as follows:

$$\chi(p) = \frac{\sigma_F(p)}{E} \tag{3.19}$$

The $\chi(p)$ term accounts for the effect of σ_0 on void growth and is normalized by E. Therefore, the q-values depending on the instant strain hardening and strengthening level can be defined as shown below:

$$\begin{aligned} q_1(p) &= m_1\, N(p) + b_1\, \chi(p) + q_1^* \\ q_2(p) &= m_2\, N(p) + b_2\, \chi(p) + q_2^* \end{aligned} \tag{3.20}$$

where m_i, b_i and q_i^* are coefficients that must be fit. A linear relationship is used in eq. (3.20) for simplicity.

Several hardening laws as well as the limits of the instantaneous hardening ($\lim_{p\to 0} N(p)$ and $\lim_{p\to\infty} N(p)$) are listed in table 3.3. The Ramberg-Osgood law, widely used in the literature [Faleskog et al., 1998; Kim et al., 2004; Tvergaard, 1981; Tvergaard et al., 1984], can be expressed as a function of the accumulated plastic strain in order to estimate the instantaneous hardening level using eq. (3.18). The Ramberg-Osgood is originally expressed as follows:

$$\varepsilon = \begin{cases} \sigma & \text{if } \sigma < \sigma_0 \\ \frac{\sigma_0}{E}\left(\frac{\sigma}{\sigma_0}\right)^{\frac{1}{n}} & \text{if } \sigma > \sigma_0 \end{cases} \tag{3.21}$$

In order to express the stress flow as a function of p, the Ramberg-Osgood can be written in an implicit form and solved using a Newton-Raphson algorithm:

$$p = \frac{\sigma_0}{E}\left(\frac{\sigma}{\sigma_0}\right)^{\frac{1}{n}} - \frac{\sigma}{E} \tag{3.22}$$

Table 3.3: Different hardening laws and the limits of the instant hardening N in eq. (3.18)

Hardening law	$\sigma_F(p)$	$\lim_{p\to 0} N(p)$	$\lim_{p\to\infty} N(p)$
Voce	$\sigma_0 + A\,(1-\exp(-bp))$	$\frac{Ab}{\sigma_0}$	0
Modified Swift	$\sigma_0\left(1+\frac{p}{p_0}\right)^n$	$\frac{n}{p_0}$	0
Ramberg-Osgood	Implicit	$\frac{En}{\sigma_0(1-n)}$	0
Mixed Voce & power	$\lambda\left[\sigma_0+\left(1+\frac{p}{p_0}\right)^n\right]+(1-\lambda)\left[\sigma_0+A\,(1-\exp(-bp))\right]$	$\frac{\lambda Ab}{\sigma_0}-\frac{\lambda n}{p_0}+\frac{n}{p_0}$	0

One must note the interesting fact that $\lim_{p\to 0} N(p)$ is equal to 0 regardless of the used hardening law.

The m_i, b_i and q_i^*, coefficients of the universal law (eq. (3.20)), are fitted over the 30 studied materials in section 3.3 (360 simulations corresponding to 3 different σ_0, 5 different n, 4 stress triaxiality levels, 3 different f_0, 2 hardening laws). The 360 simulations are considered in the objective function that is minimized as discussed in section 3.4. The optimum coefficients are listed in table 3.4. Using these coefficients, the homogenized cell gives results that are in good agreement with the unit cell for the 30 studied materials. The latter cover a wide range of yield strengths, strain hardening and f_0. Therefore, one expect that these coefficients can model new materials. This matter is discussed in the following paragraph.

The optimum q^* coefficients shown in table 3.4 are in good agreement with values recommended by Koplik et al., 1988 for non-hardening materials ($q_1 = 1.25,\ q_2 = 1$). For a non-hardening material, the instantaneous hardening level is null, (i. e. $N(p) = 0$). Therefore, eq. (3.20) is reduced to $q_1(p) = b_1\ \sigma_0/E + q_1^*$ and $q_2(p) = b_2\ \sigma_0/E + q_2^*$.

	m	b	q^*
q_1	-0.014	2.1	1.24
q_2	-0.022	1.6	1.03

Table 3.4: Coefficients of the q-values analytical q-formula (eq. (3.20)). q_1 and q_2 are expressed as a function of the instantaneous strain hardening $N(p)$ (see eq. (3.18)) and strength to Young's modulus ratio $\chi(p)$ (see eq. (3.19))

3.5.2 *Testing the analytical q-formula on new materials*

3.5.2.1 *Sensibility of the analytical q-formula to change in strain hardening*

In order to challenge the universal analytical q-formula, a new hardening law with a mixed elastic–plastic behavior between Voce and power laws is defined as follows:

$$\sigma_F(p) = \lambda \left[\sigma_0 + \left(1 + \frac{p}{p_0}\right)^n\right] + (1-\lambda)\left[\sigma_0 + A\left(1 - \exp(-bp)\right)\right] \tag{3.23}$$

The λ is taken equal to 0.5 while the equivalent n Voce and n power law are mixed as shown in fig. 3.8.

Figure 3.9 displays the unit vs. homogenized GTN cell curves on the three materials in fig. 3.8. The analytical q-formula is used to estimate the q-values in the homogenized cell. The results in fig. 3.9 demonstrate the fact that the analytical q-formula can be applied to new materials and the q-values given by the analytical q-formula produce good results.

Figure 3.9 brings attention to the fact that the analytical formula is sensible to the change in strain hardening.

3.5.2.2 *Sensibility of the analytical q-formula to change in yield strength*

Figure 3.10 highlights the fact that the analytical q-formula is sensible to the change in σ_0. Regardless the fact that σ_0 has a lower effect on void growth when compared to hardening, the universal law is still capable to differentiate the void growth curves of 3 different σ_0 as shown in fig. 3.10. In the latter, the power law n exponent is fixed to 0.05, while the Voce parameters are taken as for material 2 in fig. 3.8. Only σ_0 is varied between 300, 500 and 700 MPa.

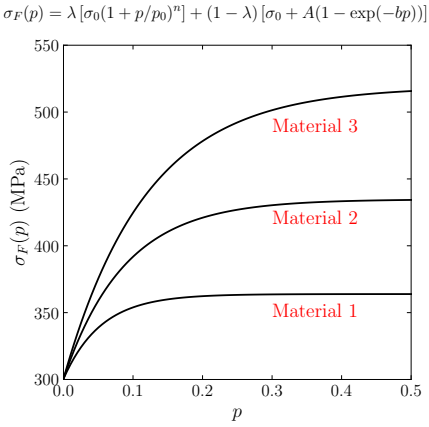

			Power law parameters		Voce law parameters		
	λ	σ_0	n	p_0	A	b	Equivalent n
Material 1	0.5	300	0.015	0.005	126.7	18.5	0.100
Material 2			0.050		268.2	11.4	0.160
Material 3			0.100		436.4	8.4	0.210

Figure 3.8: Strain hardening exponents and flow stress vs. p of the materials used for testing the q-values analytical formula (eq. (3.20)). The plastic flow is expressed as shown in eq. (3.23). Unit cell & GTN + q-values analytical formula results are presented in fig. 3.9 and fig. 3.10.

3.5.2.3 *Applying the analytical q-formula to a cell with a Ramberg-Osgood elastic–plastic behavior*

As mentioned above, the Ramberg-Osgood hardening law is widely used in the literature and is usually coupled with the GTN model. Therefore, the aim of this section is to test the universal law in a model using the Ramberg-Osgood hardening. Two materials are chosen from table 1 in the work of Faleskog et al., 1998 and are modeled in this work. The chosen materials have the lowest ($n = 0.025$) and highest ($n = 0.2$) hardening and $\sigma_0/E = 0.004$. Unit cell simulations are carried out using the new hardening parameters. Then, the homogenized model using the universal q-formula is compared to the unit cell model in fig. 3.11. The latter shows a good agreement regarding void growth curves and slight differences regarding stress—strain curves for the highest hardening material. This results approves the fact that the universal q-formula can be used with various hardening laws/materials and good predictions of void growth are achieved.

Results from this section are promising since the analytical q-formula provides optimum q-values for different elastic–plastic behaviors without the need of calibrating q-values on the unit cell model. The following section applies the analytical q-formula to a real-life case study to model the fracture toughness of irradiated aluminum alloys.

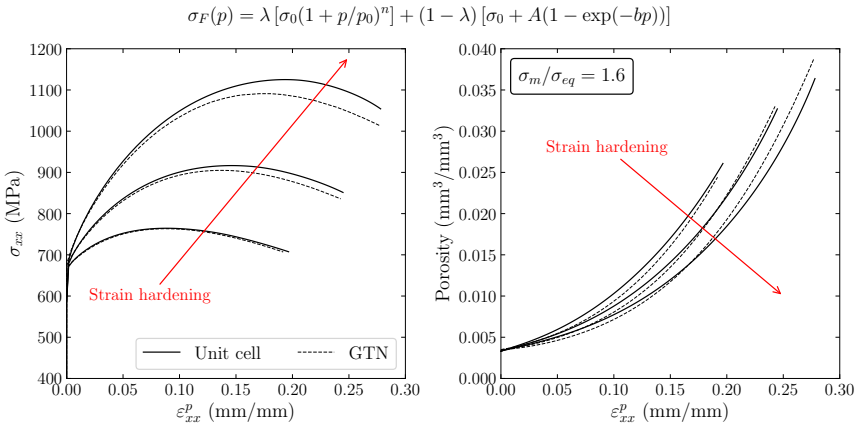

Figure 3.9: GTN simulation results using the analytical q-formula in eq. (3.20) compared to the unit cell. The strain hardening exponent is varied to test if the analytical q-formula is sensible to the strain hardening change.

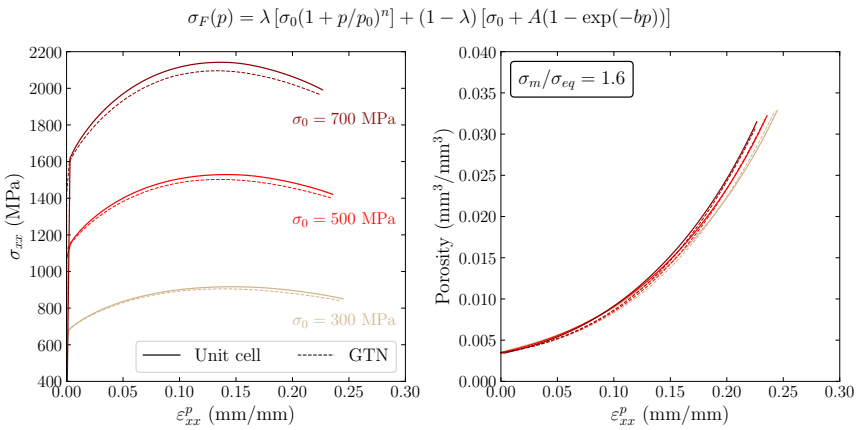

Figure 3.10: GTN simulation results using the analytical q-formula in eq. (3.20) compared to the unit cell. The yield strength is varied to test if the analytical q-formula is sensitive to σ_0.

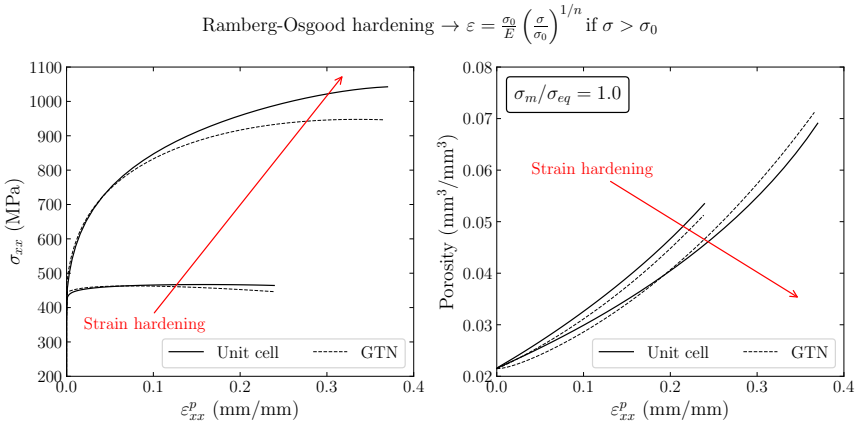

Figure 3.11: GTN simulation results using the analytical q-formula in eq. (3.20) compared to the unit cell. The yield strength is varied to test if the analytical q-formula is sensitive to σ_0.

3.6 EXTENSION TO CASE STUDY: VOID GROWTH IN RADIATION-INDUCED HARDENING ALUMINUM 6061-T6 ALLOYS

In this section, the proposed q-values analytical formula is used to simulate crack propagation in radiation hardened aluminum 6061-T6 alloys. The radiation-induced hardening effect is interesting for this study since an increase in the radiation dose causes an increase in σ_0 and a decrease in the strain hardening capacity [Farrell, 2012]. A study reports 45 and 60% increase in the 0.2% flow stress and ultimate tensile strength of an irradiated 6061-T6 alloy respectively, while the ductility at failure drops from 15 to 9% [Farrell et al., 1979]. This real-life case study puts into practice the universal analytical formula in structure FE simulations on Compact-Tension (CT) fracture toughness samples.

3.6.1 *Material behavior*

A phenomenological plastic flow rule is developed in order to model the elastic–plastic behavior of the 6061-T6 alloy while accounting for the irradiation dose via the thermal fluence (Φ_{th}). The calibration process of the phenomenological plastic flow rule is out of the scope of this study. The phenomenological plastic flow rule is expressed in the same manner as the previously used Voce law in eq. (3.5). The material parameters σ_0, A and b depend on the thermal fluence as shown in fig. 3.12. Two Φ_{th} are chosen in this study as well as the unirradiated alloy $\Phi_{th} = 0$ to highlight the influence of strengthening and hardening loss on void growth. At $\Phi_{th} = 0 \times 10^{21}\ n/cm^2$, the alloy has the highest strain hardening capacity and the lowest yield strength. At contrast, the alloy is at the lowest strain hardening capacity and highest yield strength at $\Phi_{th} = 100 \times 10^{21}\ n/cm^2$.

The GTN parameters are taken as follows: $f_0 = 0.35\%, \dot{f}_n = 0, f_c = 3.8\%$ and $f_r = 15.4\%$. The latter are optimized in other work [Shokeir et al., 2022]. Void nucleation is not considered in order to focus on the effect of the universal law on void growth. However, void nucleation in aluminum alloys is important to be modeled. Void coalescence is taken into account via the f_* approach shown in eq. (3.13). A material integration point is considered as broken when f_* reaches $1/q_1 - \epsilon$ (with $\epsilon = 10^{-3}$). Then, its behavior is replaced by an elastic behavior with a very low stiffness (Young modulus: $E = 1$ MPa). When 4 out of 8 integration points are considered as broken in the 3D element, the latter is removed from the mesh. Displacement increments at nodes belonging to removed elements are then fixed to avoid a singular global stiffness matrix.

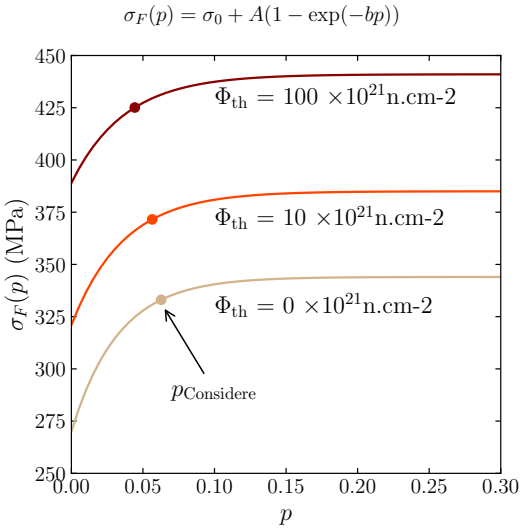

Φ_{th}	σ_0	A	b	Equivalent n
$0 \times 10^{21}\ n/cm^2$	270	74	30.49	0.058
$10 \times 10^{21}\ n/cm^2$	321	64	27.62	0.051
$100 \times 10^{21}\ n/cm^2$	389	52	26.74	0.039

Figure 3.12: Material parameters and flow stress vs. p of the phenomenological plastic flow law accounting for radiation-induced hardening via the thermal fluence (Φ_{th})

3.6.2 *Compact-Tension (CT) mesh*

Figure 5.19 shows the boundary conditions applied on the studied CT samples. Only one-fourth of the CT sample is meshed thanks to the symmetries. To assure one of the symmetries, u_z is constrained for elements on the $u_z = 0$ plane (see fig. 5.19). 8-node 3D hexahedral elements with 8 integration points are used to mesh the sample. The mesh size is fixed to $100 \times 100 \times 100\ \mu m^3$. The used GTN model leads to material softening which results in strain and damage localization within one row of elements. As a result, the simulation results strongly depend on the mesh size. To overcome this issue, models integrating material internal lengths can be used (e. g. Feld-Payet et al., 2011; Mediavilla et al., 2006). However, these models are still in an early development phase. The pragmatic solution chosen in this study is to fix a mesh size along the crack path [Liu et al., 1994; Rousselier, 1987]. The fixed mesh size controls the fracture energy in the case of mesh dependent simulations [Siegmund et al., 2000].

The selective integration procedure is used to avoid volume locking at large strains [Hughes, 1980]. The crack propagation in CT sample FE simulation is displacement controlled. Displacement is applied in the y-direction while the crack propagation takes place in the ligament (initially fixed nodes).

3.6.3 *Fracture toughness of the irradiated aluminum alloys*

The J-integral is calculated in a post-processing routine using formulas in the ASTM standards [ASTM-1820, 2017]. The $J - \Delta a$ curves are displayed in fig. 3.13. The latter shows as well the q_1 and q_2 values given by the analytical formula in two CT samples ($\Phi_{th} = 0$ & $100 \times 10^{21}\ n/cm^2$). The displayed q_1 and q_2 values correspond to the time step at which the u_y displacement (CMOD) is equal to 0.6 mm (see CMOD—Load graph in fig. 3.13). The $J - \Delta a$ results show that strain hardening drop between $\Phi_{th} = 0$ and $\Phi_{th} = 100$ leads to an increase in void growth. This is expected and can be explained in two arguments. Firstly, the CT sample with $\Phi_{th} = 100$ has a mean $q_1 > 1.14$ and $q_2 > 0.96$ far from the crack tip while the CT sample with $\Phi_{th} = 0$ has a mean $q_1 \sim 1.04$ and $q_2 \sim 0.94$ (see fig. 3.13). Therefore, the σ_0 effect is taken into account via the analytical formula. Secondly, the lower strain hardening capacity in the $\Phi_{th} = 100$ sample leads to high q-values on a longer distance beyond the crack tip as shown in red in fig. 3.13. The high q-values in the $\Phi_{th} = 0$ sample are spread over a shorter distance in the ligament. As a reminder the maximum q-values depend on $N(p)$ and $\chi(p)$. $N(p)$ tends to 0 at a rate that depends on the strain hardening capacity (see $\lim_{p\to\infty} N(p) = 0$ in table 3.3). At low hardening levels (i. e. $\Phi_{th} = 100$), N tends to 0 at a high rate and the maximum q-values are reached rapidly ($q_{\max}(p) = b\ \chi(p) + q^*$).

The analytical formula can be easily applied to model damage and crack propagation as shown in this section. The implementation cost of the analytical formula is negligible since the equations depend on the elastic–plastic behavior which is already implemented in advance.

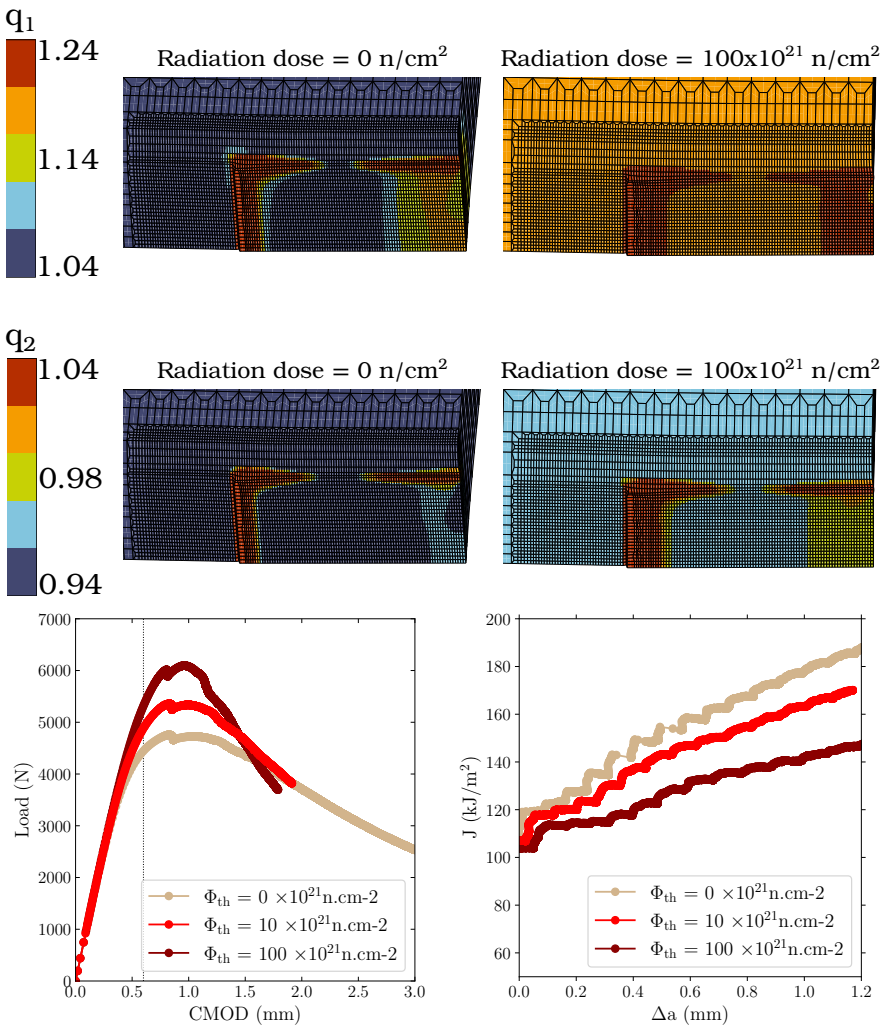

Figure 3.13: q-values given by the analytical formula in two CT samples ($\Phi_{th} = 0$ & 100×10^{21} n/cm^2) at the same time step (taken at CMOD = 0.6 mm as shown in the Load—CMOD graph) and $J - \Delta a$ curves of the 3 simulated CT samples. The $\Phi_{th} = 100$ CT reaches the highest load but has the steepest load drop. This results in the lower J values for the $\Phi_{th} = 100$ CT.

3.7 CONCLUSIONS

This main objective of this work is to propose an analytical formula to find the optimum q-parameters without any FE simulations. On one hand, the $q_1 = 1.5$ and $q_2 = 1$. proposed by Tvergaard, 1981 cannot be taken as universal parameters for all materials. On the other hand, the q-parameter calibration process (based on the unit cell model) developed by Faleskog et al., 1998 might be time consuming when one needs to simulate materials with different behaviors. This work examines the material characteristics (yield strength, strain hardening, Young's modulus, initial void volume fraction) that could influence void growth in the unit cell model. Based on the unit cell results, an analytical formula for optimum q-values is developed. This universal

formula depends on the instant strain hardening level and the flow stress to Young's modulus ratio. The analytical formula is applied to a real-life case study to model crack propagation in irradiated aluminum CT samples. The main conclusions that must be highlighted in this work are:

- The Young's modulus, yield strength and strain hardening capacity have respectively a weak, moderate and strong effect on void growth. A low Young's modulus ($E \sim 35$ GPa and $\sigma_0/E = 0.0043$) slightly increases void growth, while at high Young's modului ($E > 70$ GPa and $\sigma_0/E = 0.0043$) void growth is not affected. The yield strength does not affect void growth at low strains while increases void growth at high strains. The strain hardening has a conspicuous effect on void growth.
- The choice of the flow stress law has an impact on void growth. The Voce hardening law accounts for the hardening saturation which results in a stronger dependency of void growth on strain hardening (especially at high stress triaxiality > 2). Power laws (Swift, Romber-Osgood, Ludwik, etc..) do not take into account the hardening saturation which leads to underestimating void growth and the porosity prior coalescence.
- The universal formula for q-optimum values is sensible to the change in strain hardening and strength. Void growth is well predicted in various materials with dissimilar elastic–plastic behaviors. The crack propagation simulations in CT samples using the analytical formula affirm the fact that the implementation cost is negligible. Moreover, it is shown that the q-values vary along the crack path during the FE simulations. The increase in q-values near the crack tip allows to increase void growth in zones with plastic localization.

APPENDIX

Unit cell mesh and boundary conditions

The mesh size (e) is defined as the number of elements (x) in the cell's edge (L) $\rightarrow$ $e = L/x$. Figure 3.14 shows three mesh sizes corresponding to $x = 3$, $x = 5$ and $x = 9$ respectively. The mesh is then accordingly refined close to the void. A mesh size convergence check is done based on the stress—plastic strain and the porosity—plastic strain curves shown in fig. 3.14. The coarsest mesh has a slightly different stress—plastic strain behavior. The "Chosen mesh" in fig. 3.14 is the least expensive mesh that behaves like the finest mesh. Therefore, this mesh size is selected for unit cell simulation.

All unit cell simulations in this study are interrupted at the coalescence onset. The latter is attained when the displacement of the face perpendicular to the loading direction (u_y) saturates as shown in fig. 3.15.

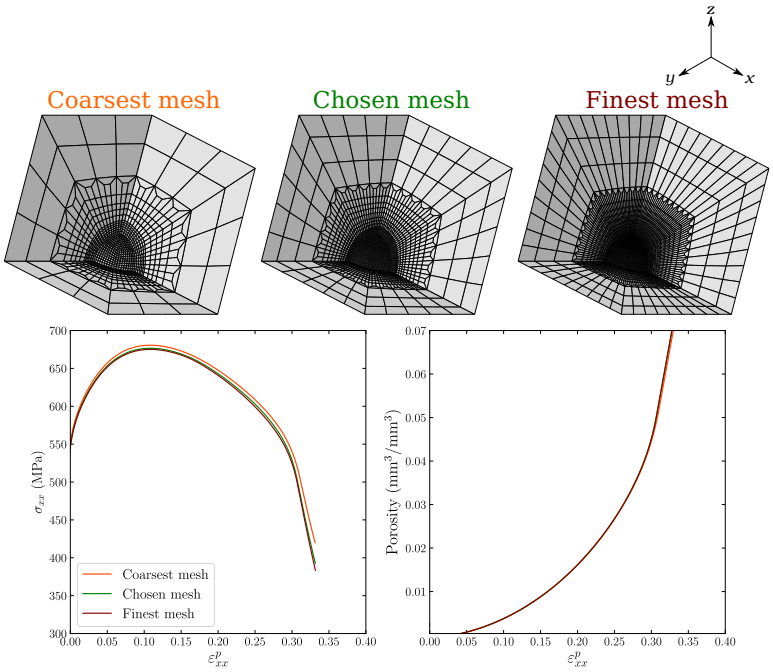

Figure 3.14: Cauchy stress—plastic strain and porosity—plastic strain curves for three unit cell meshes with different element sizes. The chosen mesh is the least expensive mesh that gives converged results compared to the finest mesh.

Effect of the initial void volume fraction f_0 on the optimum q-values

The initial void volume fraction f_0 is a material characteristic that is examined to understand if it has an influence on void growth. Section 3.4 presents the q-values calibration process based on minimizing the objective function defined in eq. (3.17). The optimum q-values result in the minimum objective function value (ϵ_{min}). Figure 3.16 displays contour plots of the error with respect to ϵ_{min} over a range of q-values ($1.0 \leq q_1 \leq 2.0$ and $0.7 \leq q_2 \leq 1.0$) and three studied f_0. The optimum q-values that give the ϵ_{min} are shown by a red cross in fig. 3.16. The q-values inside the ellipse surrounding the red cross result in an error of 1.5%.

When the ellipses in fig. 3.16 are plotted on the same graph, an intersection is found between the three studied f_0. This means that if all studied f_0 are considered in the objective function, the optimum q-values should be found in the shaded gray area in fig. 3.16. This hypothesis is verified in the contour plot in fig. 3.18. The latter shows the optimum q-values resulting from the optimization process on all f_0. The optimum q-values lie in the intersection region created between the optimization carried out on each f_0 separately in fig. 3.17.

The stress—plastic strain and porosity—plastic strain curves in fig. 3.18 are plotted to compare the homogenized cell's behavior using the optimum q-values and the q-values lying on the vertices of the 1.5% error ellipse (q-values #1 and q-values #2 in fig. 3.18). Results with the optimum q-values are, with no surprise, in good agreement

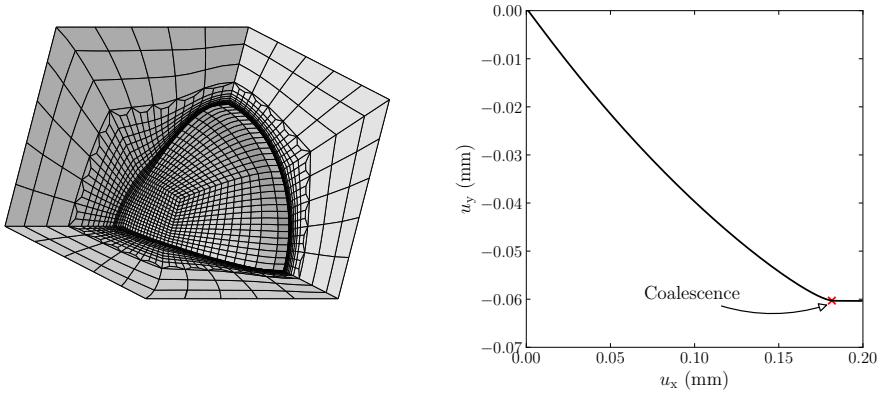

Figure 3.15: A unit cell simulation interrupted at the coalescence onset which is detected when the displacement of the face perpendicular to the loading direction (u_y) saturates

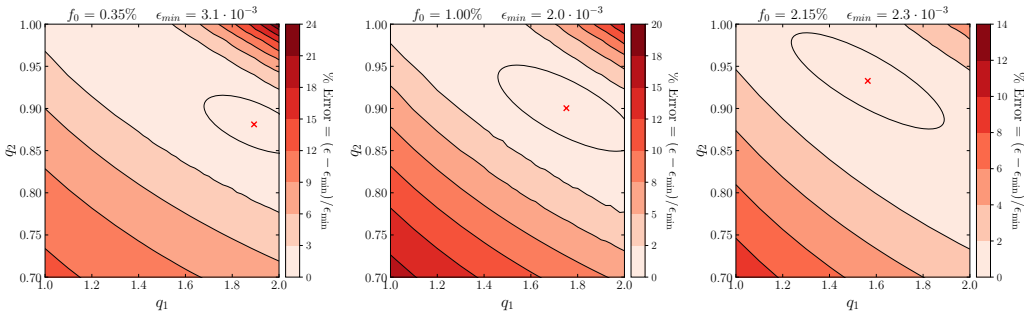

Figure 3.16: Contour plots of the error with respect to the minimum value of the objective function (ϵ_{min}) for three studied f_0. The optimum q-values are displayed by a red cross while the q-values inside the ellipse surrounding the red cross result in an error of 1.5%.

with the unit cell behavior. However, the interesting fact in fig. 3.18 is that the results using the q-values on the vertices of the 1.5% error ellipse are almost identical to the optimum q-values' results. This is true for the three studied f_0. This means that f_0 has no effect on the void growth rate over a finite domain. The latter is subjectively defined in this work by the 1.5% error ellipse. Fritzen et al., 2012 proposed analytical formulas to relate q-values to f_0. However, it is clearly shown in this study that the effect of f_0 over the defined finite domain is negligible when compared to the hardening and yield strength effects thoroughly discussed in section 3.3. To conclude, it is recommended to include several f_0 that are representative of real materials when searching for the optimum q-values.

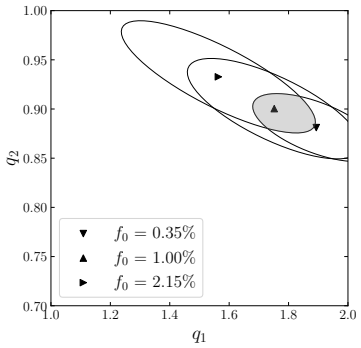

Figure 3.17: Optimum q-values and the corresponding 1.5% error ellipses shown in fig. 3.16 for three studied f_0. Intersection between the three ellipses is shaded in gray.

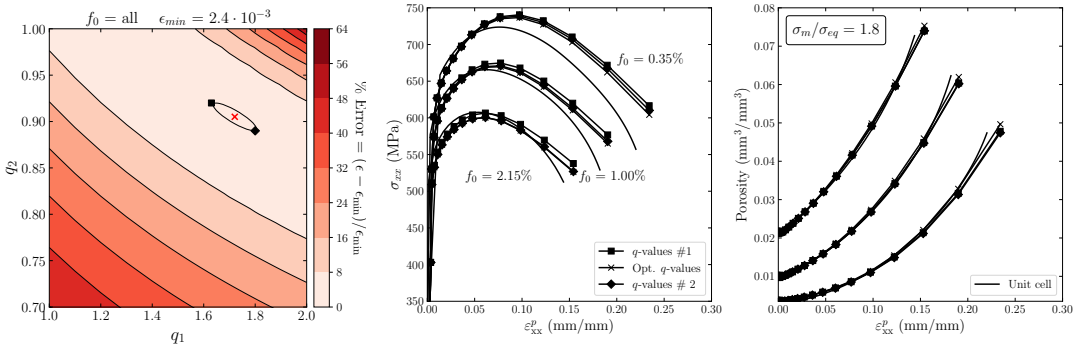

Figure 3.18: *Left:* Contour plots of the error around the minimum value of the objective function (ϵ_{min}) for all studied f_0. The optimum q-values are displayed by a red cross while the q-values inside the ellipse surrounding the red cross result in an error of 1.5%. *Middle and right:* Stress—plastic strain and porosity—plastic strain curves for comparison between the optimum q-values and the q-values lying on the vertices of the 1.5% error ellipse.

BIBLIOGRAPHY

ASTM-1820 (2017). *Standard Test Method for Measurement of Fracture Toughness*. Technical report. DOI: 10.1520/E1820-17 (see p. 79).

Argon, A. et al. (1975). 'Cavity formation from inclusions in ductile fracture.' In: *Met. Trans.* 6A, pages 825–837 (see p. 58).

Becker, R. and R. Smelser (1994). 'Simulation of strain localization and fracture between holes in an aluminum sheet.' In: *J. Mech. Phys. Solids* 42.5, pages 777–796. DOI: 10.1016/0022-5096(94)90042-6 (see p. 59).

Benzerga, A. et al. (1999). 'Coalescence–controlled anisotropic ductile fracture.' In: *J. Engng Mater. Technol.* 121, pages 121–129 (see p. 58).

Benzerga, A. and J.-B. Leblond (2010). 'Ductile Fracture by Void Growth to Coalescence.' In: *Advances in Applied Mechanics* 44, 169–305 (see p. 58).

Benzerga, A. et al. (2016). 'Ductile Failure Modeling.' In: *Int. J. Frac.* 201, pages 29–80. DOI: 10.1007/s10704-016-0142-6 (see p. 58).

Besson, J. (2009). 'Damage of ductile materials deforming under multiple plastic or viscoplastic mechanisms.' In: *Int. J. Plasticity* 25, pages 2204–2221 (see p. 58).

Besson, J. (2010). 'Continuum models of ductile fracture: a review.' In: *Int. J. Damage Mech.* 19, pages 3–52 (see p. 58).

Besson, J. and R. Foerch (1997). 'Large scale object–oriented finite element code design.' In: *Comp. Meth. Appl. Mech. Engng* 142, pages 165–187 (see p. 61).

Besson, J. et al. (2001). 'Modeling of crack growth in round bars and plane strain specimens.' In: *Int. J. Solids Structures* 38.46–47, pages 8259–8284 (see p. 69).

Borg, U. et al. (2008). 'Size effects on void growth in single crystals with distributed voids.' In: *Int. J. Plasticity* 24.4, pages 688–701. ISSN: 0749-6419. DOI: 10.1016/j.ijplas.2007.07.015 (see p. 59).

Brocks, W. et al. (1995). 'Verification of the transferability of micromechanical parameters by cell model calculations with visco-plastic materials.' In: *Int. J. Plasticity* 11, pages 971–989 (see p. 60).

Broggiato, G. et al. (2007). 'Identification of Material Damage Model Parameters: an Inverse Approach Using Digital Image Processing.' In: *Meccanica* 42, pages 9–17. DOI: 10.1007/s11012-006-9019-5 (see p. 58).

Chien, W. et al. (July 2000). 'Modified Anisotropic Gurson Yield Criterion for Porous Ductile Sheet Metals.' In: *J. Engng Mater. Technol.* 123.4, pages 409–416. ISSN: 0094-4289. DOI: 10.1115/1.1395023 (see p. 59).

Chu, C. and A. Needleman (1980). 'Void nucleation effects in biaxially stretched sheets.' In: *J. Engng Mater. Technol.* 102, pages 249–256 (see p. 58).

Considère, A. (1885). 'Mémoire sur l'emploi du fer et de l'acier dans les constructions.' In: *Annales des ponts et chaussées*, pages 574–775 (see p. 62).

Fabrègue, D. and T. Pardoen (2008). 'A constitutive model for elastoplastic solids containing primary and secondary voids.' In: *J. Mech. Phys. Solids* 56, pages 719–741 (see p. 59).

Faleskog, J. et al. (1998). 'Cell model for nonlinear fracture analysis — I. Micromechanics calibration.' In: *Int. J. Frac.* 89, pages 355–373 (see pp. 59, 66, 71, 73, 75, 80).

Farrell, K. (2012). 'Performance of Aluminum in Research Reactors.' In: *Comprehensive Nuclear Materials*, 147–175. DOI: 10.1016/B978-0-08-056033-5.00113-0 (see p. 77).

Farrell, K. and R. King (1979). 'Tensile Properties of Neutron-Irradiated 6061 Aluminum Alloy in Annealed and Precipitation-Hardened Conditions.' In: *Effects of Radiation on Mater.*, pages 440–449. DOI: 10.1520/STP38180S (see p. 77).

Feld-Payet, S. et al. (2011). 'Finite element analysis of damage in ductile structures using a nonlocal model combined with a three-field formulation.' In: *Int. J. Damage Mech.* 20, pages 655–680 (see p. 78).

Fritzen, F. et al. (2012). 'Computational homogenization of elasto-plastic porous metals.' In: *Int. J. Plasticity* 29, 102–119 (see p. 83).

Garrison, W. M. and N. R. Moody (1987). 'Ductile Fracture.' In: *J. Phys. Chem. Solids* 48.11, pages 1035–1074 (see p. 58).

Goods, S. and L. Brown (1979). 'The nucleation of cavities by plastic deformation.' In: *Acta Metall.* 27, pages 1–15 (see p. 58).

Gurson, A. L. (1977). 'Continuum theory of ductile rupture by void nucleation and growth: Part I— Yield criteria and flow rules for porous ductile media.' In: *J. Engng Mater. Technol.* 99, pages 2–15 (see p. 58).

Han, X. et al. (2013). 'A yield function for single crystals containing voids.' In: *Int. J. Solids Structures* 50, pages 2115–2131. DOI: 10.1016/j.ijsolstr.2013.02.005 (see p. 60).

Hosseini, N. et al. (2022). 'The effect of material orientation on void growth.' In: *Int. J. Plasticity* 148, page 103149. ISSN: 0749-6419. DOI: 10.1016/j.ijplas.2021.103149 (see p. 59).

Hughes, T. (1980). 'Generalization of selective integration procedures to anisotropic and non linear media.' In: *Int. J. Numer. Meth. Engng* 15, pages 1413–1418. DOI: 10.1002/nme.1620150914 (see p. 78).

Kim, J. et al. (2004). 'Modeling of void growth in ductile solids: effects of stress triaxiality and initial porosity.' In: *Eng. Fract. Mech.* 71.3 (see pp. 59, 73).

Kocks, U. and H. Mecking (2003). 'Physics and phenomenology of strain hardening: the FCC case.' In: *Progress in Materials Science* 48.3, pages 171–273. DOI: 10.1016/S0079-6425(02)00003-8 (see p. 62).

Koplik, J. and A. Needleman (1988). 'Void growth and coalescence in porous plastic solids.' In: *Int. J. Solids Structures* 24.8, pages 835–853 (see pp. 59, 73).

Kuna, M. and D. Sun (1996). 'Three-dimensional cell model analyses of void growth in ductile materials.' In: *Int. J. Frac.* 81, pages 235–258 (see p. 59).

Lecarme, L. et al. (2011). 'Void growth and coalescence in ductile solids with stage III and stage IV strain hardening.' In: *Int. J. Plasticity* 27.8, pages 1203–1223. DOI: 10.1016/j.ijplas.2011.01.004 (see pp. 62, 67).

Lemaitre, J. and R. Desmorat (2005). *Engineering damage mechanics*. Springer (see p. 58).

Li, Z. et al. (1994). 'A study of the internal parameters of ductile damage theory.' In: *Fatigue and Fract. Engng Mater. Struct.* 17.9, pages 1075–1087 (see p. 58).

Ling, C. et al. (2016). 'An elastoviscoplastic model for porous single crystals at finite strains and its assessment based on unit cell simulations.' In: *Int. J. Plasticity* 84, pages 58–87. DOI: 10.1016/j.ijplas.2016.05.001 (see p. 59).

Liu, Y. et al. (1994). 'Mesh–dependence and stress singularity in finite element analysis of creep crack growth by continuum damage mechanics approach.' In: *Eur. J. Mech./A* 13A.3, pages 395–417 (see p. 78).

Mc Clintock, F. A. (1968). 'A criterion for ductile fracture by the growth of holes.' In: *J. App. Mech.* 35, pages 363–371 (see p. 58).

Mediavilla, J. et al. (2006). 'Discrete crack modelling of ductile fracture driven by non-local softening plasticity.' In: *Int. J. Numer. Meth. Engng* 66.4, pages 661–688 (see p. 78).

Needleman, A. (1972). 'Void growth in an elastic-plastic medium.' In: *J. Applied Mech.* 39, pages 964–970 (see p. 59).

Needleman, A. (1987). 'A continuum model for void nucleation by inclusion debonding.' In: *J. Applied Mech.* 54, pages 525–531 (see p. 58).

Needleman, A. and A. Kushner (1990). 'An analysis of void distribution effects on plastic flow in porous solids.' In: *Eur. J. Mech./A* 9A, pages 193–206 (see p. 61).

Pardoen, T. and J. Hutchinson (2000). 'An extended model for void growth and coalescence.' In: *J. Mech. Phys. Solids* 48.12, pages 2467–2512 (see pp. 58, 59).

Pardoen, T. et al. (1998). 'Experimental and numerical comparison of void growth models and void coalescence criteria for the prediction of ductile fracture in copper bars.' In: *Acta Mater.* 46.2, pages 541–552 (see p. 58).

Petch, N. J. (1954). 'The fracture of metals.' In: *Progress in Metal Physics* 5, pages 1–52. DOI: 10.1016/0502-8205(54)90003-9 (see p. 58).

Puttick, K. E. (1959). 'Ductile fracture in metals.' In: *The Philosophical Magazine: A Journal of Theoretical Experimental and Applied Physics* 4.44, pages 964–969. DOI: 10.1080/14786435908238272 (see p. 58).

Ramberg, W. and W. Osgood (1943). *Description of stress-strain curves by three parameters*. Technical report (see p. 59).

Rice, J. R. and D. M. Tracey (1969). 'On the ductile enlargement of voids in triaxial stress fields.' In: *J. Mech. Phys. Solids* 17, pages 201–217 (see p. 58).

Rousselier, G. (1987). 'Ductile fracture models and their potential in local approach of fracture.' In: *Nucl. Eng. Des.* 105, pages 97–111 (see p. 78).

Shinohara, Y. et al. (2016). 'Anisotropic ductile failure of a high-strength line pipe steel.' In: *Int. J. Frac.* 197, pages 127–145 (see p. 72).

Shokeir, Z. et al. (2022). 'Edge tracing technique to study post–necking behavior and failure in Al–alloys and anisotropic plasticity in line pipe steels.' In: *Fatigue and Fract. Engng Mater. Struct.*, pages 1–16. DOI: 10.1111/ffe.13754 (see pp. 67, 77).

Sidoroff, F. and A. Dogui (2001). 'Some issues about anisotropic elastic-plastic models at finite strain.' In: *Int. J. Solids Structures* 38, pages 9569–9578 (see p. 61).

Siegmund, T. and W. Brocks (2000). 'A numerical study on the correlation between the work of separation and the dissipation rate in ductile fracture.' In: *Eng. Fract. Mech.* 67, pages 139–154 (see p. 78).

Springmann, M. and M. Kuna (2006). 'Determination of Ductile Damage Parameters by Local Deformation Fields: Measurement and Simulation.' In: *Arch. of Appl. Mech.* DOI: 10.1007/s00419-006-0033-9 (see p. 58).

Steglich, D. et al. (2010). 'Interaction between anisotropic plastic deformation and damage evolution in Al 2198 sheet metal.' In: *Eng. Fract. Mech.* 77.17, 3501–3518 (see p. 59).

Tang, A. et al. (2021). 'Mesoscopic origin of damage nucleation in dual-phase steels.' In: *Int. J. Plasticity* 137, page 102920. ISSN: 0749-6419. DOI: 10.1016/j.ijplas.2020.102920 (see p. 58).

Thomson, C. et al. (2003). 'Void coalescence within periodic clusters of particles.' In: *J. Mech. Phys. Solids* 51.1, pages 127–146 (see p. 61).

Tvergaard, V. (1981). 'Influence of voids on shear band instabilities under plane strain condition.' In: *Int. J. Frac.* 17.4, pages 389–407 (see pp. 58, 73, 80).

Tvergaard, V. (1982). 'On the localization in ductile materials containing spherical voids.' In: *Int. J. Frac.* 18.4, pages 237–252 (see p. 58).

Tvergaard, V. and A. Needleman (1984). 'Analysis of the cup–cone fracture in a round tensile bar.' In: *Acta Metall.* 32, pages 157–169 (see pp. 58, 68, 73).

Voce, E. (1995). 'A Practial Strain-hardening Function.' In: *Metallurgia* 51, pages 219–226 (see p. 62).

Wen, J. et al. (2005). 'The modified Gurson model accounting for the void size effect.' In: *Int. J. Plasticity* 21.2, pages 381–395. ISSN: 0749-6419. DOI: 10.1016/j.ijplas.2004.01.004 (see p. 59).

Worswick, M. and R. Pick (1990). 'Void growth and constitutive softening in a periodically voided solid.' In: *J. Mech. Phys. Solids* 38, pages 601–625 (see p. 59).

Xia, L. et al. (1995). 'A computational approach to ductile crack growth under large scale yielding conditions.' In: *J. Mech. Phys. Solids* 43.3, pages 389–413 (see p. 58).

Zhang, K. et al. (2001). 'Numerical analysis of the influence of the Lode parameter on void growth.' In: *Int. J. Solids Structures* 38.32-33, pages 5847–5856 (see p. 59).

Zhang, Z. (1996). 'A Sensitivity Analysis of Material Parameters for the Gurson Constitutive Model.' In: *Fatigue and Fract. Engng Mater. Struct.* 19, pages 561 –570. DOI: 10.1111/j.1460-2695.1996.tb00992.x (see p. 58).

Zhang, Z. et al. (2000). 'A complete Gurson model approach for ductile fracture.' In: *Eng. Fract. Mech.* 67.2, pages 155–168 (see p. 58).

4

EDGE TRACING TECHNIQUE TO STUDY POST–NECKING BEHAVIOR AND FAILURE IN AL–ALLOYS AND ANISOTROPIC PLASTICITY IN LINE PIPE STEELS

PREAMBLE

This chapter is published in the journal of Fatigue Fracture Engineering Materials and Structures as follows:

Shokeir Z, Besson J,Belhadj C, Petit T, Madi Y. Edge tracing technique to study post-necking behavior and failure in Al alloys and anisotropic plasticity in line pipe steels. Fatigue Fract Eng Mater Struct. 2022;1-16. doi:10.1111/ffe.13754

RÉSUMÉ

La méthode Edge Tracing (ET) récemment développée permet d'estimer la déformation radiale dans des éprouvettes de traction axisymétriques via l'analyse d'images numériques enregistrées pendant les expériences. Les images sont traitées pour détecter les contours de l'éprouvette et ainsi estimer le diamètre minimal de la section transversale. Cette technique a été principalement développée pour caractériser le comportement plastique bien au-delà de la contrainte critique. L'objectif de ce travail est d'appliquer la méthode ET à deux nouvelles études de cas. Premièrement, la rupture d'un alliage d'aluminium à faible ductilité est étudiée. Les alliages à faible ductilité ont tendance à se rompre brutalement après avoir atteint la charge maximale. Le résultat principal est la capture de la forte chute de charge qui a permis de calibrer les paramètres du modèle d'endommagement GTN. Deuxièmement, le comportement élastique-plastique anisotrope d'un acier de pipe-line "vintage" est caractérisé par une mesure directe du coefficient de Lankford. Les données expérimentales assemblées ont permis de modéliser la plasticité anisotrope au-delà de la contrainte critique dans différentes directions de chargement.

4.1 INTRODUCTION

Engineering problems modeled by the finite element method require in some cases sufficient information about the large deformations occurring in the material. Metal

forming and ductile failure are perfect examples of cases that necessitate the material's response prior and beyond the necking strain [Tu et al., 2019; Zhang et al., 1999]. Tensile tests carried out on round dog bone simple tensile samples (ST) provide the material's engineering stress—strain curve. During testing, diffuse necking occurs as the plastic deformation is localized in a thin ligament called the "neck". At this phase, the stress triaxiality increases in the neck. The output stress—strain curve must then be corrected to obtain a full true stress—logarithmic strain curve. The most commonly used correction equation is proposed by Bridgman, 1945 and is modified by Bao et al., 2004. Other authors as Tu et al., 2018a, 2019, 2020, Versaillot et al., 2021, Bao et al., 2005, Bai et al., 2009 and Mirone, 2004 point out the fact that the Bridgman correction leads to significant errors. Therefore, they develop other analytical corrections to obtain the true stress—logarithmic strain curve.

Zhang et al., 2001 propose to use round notched tensile bars (NT) as an alternative method for the assessment of the material's behavior at large strain. Diameter reduction can be recorded by a radial extensometer located at the specimen's minimum cross section. The difficulty of this setup is to assure that the extensometer does not slide so that the measurements are continuously taken at the minimum cross section. Moreover, the extensometer knife-edges may damage the notch surface and affect the test results [Olden et al., 2002]. The cited authors apply the above explained experimental procedure using radial extensometers to obtain load—diameter reduction curves in welded joints in a high strength 690 MPa structural steel. The true stress—strain curves are then obtained using a correction factor on the net stress. The correction factor is a function of the notch geometry and the maximum recorded load.

Later, Hopperstad et al., 2003, Vilamosa et al., 2014 and Tu et al., 2018b, 2019 proposed the Edge Tracing (ET) method to obtain the diameter reduction of ST and axisymmetric NT specimens via analysis of digital images taken during the experiment. Digital camera(s) are used to take pictures which are each associated to the corresponding load. Each image is analyzed separately by simple algorithms to correlate the given load to a radial deformation calculated by detecting the smallest cross-section diameter in the notch. Each pixel in the *8bits* image represents a gray value ranging from 0 to 255. The specimen contour can be detected only if a sharp contrast is maintained between the specimen and the background. Accordingly, the section reduction is calculated at the output. More technical details concerning the method are given in the following section.

The ET method is used in tensile testing in the literature by several authors to study the plastic behavior of different materials. Firstly, Hopperstad et al., 2003 investigate the effect of strain rate and stress triaxiality on the elastic–plastic flow of Weldox 460 E steels. Only one camera is used in this work to take images of the samples from a single angle. Secondly, Tu et al., 2018b, 2019 study the effect of low temperature ($-60°C$) on the strain at failure of a 420 MPa structural steel. For the first time,

images of the samples are taken from different viewing angles using a two-mirror system. Thirdly, Defaisse et al., 2018 focus on the identification of the elastic–plastic behavior of a ML340 ultra high strength steel. Unlike the subpixel method proposed in this study, the cited authors use a pixel resolution which results in less accurate measurements. Lastly, Kondori et al., 2019 analyze the anisotropic plastic behavior of a magnesium alloy. The cited authors use the same pixel method use by Defaisse et al., 2018 to estimate the average measured diameter prior necking to evaluate the volume change in the sample. The ET method is not limited to applications mentioned above. However, it can be extended to study the evolution of the Lankford factor (in materials that undergo anisotropic plasticity) as a function of strain. To illustrate, Fourmeau et al., 2011 and Khadyko et al., 2014 study the evolution of the plastic anisotropy in 7xxx and 6xxx aluminum alloys respectively. The cited authors do not use the ET method explained above. However, they use two perpendicular lasers fixed on a mobile frame to continuously measure the minimum cross section diameter. Unlike the ET method, the laser method gives a diameter measurement and not the whole sample's profile. The latter gives information regarding the evolution of the notch radius as a function of strain.

This study investigates two challenging mechanical problems not mentioned above by the cited authors. Firstly, the failure assessment of aluminum alloys that fail rapidly after reaching the maximum bearing load during tensile testing. Secondly, the evolution of the Lankford factor during plastic deformation in line pipe steels. Both mechanical problems require the characterization of the plastic behavior beyond necking. As highlighted in the work of Tu et al., 2020, an elastic–plastic model must be calibrated over the pre– and post–necking phases to study problems with large strains (e. g. fracture). Therefore, the aim of this work is to make use of the ET method to study the two above mentioned engineering problems:

1. The post–necking behavior of low ductility aluminum alloys is investigated via a combination of deformation controlled tensile testing together with the ET method. The post—necking behavior of the studied aluminum alloys is extremely hard to analyze since the material tends to fail rapidly after reaching its maximum bearing load. The post—necking phase is crucial for failure assessment. The Gurson-Tvergaard-Needleman (GTN) damage model cannot be evaluated on stress—strain curves if the post—necking phase is missing. It is known that identifying parameters of the GTN model on experimental data is a challenging problem [Zhang et al., 2021; Zhang, 1996]. This case study confirms the importance of deformation controlled tensile testing to obtain the post—necking phase and the usefulness of this phase in the calibration of the GTN failure parameters.

2. The anisotropic plastic behavior of a vintage line pipe steel is studied. Steels can undergo a hot/cold rolling process to obtain the desired shape and dimensions.

During the rolling process, a specific crystallographic texture can emerge which leads to an anisotropic plastic behavior. The anisotropic plastic behavior of line pipe steels is usually investigated on fracture surfaces of tensile samples. One has no idea if the Lankford factor evolves during plastic deformation. The lack of information regarding the anisotropic plastic behavior of steels makes it challenging to model the material's elastic–plastic behavior which is an essential preliminary step before modeling the material's fracture behavior. This case study shows how the ET method can be used to investigate the evolution of plastic anisotropy during plastic strain.

In the following section, the testing apparatus is described as well as the image analysis process. In the third section of this paper, a case study on failure assessment in a 6061-T6 aluminum alloy is carried on NT specimens using the ET method. NT specimens can cover a wide range of stress triaxiality levels (0.6–2.0) that can be used to calibrate damage models. The chosen alloy has a challenging feature: its brief necking phase (i. e. failure occurs brutally after reaching the maximum force). In the fourth section of this paper, a case study is carried on a X52–API grade steel to highlight the ET method's advantages in determining the anisotropic plastic behavior of textured materials. Parameters of a plastic flow law with an anisotropic criterion are determined by the analysis of the tensile tests prior the onset of failure.

4.2 SPECIMENS AND EXPERIMENTAL TECHNIQUES

4.2.1 *Specimens and testing*

In this study, tests are carried on smooth (ST) and notched (NT) axisymmetric tensile specimens. fig. 4.1 shows a sketch of the NT specimens. For a fixed minimum cross-section diameter (Φ_0), varying the notch curvature radius R_0 results in different stress triaxiality levels [Hancock et al., 1976]. Given the initial curvature radius R_0 and minumum cross-section diameter Φ_0, each NT sample gets its name as follows: NTX $= 10\, R_0 \,/\, \Phi_0$, where X is the sample's name (e. g. NT10, NT4, NT2). Small 'v' notches are also machined in the specimens beyond the notch area to easily attach an axial extensometer (gauge length L_0 in fig. 4.1) during the test. The 'v' notches prevent the extensometer knives from sliding. Smooth tensile bars are machined following the ASTM–E8 standard. The exact dimensions (R_0, Φ_0, L_0) are detailed in each case study.

Figure 4.2 shows the test setup for ST and NT specimens. The knife–edged extensometer is attached to the sample by rubber bands and is used to control the machine displacement as well as to measure the axial displacement. All experiments are carried at room temperature. Tests are carried out using a strain rate of about 5.10^{-4} s^{-1}. The gauge length used to calculate the strain rate in NT samples corresponds to the notch length in the axial direction (l_0 in fig. 4.1). The strain rate in notched specimens is then approximated to the ratio between the machine displacement rate and l_0.

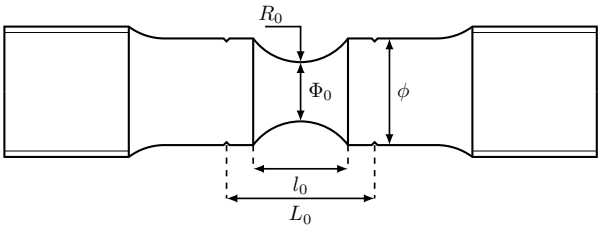

Figure 4.1: Geometry of NT tested samples. $\phi = 1.8 \times \Phi_0$. Each NT sample gets its name as follows: NTX = 10 R_0 / Φ_0, where X is the sample's name (e. g. NT10, NT4, NT2).

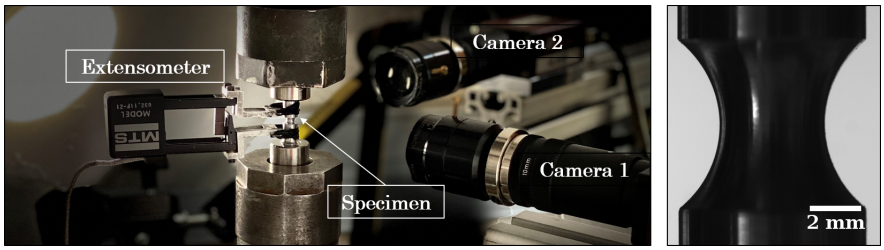

Figure 4.2: Test setup of deformation controlled ST and NT experiments. Two digital cameras on two orthogonal planes with retro-lighting are required to obtain a significant difference between the sample and the background gray levels as shown. The knife–edged extensometer is attached to the sample by rubber bands and used to control the machine displacement as well as to measure the axial displacement.

Time, load, machine displacement and extensometer opening are continuously monitored during the test. The digital cameras are placed on two orthogonal planes to record images taken against a white background retro–lit by two LED lamps (see fig. 4.2). The cameras are fixed in the directions of interest. The testing machine controller is used to trigger image capturing (1 image/second). The setup is designed in order to obtain a high contrast between the specimen and the background to facilitate image processing.

Tensile tests conducted using a machine displacement control may display an unstable behavior after the onset of the sharp load drop which corresponds to crack initiation in the center of the sample. The stress triaxiality is higher in the sample's center which leads to strain localization and damage initiation in the center [Tekoğlu et al., 2015]. The strain localization in the neck area leads to a higher local strain rate. In order to avoid a local increase in the strain rate in the neck area, the machine displacement must be decreased. Otherwise, the sample might fail in an unstable manner without having a stable load drop phase. To be able to record the post–crack initiation behavior, tests are conducted using an extensometer opening control (hereby referred to as "deformation control"). The results are exemplified in fig. 4.3 which

displays both force—machine displacement and force—extensometer opening curves. The slope of the curve after the crack initiation is steeper in the first case which explains why machine displacement control leads to an instability as explained in Petit et al., 2018.

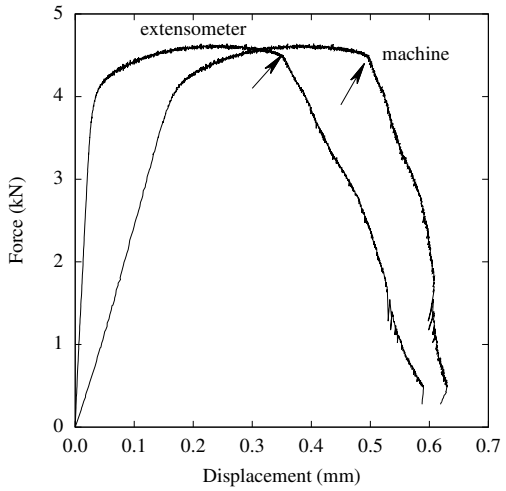

Figure 4.3: Test control for a test conducted on a NT10 (6061-T6 Al alloy). Load vs. machine displacement and Load vs. extensometer opening. Arrows point to the failure initiation.

4.2.2 *The Edge Tracing (ET) method*

Two digital cameras with a resolution of 2048×2048 pixels are placed on two orthogonal planes as shown in fig. 4.2 and used to acquire high resolution images. Images are saved as 8bit grayscale (grayscale levels range from 0 (black) to 255 (white)). The retro–lighting should be correctly adjusted to obtain a significant difference between the sample and the background gray levels. The images are then treated using a Python script which detects the specimen contours, evaluate the minimum diameter ($\phi_{\min}$) and the notch curvature radius (R). The main steps of the algorithm used to process the images are explained below:

1. The input image is filtered by a non-local image denoising method [Buades et al., 2011] in order to enhance the sharp gray level contrast between the sample and the background, see fig. 4.4 (a).

2. The image is manipulated as an array of pixels. For each j^{th} row of pixels in the array:

   a) A threshold is defined (via the OTSU method [Xu et al., 2011]) to detect the sample's contour. This threshold is used to define the sample's contour and thus, the diameter ("Pixel raw distance" in fig. 4.4 (b)).

b) The "Raw signal" in fig. 4.4 (b) is then interpolated to get an accurate estimation of the gray transition interface (sample–white background interface) at the sub–pixel level ("Pixel interpolated signal" in fig. 4.4 (b)). The diameter on the j^{th} row of the image array is estimated via the "Pixel interpolated distance" in fig. 4.4 (b).

c) Steps **a** and **b** are repeated on all rows in the array to trace the whole sample's contour and then deduce the minimum cross–section diameter Φ_{min}, see fig. 4.4 (c).

3. Once the sample's contour is traced, the notch curvature radius R can be estimated. The arc used to fit the notch radius on the left and right contours is restricted between two limits located at $\pm\,\eta\,\Phi_{min}$ (see green arcs in fig. 4.5 (a)). The effect of η on the calculated R is illustrated in fig. 4.5 (b). The latter shows the estimated R as a function of η for a given level of plastic deformation. The best range of η lies between 0.5 and 1.0. For each sample, an optimal value of η must be given to the algorithm for the computation of R. As shown in fig. 4.4 (b), η does not affect the computed R at low deformation levels (e. g. $\Delta\Phi/\Phi_0 = 2.6\%$) as the notch curvature radius can be fit by a circle. However, η has a significant effect on the computed R at high deformation levels (e. g. $\Delta\Phi/\Phi_0 = 13.57\%$ shown in fig. 4.4 (b)) since re-notching might occur and thus, the sample's notch cannot be fit by a circle anymore. One can note that the Bridgman correction (and similar corrections based on the notch curvature radius) cannot be applied to such high deformation levels with the renotching effect.

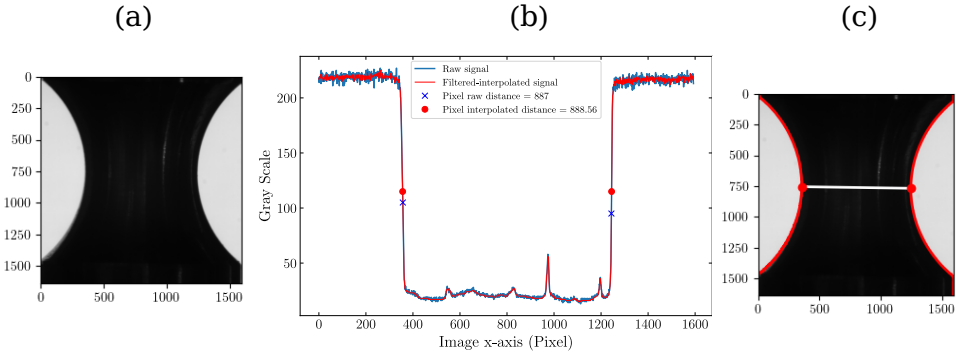

Figure 4.4: (a) Filtered input image to enhance the sharp gray level contrast between the sample and the background. (b) Contour tracing and diameter detection for each row in the image pixel array. (c) Minimum cross–section diameter Φ_{min} detection after treating all rows in the image array. The step-by-step ET method is explained in the text.

During testing, a series of images is taken (1 image/second) and then analyzed by the ET method to calculate $\frac{\Delta\Phi}{\Phi_0}$ and the notch curvature radius R. The Φ_{min} of the first image corresponds to a number of pixels that is used as a reference Φ_0 for calculating

the radial deformation: $\frac{\Delta\Phi}{\Phi_0}$. The images may be cropped to reduce the computation time by only taking into account the zone of interest around the notch.

After testing and only if the test is interrupted before complete fracture, the sample's notch is laser scanned to measure the notch diameter every 0.1 mm in the longitudinal axis. The notch is then virtually reconstructed by the stack of measurements to calculate the Φ_{min} and compare to the ET measurement (see section 4.3.2).

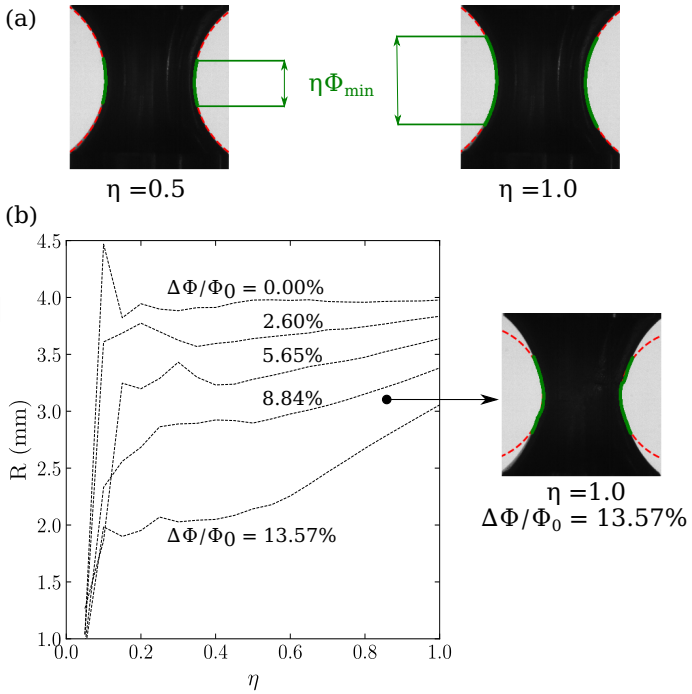

Figure 4.5: (a) Illustration of η and its effect on the limited area shaded by green arcs and used for estimating the notch curvature radius R. Two values of η are given and their limited area corresponds to $\pm\eta\,\Phi_{min}$ where Φ_{min} is the minimum cross section diameter. (b) Calculated notch curvature radius R as a function of η. At high deformation levels, the notch cannot be fit by a circle.

4.3 CASE STUDY 1: PLASTICITY AND FAILURE OF A 6061-T6 ALUMINUM ALLOY

4.3.1 *6061-T6 aluminum alloy*

The studied 6061-T6 aluminum alloy has two major alloying elements (Mg and Si) as shown in table 4.1. Both elements form nano–sized Mg_xSi_y precipitates during the 8 hours age hardening treatment at 175°C (T6 heat treatment [Hasting et al., 2007]). The alloy is characterized by a 255 MPa yield strength, 305 MPa tensile strength, and a 7.5% uniform elongation. Coarse Mg_2Si spherical precipitates ($\sim 5\mu$m) as well as iron rich particles ($\sim 10\mu$m long) are also present in the matrix; they are considered as damage initiators during straining [Petit et al., 2019; Shen et al., 2013].

Table 4.1: Studied AA6061-T6 chemical composition by %wt.

Mg	Si	Fe	Cu	Cr	Mn	Zn	Ti	Al
0.58	1.00	0.16	0.28	0.19	0.06	0.03	0.02	bal.

4.3.2 *Tests on NT and ST tensile specimens*

The studied specimens have a minimal diameter Φ_0 of 4 mm and a radius R_0 equal to 4, 1.6 and 0.8 mm (respectively corresponding to NT10, NT4 and NT2 specimens). The extensometer initial length (L_0) is 10 mm for NT specimens and 17.8 mm for ST specimens. Tests are carried by the deformation control technique to capture the post–necking phase. Recorded images are treated to obtain the radial deformation. fig. 4.6 shows the macroscopic mechanical behavior of ST, NT10, NT4, and NT2 samples (two samples are tested from each geometry). The sharp load drop observed on all specimens corresponds to a crack initiation at the center of the specimens. The crack propagates towards the free surface up to full failure. These tests are usually unstable and the load decrease cannot be controlled unless the deformation control technique described above is applied. For instance, Nguyen et al., 2018 and He et al., 2021 did not obtain the post–necking phase during tensile testing of a similar 6061 aluminum alloy. The cited authors use a machine displacement control which leads to an unstable failure. Nonetheless, the controlled load drop is more difficult to achieve for NT2 and ST specimens.

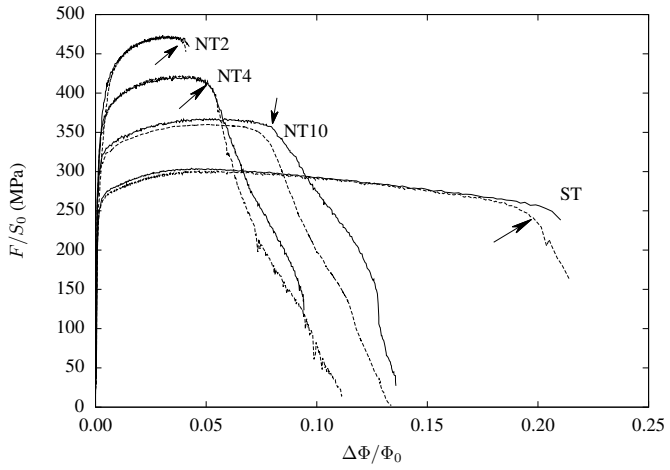

Figure 4.6: Deformation controlled ST and NT tensile tests (AA6061-T6). Two tests are shown (solid and dashed lines) for each specimen type. Arrows indicate fracture initiation.

Some specimens are interrupted before complete failure. The specimens are then laser scanned to map their diameters as a function of the axial position (every 0.1 mm) and the viewing angle (every 5°). Results can then be compared to the ET measurements. This comparison is shown in fig. 4.7 for the minimum cross–section diameter in a NT10 specimen. The ET measurement compared to the scan shows good agreement

with a maximum absolute difference of 0.014 mm between both measurements. The measured difference is attributed to the specimen surface roughness due to the deformation of large grains (mean grain size 30 μm). Therefore, the radial deformation calculated by the ET method gives an accurate estimate of the real radial deformation that would have been measured by radial extensometers. Figure 4.7 also shows that the minimum measured diameter is almost constant as a function of the viewing angle. This reveals the fact that the studied 6061-T6 aluminum alloy does not undergo plastic anisotropy. The samples are cut from a 6061-T6 aluminum product that did not go through either a rolling or extrusion process.

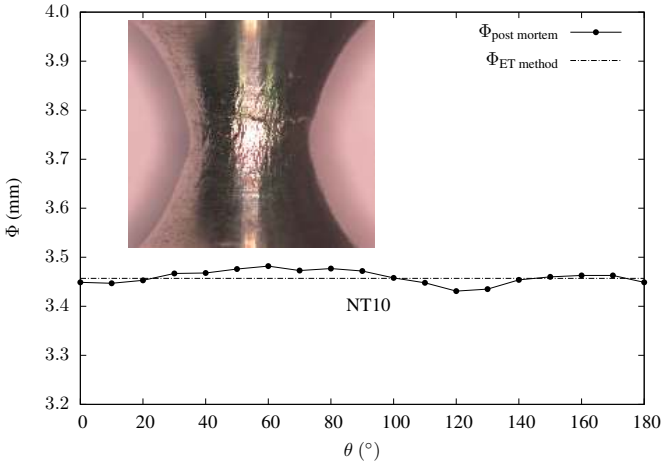

Figure 4.7: Minimum cross–section notch diameter Φ_{min} laser scanned after an interrupted NT10 test compared to the final Φ_{min} obtained by the ET-method. Image showing the initiated crack on the surface of the interrupted NT10 test.

4.3.3 *Using the ET measurements to model the material behavior: plasticity*

With the increasing efficiency of computers, it is now possible to use optimization methods based on finite element simulations of specimens to adjust the elastic–plastic behavior on the experimental results. The method uses the difference between experimental and finite element results as an objective function to be minimized. This "brute force" methodology is recently employed in the work of Defaisse et al., 2018; Mohr et al., 2015. The fit of the hardening function is first done assuming von Mises plasticity; this assumption is validated after fitting. The fit is performed using the load—diameter reduction curves before the onset of sharp load drop (see arrows in fig. 4.6). Elongation up to the onset of necking and diameter reductions for all specimens are used to define the objective function. The flow stress σ_F is expressed as a function of the accumulated plastic strain p as:

$$\sigma_F(p) = \sigma_0 + Q_1(1 - \exp(-b_1 p)) + Q_2(1 - \exp(-b_2 p)) \tag{4.1}$$

where σ_0, Q_1, b_1, Q_2 and b_2 are coefficients to be fit. The fitting is done by minimizing the value of the objective function mentioned above. The optimized values are: $\sigma_0 =$ 243 MPa, $Q_1 = 85$ MPa, $b_1 = 17.4$, $Q_2 = 17.5$ MPa and $b_2 = 262$.

In the following section, use is made of the sharp load drop part of the curve corresponding to crack propagation in the minimum cross section (beyond arrows in fig. 4.6) to fit parameters of a damage model.

4.3.4 *Using the ET measurements to model the material behavior: Ductile damage*

The ductile failure of an AA6061-T6 is characterized by a void nucleation phase on intermetallic particles, followed by growth of these microcavities and their coalescence [Dorbane et al., 2015; Farahani et al., 2017; Petit et al., 2019; Shen et al., 2013]. The AA6061-T6 along with other ductile alloys containing micron sized precipitates undergo a void nucleation phase during loading. This phenomenon is not easy to model since the damage must be studied on various stress triaxiality levels to fit a well predictive damage model. The failure of the AA6061-T6 is often simulated by the GTN model [Chu et al., 1980; Tvergaard, 1981, 1982] to take into account the void nucleation, growth and coalescence. Parameters of this model can be determined by the aid of *insitu* experiments and/or unit cell simulations [Faleskog et al., 1998; Gao et al., 1998; Pardoen et al., 2000; Shen et al., 2013; Xia et al., 1995a,b]. In both cases, all these authors agree that the porosity evolution in this model is sensitive to the stress triaxiality.

4.3.4.1 *Gurson damage model*

The GTN model used in this work is fully described below. The model uses the void volume fraction (f) as a damage variable. The porosity is expressed as the sum of the porosity due to void growth (f_g) and the porosity due to void nucleation (f_n) Tvergaard et al., 1984. The model is based on the definition of an effective stress ($\sigma_\star$) used to define the yield condition as follows Besson et al., 2001:

$$S = \sigma_\star - \sigma_F(p) \tag{4.2}$$

where σ_F is the flow stress of the undamaged material. The plastic strain rate tensor is obtained using the normality rule as follows:

$$\underline{\dot{\varepsilon}}^{\mathrm{p}} = (1-f)\,\dot{p}\,\frac{\partial \sigma_\star}{\partial \underline{\sigma}} \tag{4.3}$$

where $\underline{\sigma}$ is the Cauchy stress tensor. The plastic multiplier $\dot{p}$ is such that $\underline{\dot{\varepsilon}}^{\mathrm{p}} : \underline{\sigma} = (1-f)\dot{p}\sigma_\star$. $\dot{p}$ is obtained either using the consistency condition (rate independent case) or a visco–plastic flow rule (rate dependent case). In the specific case of the GTN

model, the effective stress is implicitly defined as a function of the stress tensor and the porosity by the following equation:

$$\left(\frac{\sigma_{\text{eq}}}{\sigma_\star}\right)^2 + 2q_1 f_\star \cosh\left(\frac{3}{2}q_2\frac{\sigma_m}{\sigma_\star}\right) - 1 - {q_1}^2 f_\star^2 \equiv 0 \tag{4.4}$$

where σ_{eq} is the von Mises equivalent stress, and σ_m the mean stress. q_1 and q_2 are two model parameters describing void growth. $f_\star$ is defined such that:

$$f_\star = \begin{cases} f & \text{if } f < f_c \\ f_c + \delta(f - f_c) & \text{otherwise} \end{cases} \tag{4.5}$$

where the "acceleration" factor $\delta \geq 1$ is expressed as:

$$\delta = \frac{1/q_1 - f_c}{f_R - f_c} \tag{4.6}$$

The function $f_\star$ is used to represent void coalescence in a simple way. Coalescence is assumed to start when f reaches a critical value f_c. f_R represents the porosity at failure. Void growth is directly obtained from the plastic flow (mass conservation) as follows:

$$\dot{f}_g = (1 - f)\text{tr}(\dot{\underline{\varepsilon}}^{\text{p}}) \tag{4.7}$$

Void nucleation plays an important role in the failure process. Assuming strain controlled nucleation [Chu et al., 1980], the nucleation rate can be expressed as shown:

$$\dot{f}_n = A_n \dot{p} \tag{4.8}$$

where A_n is a function of the material state which is often expressed as a function of the plastic strain p [Chu et al., 1980; Zhang et al., 2000] but may also depend on the stress state [Dalloz et al., 2009; Petit et al., 2019]. The following nucleation law (A_n) is adjusted by trial and error following the ideas proposed in the work of Petit et al., 2019:

$$A_n = A_n^s \left\langle \sigma_{I_\star}/\sigma_0 - 1 \right\rangle^N + A_n^0 \tag{4.9}$$

where σ_0, A_n^s, A_n^0 and N are parameters to be identified via experimental data. Equation (4.9) accounts for the stress effect on nucleation in the first part ($A_n^s \langle ... \rangle$) and the plastic deformation in the second added part (A_n^0). The parameter σ_0 is a critical stress threshold below which the first nucleation term is not activated. The effective maximum principal stress ($\sigma_{I_\star}$) is defined as the ratio between the effective stress and equivalent von Mises stress multiplied by the maximum principal stress (i. e. $\sigma_{I_\star} = \sigma_I \times \frac{\sigma_\star}{\sigma_{\text{vM}}}$). Nucleation is only active if:

Table 4.2: Parameters of the GTN ductile damage model. Parameters marked with a † are *a priori* fixed while the remaining parameters are calibrated via the ET method. h represents the element size.

$f_0{}^\dagger$	$q_1{}^\dagger$	$q_2{}^\dagger$	$f_c{}^\dagger$	$f_R{}^\dagger$	$p_c{}^\dagger$	$f_N{}^\dagger$	$\sigma_0{}^\dagger$	A_n^s	A_n^0	N	$h^\dagger$
0.0035	2.	1.	0.05	0.2	0.03	0.0215	250 MPa	0.11	0.02	4	0.1 mm

1. The plastic strain p is larger than a critical strain p_c (taken from Petit et al., 2019 as 3%, see table 4.2).
2. The effective maximum principal stress ($\sigma_{I_\star}$) is greater than the critical stress σ_0 (taken as the yield stress, see table 4.2).
3. The nucleated porosity f_n is less than the volume fraction of particles which can cause void nucleation (f_N) (taken as the measured volume fraction of Fe rich particles).

The model has many parameters so that some of them are *a priori* fixed. The initial porosity f_0 corresponds to the volume fraction of coarse Mg_2Si particles that easily detach from the aluminum matrix [Petit et al., 2019]. q_1, q_2 and f_c are calibrated on unit cell calculations [Faleskog et al., 1998] carried out using the fit hardening law (eq. (4.1)) as well as the measured f_0. The maximum nucleation porosity f_N is taken as the measured volume fraction of iron and silicon rich particles. The reference stress σ_0 is taken equal to the yield stress. Finally, the (A_n^s, N and A_n^0) parameters must be adjusted to represent crack initiation in smooth tensile and notched tensile samples. An attempt is done using the identified parameters in the work of Petit et al., 2019 who studied the same alloy. The cited authors determined the GTN parameters on compact tension specimens with high stress triaxiality levels (> 2.5). Those GTN parameters under estimated the porosity evolution when used to simulate the ductile behavior of NT samples in this study. This is of no surprise since the stress triaxiality level in the NT samples is lower than in the compact tensions samples. Consequently, the same GTN parameters (A_n^s, N and A_n^0) are reevaluated in this work to cover low and medium stress triaxiality levels (from 0.33 up to 2.0). The (f_c and f_R) parameters are also fit on the post–crack initiation phase of experiments in this work.

4.3.4.2 *Numerical results*

Figure 4.8 displays simulations carried with the newly calibrated GTN parameters listed in table 4.2. More details concerning the finite element simulations and the used numerical methods are given in the appendix.The model provides good predictions of the damage behavior as the experimental and numerical crack–initiation and propagation phases are quite similar. Images from the tests are compared to the mesh images from the simulation to assure the similarity in both experimental and

numerical post–necking phases. Elements of the numerical mesh are filled in black to be able to apply the ET method to the mesh images. Figure fig. 4.9 compares the measured and simulated curvature radii based on sample and mesh images respectively. These encouraging results emphasize the advantage of the ET method in calibrating and validating the simulated post–crack initiation phase on such a low ductility alloy.

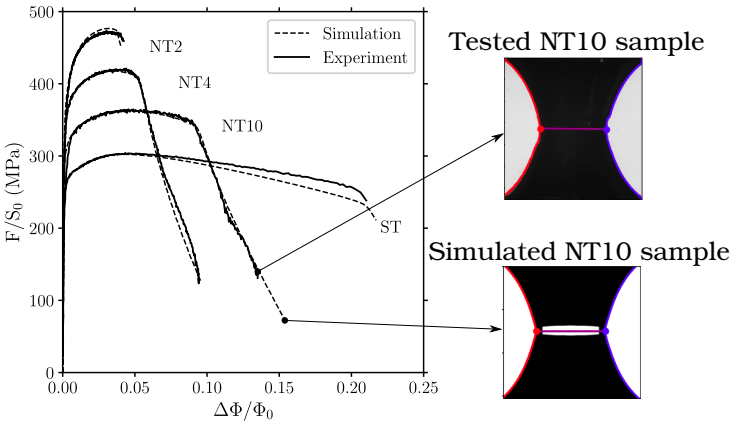

Figure 4.8: Simulated tensile tests with the new damage GTN model parameters calibrated on the post–necking phase in ST and NT experiments. The white space in the center of the simulated NT10 sample represents the crack.

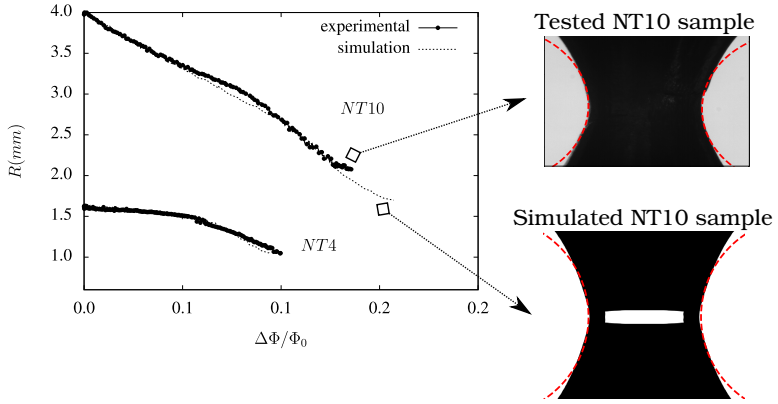

Figure 4.9: Notch curvature radius R calculated ($\eta = 1$) by applying the ET method on test and numerical mesh images. Bottom image displays a numerical mesh with a propagated crack while the top image is taken from a NT10 experimental test.

4.4 CASE STUDY 2: ET METHOD APPLIED TO THE STUDY OF THE ANISOTROPIC ELASTIC–PLASTIC BEHAVIOR OF A X52 STEEL

4.4.1 *Material*

Construction steels for pipelines are fabricated from hot rolled sheet metals. Large diameter pipes are then produced by UOE forming[1]. The material has an anisotropic plastic behavior due to crystallographic texture developed during the fabrication process [Tanguy et al., 2008]. Thus, it is important to keep track of the material principal axes (with respect to the metal forming process). The longitudinal direction corresponding to the rolling direction is hereby referred to as L; the transverse direction as T and the short transverse (thickness) direction as S. D stands for the diagonal direction (45° between direction L and T in the sheet plane).

In this study, the behavior of a "vintage" (produced in 1968) X52 API grade steel is investigated. Its chemical composition is shown in table 4.3. One can notice the high sulfur content which is 10 times higher than in modern steels.

Table 4.3: Studied X52 grade of steel chemical composition by %wt.

C	Mn	S	Al	Si	Cr	Cu	Mo	V	Ti	Fe
0.17	1.22	0.054	0.036	0.27	≤ 0.01	0.06	≤ 0.01	≤ 0.01	≤ 0.01	bal.

4.4.2 *Anisotropic plastic behavior*

The plastic anisotropic behavior of the material is studied using smooth and notched tensile bars. The ET method is employed using two cameras (see fig. 4.2) which track the radial deformation in the chosen directions perpendicular to the loading direction. For example, deformation is tracked along T and S for a test loaded in the L direction. The same protocol as in the case of the AA6061-T6 tests is used. The specimens have a minimal diameter Φ_0 of 6 mm and a radius R_0 equal to 6, 2.4 and 1.2 mm (respectively corresponding to NT10, NT4 and NT2 specimens). The extensometer initial length (L_0) is 25 mm for NT specimens and 13.2 mm for ST specimens. As the study is only concerned with the elastic–plastic behavior, results are shown up to the onset of failure. It is assumed that ductile damage has a negligible effect on the overall behavior before the onset of failure. Tests are repeated twice or thrice. Only one test is shown for every given specimen/loading direction configuration.

1 UOE forming is a manufacturing process where the plate material is first deformed into an U-shape then an O-shape. The pipe seam is then welded. The pipe is finally expanded using an internal mandrel. To achieve low ovality, the pipe is typically expanded by 0.8–1.3% from its diameter after the O-step [Herynk et al., 2007].

Results of ST specimens tested along the L, T and D directions are shown in fig. 4.10 (a, b). Figure 4.10 (a) shows the nominal stress (F/S_0) as a function of the nominal strain ($\Delta l/l_0$) up to the onset of necking. A Lüders plateau is observed in all cases up to a strain equal to 2%. A slight stress anisotropy is observed. Table 4.4 summarizes the tensile properties and number studied ST samples along different loading directions.

Table 4.4: Monotonic tensile properties and number of studied X52 steel ST samples in three loading directions: T, L and D

Loading direction	Tested samples	Yield strength (MPa)		Ultimate tensile strength (MPa)		Uniform elongation (%)	
		Avg.	*Std. dev. (%)*	*Avg.*	*Std. dev. (%)*	*Avg.*	*Std. dev. (%)*
T	5	408	5.0	551	3.6	17.4	1.0
L	4	410	8.2	553	7.4	15.3	0.5
D	2	410	0.5	559	1.5	16.5	0.5

Figure 4.10 (b) shows the true strain along the direction orthogonal to both the loading direction and the S–direction ($\varepsilon_\perp = \log(\Phi_\perp/\Phi_0)$) as a function of the true strain along the S–direction ($\varepsilon_S = \log(\Phi_S/\Phi_0)$). $\Phi_\perp$ and Φ_S are respectively the diameters measured for the orthogonal and the S directions. The ET method allows measuring strain beyond the onset of necking which is indicated by dots. Results remarkably show that the initial strain ratio (Lankford's coefficient) $\mathcal{L} = \varepsilon_\perp/\varepsilon_S$ remains unchanged after the onset of necking. Lankford's coefficients for the three loading directions are 0.81, 0.74 and 1.01 for the T, L and D directions respectively. The lower maximum strain for testing along the T direction is due to the lower ductility of the material when tested in that direction. This behavior is often observed in line pipe steels [Madi et al., 2019; Shinohara et al., 2016]. The Lankford coefficient are lower than 1 for L and T loadings whereas it is close to 1 for D loading. These trends are commonly observed for UOE pipes [Shinohara et al., 2010; Tanguy et al., 2008]. In the present case, the Lankford coefficients are evaluated for the entire strain range. They are computed using the total strain as it is impossible to experimentally separate elastic and plastic stains after necking.

Diameter variations for ST and NT specimens are shown in fig. 4.10 (c, d) for both L and T loading directions. NT samples' results are consistent with the obtained results on smooth tensile bars. Three NT samples are tested for each geometry and every loading direction. Deformation tends to be maximum along the S direction for both loading directions. Stress anisotropy is negligible. One can also notice that strain to failure is smaller for T loading. Diameter variations given by the ET method can also allow estimate the radial strain–rate in the pre– and post–necking phases. The strain–rate in the pre– and post–necking phases of the ST sample (L loading) is equal to $2 \times 10^{-4}\ s^{-1}$ (constant) and increases till $2 \times 10^{-3}\ s^{-1}$ (maximum value before failure) respectively.

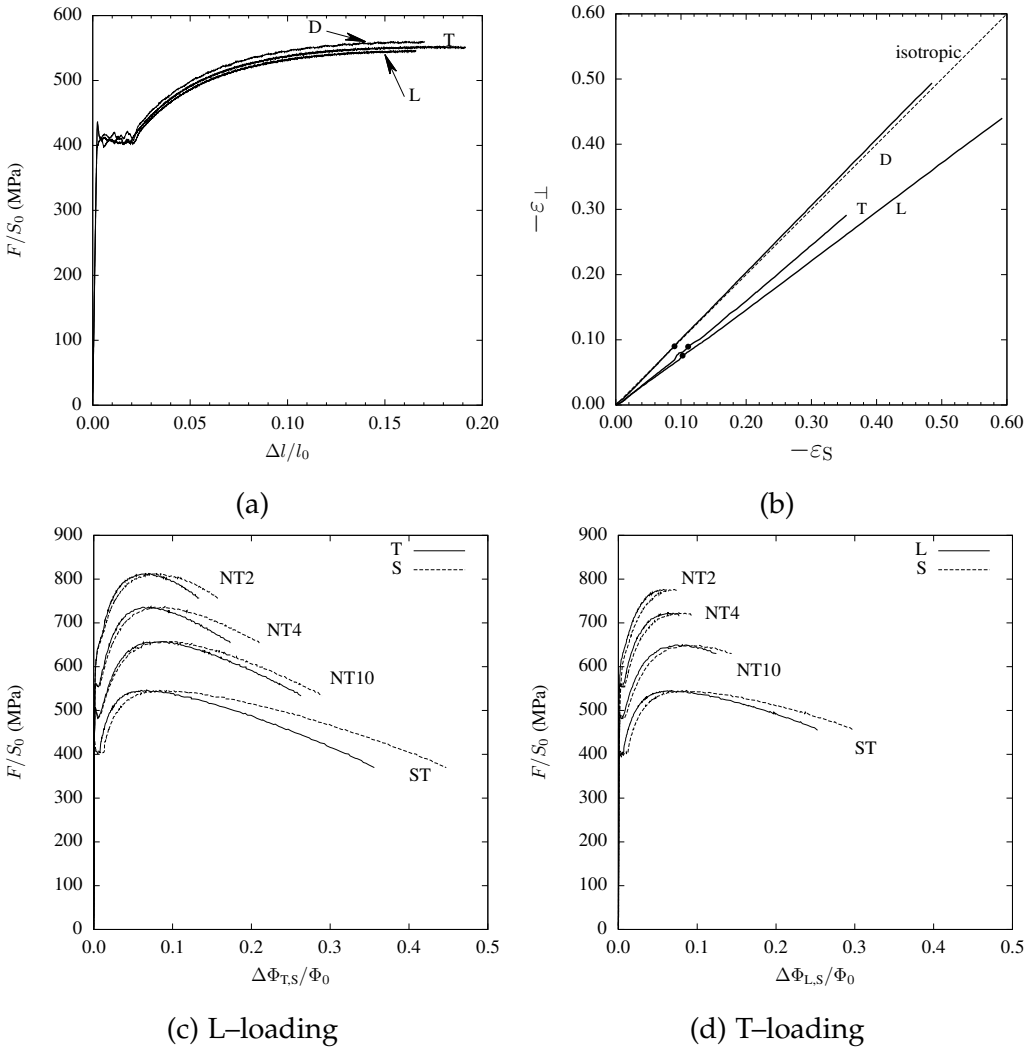

Figure 4.10: Tensile tests performed on the X52 vintage steel. (a) Nominal stress—strain curves along L, T, and D directions, (b) Deformation ($-\Delta\Phi_\perp/\Phi_0$) along the direction orthogonal to both the loading direction and the S–direction as a function of the deformation along the S–direction ($-\Delta\Phi_S/\Phi_0$). Dots indicate the onset of necking. Normalized force — diameter variation curves for (c) L—loading and (d) T—loading.

4.4.3 *Identification of a model for plastic anisotropy*

Experimental results presented in the previous section are now used to adjust a model to represent the plastic anisotropy of the material. In ST specimens, the ET technique can be used beyond the necking point so that work hardening can be adjusted with a good accuracy over a large plastic strain range which guarantees that no extrapolation is used to simulate the behavior of the entire database. As the material exhibits a very low stress anisotropy but a pronounced plastic flow anisotropy, a Hill type model [Hill, 1950] cannot be used in the present case. This is because the normality rule links stress and strain anisotropies. Given the reduced number of material parameters, both phenomena cannot be simultaneously adjusted. The same also holds for the non–quadratic law proposed by Barlat et al., 1991. The model proposed to describe the anisotropic plastic behavior of the material circumvents this limitation and is briefly presented below.

The BB04 model used in this study to describe plastic anisotropy is initially developed in the case of aluminum alloys [Bron et al., 2004; Zhang et al., 2014] but is also applied to line pipe steels [Shinohara et al., 2010, 2016; Tanguy et al., 2008]. It is a generalization of previously published models [Barlat et al., 1991; Karafillis et al., 1993]. An anisotropic scalar stress measure, σ_E, is defined as a weighted average of N anisotropic scalar stress measures σ_{Ei}:

$$\sigma_E = \left(\sum_{k=1}^{N} \alpha_k \sigma_{Ek}^a \right)^{1/a} \tag{4.10}$$

where α_k are weight factors such that $\sum_k \alpha_k = 1$. In the following, two anisotropic scalar stress measures ($N = 2$) are used to define σ_E as in the work of Bron et al., 2004; Tanguy et al., 2008. One first defines two modified stress deviators:

$$\underline{s}_k = \underline{\underline{\mathbf{L}}}_k : \underline{\sigma} \qquad k = 1, 2 \tag{4.11}$$

where the fourth order tensors $\underline{\underline{\mathbf{L}}}_k$ are expressed using Voigt notations as follows:

$$\underline{\underline{\mathbf{L}}}_k = \begin{pmatrix} \frac{1}{3}(c_{LL}^k + c_{SS}^k) & -\frac{1}{3}c_{SS}^k & -\frac{1}{3}c_{LL}^k & 0 & 0 & 0 \\ -\frac{1}{3}c_{SS}^k & \frac{1}{3}(c_{SS}^k + c_{TT}^k) & -\frac{1}{3}c_{TT}^k & 0 & 0 & 0 \\ -\frac{1}{3}c_{LL}^k & -\frac{1}{3}c_{TT}^k & \frac{1}{3}(c_{TT}^k + c_{LL}^k) & 0 & 0 & 0 \\ 0 & 0 & 0 & c_{TL}^k & 0 & 0 \\ 0 & 0 & 0 & 0 & c_{LS}^k & 0 \\ 0 & 0 & 0 & 0 & 0 & c_{ST}^k \end{pmatrix} \tag{4.12}$$

$c_{LL}^k \dots c_{ST}^k$ are coefficients introduced to represent anisotropy. Using the eigenvalues of $\underline{s}_k$ ($s_k^1 \geq s_k^2 \geq s_k^3$), the stress measures σ_{Ek} are defined as:

$$\sigma_{E1} = \left(\frac{1}{2}\left(|s_1^2 - s_1^3|^{b_1} + |s_1^3 - s_1^1|^{b_1} + |s_1^1 - s_1^2|^{b_1}\right)\right)^{1/b_1} \tag{4.13}$$

$$\sigma_{E2} = \left(\frac{3^{b_2}}{2^{b_2}+2}\left(|s_2^1|^{b_2} + |s_2^2|^{b_2} + |s_2^3|^{b_2}\right)\right)^{1/b_2} \tag{4.14}$$

The exponents a, b_1 and b_2 are used to modify the shape of the yield surface. In the following, one will assume $a = b_1 = b_2$. The yield surface is then expressed while assuming pure isotropic hardening as follows:

$$S = \sigma_E - \sigma_F(p) \tag{4.15}$$

where $\sigma_F(p)$ is a function of the accumulated plastic strain (p) representing the flow stress. The plastic strain rate tensor, $\underline{\dot{\varepsilon}}^p$, is obtained assuming the normality rule so that: $\underline{\dot{\varepsilon}}^p = \dot{p}\partial S/\partial\underline{\sigma}$. p is such that: $\underline{\dot{\varepsilon}}^p : \underline{\sigma} = \dot{p}\sigma_E$.

The various parameters of the model are adjusted using the guidelines proposed in Bron et al., 2004. Fitted values are gathered in table 4.5. The flow stress is defined as:

$$\sigma_F(p) = \max\left(\sigma_L, \sigma_0 + Q_1(1 - \exp(-b_1 p)) + Q_2(1 - \exp(-b_2 p)) + Hp\right) \tag{4.16}$$

where σ_L represents the Lüders stress which is fixed to 400 MPa. The hardening function combines a linear and two non linear terms in order to be able to represent hardening over a large strain range ($p \in [0 : 1.2]$). The Young's modulus is equal to 210 GPa and the Poisson's ratio is 0.3. The simulated length of the Lüders plateau is about 1%.

Table 4.5: Model parameters used to define the anisotropic scalar stress measure (σ_E) and the flow stress ($R(p)$)

$\mathbf{a = b_1 = b_2}$			$\mathbf{ff_1}$	$\mathbf{ff_2}$	
13.8			0.64	0.36	
$\mathbf{c^1_{TT}}$	$\mathbf{c^1_{LL}}$	$\mathbf{c^1_{SS}}$	$\mathbf{c^1_{TL}}$	$\mathbf{c^1_{LS}}$	$\mathbf{c^1_{ST}}$
0.82	1.00	0.91	0.98	1.50	1.15
$\mathbf{c^2_{TT}}$	$\mathbf{c^2_{LL}}$	$\mathbf{c^2_{SS}}$	$\mathbf{c^2_{TL}}$	$\mathbf{c^2_{LS}}$	$\mathbf{c^2_{ST}}$
1.18	1.17	0.94	0.94	1.33	0.77

σ_L	σ_0	Q_1	b_1	Q_2	b_2	H
400 (MPa)	368 (MPa)	292 (MPa)	7.4	82 (MPa)	28	63 (MPa)

The predictions of the model are compared with experiments in fig. 4.11. More details concerning the numerical methods are given in the appendix. The latter

elaborates the fact that the model is able to represent the quasi–isotropic stress behavior (fig. 4.11(a)) while, at the same time, it also well represents the anisotropic strain behavior (fig. 4.11(b)).

Comparisons between experimental and simulated results are also shown in fig. 4.11 (c, d) for both L (fig. 4.11 (c)) and T (fig. 4.11 (d)) loading directions. A good agreement is found between experimental and simulated results.

To illustrate the benefit of the developed model for plastic anisotropy, simulations using von Mises plasticity are also plotted in fig. 4.11(c, d) (red dashed lines). The hardening function is fitted using the F/S_0—$\Delta\Phi/\Delta\Phi_S$ curves for tests carried along the D direction as the strain behavior is almost isotropic in this case. Fitting the behavior for T or L loading can also be performed using the geometric mean of the diameters along the S and $\perp$ directions in order to keep the same cross section. One must note that fitting the model for strains less than the necking strain (≈ 0.17) leads to a very poor representation of F/S_0—$\Delta\Phi/\Phi_0$ curves as the fitted hardening is used far beyond its identification domain (extrapolation).

Comparisons between experiments and simulations using the BB04 model show a relatively good agreement for tensile tests. As notch severity is increased, the predicted maximum load overestimates the maximum load which is well represented by the BB04 model. This observation is also noted in the work of Bron et al., 2004. This corresponds to a non quadratic yield surface width $a > 4$.

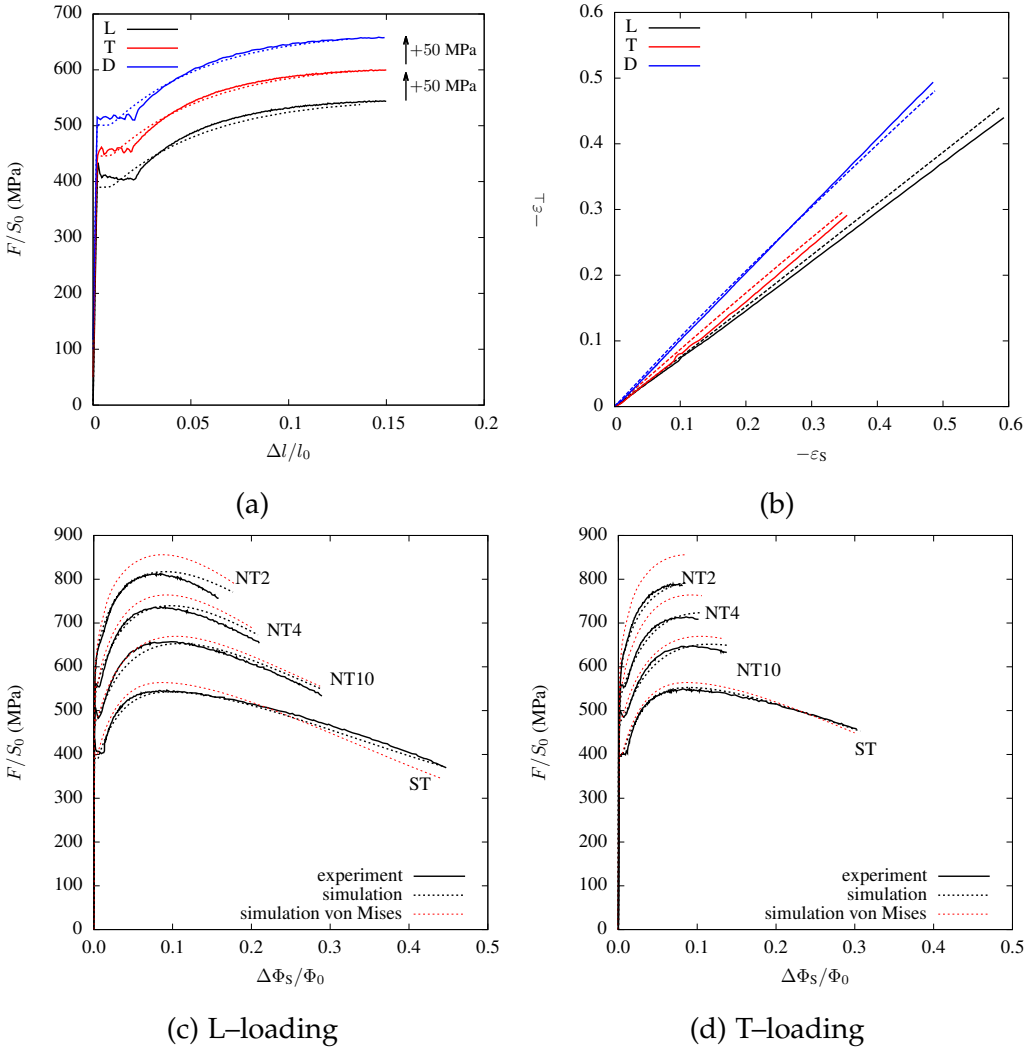

Figure 4.11: Comparison between experimental and simulated (a) nominal stress — elongation ($\Delta l/l_0$), a shift of 50MPa is applied to differentiate between L, T and D directions, (b) $\Delta\Phi_\perp/\Phi_0$ — $\Delta\Phi_S/\Phi_0$ curves, nominal stress — diameter variation along S curves for (c) L—loading and (d) T—loading (X52 steel) (Full lines: experiment, dashed lines: simulation, red dashed lines (c, d): simulation obtained assuming von Mises plasticity).

4.5 CONCLUSIONS AND REMARKS

The ET technique was developed in other studies to characterize the plastic behavior well beyond the necking strain. The strain–hardening models must be calibrated over the pre– and post–necking phases in order to study engineering problems with large strains (e. g. fracture). The Bridgman analytical correction formulas can be used to characterize the plastic behavior beyond necking. However, the Bridgman analytical correction formulas lead to significant errors as widely discussed in the literature. The advantage of the ET method is the fact that the post–necking behavior is directly characterized without correction formulas and by using simple equipment (cameras and adequate lighting). Till now, the ET method has not been used to study fracture.

The aim of this work is to extend the ET method to two challenging case studies: the fracture behavior in a low ductility AA6061-T6 and the plastic anisotropic behavior of line pipe steels. The mentioned case studies cannot be carried out using the conventional extensometer–based measuring techniques.

In the first case study, it is necessary to carry out the failure assessment on various stress triaxiality levels. This is achieved via a campaign of tensile testing on round notched samples with different curvature radii (i. e. different stress triaxiality levels). The principal conclusions made on the obtained results from the first case study are highlighted below:

- The AA6061-T6 usually incurs rapid failure after the maximum load is reached during the tensile test. However, the post–necking phase is captured in this work thanks to the "deformation controlled" technique. The latter helped in maintaining a relatively stable crack propagation phase. This technique is proved to be essential for calibrating the GTN damage parameters on tensile experimental data.

- The GTN damage parameters are first taken from other work that studied the same alloy under high stress triaxiality levels (> 2.5 in CT samples). The initial model parameters overestimated the deformation at failure in the simulated ST and NT sample. However, the post–necking data obtained by the ET method help reevaluate the damage parameters. The latter fit low (0.33 in ST samples) and medium (0.6-2.0 in NT samples) stress triaxiality levels. As a result, the simulated stress—radial deformation curves are in good agreement with the experiments.

The ET method is secondly employed to study the continuous evolution of the anisotropic behavior of line pipe steels to better understand the macroscopic behavior of the studied steel. The main conclusions made on the obtained results from the second case study are highlighted below:

- The ET method allows continuously observing the anisotropical behavior of line pipe steels during the entire tensile test. The "old-fashioned" alternative is to

rely on the post–mortem study of the fracture surfaces to analyze the anisotropy. However, in this study, the evolution of Lankford factor is continuously estimated for both tested directions during the tests conducted on ST specimens.

- The collected experimental data via the ET method give significant amount of information regarding the true radial strain in different loading directions. As a result, the parameters of the BB anisotropic plastic constitutive law are identified accurately. The accurate identification of the anisotropic plastic behavior is essential in order to study fracture in future work.

4.6 APPENDIX: NUMERICAL METHODS

Finite element (FE) simulations are carried out in this study via the Zset general purpose object oriented finite element software [Besson et al., 1997]. Ductile failure in aluminum alloys or plastic anistoropy in line pipe steels are two mechanical engineering problems that require a finite–strain formalism when implementing the constitutive equations. This is done by a generic formulation based on a reference frame which assures maintaining the standard small strain formulation while using an additive strain rate decomposition (i. e. $\underline{\dot{\varepsilon}}^{to} = \underline{\dot{\varepsilon}}^{el} + \underline{\dot{\varepsilon}}^{p}$ where $\underline{\dot{\varepsilon}}^{to}$ is the strain rate tensor and $\dot{\varepsilon}_e$ the elastic strain rate tensor) [Sidoroff et al., 2001].

4.6.1 *FE simulations in case study 1: Plasticity and failure of a 6061-T6 aluminum alloy*

For FE simulations carried out in the first case study, 2D meshes of the axisymmetric ST and NT samples are obtained with 8-node quadrangle elements containing 4 integration points (reduced integration). Symmetry conditions are used so that only $^1/_4$ of the ST and NT samples are meshed. The mesh size (h in table 4.2) is taken as $100 \times 100\ \mu m^2$ which is based on the average estimated distance between large constituent particles in the AA6061-T6 studied alloy.

The used GTN damage models leads to material softening which results in strain and damage localization within one row of elements. As a result, the simulation results strongly depend on the mesh size. To overcome this issue, models integrating material internal lengths can be used (e. g. [Feld-Payet et al., 2011; Mediavilla et al., 2006]). However, these models are still in an early development phase. The pragmatic solution chosen in this study is to fix a mesh size along the crack path [Liu et al., 1994; Rousselier, 1987] (minimal cross-section diamater in tensile samples). The fixed mesh size controls the fracture energy in the case of mesh dependent simulations [Siegmund et al., 2000].

The material integration point is considered as broken when f_* reaches $1/q_1 - \epsilon$ (with $\epsilon = 10^{-3}$). Then, its behavior is replaced by an elastic behavior with a very

low stiffness (Young modulus: $E = 1$ MPa). When 2 out of 4 integration points are considered as broken in the 2D element, the latter is removed from the mesh. Displacement increments at nodes belonging to removed elements are then fixed to avoid a singular global stiffness matrix.

4.6.2 *FE simulation in case study 2: ET method applied to the study of the anisotropic elastic–plastic behavior of a X52 steel*

Elastic–plastic FE simulations carried out in the second case study are mainly used to optimize parameters of the hardening law (see eq. (4.16) and table 4.5). Unlike the first case study, the line pipe steels have a significant anistropic plastic behavior. Therefore, 3D meshes are necessary. A 20-node 3D hexahedral element with 8 integration points (reduced integration) is used to mesh the ST and NT samples. The mesh size is taken as $100 \times 100 \times 100$ μm^3.

BIBLIOGRAPHY

Bai, Y. et al. (2009). 'On the Application of Stress Triaxiality Formula for Plane Strain Fracture Testing.' In: *J. Engng Mater. Technol.* 131.2. DOI: 10.1115/1.3078390 (see p. 91).

Bao, Y. and T. Wierzbicki (2004). 'On fracture locus in the equivalent strain and stress triaxiality space.' In: *Int. J. Mech. Sci.* 46.1, pages 81–98 (see p. 91).

Bao, Y. and T. Wierzbicki (2005). 'On the cut-off value of negative triaxiality for fracture.' In: *Eng. Fract. Mech.* 72, pages 1049–1069 (see p. 91).

Barlat, F. et al. (1991). 'A six–component yield function for anisotropic materials.' In: *Int. J. Plasticity* 7, pages 693–712 (see p. 107).

Besson, J. and R. Foerch (1997). 'Large scale object–oriented finite element code design.' In: *Comp. Meth. Appl. Mech. Engng* 142, pages 165–187 (see p. 112).

Besson, J. et al. (2001). 'Modeling of crack growth in round bars and plane strain specimens.' In: *Int. J. Solids Structures* 38.46–47, pages 8259–8284 (see p. 100).

Bridgman, P. W. (1945). 'Effects of High Hydrostatic Pressure on the Plastic Properties of Metals.' In: *Rev. Mod. Phys.* 17 (1), pages 3–14. DOI: 10.1103/RevModPhys.17.3 (see p. 91).

Bron, F. and J. Besson (2004). 'A yield function for anisotropic materials. Application to aluminium alloys.' In: *Int. J. Plasticity* 20, pages 937–963 (see pp. 107–109).

Buades, A. et al. (2011). 'Non-Local Means Denoising.' In: *IPOL J. Image Processing Online*, pages 208 –212. DOI: 10.5201/ipol.2011.bcm_nlm (see p. 95).

Chu, C. and A. Needleman (1980). 'Void nucleation effects in biaxially stretched sheets.' In: *J. Engng Mater. Technol.* 102, pages 249–256 (see pp. 100, 101).

Dalloz, A. et al. (2009). 'Effect of shear cutting on ductility of a dual phase steel.' In: *Eng. Fract. Mech.* 76.10, pages 1411–1424 (see p. 101).

Defaisse, C. et al. (2018). 'Ductile fracture of an ultra-high strength steel under low to moderate stress triaxiality.' In: *Eng. Fract. Mech.* 194, pages 301–318 (see pp. 92, 99).

Dorbane, A. et al. (2015). 'Observations of the mechanical response and evolution of damage of AA 6061-T6 under different strain rates and temperatures.' In: *Mater. Sci. Engng A* 624, pages 239–249. DOI: 10.1016/j.msea.2014.11.074 (see p. 100).

Faleskog, J. et al. (1998). 'Cell model for nonlinear fracture analysis — I. Micromechanics calibration.' In: *Int. J. Frac.* 89, pages 355–373 (see pp. 100, 102).

Farahani, B. et al. (2017). 'A GTN Failure Analysis of an AA6061-T6 Bi-Failure Specimen.' In: *Procedia Structural Integrity* 5, pages 981–988. DOI: 10.1016/j.prostr.2017.07.147 (see p. 100).

Feld-Payet, S. et al. (2011). 'Finite element analysis of damage in ductile structures using a nonlocal model combined with a three-field formulation.' In: *Int. J. Damage Mech.* 20, pages 655–680 (see p. 112).

Fourmeau, H. et al. (2011). 'On the plastic anisotropy of an aluminium alloy and its influence on constrained multiaxial flow.' In: *Int. J. Plasticity* 27.12, pages 2005–2025. DOI: 10.1016/j.ijplas.2011.05.017 (see p. 92).

Gao, X. et al. (1998). 'Cell model for nonlinear fracture analysis — II. Fracture–process calibration and verification.' In: *Int. J. Frac.* 89, pages 375–398 (see p. 100).

Hancock, J. and A. Mackenzie (1976). 'Mechanisms of ductile failure in high-strength steels subjected to multi- axial stress states.' In: *J. Mech. Phys. Solids* 24, pages 147–160 (see p. 93).

Hasting, H. et al. (2007). 'Comparative study of the β'' phase in a 6xxx Al alloy by 3DAP and HRTEM.' In: *Surf. Interface Anal.* 39.7, pages 189–194. DOI: 10.1002/sia.2487 (see p. 97).

He, Z. et al. (2021). 'An improved shear modified GTN model for ductile fracture of aluminium alloys under different stress states and its parameters identification.' In: *Int. J. Mech. Sci.* 192, page 106081. ISSN: 0020-7403. DOI: 10.1016/j.ijmecsci.2020.106081 (see p. 98).

Herynk, M. D. et al. (2007). 'Effects of the UOE/UOC pipe manufacturing processes on pipe collapse pressure.' In: *Int. J. Mech. Sci.* 49.5, 533–553 (see p. 104).

Hill, R. (1950). *The mathematical theory of plasticity*. Clarendon Press, Oxford (see p. 107).

Hopperstad, O. et al. (2003). 'On the influence of stress triaxiality and strain rate on the behaviour of a structural steel. Part I. Experiments.' In: *Eur. J. Mech./A* 22.1, 1–13. DOI: 10.1016/S0997-7538(02)00006-2 (see p. 91).

Karafillis, A. and M. Boyce (1993). 'A general anisotropic yield criterion using bounds and a transformation weighting tensor.' In: *J. Mech. Phys. Solids* 41, pages 1859–1886 (see p. 107).

Khadyko, M et al. (2014). 'An experimental–numerical method to determine the work-hardening of anisotropic ductile materials at large strains.' In: *Int. J. Mech. Sci.* 88, pages 25–36. ISSN: 0020-7403. DOI: 10.1016/j.ijmecsci.2014.07.001 (see p. 92).

Kondori, B. et al. (2019). 'Evolution of the 3D plastic anisotropy of HCP metals: Experiments and modeling.' In: *Int. J. Plasticity* 117, 71–92 (see p. 92).

Liu, Y. et al. (1994). 'Mesh–dependence and stress singularity in finite element analysis of creep crack growth by continuum damage mechanics approach.' In: *Eur. J. Mech./A* 13A.3, pages 395–417 (see p. 112).

Madi, Y. et al. (2019). 'On the origin of the anisotropic damage of X100 line pipe steel. Part I: In-situ synchrotron tomography experiments.' In: *Integrating Material and Manufacturing Innovations* (see p. 105).

Mediavilla, J. et al. (2006). 'Discrete crack modelling of ductile fracture driven by non-local softening plasticity.' In: *Int. J. Numer. Meth. Engng* 66.4, pages 661–688 (see p. 112).

Mirone, G. (2004). 'A new model for the elastoplastic characterization and the stress–strain determination on the necking section of a tensile specimen.' In: *Int. J. Solids Structures* 41, pages 3545–3564 (see p. 91).

Mohr, D. and S. Marcadet (2015). 'Micromechanically-motivated phenomenological Hosford-Coulomb model for predicting ductile fracture initiation at low stress triaxialities.' In: *Int. J. Solids Structures* 67-68, 40–55 (see p. 99).

Nguyen, H. et al. (2018). 'Ductile fracture prediction and forming assessment of AA6061-T6 aluminum alloy sheets.' In: *Int. J. Frac.* 209, pages 143–162. DOI: 10.1007/s10704-017-0249-4 (see p. 98).

Olden, V. et al. (2002). 'Notch tensile testing of high strength steel weldments.' In: *2nd International Symposium on High Strength Steel, 23.-24.* DOI: 10.13140/2.1.4739.9681 (see p. 91).

Pardoen, T. and J. Hutchinson (2000). 'An extended model for void growth and coalescence.' In: *J. Mech. Phys. Solids* 48.12, pages 2467–2512 (see p. 100).

Petit, T. et al. (2018). 'Impact of machine stiffness on "pop-in" crack propagation instabilities.' In: *Eng. Fract. Mech.* 202, pages 405–422 (see p. 95).

Petit, T. et al. (2019). 'Effect of hardening on toughness captured by stress-based damage nucleation in 6061 aluminum alloy.' In: *Acta Mater.* 180, 349–365. DOI: 10.1016/j.actamat.2019.08.055 (see pp. 97, 100–102).

Rousselier, G. (1987). 'Ductile fracture models and their potential in local approach of fracture.' In: *Nucl. Eng. Des.* 105, pages 97–111 (see p. 112).

Shen, Y. et al. (2013). 'Three-dimensional quantitative in situ study of crack initiation and propagation in AA6061 aluminum alloy sheets via synchrotron laminography and finite-element simulations.' In: *Acta Mater.* 61, pages 2571–2582. DOI: 10.1016/j.actamat.2013.01.035 (see pp. 97, 100).

Shinohara, Y. et al. (2010). 'A combined phenomenological model for the representation of anisotropic hardening behavior in high strength steel line pipes.' In: *Eur. J. Mech./A* 29.6, pages 917–927 (see pp. 105, 107).

Shinohara, Y. et al. (2016). 'Anisotropic ductile failure of a high-strength line pipe steel.' In: *Int. J. Frac.* 197, pages 127–145 (see pp. 105, 107).

Sidoroff, F. and A. Dogui (2001). 'Some issues about anisotropic elastic-plastic models at finite strain.' In: *Int. J. Solids Structures* 38, pages 9569–9578 (see p. 112).

Siegmund, T. and W. Brocks (2000). 'A numerical study on the correlation between the work of separation and the dissipation rate in ductile fracture.' In: *Eng. Fract. Mech.* 67, pages 139–154 (see p. 112).

Tanguy, B. et al. (2008). 'Plastic and damage behavior of a high strength X100 pipeline steel: experiments and modelling.' In: *Int. J. of Pressure Vessels and Piping* 85.5, pages 322–335 (see pp. 104, 105, 107).

Tekoğlu, C. et al. (2015). 'On localization and void coalescence as a precursor to ductile fracture.' In: *Philosophical transactions of the Royal Society of London. A* 373. DOI: 10.1098/rsta.2014.0121 (see p. 94).

Tu, S. et al. (2018a). 'A method for determining material's equivalent stress-strain curve with any axisymmetric notched tensile specimens without Bridgman correction.'

In: *Int. J. Mech. Sci.* 135, pages 656–667. ISSN: 0020-7403. DOI: 10.1016/j.ijmecsci.2017.12.012 (see p. 91).

Tu, S. et al. (2018b). 'Study of low-temperature effect on the fracture locus of a 420 MPa structural steel with the edge tracing method.' In: *Fatigue and Fract. Engng Mater. Struct.* 41, pages 1649–1661. DOI: 10.1111/ffe.12803 (see p. 91).

Tu, S. et al. (2019). 'Experimental measurement of temperature-dependent equivalent stress-strain curves of a 420 MPa structural steel with axisymmetric notched tensile specimens.' In: *Eng. Fail. Anal.* 100, pages 312–321. DOI: 10.1016/j.engfailanal.2019.02.043 (see p. 91).

Tu, S. et al. (2020). 'Stress–strain curves of metallic materials and post–necking strain hardening characterization: A review.' In: *Fatigue and Fract. Engng Mater. Struct.* 43, pages 3–19. DOI: 10.1111/ffe.13134 (see pp. 91, 92).

Tvergaard, V. (1981). 'Influence of voids on shear band instabilities under plane strain condition.' In: *Int. J. Frac.* 17.4, pages 389–407 (see p. 100).

Tvergaard, V. (1982). 'On the localization in ductile materials containing spherical voids.' In: *Int. J. Frac.* 18.4, pages 237–252 (see p. 100).

Tvergaard, V. and A. Needleman (1984). 'Analysis of the cup–cone fracture in a round tensile bar.' In: *Acta Metall.* 32, pages 157–169 (see p. 100).

Versaillot, P. et al. (2021). 'A new theoretical method for predicting the elastoplastic behavior of ductile metallic materials.' In: *Int. J. Mech. Sci.* 200, page 106450. ISSN: 0020-7403. DOI: https://doi.org/10.1016/j.ijmecsci.2021.106450 (see p. 91).

Vilamosa, V. et al. (2014). 'Local Measurement of Stress–Strain Behaviour of Ductile Materials at Elevated Temperatures in a Split-Hopkinson Tension Bar System.' In: *Strain* 50.3, pages 223–235. DOI: 10.1111/str.12084 (see p. 91).

Xia, L. and C. F. Shih (1995a). 'Ductile crack growth — I. A numerical study using computational cells with microstructurally-based length scales.' In: *J. Mech. Phys. Solids* 43, pages 233–259 (see p. 100).

Xia, L. and C. F. Shih (1995b). 'Ductile crack growth — II. Void nucleation and geometry effects on macroscopic fracture behaviour.' In: *J. Mech. Phys. Solids* 43, pages 1953–1981 (see p. 100).

Xu, X. et al. (2011). 'Characteristic analysis of Otsu threshold and its applications.' In: *Pattern Recognition Letters* 32.7, pages 956–961. ISSN: 0167-8655. DOI: 10.1016/j.patrec.2011.01.021 (see p. 95).

Zhang, S. et al. (2014). 'Calibration of anisotropic yield criterion with conventional tests or biaxial test.' In: *Int. J. Mech. Sci.* 85, 142–151 (see p. 107).

Zhang, T. et al. (2021). 'A novel method to uniquely determine the parameters in Gurson–Tvergaard–Needleman model.' In: *Fatigue and Fract. Engng Mater. Struct.* 44.12, pages 3399–3415. DOI: 10.1111/ffe.13568 (see p. 92).

Zhang, Z. (1996). 'A Sensitivity Analysis of Material Parameters for the Gurson Constitutive Model.' In: *Fatigue and Fract. Engng Mater. Struct.* 19, pages 561 –570. DOI: 10.1111/j.1460-2695.1996.tb00992.x (see p. 92).

Zhang, Z. et al. (1999). 'Determining material true stress–strain curve from tensile specimens with rectangular cross–section.' In: *Int. J. Solids Structures* 36, pages 3497–3516 (see p. 91).

Zhang, Z. et al. (2000). 'A complete Gurson model approach for ductile fracture.' In: *Eng. Fract. Mech.* 67.2, pages 155–168 (see p. 101).

Zhang, Z. et al. (2001). 'A notched cross weld tensile testing method for determiningtrue stressstrain curves for weldments.' In: *Eng. Fract. Mech.* 69, pages 353–366. DOI: 10.1016/S0013-7944(01)00075-3 (see p. 91).

5

DUCTILE FAILURE IN 6061 ALUMINUM ALLOYS AT LOW, MEDIUM AND HIGH STRESS TRIAXIALITY

RÉSUMÉ

Ce travail a deux objectifs principaux. Le premier concerne la calibration des paramètres GTN pour modéliser la rupture à faible, moyenne et forte triaxialité des contraintes (T). Le second est la modélisation de la coalescence de cavités à travers une population secondaire de vides. Une porosité critique de coalescence qui dépend de T est ajustée sur les triaxialités étudiées et utilisée dans le modèle GTN. Une formule analytique est utilisée pour trouver les paramètres optimaux de croissance de cavités q_1 et q_2 sans calibration supplémentaire. Ensuite, les paramètres de croissance sont adaptés pour tenir compte de la distribution hétérogène des particules. Les paramètres de nucléation des vides sont identifiés par des essais de traction *insitu*. Le modèle GTN calibré fournit de bonnes prédictions lorsqu'il est utilisé pour modéliser des échantillons de traction simple (faible T), de traction avec entaille (T moyen) et de traction compacte (T élevé) avec différentes épaisseurs.

5.1 INTRODUCTION

The Gurson-Tvergaard-Needleman (GTN) damage model is extensively used in the literature to study materials that fail due to nucleation, growth and coalescence of microvoids. In addition, the GTN model is continuously improved and modified in the literature to account for cases that are not represented by the original model as: kinematic hardening [Besson et al., 2003; Leblond et al., 1995; Mear et al., 1985], plastic anisotropy Benzerga et al., 2001; Doege et al., 1995; Grange et al., 2000; Liao et al., 1997; Rivalin et al., 2000, void shape effect [Gologanu et al., 1993, 1994, 1997; Pardoen et al., 2000], viscoplasticity [Klocker et al., 2003; Leblond et al., 1994; Moran et al., 1990; Tvergaard, 1990], two void populations [Perrin et al., 2000], and shear–dominated stress states [He et al., 2021; Jiang et al., 2016; Nahshon et al., 2008; Nielsen et al., 2009]. The GTN extensions for shear–dominated stress states are motivated by the fact that the original GTN model is not able to capture void growth under low stress triaxiality (< 0.5) [Nielsen et al., 2009]. As the stress triaxiality drops below 0.5, void growth becomes insignificant and the material fails with subdued grown voids [Bao

et al., 2004b]. On the contrary, at medium ($0.5 < T < 1.5$) and high stress triaxiality ($T > 2$), void growth and coalescence become significant and can describe material failure Pineau et al., 2016.

Experimental evidence in the work of Barsoum et al., 2007 explains that voids dilate under high stress triaxiality which leads to significant increase in void growth followed by void coalescence via the reduction of the inter–void ligament (i. e. internal necking) [Barsoum et al., 2007; Benzerga et al., 2010; Besson, 2010]. However, under low stress triaxiality, voids elongate, rotate and interact with the smaller population of voids that nucleate between the primary voids. This leads to void coalescence in a shear band (i. e. void sheet) [Fabrègue et al., 2008; Hahn et al., 1975; Pardoen et al., 2000; Tvergaard, 2008, 2009]. Small voids interrupt void growth as the primary voids are linked by the smaller voids in the inter–void ligament [Benzerga et al., 2010; Hannard et al., 2018; Liu et al., 2011; Trejo-Navas et al., 2018]. Therefore, the void growth and coalescence mechanisms are dictated by the stress triaxiality and the microstructure (void volume fraction and size of secondary phases).

Aluminum alloys (2xxx, 5xxx and 6xxx) contain micron–sized intermetallic particles that fracture under plastic strain and create microvoids [Bron et al., 2004; Butcher et al., 2011; Morgeneyer et al., 2008]. The 6xxx aluminum alloys contain two types of micron–sized particles: Mg_2Si (diameter ~ 5 μm) and intermetallics Al(FeMn)Si (length $1 - 10$ μm according to Ghahremaninezhad et al., 2013; Lassance et al., 2007). The Mg_2Si fail at an early stage (during the elastic phase) as observed in the work of Maire et al., 2005 and Petit et al., 2019. The volume fraction of intermetallic particles in 6061 alloys is around 1% [Ghahremaninezhad et al., 2013; Lassance et al., 2007] and can reach 2% in some cases [Petit et al., 2019]. This leads to the fact that damage in the 6061 alloy is mainly "nucleation controlled" [Ghahremaninezhad et al., 2013]. This term refers to alloys that mainly fail due to nucleated voids. Void nucleation models in the literature are divided into two classes: strain–based and stress–based models [Chu et al., 1980; Needleman, 1987]. The latter result in better predictions as they account for the hydrostatic stress and therefore, the stress triaxiality effect on void nucleation [Butcher et al., 2011; Hannard et al., 2016]. A nucleation model can be decomposed into two parts: a threshold for activating void nucleation and a nucleation rate. Butcher et al., 2011 use a stress–based nucleation model in which the threshold and nucleation rate depend on the stress state. Petit et al., 2019 use a mix of strain– and stress–based nucleation model. The threshold is a function of strain while the nucleation rate is a function of the stress states.

The 2xxx and 6xxx aluminum alloys also contain submicron particles which are also called dispersoids (e. g. CrMn particles, diameter ~ 500 nm and volume fraction between $0.5 - 1$% in the 6061 alloy) [Asserin-Lebert et al., 2005; Hahn et al., 1975; Haynes et al., 1998]. Under plastic strain, the latter lead to a secondary void nucleation which is observed on fracture surfaces in the work of Asserin-Lebert et al., 2005, Ueda et al., 2014 and Tancogne-Dejean et al., 2021. The small size of dispersoid

particles raises a serious issue when it comes to the experimental characterization of the secondary void nucleation. At the moment, no *insitu* experimental evidence in the literature allow to calibrate void nucleation and growth mechanisms on dispersoid particles. Furthermore, the coalescence of primary voids is accelerated by secondary voids in the inter–void ligament (void coalescence by void sheeting). Experimental evidence of primary voids linked via thin shear bands is illustrated in a previous study [Petit et al., 2019].

Due to the lack of experimental data, the modeling of void coalescence by void sheeting is a challenging problem. On one hand, Bandstra et al., 2001, Faleskog et al., 1997 and Tvergaard, 1998 incorporate secondary voids in a cell model to investigate the effect of a second population of voids on the overall ductility in the cell model. On the other hand, Brocks et al., 1995 and Fabrègue et al., 2008 use a unit cell with a Gurson behavior in the matrix to represent the secondary voids. Either way, it is shown that the secondary void population has a significant effect on the onset of coalescence and the overall cell ductility. The only attempt to incorporate explicitly a second population of voids in the GTN equations is explained in the work of Perrin et al., 2000 and Enakoutsa, 2013. The drawback of the proposed model is that it accounts for secondary voids only in the growth phase (i. e. no void nucleation nor coalescence over secondary voids, no interaction between primary and secondary voids). That being said, the effect of secondary voids on void growth and coalescence can be taken into account in the GTN model via two approaches that are presented in the literature. The advantages and drawbacks of each approach are discussed below.

The first approach is based on adjusting the critical GTN porosity (onset of coalescence) to account for void coalescence through void sheeting as explained in the work of Gao et al., 2006. Even though this approach is attractive for its simplicity, it neglects the relation between growth of secondary voids and the stress triaxiality. The second approach is based on introducing a secondary nucleation model as explained in the work of Morgeneyer et al., 2009 and Ueda et al., 2014. The latter analyze void growth in a 2139 aluminum alloy. They compare void growth predicted by the GTN model with the void growth measured via X-ray tomography techniques. They represent the secondary population of voids by a void nucleation model which is calibrated on macroscopic results. As a result, they observe a calculated void growth that is 4 times higher than the measured values. Conclusions are made that the approach of indirectly integrating coalescence through void sheeting via the secondary nucleation model leads to overestimating the onset of coalescence as no interaction takes place between primary and secondary voids. In reality, coalescence by void sheeting can interrupt the growth of primary voids even at high stress triaxiality. To illustrate this point, Shen et al., 2013 measure a 1% average void critical volume fraction at coalescence using X-ray tomography techniques. This value is much less than the critical porosity at coalescence of 4% and 4.5% used in the GTN model in the work of Petit et al., 2019 and Ueda et al., 2014.

At this stage, two main issues are raised. These two issues underline the objectives of this paper. The first issue is regarding the void coalescence through void sheeting in aluminum alloys that is still not properly simulated in the literature. The second issue is regarding the fact that no attempts are made in the literature to use the same GTN parameters to model low, medium and high stress triaxialities. Table 5.1 inventories the work of authors that model void nucleation, growth and coalescence in 6xxx aluminum alloys. It is clear that none of the cited authors simulate low, medium and high stress triaxialities. The most common range of stress triaxiality is between 0.33 and 1.5. This range is covered by simple and notched tensile samples as shown in the work of Huber et al., 2005; Lassance et al., 2007; Nguyen et al., 2018; Shen et al., 2013; Shokeir et al., 2022b. Fewer authors model fracture under high stress triaxiality [Gilioli et al., 2014; Petit et al., 2019; Tu et al., 2019]. The GTN parameter optimization process is less challenging when carried out over tensile samples. This is due to the absence of stable crack propagation in tensile samples. On the contrary, simulating stable crack propagation (e. g. in CT samples) requires a rigorous parameter calibration. In addition, calibrating parameters for both tensile and CT samples (i. e. low to high stress triaixality) is highly challenging. This explain why it is not yet done in the literature as shown in table 5.1.

Therefore, the first objective of this paper is to simulate coalescence through void sheeting. The second objective is to calibrate a GTN model that can predict ductile failure over a wide range of stress triaxiality ($0.33 < T < 3$). This paper is divided into three sections after this literature review section. Section 5.2, "Experimental study", is divided into three parts: microstructure of the studied material, tensile and fracture toughness testing and failure micromechanisms. The first part gives an overview of the microstructure of the studied 6061-T6 aluminum alloy. In the second part, *exsitu* tensile and fracture toughness tests are carried out to analyze the effect of stress triaxiality on fracture. In addition, *insitu* tensile testing is carried out to investigate void nucleation. In the third part, the micro-damage mechanisms (void nucleation and coalescence by void sheeting) are presented via experimental evidence. Section 5.3, "GTN model calibration", is divided into two parts: presentation of the GTN model and identification of the GTN parameters The first part presents the different components of the used GTN model (e. g. void nucleation and void coalescence through void sheeting laws). The second part illustrates the experimental and numerical methods used to calibrate the GTN parameters. Section 5.4, "Modeling damage under a wide range of stress triaxiality", is dedicated to the application of the GTN model over a wide range of stress triaxiality by modeling the samples tested in section 5.2. The aim of this section is to test if the calibrated GTN model can predict damage under low, medium and high stress triaxialities.

Table 5.1: Authors that model void nucleation, growth and coalescence in 6xxx alloys

Author(s)	Al alloy	Damage model	Modeled samples	Stress triaxiality
Shokeir et al., 2022b	6061-T6	GTN	Simple and notched axisymmetric tensile	$0.33 < T < 1.5$
He et al., 2021	6061	Gurson extension for shear	Flat simple, notched and shear tensile	$0 < T < 0.33$
Petit et al., 2019	6061	GTN	Compact-tension (CT)	$T \simeq 3$
Tu et al., 2019; Tu et al., 2016	6061-T651	Rousselier, 2001	Flat simple tension and Compact-tension (CT)	$T \simeq 0.33$ and $T > 2$
Nguyen et al., 2018	6061-T6	Gurson extension for shear	Flat simple, notched and shear tensile + Axisymmetric notched tensile	$0.33 < T < 1.3$
Safdarian, 2018	6061-T6	GTN	Flat punch test samples	-
Farahani et al., 2017	6061-T6	GTN	Bi-failure sample Driemeier et al., 2015	$-0.3 < T < 0.7$
Hannard et al., 2016	6061	Rice et al., 1969	Cellular automaton	-
Zhu et al., 2018	6061-T6	Mixed proposed model: Rice et al., 1969 and Modified Mohr-Coulomb model Bai et al., 2010	Cylindrical rods	$0.07 < T < 0.52$
Gilioli et al., 2014	6061-T6	Bao et al., 2004a	Compact-tension	$T > 2$

Author(s)	Al alloy	Damage model	Modeled samples	Stress triaxiality
Yu et al., 2014	6061	Gurson extension for shear	Flat tensile	$T \simeq 0.33$
Shen et al., 2013	6061	GTN	Compact-tension (CT)	$0.6 < T < 1.4$
Gilioli et al., 2010	6061-T6	Bao et al., 2004a	Simple and notched axisymmetric tensile	$T \simeq 0.33$ and $T < 1.5$
Simar et al., 2010	6005	Gurson extension Gologanu et al., 1997	Simple tensile bars	$T \simeq 0.33$
Lassance et al., 2007	6060	Gurson extension Gologanu et al., 1997	Simple and notched axisymmetric tensile	$0.33 < T < 0.9$
Huber et al., 2005	Al-Si11-Mg0.3	Gurson extension Gologanu et al., 1997	Axisymmetric notched tensile	$0.33 < T < 1.2$
Frodal et al., 2022	6063 and 6110	Crystal plasticity damage model (inspired by GTN, see Frodal et al., 2021)	Simple tensile bars	$T \simeq 0.33$

5.2 EXPERIMENTAL STUDY

5.2.1 *Microstructure - aluminum alloy 6061-T6*

The chemical composition by %wt. of the studied 6061-T6 aluminum alloy is shown in table 5.2. The alloy is fabricated by backward extrusion to obtain a 1400 mm tall and 20 mm thick cylindrical vessel.

Table 5.2: Studied 6061-T6 aluminum alloy chemical composition by %wt.

Mg	Si	Fe	Cu	Cr	Mn	Zn	Ti	Al
0.58	1.00	0.16	0.28	0.19	0.06	0.03	0.02	bal.

During solidification, two types of large intergranular particles are formed: Mg_2Si and Al(FeMn)Si [Totten et al., 2018]. Figure 5.1 (a) displays the microstructure of the studied 6061-T6 aluminum alloy observed in a Scanning Electron Microscope (SEM) using a BackScattered Electron (BSE) detector. Mg_2Si are found as black particles that usually have a spherical form and a diameter between 1 and 5 μm as shown in fig. 5.1 (a). Initial pores also exist in the material. Initial pores have the same size and shape as spherical Mg_2Si particles. However, intial pores appear darker in color than Mg_2Si particles [Petit et al., 2019; Shen, 2012]. Figure 5.1 (a) also shows Al(FeMn)Si particles that are rather found as clusters elongated along the grain boundaries. Figure 5.1 (b) displays the grains revealed by an anodic oxidation etching and observed under an optical microscope. It is clear that the secondary phases are found between grain boundaries.

Figure 5.1 (c) displays a single CrMn dispersoid particle. Dispersoid particles are beneficial for the 6xxx aluminum alloys during the thermomechanical processing. They control recrystallization and grain growth [Totten et al., 2018]. However, their precipitation must be controlled to obtain finely distributed particles (< 0.3 μm) that are mainly composed of Cr and Mn. The maximum solubility of Cr and Mn in solid solution is 0.35 and 0.6% respectively [Massalski et al., 1986]. This means that the amount of Cr and Mn that can be retained in solid solution is limited (0.19 and 0.06 wt. % of Cr and Mn respectively according to table 4.1). Therefore, the maximum volume fraction of dispersoids that can be precipitated in aluminum is small ($< 1\%$) [Totten et al., 2018]. This explains why the disperoids do not contribute to the material strengthening [Fabrègue et al., 2008; Totten et al., 2018].

The grain and subgrain structure is revealed in the Electron BackScatter Diffraction (EBSD) map shown in fig. 5.1 (d). Grains are outlined with black boundaries assuming a 15° mismatch angle between grains. The grain size is highly heterogeneous (varies between 100 and 200 μm, see fig. 5.1 (d)). As mentioned above, the fabricated alloy undergoes a backward extrusion process to obtain the desired shape. This results

in equiaxed grains that are slightly elongated in the extrusion direction as shown in fig. 5.1 (d). All microstructures observed in fig. 5.1 are viewed in the same plane which is parallel to the extrusion direction. It is confirmed in previous work [Shokeir et al., 2022b] that the studied 6061-T6 alloy does not undergo plastic anisotropy.

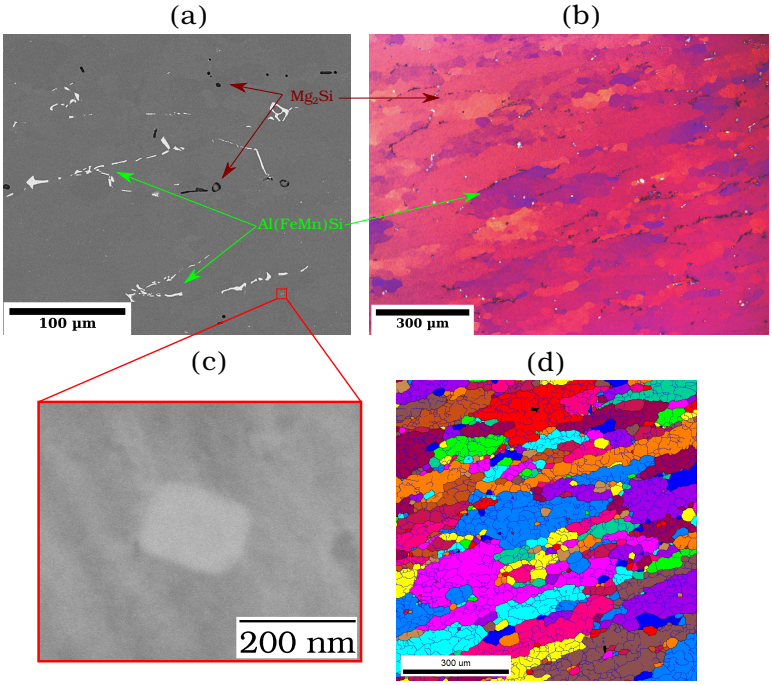

Figure 5.1: (a) SEM (back-scattered electrons) image of the microstructure of the studied 6061-T6 aluminum alloy, (b) revealed grains and inter-granular particles after anodic oxidation, (c) SEM (back-scattered electrons) image of a CrMn disperoid particle, (d) grain and subgrain structure shown in an electron backscatter diffraction map, grains are outlined with black boundaries assuming a 15° tolerance angle.

The surface fraction of Al(FeMn)Si and Mg_2Si are measured on polished cross sections and plotted against the length of the studied elementary cube in fig. 5.2 (a). An average surface fraction of 0.52% and 0.44% are found for Al(FeMn)Si and (Mg_2Si + initial pores) respectively. Initial pores are counted with Mg_2Si particles and hereby noted Mg_2Si for simplicity. As mentioned in section 5.1, Mg_2Si particles break at an early stage and can be considered as initial porosity in the material. Due to the low surface fraction of both Al(FeMn)Si and Mg_2Si particles, the distribution of particles is heterogeneous as they tend to form clusters. As a result, the size of a representative elementary volume (REV) is significantly large. Figure 5.2 (a) also shows the standard deviation (SD) related to the measured particle surface fraction. The SD decreases as the length of the square studied surface area increases. For instance, the SD drops below 0.08% for a length of 2 mm. In this study, SD $<$ 0.08% is assumed to be tolerable and therefore, a reasonable REV should have a minimum cube length of 2 mm. However, damage characterization requires high magnifications to analyze void nucleation and growth over particles that vary from 2 to 10 μm. As

a result, it impossible to maintain the representative elementary volume (i. e. cube length of 2 mm) and study damage over micron-sized particles. Attention must be drawn to the fact that damage analysis will be carried out over regions of interest with a smaller size than the REV.

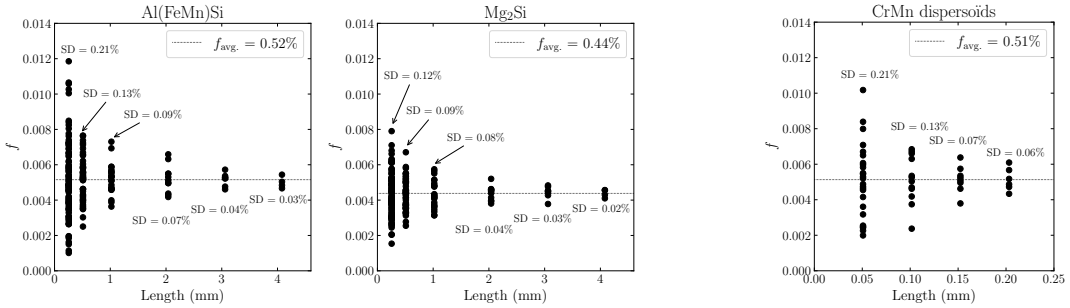

(a) Al(FeMn)Si and Mg_2Si surface fraction (b) CrMn dispersoids surface fraction

Figure 5.2: (a) surface fraction of Al(FeMn)Si and Mg_2Si particles measured on polished cross sections, (b) surface fraction of CrMn dispersoid particles measured on polished cross sections. The standard deviation (SD) decreases as the length of the analyzed surface area increases.

Figure 5.2 (b) shows a plot of the measured surface fraction of CrMn dispersoids on polished cross sections versus the length. As explained above for larger particles, a standard deviation below 0.08% is found for an analyzed area with a length of 0.15 mm. It is harder to count CrMn dispersoids than Al(FeMn)Si and Mg_2Si particles due to their smaller size. High magnifications are required to observe CrMn dispersoids.

5.2.2 *Tensile and fracture toughness testing*

Tensile tests are carried out on round bar tensile (ST) and notched tensile (NT) axisymmetric specimens. A sketch of a NT sample is shown in fig. 5.3 (a). For a fixed minimum cross-section diameter (Φ_0), varying the initial notch curvature radius (R) increases the stress triaxiality level [Hancock et al., 1976]. The NT10, NT4 and NT2 have an initial R of 4, 1.6 and 0.8 mm respectively and an initial minimum cross-section diameter $\Phi_0 = 4$ mm. Given the initial R and Φ_0, each NT sample gets its name as follows: $\text{NT}_x = 10\, R\, /\, \Phi_0$, where x is the sample's name. Small 'v' notches are machined in the NT specimens beyond the notch area to easily attach an axial extensometer during the test (gauge length $L_0 = 10$ mm for all NT samples as shown in fig. 5.3 (b)). The 'v' notches prevent the extensometer knives from sliding. Smooth tensile bars are machined following the ASTM–E8 standard. The reduced section in the ST sample is 20 mm long, the initial minimum cross-section diameter $\Phi_0 = 4$ mm and the extensometer gauge length $L_0 = 17.8$ mm.

All tensile tests are carried out using a strain rate of about $5 \times 10^{-4}\ s^{-1}$. The Edge Tracing (ET) method is used to take images of the sample during the experiment and calculate the radial deformation. The ET method is detailed in previous work [Shokeir et al., 2022b].

Nominal stress—radial deformation curves of ST and NT samples are plotted in fig. 5.3 (b). The interesting observation is that the stress drops below 20 MPa for NT10 and NT4 samples. This is achieved via the extensometer control technique explained in previous work [Shokeir et al., 2022b]. The controlled load drop is more difficult to achieve for NT2 and ST specimens. The stress triaxiality is higher in the sample's center which leads to strain localization and damage initiation in the center [Besson, 2010; Tekoğlu et al., 2015]. The strain localization in the neck area leads to a higher local strain rate. In order to avoid a local strain rate increase in the neck area, the machine displacement rate must be decreased. Otherwise, the sample might fail in an unstable manner without having a stable load drop phase (examples of unstable failure in 6061-T6 aluminum tensile tests are shown in the work of He et al., 2021; Nguyen et al., 2018).

The post–necking load drop phase is important for damage characterization. All four samples (3 NT and 1 ST) are interrupted and elastically unloaded as shown in fig. 5.3 (c). Polished cross-section of each sample are prepared to analyze the void nucleation along the sample's longitudinal axis.

Fracture toughness tests are carried out on Compact-Tension (CT) samples that are shown in fig. 5.4 (a). Four CT samples are machined to have the same dimensions except the thickness (B) that is varied to obtain a wide range of stress triaxiality (B = 12.5, 6, 3 and 1.5 mm). As the thickness increases, the stress triaxiality at mid-thickness increases. Thereby, the four tested CT samples are named after their thicknesses as follows: CT12.5, CT6, CT3 and CT1.5. A 2D sketch of all tested CT samples is shown in fig. 5.4 (a). CT samples are machined according to the ASTM E1820 standard [ASTM-1820, 2017]. The sample length $W = 25$ mm, while other dimensions are a function of the thickness (B). The net thickness $B_n = 0.8\ B$ and the side groove depth is equal to $B/10$. The side grooves shown in fig. 5.4 (a) on the crack propagation line are machined in order to facilitate a uniform crack propagation without deviation. The side grooves are machined at an angle of 45° as shown in the mechanical sketch in fig. 5.4 (a).

A pre-crack is introduced in all samples by fatigue loading on a hydraulic tensile machine. The frequency is maintained between 8 Hz and 12 Hz till the pre-crack a_0 length reaches about 15 mm ($a_0/W \simeq 0.6$). All CT samples are tested under a monotonic tension load with a cross–head speed of 0.16 mm/min. The Crack Mouth Opening Displacement (CMOD) is registered by a clip extensometer mounted on the mouth of the notch.

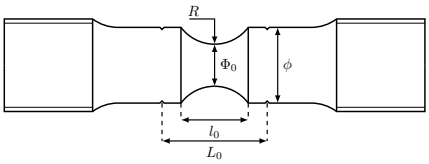

(a) Dimensions of NT specimens

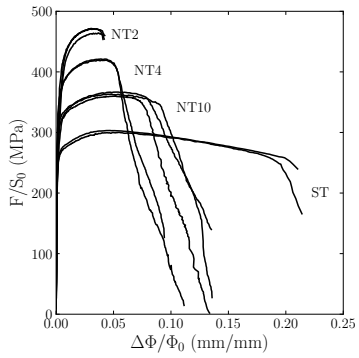

(b) Nominal stress—radial deformation

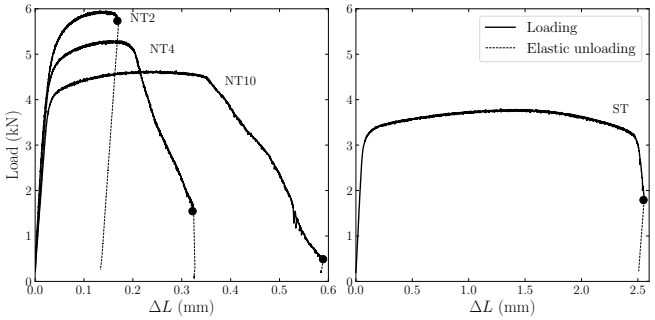

(c) Load—extensometer displacement curves of interrupted tests

Figure 5.3: (a) Dimensions of the tested NT samples, (b) stress—radial deformation of all tested ST and NT samples, (c) load—extensometer displacement curves of 4 interrupted tests. The interrupted samples are elastically unloaded to analyze void nucleation in polished cross-sections.

Figure 5.4 (b) shows the load—CMOD curves of all tested CT samples. The maximum load decreases as the sample thickness decreases. For a given CT (e. g. CT6), the difference in the maximum load is due to the different initial pre-crack length (a_0) between samples. The pre-crack length—CT length ratio (a_0/W) of the tested samples varies between 0.53 and 0.68 as noted in fig. 5.4 (b). The a_0 is estimated before testing using the compliance method and confirmed after testing using the nine measurement points along the crack front (see ASTM-1820, 2017). The confirmed a_0 value gives the slope of the elastic phase at the beginning of the test. During testing, two slopes are observed in the the elastic phase. The first slope (from 0 till $\sim$ 10% of the maximum load) is stiffer and does not correspond to the measured a_0. The second slope corresponds to the measured a_0. Therefore, the load—CMOD curves in fig. 5.4 (b) are shifted so that the second slope passes by the origin. The obtained results are essential for the main objective of this paper: develop a GTN model that can predict damage over a wide range of stress triaxiality. Therefore, the curves in fig. 5.4 (b) are to be simulated in section 5.4.

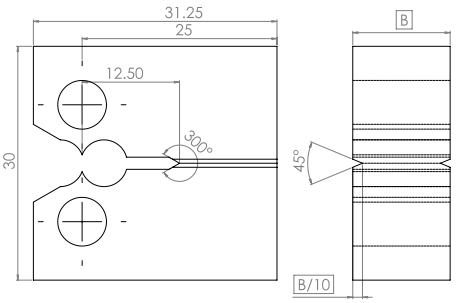

(a) Dimensions of fracture toughness Compact-Tension (CT) samples

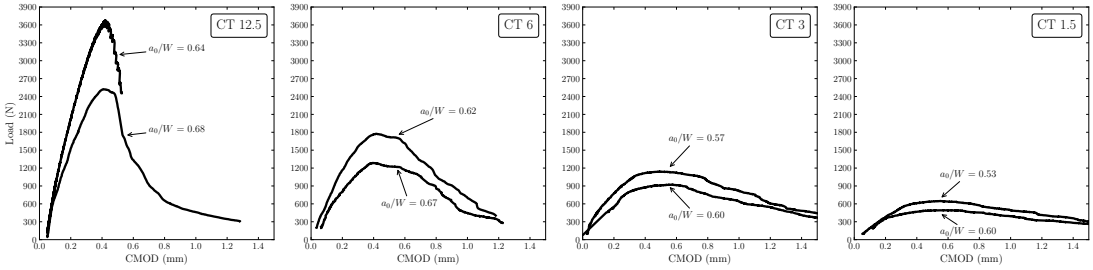

(b) Load—CMOD curves of the tested CT samples

Figure 5.4: (a) Tested CT samples. Sample thickness (B) is decreased to decrease the stress triaxiality and study its effect on damage. (b) Load—CMOD curves of the tested CT samples as well as the a_0/W of each sample ($a_0/W \rightarrow$ initial crack length/sample width).

5.2.3 *Failure micromechanisms – aluminum alloy 6061-T6*

5.2.3.1 *Observations of void nucleation*

Figure 5.5 illustrates the void nucleation mechanisms in a 6061-T6 alloy. The Mg_2Si and Al(FeMn)Si particles fracture during loading as displayed in fig. 5.5. Void nucleation at the Mg_2Si–matrix interface is referred to as nucleation by particle decohesion [Babout et al., 2004]. As mentioned earlier, Mg_2Si fail at an early stage (during the elastic phase) as it is observed in the work of Maire et al., 2005, Shen et al., 2013 and Petit et al., 2019. Therefore, the Mg_2Si can be considered as pre-existing voids when modeling damage in 6xxx alloys.

No particle decohesion is observed at the intermetallic particle–matrix interface. However, particle failure is the observed nucleation mode regarding intermetallic particles as shown in fig. 5.5. For a given alloy with its secondary phases, the factors that favor one mode of nucleation over the other are: matrix elastic–plastic properties (yield strength and hardening capacity), particle shape and orientation with respect to the loading direction [Benzerga et al., 2010]. In order to properly model the void

nucleation taking place over intermetallic particles, *insitu* tensile testing is carried out in the following section.

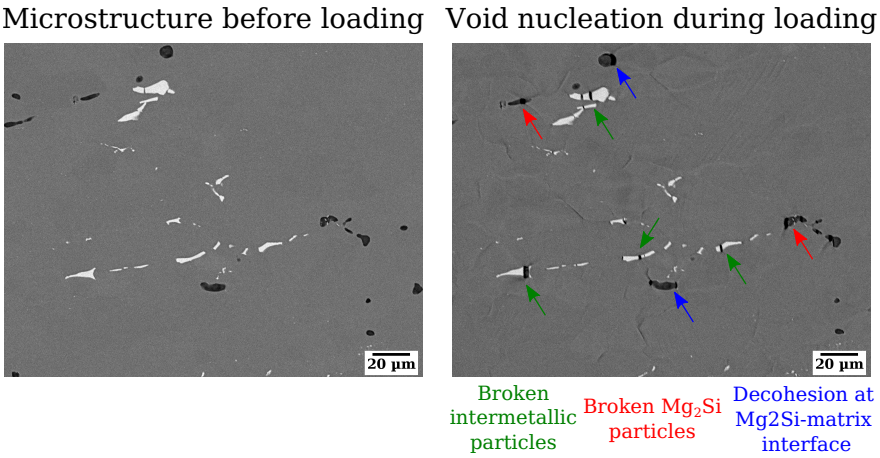

Figure 5.5: Void nucleation mechanisms observed during *insitu* tensile testing in the 6061-T6 aluminum alloy. Voids nucleate due to failure or decohesion of Mg_2Si and intermetallic particles.

5.2.3.2 *Void nucleation characterization via polished cross-sections*

Each of the interrupted tensile samples in fig. 5.3 (c) is cut along the longitudinal axis at mid-thickness then polished in order to investigate the quantity of broken Al(FeMn)Si particles (i. e. void nucleation). Polishing is carried out on 1200-grit followed by 2400-grit wet sandpaper. Further polishing is done on lapping cloths with $7-\mu$m, $3-\mu$m then $1-\mu$m diamond suspension. The final polishing step is carried out with a 0.06-μm colloidal silica suspension to obtain the required surface finish. Special care is taken regarding the applied pressure during all polishing steps. The same polishing protocol is applied to all samples analyzed in this work. The same polishing protocol is used for all polished samples in this work.

Figure 5.6 shows plots of the percentage of broken Al(FeMn)Si particles against the longitudinal distance of ST and NT samples. Each sample is scanned in a SEM and broken particles are counted to calculate a percentage of broken/total number of particles. A particle is considered broken if an obvious crack is observed as shown in fig. 5.5. In order to observe the crack(s) in broken Al(FeMn)Si particles (< 1 μm), high resolution images are required (pixel size = 155 nm). Each plot in fig. 5.6 shows the polished cross-section of the studied sample. An open crack is observed in the neck area of each sample. The crack is more open in the NT10 sample as the test is interrupted at a very low load (see fig. 5.3 (c)).

The ST graph in fig. 5.6 shows that 100% of Al(FeMn)Si particles are broken over the gauge length till a $z \simeq 10$ mm. The longitudinal axis in tensile samples presents a strain gradient. The strain is highest in the neck area ($z = 0$) and is lowest far from

the neck area. In the case of NT samples, the strain is quasi-elastic outside of the notched area. This explains why the % of broken Al(FeMn)Si particles drops to 0 at $z > 2$ mm, $z > 1$ mm and $z > 1$ mm for the NT10, NT4 and NT2 samples respectively. This analysis defines a critical z for each sample that is used to define a critical strain for void nucleation and used to calibrate GTN parameters in section 5.3.3.

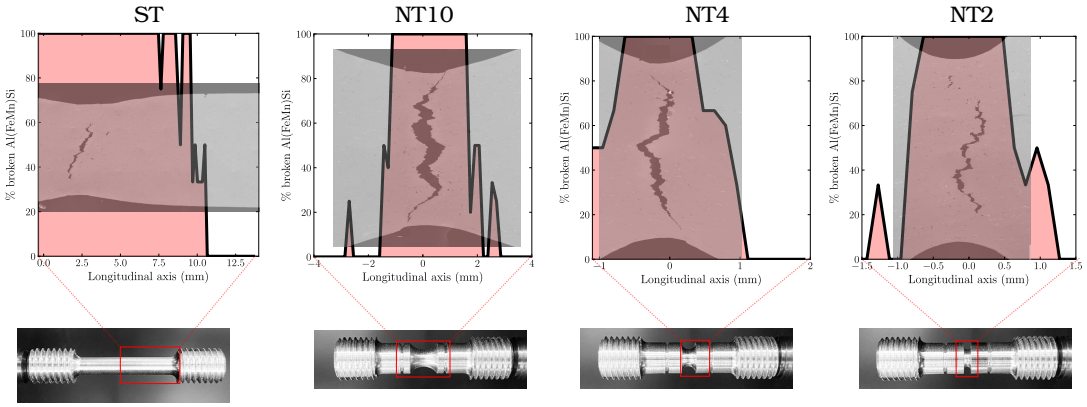

Figure 5.6: Percentage of broken Al(FeMn)Si particles along the longitudinal axis in the ST, NT10 and NT2 samples.

5.2.3.3 *Void nucleation characterization via* insitu *tensile testing*

Figure 5.7 (a) shows the dimensions of the flat notched tensile (FNT) sample. The sample is 1 mm thick before polishing. The final measured thickness after polishing is 0.94 mm. Seven regions of interest (ROI) in the notched area are chosen for this analysis. The ROI 1 (1×1 mm^2 large) shown in fig. 5.7 (a) is used to have an overall view of the notch while ROIs 2 to 7 (120×120 μm^2) are used to study void nucleation over intermetallic particles. Most of the intermetallic particle clusters are found inside ROIs 2 to 7. A very few particles are found outside ROIs 2 to 7. This confirms the fact discussed earlier: Al(FeMn)Si and Mg_2Si particles are heterogeneously distributed in the aluminum matrix and tend to form clusters.

The FNT sample is mounted on a tensile stage which is inserted and fixed in a FEI Nova NanoSEM 450 SEM. Small displacements (~ 20 μm) are applied in order to capture the whole history of the void nucleation phase. Figure 5.7 (b) shows the load—displacement curve as well as the stops during the test. At each stop, an image of each ROI is registered before passing to the next step. For each of the analyzed ROIs, the total number of Al(FeMn)Si particles is listed in table 5.3. The latter also shows the number of broken particles. A particle is considered broken when a crack is observed as shown in fig. 5.5. According to table 5.3, 65% of the studied particles are broken at the last step of the test (see last point in fig. 5.7 (b)). However, it is important to note that this analysis is carried out at the surface of the sample. An intermetallic particle (~ 10 μm long) can be broken beneath the surface and yet, no crack is observed over the polished surface. Unlike fig. 5.6 where the broken particles

are counted at mid-thickness of the samples, table 5.3 shows counted broken particles at the surface of the sample.

Figure 5.7 (b) also shows the load—plastic displacement curve obtained by a finite element simulation (without damage, elastic–plastic behavior presented in section 5.3.1). The finite element mesh is shown in section 5.5. The ROIs shown in fig. 5.7 (a) are transposed over the mesh so that each ROI is represented by a 3D hexahedral element. During the FE simulation, only the time steps that correspond to the stops during the test (see fig. 5.7 (a)) are saved. When an intermetallic particle fails, the plastic strain in the hexahedral element corresponding to the ROI is noted and used to calibrate the void nucleation parameters in section 5.3.3.

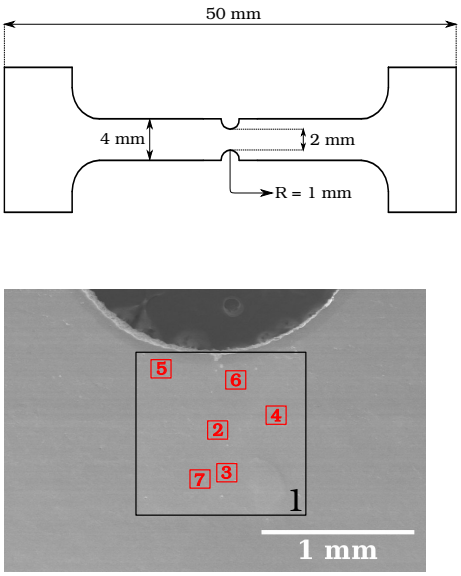

(a) Dimensions of tested FNT specimen & ROIs (from 1 to 7)

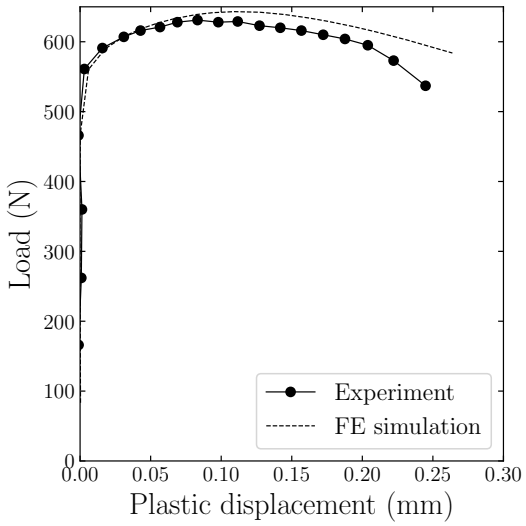

(b) Load—plastic displacement curves

Figure 5.7: (a) Dimensions of the tested flat notched tensile (FNT) and the 7 studied regions of interest (ROI). (b) Load—plastic displacement curve of the tested FNT sample and the 22 registered stops, an image of each ROI is registered before passing to the next stop, a FE simulation is carried out to calibrate the void nucleation model in section 5.3.3. Plastic displacement is obtained by removing the elastic displacement (σ/E where σ = load/cross-section area and E the Young's modulus) from the total displacement.

5.2.3.4 *Observations of void coalescence*

A schematic representation (*left*) as well as a an example of void coalescence by void sheeting in the 6061-T6 alloy (*right*) are displayed in fig. 2.5. The latter shows a thin ligament that interconnects the large voids observed on a polished cross-section of a

Table 5.3: Number of total Al(FeMn)Si particles and % of broken Al(FeMn)Si particles in the studied ROIs shown in fig. 5.7.

ROI	Al(FeMn)Si total particles	Al(FeMn)Si broken particles
2	8	3
3	6	3
4	8	5
5	4	3
6	8	7
7	9	7
Total	43	28
Total %	100%	65%

tested CT12.5 sample. The growth of primary voids is interrupted by the void sheeting mechanism [Ueda et al., 2014]. Figure 5.8 shows a zoom in the thin ligament with evidence of void nucleation on CrMn dispersoid particle. Due to the size of CrMn particles (< 300 nm), it is difficult to analyze the kinetics of void nucleation and growth taking place over dispersoids [Perrin et al., 2000]. Therefore, the only evidence of coalescence by void sheeting is found *post-mortem*. The thin ligament in fig. 5.8 is not observed in polished surface of tensile samples presented in fig. 5.6. This is due to the unstable crack propagation in tensile samples that lead to a brutal crack opening which results in complete failure.

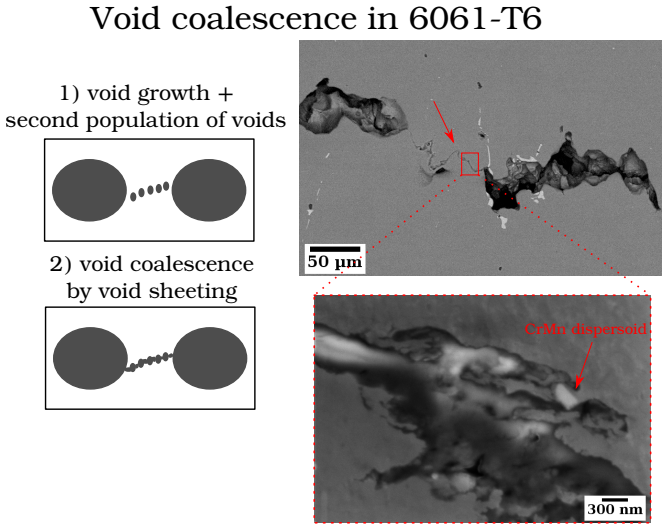

Figure 5.8: Schematic representation of void coalescence through void sheeting in the 6061-T6 aluminum alloy (*left*). An example of void coalescence by void sheeting (*right*) observed on a polished cross-section of a tested CT12.5 sample. Coalescence takes place in a shear band with a secondary population of voids.

5.2.3.5 *Fracture surfaces*

Figure 5.9 (a) reveals the fracture surface of the 6061-T6 alloy using a Secondary Electrons (SE) detector on the left and a BackScattered Electrons (BSE) detector on the right. The left and right images in fig. 5.9 (a) display the same fracture surface using the two above mentioned detectors. The BSE detector allows to differentiate intermetallic particles (white) from Mg_2Si particles (black). The right image shows fractured intermetallic and Mg_2Si particles that result in void nucleation. The secondary population of voids which nucleated on CrMn particles are also observed. The left image shows spherical dimples that indicate void growth over pre-existing or nucleated voids. A microcrack is observed in the left image which indicates coalescence of micro voids.

Figure 5.9 (b) displays the fracture surfaces of ST, NT4, CT3 and CT12.5 samples. For tensile samples (ST and NT4), the samples' center is analyzed (i. e. far from the surface). For the CT samples (CT3 and CT12.5), a mid-thickness zone in the crack propagation region is observed (i. e. far from the fatigue pre-crack and the surface). No significant differences regarding dimple size is observed when comparing the fracture surfaces in fig. 5.9 (b). However, dimples are relatively smaller in the CT3 and CT12.5 with respect to the ST and NT4 samples.

The fact that the fracture surfaces at low (ST) and high (CT12.5) stress triaxiality are similar implies that void growth is subdued in the 6061-T6 alloy. Ghahremaninezhad et al., 2013 claim minor void growth in a studied 6061-T6 (compared to steels with significant void growth [Puttick, 1959]). Authors conclude that void nucleation is followed by a short period of void growth before the material fails. Ueda et al., 2014 observe low void growth in a 2139 aluminum alloy when compared to the simulated void growth. Authors conclude that void growth is interrupted by coalescence in shear bands (void sheeting). Therefore, the established fact that the strain at failure depends on void growth (thus, on stress triaxiality) should not be taken as the key element when modeling damage in such aluminum alloys. The available micromechanics models (Mc Clintock, 1968, Rice et al., 1969, Gurson, 1977) suppose that the relationship between void growth and stress triaxiality has a first order effect on the strain at failure. However, the fracture surfaces in fig. 5.9 (b) confirm that the strain at failure depends as well on the void sheeting mechanism which is still not taken into account in the above mentioned models.

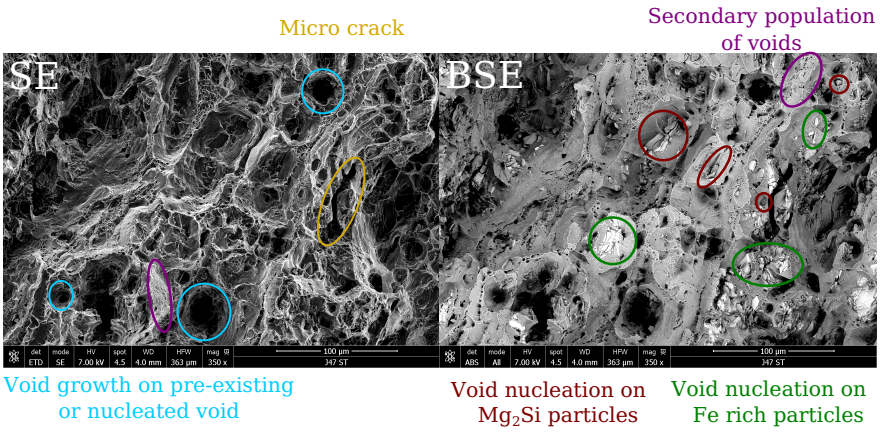

(a) Fracture surface of a tested ST sample

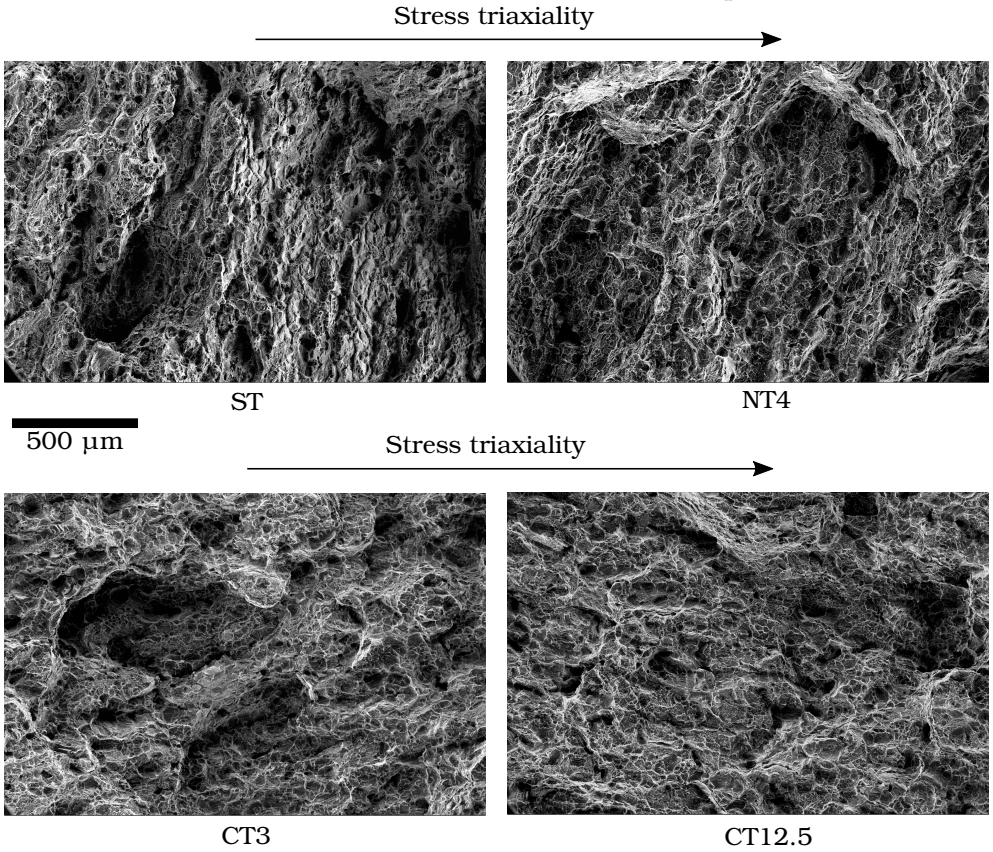

(b) Fracture surfaces of ST, NT4, CT3 and CT12.5 samples

Figure 5.9: (a) Fracture surface observed in a SEM using a Secondary Electrons (SE) detector on the left and a BackScattered Electrons (BSE) detector on the right. The left and right images reveal the same fracture surface using the two above mentioned detectors. All observed micro-damage features are commented in the figure and the above text. (b) Fracture surfaces of ST, NT4, CT3 and CT12.5 samples. Fracture surfaces are ordered in the ascending order of stress triaxiality. Dimple size do not vary as a function of stress triaxiality which indicates that void coalescence by void sheeting interrupts void growth even at high stress triaxiality.

5.3 GTN MODEL CALIBRATION

5.3.1 *Elastic–plastic behavior*

The hardening law shown in eq. (5.1) is used to model the elastic–plastic behavior of the studied alloy. The flow stress (σ_F) depends on the accumulated plastic strain (p) and material parameters ($\sigma_0, A_1, b_1, A_2, b_2$) shown in table 5.4. The material's elastic limit is given by the σ_0 parameter.

$$\sigma_F(p) = \sigma_0 + \sum_{i=1}^{2} A_i \ (1 - \exp(-b_i \ p)) \tag{5.1}$$

Parameters of the hardening model are fit over the smooth and notched tensile tests shown in fig. 5.3. Finite element simulations are carried out to assess parameters of the hardening model. The simulated results are compared with the stress—strain curves in fig. 5.3 (till the onset of sharp load drop). An objective function is minimized to find the best set of parameters shown in table 5.4. This optimization method is explain in Shokeir et al., 2022b. It assures that the plastic behavior is well modeled beyond the necking phase which is crucial when modeling damage at large strains. Section 5.5 illustrates the used FE meshes for all tensile samples.

Table 5.4: Hardening law parameters

σ_0	A_1	b_1	A_2	b_2
243 MPa	85 MPa	17.4	17.5 MPa	262

5.3.2 *GTN model*

Damage is incorporated in the GTN model via the porosity (f). The latter is expressed as the sum of increase in volume fraction due to void growth (f_g) and void nucleation (f_n) [Tvergaard et al., 1984]. The model relies on the definition of an effective stress ($\sigma_\star$) used to define the yield criterion as follows [Besson et al., 2001]:

$$S = \sigma_\star - \sigma_F(p) \tag{5.2}$$

where σ_F is the flow stress of the undamaged material shown in eq. (5.1). The plastic strain rate tensor is obtained using the normality rule as follows:

$$\underline{\dot{\varepsilon}}^{\mathrm{p}} = (1 - f)\, \dot{p}\, \frac{\partial S}{\partial \underline{\sigma}} \tag{5.3}$$

where $\underline{\sigma}$ is the Cauchy stress tensor. The plastic multiplicator $\dot{p}$ is given such that $\underline{\dot{\varepsilon}}^{\mathrm{p}} : \underline{\sigma} = (1-f)\dot{p}\sigma_{\star}$. Furthermore, $\dot{p}$ is obtained either using the consistency condition (rate independent case) or a visco–plastic flow rule (rate dependent case). The effective stress of the GTN model is implicitly defined as a function of the stress tensor and the porosity as shown below:

$$\left(\frac{\sigma_{\mathrm{eq}}}{\sigma_{\star}}\right)^2 + 2q_1 f_* \cosh\left(\frac{3}{2}q_2\frac{\sigma_m}{\sigma_{\star}}\right) - 1 - {q_1}^2 f_*^2 \equiv 0 \tag{5.4}$$

where σ_{eq} is the von Mises equivalent stress, and σ_m the mean stress. f_* is defined such that:

$$f_* = \begin{cases} f & \text{if } \Delta f_g < \Delta f_{g\ \mathrm{crit.}} \\ f + \delta\ \left(\Delta f_g - \Delta f_{g\ \mathrm{crit.}}\right) & \text{otherwise} \end{cases} \tag{5.5}$$

where the "acceleration" factor $\delta > 0$ is a material parameter. Tvergaard et al., 1984 define the onset of coalescence over the total porosity (i. e. coalescence is triggered when $f \geq f_c$, where f is the total porosity $f = f_g + f_n$ and f_c the total critical porosity). Unlike the f_* formula proposed by Tvergaard et al., 1984, in this study coalescence is triggered when the increase in void growth (Δf_g, where $\Delta f_g = f_g - f_0$ and f_0 the initial porosity) reaches the critical value $\Delta f_{g\ \mathrm{crit.}}$. The reason behind this is the theory that the primary void growth (i. e. growth of voids from broken large intermetallic particles shown in fig. 5.5) is interrupted as soon as secondary voids (nucleated over submicron particles) grow enough to create void sheets (as shown in fig. 5.8) and link primary voids [Tvergaard, 2009; Ueda et al., 2014]. In other words, while $\Delta f_g < \Delta f_{g\ \mathrm{crit.}}$, secondary voids do not interact with primary voids for three reasons: primary voids are still small in size, secondary voids still do not exist or secondary voids are still small in size to link primary voids. As soon as $\Delta f_g \geq \Delta f_{g\ \mathrm{crit.}}$, secondary voids have grown enough to interact with the primary voids and trigger void coalescence. Replacing f by Δf_g in the f_* model allows to make sure that enough primary void growth took place before coalescence is triggered via secondary voids. Otherwise, taking f as a criterion would not make sense since an increase in total porosity can be due to growth (f_g) and/or primary void nucleation (f_n). However, increase in porosity due to f_n is not sufficient to trigger void coalescence via void sheeting. Nucleated voids must grow before interacting with secondary voids.

The nucleation and growth of secondary voids cannot be determined via experimental techniques [Perrin et al., 2000]. It is supposed that the $\Delta f_{g\ \mathrm{crit.}}$ depends on the stress triaxiality ($\sigma_m/\sigma_{\mathrm{eq}}$) as follows:

$$\Delta f_{g\ \mathrm{crit.}} = \alpha\ \exp\left(-\beta\ \frac{\sigma_m}{\sigma_{\mathrm{eq}}}\right) + \gamma \tag{5.6}$$

where α, β and γ are material parameters. The f_c parameter (in the f_* model proposed by Tvergaard et al., 1984) can be calibrated via unit cell simulations as explained in the work of Morgeneyer et al., 2009. However, this calibration method leads to overestimating the critical porosity as the unit cell model is an idealized case that does not account for interaction between primary and secondary voids. Actually, Ueda et al., 2014 use the f_c parameter calibrated in the work of Morgeneyer et al., 2009 and observe an overestimated simulated void growth as discussed in section 5.1. Furthermore, Gao et al., 2006 decrease the f_c value to account for void coalescence by a second population of voids. However, the void growth and coalescence of secondary voids depend on the stress state. As a result, a constant f_c value (decreased to account for void sheeting) would only allow to model a limited range of stress triaxiality and not the wide range ($0.33 < T < 3$) as proposed in this work. Equation (5.6) is used to account for void coalescence by void sheeting and its dependence on the stress state. This is explains why the critical void growth porosity (onset of coalescence, $\Delta f_{g\ \text{crit.}}$) depends on the stress triaxiality ($\sigma_m/\sigma_{\text{eq}}$ in eq. (5.6)). Parameters in eq. (5.6) are to be calibrated in section 5.3.3 via a novel cell model. Finally, void growth is directly obtained from the plastic flow (mass conservation) as follows:

$$\dot{f}_g = (1-f)\text{tr}(\underline{\dot{\varepsilon}}^{\text{p}}) \tag{5.7}$$

Void nucleation is modeled by the Beremin model [Beremin, 1981] which defines the stress inside the particle as the sum of the stress in the matrix and an additional stress transfer arising from the deformation mismatch between the particle and the matrix. Particles are considered as brittle solids that fracture when the maximum principal stress in the particle reaches the nucleation critical stress:

$$\sigma_I^{\text{particle}} = \sigma_c \tag{5.8}$$

The maximum principal stress in the particle ($\sigma_I^{\text{particle}}$) can be expressed as proposed by Beremin, 1981:

$$\sigma_I^{\text{particle}} = \sigma_I^{\text{matrix}} + k_b\ (\sigma_{\text{eq}} - \sigma_0) \tag{5.9}$$

where σ_I^{matrix} is the maximum principal stress in the matrix, k_b is a stress concentration factor that depends on the particle shape and orientation, σ_{eq} and σ_0 are the von Mises equivalent stress and yield stress respectively. The geometrical factor k_b is equal to 1 for perfect spherical particles. However, k_b increases with increasing the particle aspect ratio (W) for a prolate particle ($W \gg 1$). $\sigma_I^{\text{particle}}$ is used to account for the stress inside the particle which is higher than the stress in the metallic matrix. Petit et al., 2019 implicitly assume that the $\sigma_I^{\text{particle}} = \sigma_I^{\text{matrix}}$ when modeling void nucleation in a 6061 aluminum alloy. Although this assumption leads to good macroscopic results, void

nucleation can be underestimated by the fact that σ_I^{matrix} is lower than the actual stress in the particle. In this work, the rate of increase in porosity due to void nucleation $\dot{f}_n$ can be expressed as a function of the plastic deformation increment:

$$\dot{f}_n = A_n \, \dot{p} \tag{5.10}$$

where A_n is expressed as a function of the particle and critical stresses:

$$A_n = \begin{cases} a_n \left(\frac{\sigma_I^{\text{particle}}}{\sigma_c} - 1 \right) & \text{if } \sigma_I^{\text{particle}} > \sigma_c \text{ and } p \geq p_n \text{ and } f_n \leq f_n^{\max} \\ 0 & \text{otherwise} \end{cases} \tag{5.11}$$

where a_n is a material parameter, p_n is the strain nucleation threshold and $f_n^{\max}$ the maximum nucleation porosity. The latter is usually taken equal to the volume fraction of particles that cause void nucleation. Since the threshold is a function of strain the nucleation rate depends on the stress in the particle in eq. (5.11), the model is a mix of strain– and stress–based nucleation (see section 5.1).

5.3.3 *GTN parameters identification*

5.3.3.1 *Void nucleation parameters*

Referring back to eq. (5.11), one can see that the material parameters are: a_n (nucleation coefficient), p_n (void nucleation strain threshold) and σ_c (void nucleation stress threshold). The maximum nucleation porosity $f_n^{\max}$ shown in eq. (5.11) is discussed later in the next section concerning void growth parameters. Firstly, to identify the void nucleation strain threshold, finite element simulations are carried out over tensile samples while using the hardening model in eq. (5.1) (without damage). The experiments previously shown in fig. 5.3 (b) are simulated till the onset of sharp load drop. Simulating the experiments till failure will lead to high values of strain in the neck area. Void nucleation takes place before the onset of sharp load drop shown in fig. 5.3 (b). Therefore, simulations are interrupted at the onset of sharp load drop for the void nucleation analysis. The critical z previously shown on polished cross-sections in fig. 5.6 indicates the maximum height after which there is no void nucleation. Therefore, the critical z can be translated to a critical plastic strain (p_n) for each sample in fig. 5.6 using the FE simulations. The estimated p_n values are 2.2%, 2.6%, 3.1% and 2.9% for ST, NT10, NT4 and NT2 samples respectively. As a result, an average critical plastic strain $p_n = 2.6\%$ is chosen for the calibrated GTN model.

Secondly, the void nucleation stress threshold (σ_c) is identified using eq. (5.9) and the ST sample. The maximum principal (σ_I) and equivalent (σ_{eq}) stresses are almost equal to the nominal stress in the ST sample before necking. Given the void nucleation

strain threshold $p_n = 2.6\%$, the nominal stress in the ST sample is identified from the stress—plastic strain curve (290 MPa). The elastic limit (σ_0) is already given in table 5.4 (243 MPa). The only unknown variable in eq. (5.9) is k_b which is taken equal to 1 as the void shape is not taken into account for the studied material that undergoes subdued void growth. Now the maximum principal stress in the particle ($\sigma_I^{\text{particle}}$) in the the ST sample can be calculated by directly substituting in eq. (5.9) as follows: $290 + (290 - 243) = 337$ MPa. Given eq. (6.6) and the previous numerical result, the critical stress $\sigma_c = 337$ MPa is chosen for the calibrated GTN model.

Finally, the nucleation coefficient (a_n) is calibrated over results from the *insitu* tensile test presented in section 5.2.3.3. Figure 5.10 shows the % of broken intermetallic particles. Each data point in fig. 5.10 represents a broken particle that is noted in table 5.3. The plastic deformation (ε_p) in fig. 5.10 is given by averaging the plastic strain in the 4 integration points close to the surface of the 3D hexahedral elements shown in fig. 5.16 (elements corresponding to studied ROIs). Afterwards, a FE simulation is performed using the nucleation law in eq. (5.11) and its identified parameters ($p_n = 2.6\%, \sigma_c = 337$ MPa, $k_b = 1, a_n = ?$). The unknown parameter a_n is calibrated by finding a good agreement between the nucleation model and experimental data points in fig. 5.10. The nucleation model is plotted by averaging the nucleation porosity on the surface of the 3D hexahedral elements shown in fig. 5.16 (elements corresponding to studied ROIs). Even though the maximum % of counted broken particles is 65%, the nucleation model saturates at 100% as shown in fig. 5.10. This is explained by the fact that the broken particles are counted at the surface during the experiment which may be misleading. An intermetallic particle is around 10 μm long which means that it can be broken beneath the polished surface and yet counted as an unbroken particle since no crack is observed at the surface. Moreover, the last images are registered before the sample failure (see last point on the curve in fig. 5.7). This means that the unbroken particles are likely to break as the sample reaches complete failure. The optimum value $a_n = 0.6$ is used to plot the nucleation model in fig. 5.10.

5.3.3.2 *Void growth parameters*

The q_1 and q_2 void growth parameters are introduced to the Gurson model by Tvergaard, 1981, 1982 to obtain better agreements between experimental and simulation data. Void growth parameters are very often taken as fixed constants $q_1 = 1.5$ and $q_2 = 1$ as recommended by Tvergaard, 1981 (e. g. [Broggiato et al., 2007; Lemaitre et al., 2005; Shen et al., 2013; Springmann et al., 2006]). Another approach is to optimize the q_1 and q_2 parameters using a unit cell model as explained in the work of Faleskog et al., 1998. However, in this study, the q-parameters are taken as functions of the

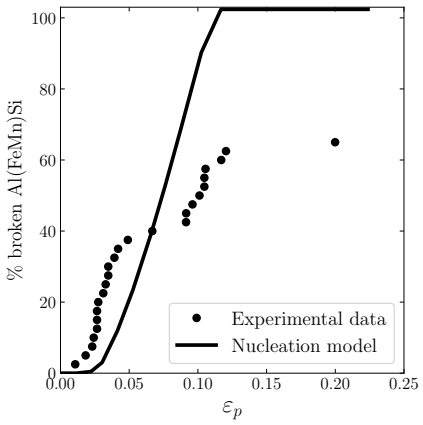

Figure 5.10: Void volume fraction of broken intermetallic particles. Percentage of broken particles is multiplied by the average surface fraction shown in fig. 5.2 to obtain the void volume fraction of broken particles in fig. 5.10 ($f_{\text{broken}} = \%_{\text{broken}} \times f_{\text{undamaged material}}$). Data points correspond to particles that are analyzed using DIC as shown in fig. 5.7 while the model is plotted using eq. (6.8) and eq. (5.11).

instantaneous hardening $N(p)$ and strengthening $\chi(p)$ levels shown in eq. (5.12) and eq. (5.13) respectively.

$$N(p) = \frac{\partial \log\left(\sigma_F(p)\right)}{\partial p} \tag{5.12}$$

$$\chi(p) = \frac{\sigma_F(p)}{E} \tag{5.13}$$

where E is the Young's modulus. The q-parameters are no longer considered as constants but as variables that are calculated at every time step and are expressed by the following "universal" formula:

$$\begin{aligned} q_1(p) &= m_1\, N(p) + b_1\, \chi(p) + q_1^* \\ q_2(p) &= m_2\, N(p) + b_2\, \chi(p) + q_2^* \end{aligned} \tag{5.14}$$

where m_i, b_i and q_i^* are coefficients that are fitted in previous work [Shokeir et al., 2022a] and presented in table 5.5.

The q-parameters given by the "universal" formula in eq. (5.14) allows to predict void growth regardless of the hardening behavior. The "universal" formula is developed to avoid fitting the q_1 and q_2 parameters over unit cell simulations every time the material hardening behavior is changed. The unit cell optimization process if costly as it requires a significant number of unit cell simulations followed by a q_1 and q_2 parameter optimization process. However, the "universal" law in eq. (5.14) makes it possible to find optimum q-values regardless of the hardening parameters and law.

	m	b	q^*
q_1	0.014	2.1	1.24
q_2	0.022	1.6	1.03

Table 5.5: Coefficients of the q-values universal q-formula (eq. (5.14)). q_1 and q_2 are expressed as a function of the instantaneous strain hardening $N(p)$ (see eq. (5.12)) and strength to Young's modulus ratio $\chi(p)$ (see eq. (5.13))

Parameters of the "universal" law in table 5.5 are optimized in previous work [Shokeir et al., 2022a] over a wide range of hardening parameters and stress triaxialities. Nonetheless, the heterogeneous particles distribution is not taken into account in the "universal" law. The latter assumes regularly distributed voids in a solid material that is represented by a 3D periodic array of unit cells with a single spherical void in the center of each cell. The particle distribution is an issue that depends on the microstructure of the studied material.

In order to emphasize the effect of particle distribution in a microstructure, finite element cell simulations are carried out over two cell models which are displayed in fig. 5.11 (a, b). A cubic cell is taken with a side length (L), a volume ($V = L^3$), a number of cavities (n_v) with radius (r) and a total void volume fraction (f) that is defined as follows:

$$f = \frac{4\pi}{3}\, n_v \left(\frac{r}{L}\right)^3 \tag{5.15}$$

The number of cavities (n_v) and initial void volume fraction (f_0) are taken as 6 and 1% respectively in the two cell models shown in fig. 5.11 (a) and (b). The cell models in fig. 5.11 (a) and (b) are hereby referred to as the "Random cell" and the "Agglomerated cell" respectively. The "Agglomerated cell" contains voids that are agglomerated in the cell's center. Therefore, it is expected that the interaction between the voids of the "Agglomerated cell" becomes significant [Koplik et al., 1988]. The meshes with 3D 10-nodes tetrahedral elements (and reduced integration to limit volume locking) are obtained by using the NETGEN software [Schöberl, 1997]. The opposite sides of the cube have identical surfaces meshes to guarantee periodicity. For both cell models, FE simulations are carried out using the hardening behavior in eq. (5.1) (used in a finite strain framework). The periodic boundary conditions and finite strain formalism are explained in the work of Cadet et al., 2021. During the meshing process of the "Random cell", each defect that intersects the side of the cube is copied on the opposite side.

During the simulations, the macroscopic stress (σ_{11}) and macroscopic strain (E_{11}) are calculated in the loading direction. The stress triaxiality is maintained constant over the cell as explained in the work of Brocks et al., 1995 and Ling et al., 2016 (see fig. 1 in the work of Han et al., 2013). To ensure that the stress triaxiality remains

constant during the simulation, the stress σ_{11} is measured in the loading direction and a portion of this stress is applied on the two other directions ($\sigma_{22} = \sigma_{33} = \eta\ \sigma_{11}$, where $\eta = (3T - 1)/(3T + 2)$ given T the stress triaxiality.

Figure 5.11 (c) shows the void growth of the "Random", "Agglomerated" cells and a single element with the GTN behavior (i. e. using the same $f_0 = 1\%$ and the "universal" formula) at two levels of stress triaxiality ($T = 1.4$ and $T = 2.4$). As expected, void growth in the "Agglomerated" cell is higher especially at medium and low stress triaxialities. The single element with the GTN behavior and the "universal" formula results in the same void growth as the "Random" cell which confirms that the "universal" formula provides calibrated q-parameters. However, at high stress triaxiality, the heterogeneous particle distribution does not have a significant impact on void growth (see stress triaxiality 2.4 in fig. 5.11 (c)). The displacement incompatibility at the void–matrix interface results in a "secondary plastic zone" around the void [Koplik et al., 1988]. When the voids are randomly distributed (e. g. "Random cell"), the secondary plastic zones do not touch. However, the smaller distance between voids in the "Agglomerated cell" leads to the interaction between "secondary plastic zone" and induce higher void growth.

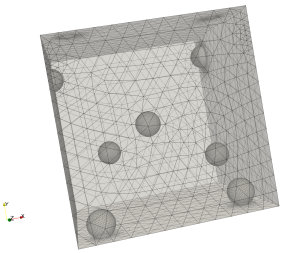

(a) **Random cell**: 6 randomly distributed voids, $f_0 = 1\%$

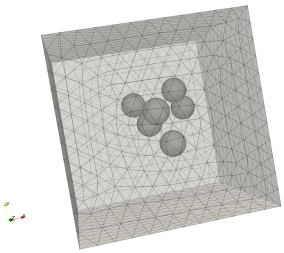

(b) **Agglomerated cell**: 6 voids agglomereated in the center, $f_0 = 1\%$

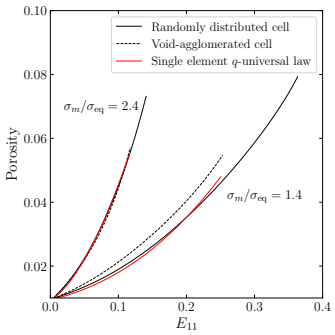

(c) Void growth in random and agglomerated cells

Figure 5.11: (a) Studied random cell, (b) studied agglomerated cell, (c) void growth in random and agglomerated cells, (d) stress—strain curves of the agglomerated ($f_0 = 1\%$) and a single FE element ($f_0 = 1$ and 1.5%)

The studied 6061-T6 aluminum alloy has a heterogeneous particle distribution and a low volume fraction of constituent particles ($< 1\%$ for each of intermetallic and Mg_2Si particles). This results in particle-rich and particle-poor zones in the microstructure. This heterogeneity is observed when the surface area fraction of particles is measured at low surface areas (< 1 mm^2) in fig. 5.2. To account for the heterogeneous particle distribution in the studied 6061-T6 alloy and its effect on void growth, each of the q-parameters is multiplied by an η factor (*i. e.* $\eta_{q1}\ q_1$ and $\eta_{q2}\ q_2$). The η_{q1} and η_{q2}

parameters are to be calibrated over macroscopic tensile and fracture toughness curves as shown in section 5.4.

5.3.3.3 *Void coalescence parameters*

The nucleation of secondary voids is usually not taken into account in the literature since it cannot be observed during experiments [Perrin et al., 2000]. Implementing a nucleation model for secondary voids raises no difficulty from a technical point of view. However, the parameters would be calibrated without sufficient evidence. Perrin et al., 2000 state that secondary voids continuously nucleate during the entire process of ductile failure. Therefore, a cell model is proposed as shown in fig. 5.12 (a) with an underlying hypothesis: secondary voids assumed to be nucleated before loading the cell.

The central void in fig. 5.12 (a) has a volume fraction of 0.44% which corresponds to a micron-sized initial void in the material. The small voids have a volume fraction of 0.51% which corresponds to the average surface fraction of CrMn dispersoids as shown in fig. 5.2. The radius of the large void is calculated using eq. (5.15) and a number of cavities $n_v = 1$. The radius of the small voids is imposed to be 6 times smaller than the radius of the large void. This radius ratio is representative of the average initial void—CrMn radius ratio in the material (i. e. ~ 2 μm versus ~ 300 nm for the initial void and CrMn respectively). Given the radius and volume fraction of smaller voids, their number $n_v = 250$ is deduced from eq. (5.15).

The mesh generation process as well as the periodic boundary conditions are as explained in section 5.3.3.2. FE simulations are performed over a range of stress triaxiality from 0.8 to 2.8. As mentioned in section 5.3.3.2, the stress triaxiality is kept constant during the simulation by applying a portion of the σ_{11} stress in the two principal directions:

$$\underline{\sigma} = \begin{bmatrix} \sigma_1 & 0 & 0 \\ 0 & \sigma_2 & 0 \\ 0 & 0 & \sigma_3 \end{bmatrix} = \sigma_{11} \begin{bmatrix} 1 & 0 & 0 \\ 0 & \eta_2 & 0 \\ 0 & 0 & \eta_3 \end{bmatrix} \tag{5.16}$$

A rotation angle can be applied to the Cauchy stress tensor ($\underline{\sigma}$) around one of the principal axes to obtain different loading conditions which are more representative of the real life cases. Cadet et al., 2022 and Barsoum et al., 2011 explain the effect of the rotation angle on the critical porosity in the cell model. They conclude that a rotation of $37 - 40^\circ$ around the second principal axis leads to the lowest critical porosity. In this study, a rotation of 37° around the second principal axis is applied.

A rotation matrix ($\boldsymbol{R}$) can be used in order to rotate the Cauchy stress tensor as follows:

$$\underline{\sigma} = \boldsymbol{R} \begin{bmatrix} 1 & 0 & 0 \\ 0 & \eta_2 & 0 \\ 0 & 0 & \eta_3 \end{bmatrix} \boldsymbol{R}^T \tag{5.17}$$

In order to emphasize the effect of the second population of voids, unit cell simulations are carried out to compare with all performed cell (with secondary voids) simulations (see fig. 5.12 (b)). The initial porosity in the unit cell is taken as the sum of large and small voids ($f_0 = 0.44 + 0.51 = 0.94\%$). Figure 5.12 (c) displays the plastic strain map at the onset of coalescence in simulations carried out a stress triaxiality = 2.6 and $\theta = 37^\circ$.

It is important to consider the stress state and its effect on the critical porosity in the cell model. The critical porosity ($\Delta f_{g\ \text{crit.}}$) is plotted as a function of the stress triaxiality in fig. 5.12 (d). The latter shows results for simulations performed with 37° rotation of the stress tensor. Three observations can be made. Firstly, the critical porosity ($\Delta f_{g\ \text{crit.}}$) decreases as a function of the stress triaxiality for both cell (with secondary voids) and unit cell models. However, the critical porosity reaches a plateau in the unit cell while it continues decreasing in the cell model with secondary voids. Secondly, the critical porosity is higher in the unit cell. In the cell model with secondary voids, the growth of the large void is affected by the surrounding smaller voids that grow in size and trigger coalescence. In the unit cell, the large void undergoes more void growth prior coalescence. Therefore, the critical porosity in a unit cell (without smaller voids) is higher as shown in fig. 5.12 (d). Lastly, the critical porosity given by the cell model with secondary voids is used to fit the parameters $\{\alpha, \beta, \gamma\}$ of eq. (6.5). To conclude, the critical porosity $\Delta f_{g\ \text{crit.}}$ given by eq. (6.5) accounts for the secondary population of voids and the effect of stress state on their growth and coalescence.

At this stage, GTN parameters are identified via experimental techniques and cell FE simulations. The stress state is taken into account during the calibration of all parameters. The aim is to apply the calibrated model over a wide range of stress triaxiality and see if the model is able to capture damage at different stress states. However, some of the above mentioned parameters $\{f_n^{\max}, \eta_{q1}, \eta_{q2}, \delta\}$ are not yet calibrated. Therefore, these parameters can be adjusted over macroscopic tensile and fracture toughness curves in the following section.

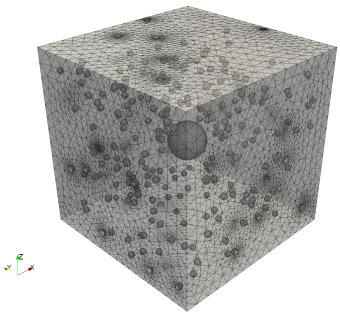

(a) Cell mesh with a large void ($f_0 = 0.44\%$) and 250 small voids ($f_0 = 0.51\%$)

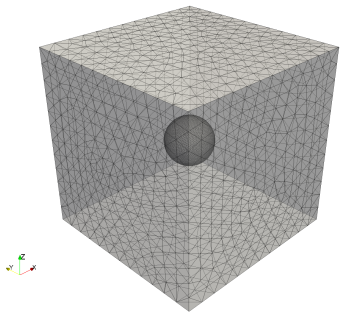

(b) Unit cell mesh with a large void ($f_0 = 0.95\%$)

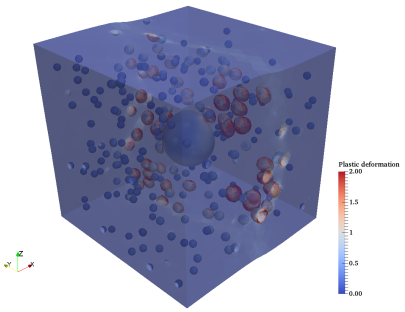

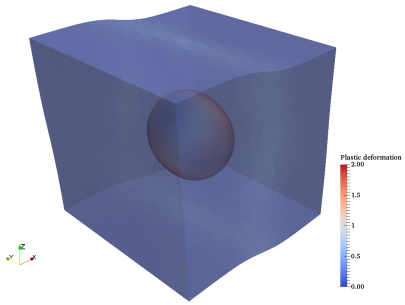

(c) Plastic deformation at onset of coalescence (stress triaxiality = 2.6)

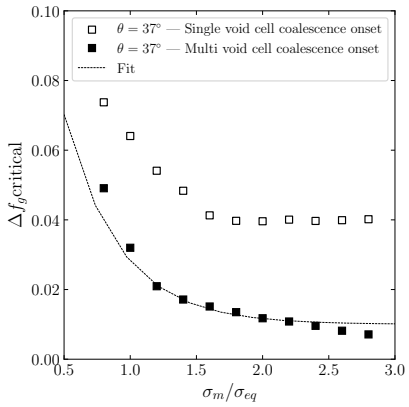

(d) Critical porosity at onset of coalescence over a range of stress triaxiality ($0.8 < T < 2.8$)

Figure 5.12: (a) Cell mesh used to study the effect of a second population of voids on the onset of coalescence. (b) unit cell mesh used to compare with (a). (c) Plastic strain at onset of coalescence. (d) Critical porosity at onset of coalescence over a range of stress triaxiality ($0.8 < T < 2.8$) for cell simulations with a 37° rotation angle of the stress tensor. The critical porosity of the cell model is used to fit the parameters $\{\alpha, \beta, \gamma\}$ in eq. (6.5).

5.4 MODELING DAMAGE UNDER A WIDE RANGE OF STRESS TRIAXIALITY

As mentioned in the previous section, the remaining parameters $\{f_n^{\max}, \eta_{q1}, \eta_{q2}, \delta\}$ are to be calibrated over the macroscopic results regarding stress—strain curves of tensile tests and load—extensometer opening of fracture toughness tests. Firstly, η_{q2} parameter which accounts for the effect of heterogeneous void distribution over void growth is taken equal 1 to simplify the optimization process. Only η_{q1} is calibrated to give good predictions of void growth. Secondly, the δ parameter is calibrated over the macroscopic results through trial and error. It is observed that the δ parameter has a dominant effect over the crack propagation in CT samples. Lastly, the $f_n^{\max}$ which is the maximum porosity of nucleated voids is calibrated in the same manner as the δ parameter. One way to identify the $f_n^{\max}$ parameter is to take it equal to the average measured surface area fractions of intermetallic particles (0.52% in fig. 5.1). However, this results in an underestimation of damage when comparing simulated and experimental tensile curves. This is explained by two reasons. The first one is the fact that the GTN model do not take into account the particle shape. The second reason is that the GTN model assumes that the mean stress drives the porosity growth (i. e. cosh(..) term in eq. (5.4)). Recalling fig. 5.5, nucleated voids result from cracking of intermetallic particles which results in prolate voids. The latter can decrease the inter-void distance and lead to a higher local damage compared to spherical voids. In addition, the growth of prolate voids is mostly driven by the axial stress which tends to open them. Therefore, $f_n^{\max}$ parameter should be greater than the measured average values and must represent the softening in tensile and fracture toughness curves presented in section 5.2.2. The $f_n^{\max}$ is taken equal to 1.2% which corresponds to the highest measurement in fig. 5.2 at a length of $\simeq 200$ μm.

Table 5.6 shows a summary of the final GTN parameters that are used to display results in fig. 5.13. All GTN parameters are calibrated via experimental evidence or cell simulations except for the $\{\eta_{q1}, \eta_{q2}, \delta\}$ that are fitted over macroscopic results in fig. 5.13. Figure 5.13 (a) shows experimental and simulated stress—strain curves of ST and NT samples while fig. 5.13 (b) shows load—extensometer opening curves of 4 CT samples. A good agreement is found between experiments and simulations over the whole range of stress triaxiality ($0.33 < T < 3$). As a reminder, the q_1 and q_2 parameters are given by the universal formula shown in eq. (5.14). Figure 5.14 shows the evolution of the q_1 and q_2 parameters in the crack propagation zone of the CT12.5 sample. As the plastic strain is higher near the crack tip, the q-parameters are higher in this area. This leads to a higher void growth in the damaged area.

Recalling table 5.1, none of the cited authors model low, intermediate and high stress triaxiality levels in 6xxx aluminum alloys using a single set of parameters. However, it is confirmed in this study that the parameters shown in table 5.6 predict damage over the whole range of stress triaxiality ($0.33 < T < 3$) as shown in fig. 5.13. Most constitutive damage models (e. g. Gurson, Rousselier, Rice and Tracey) relate damage

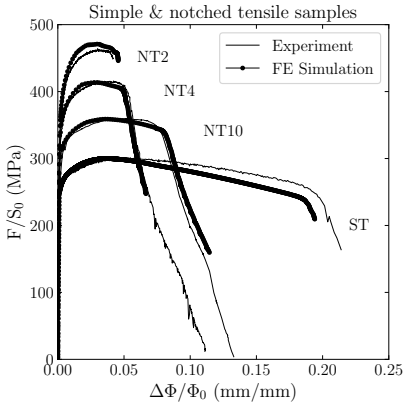

(a) FE simulation results in tensile samples

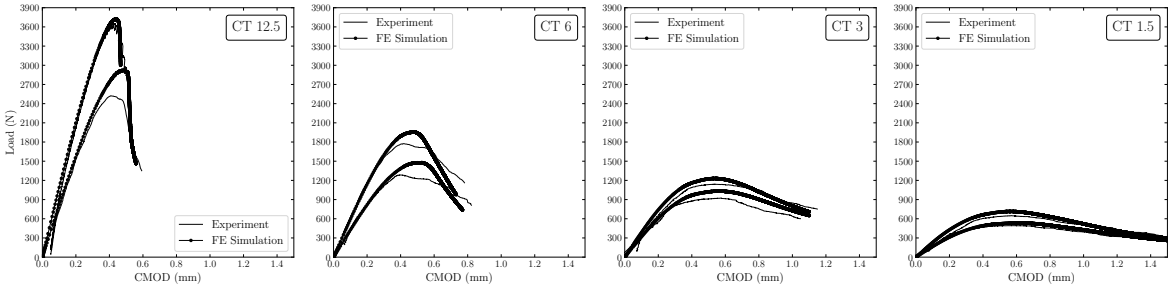

(b) FE simulation results in CT samples

Figure 5.13: FE simulation versus experimental curves for (a) simple and notched tensile tests ($0.33 < T < 2$) and (b) fracture toughness tests over CT samples ($0.7 < T < 3$). All FE simulations are performed using the same GTN parameters presented in table 5.6.

(i. e. porosity) to the hydrostatic stress. This leads to more significant damage as the hydrostatic stress increases (i. e. stress triaxiality increases). Yet, this is not sufficient to model a wide range of stress triaxiality in alloys that undergo void nucleation and coalescence by void sheeting. Therefore, there are two important factors considered in this study which allow to model a wide range of stress triaxiality.

Firstly, the mixed strain- and stress-based nucleation model used in this study (see (5.11)) relates the nucleation rate (A_n) to the maximum principal stress. The latter increases as the stress triaxiality increases. Therefore, this leads to an accelerated void nucleation rate at high stress triaxiality. On the contrary, purely strain-based nucleation models (e. g. Chu and Needleman model [Chu et al., 1980]) relate the nucleation rate to strain. As a result, void nucleation is underestimated in samples that undergo minor strain before failure but have a high stress triaxiality level (e. g. NT2 sample). This issue is demonstrated in previous work [Petit et al., 2019]. Another comparison between stress-based and strain-based nucleation models is carried out in the work of Butcher et al., 2011. In order to verify that nucleation model used

Table 5.6: Calibrated GTN parameters

Pre-existing voids and void nucleation					**Void growth**		**Void coalescence**				**Mesh size**
f_0	Void nucleation law				η_{q1}	η_{q2}	α	β	γ	δ	h
	$f_n^{\max}$	a_n	p_n	σ^{critical}							
%	%	-	%	MPa	-	-	-	-	-	-	μm
0.44	1.2	0.6	2.6	337	1.8	1.0	0.2	2.4	0.01	1.5	100

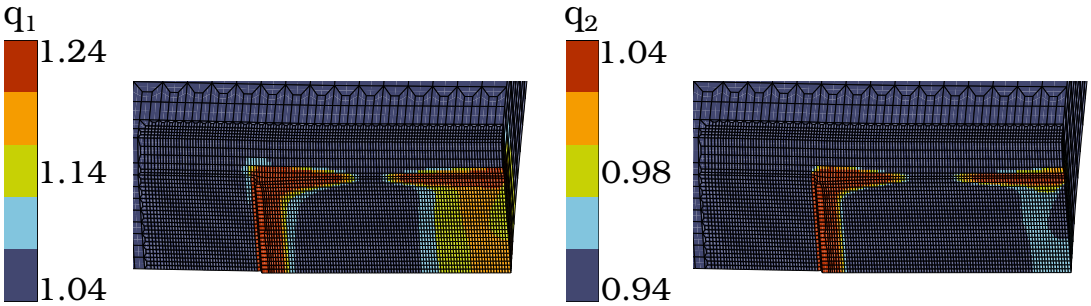

Figure 5.14: q_1 and q_2 parameters in the crack propagation zone of the CT12.5 sample. q_1 and q_2 parameters are estimated by the universal formula shown in eq. (5.14).

in this study leads to accurate results, the void nucleation maps of simulated ST and NT samples are compared with results obtained in fig. 5.6. Figure 5.15 shows the void nucleation maps of the simulated ST and NT samples. Arrows indicate the critical z identified in polished cross-sections shown in fig. 5.6. The critical z is the longitudinal distance after which no void nucleation is observed. One can conclude that the nucleation model used in this study gives fair predictions of void nucleation.

Secondly, the modified f_* formula (see eq. (5.5)) relates the onset of void coalescence to stress triaxiality. The phenomenological explanation behind the dependency of the onset of void coalescence on stress triaxiality is illustrated via the cell model in section 5.3.3.3. From an experimental point of view, this is explained by the fact that void growth is interrupted by the secondary population of voids. Secondary voids nucleate over submicron particles and grow at a higher rate when the stress triaxiality is high [Ueda et al., 2014]. Therefore, void coalescence is triggered at lower growth porosity levels (f_g) when the stress triaxiality is high.

To sum up, the presented parameters calibration method in this work can be adapted to other aluminum alloys that undergo failure by void nucleation, growth and coalescence through void sheeting.

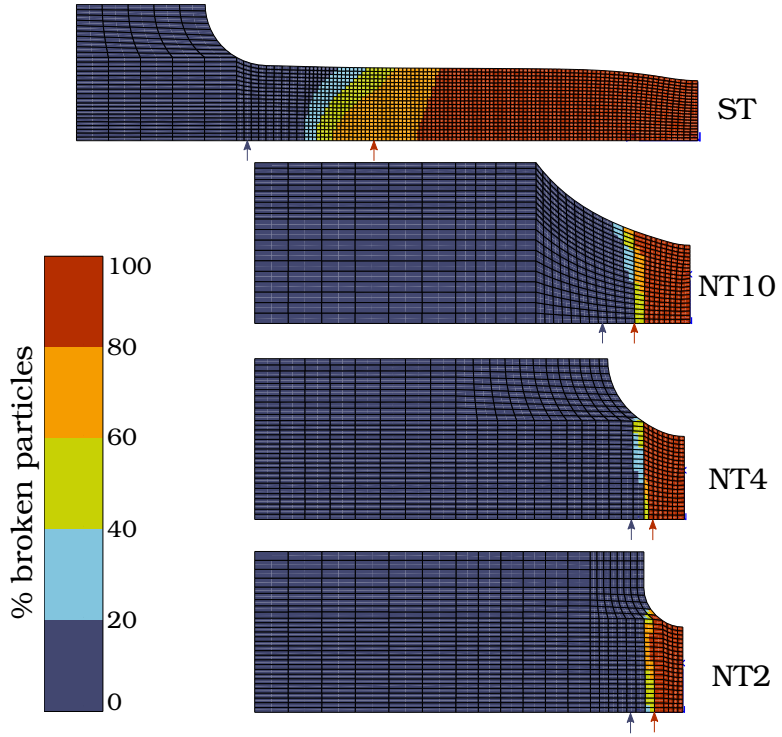

Figure 5.15: Nucleation porosity maps in simulated ST and NT samples. Blue arrows indicate the critical z identified in polished cross-sections shown in fig. 5.6. There is no void nucleation observed in tested samples beyond the critical z. Red arrows indicate the z at which void nucleation drops below 100% in fig. 5.6.

5.5 CONCLUSION

To conclude, there are some research gaps in the literature regarding two problems. The first problem is the modeling of void coalescence by void sheeting in alloys with secondary population of voids. The second problem is the the calibration of GTN parameters to model low, medium and high stress triaxility (see table 5.1).

This work proposes solutions to the two above mentioned problems. Firstly, a novel cell model is developed with two populations of voids. A large central void is surrounded by a realistic amount and size of secondary voids to study the interaction between the two void populations under a wide range of stress triaxiality ($0.8 < T < 2.8$). The growth of the primary void is interrupted as the secondary voids grow in the inter–void ligament and trigger coalescence. A critical porosity that accounts for the interaction between primary and secondary voids as well as the stress state is estimated in the cell model. This critical porosity decreases as the stress triaxiality increases. As a result, an exponential function is used to relate the stress triaxility to the GTN critical porosity based on void coalescence via secondary voids.

Secondly, a detailed GTN parameter calibration section is presented to illustrate the parameter identification process over a wide range of stress triaxiality. Void nucleation parameters are calibrated via *insitu* SEM tensile testing. Void growth q_1

and q_2 parameters are not taken as constants. A universal q-parameter formula is used to estimate the local q_1 and q_2 parameters in each finite element based on the instantaneous hardening level. The q-parameter universal formula can be applied to other materials in future work without need of further calibration. Finally, the calibrated GTN model is used to simulate simple tensile ($T \simeq 0.33$), notched tensile ($0.5 < T < 2$) and CT ($0.7 < T < 3$) samples. A good agreement is found between experimental and simulated data which confirms that the GTN model can capture void growth at low, medium and high stress triaxiality if the parameters are properly identified. The GTN calibration methodology presented in this work can be applied to other materials in future work.

APPENDIX

Flat tensile mesh

Figure 5.16 shows the 3D mesh of the FNT sample as well as the boundary conditions applied on the sample to perform displacement controlled simulations. Only one-fourth of the sample is meshed thanks to the symmetries. 8-node 3D hexahedral elements with 8 integration points are used to mesh the sample. The mesh size is fixed to $100 \times 100 \times 9.4$ μm^3. The element thickness (9.4 μm) is reduced to obtain a fine discretization near the surface. This allows to achieve strain values on the mesh surface that can be compared with *insitu* test in section 5.2.3.3. The ROIs shown in fig. B.1 are transposed over the mesh as shown in fig. 5.16.

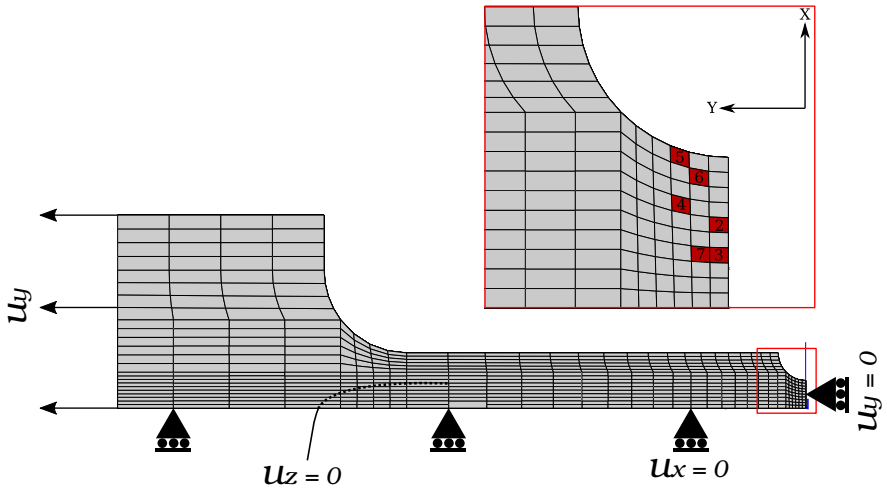

Figure 5.16: 3D mesh of the tested FNT sample in section 5.2.3.3. The ROIs shown in fig. B.1 are transposed over the mesh as shown.

Simple tensile and notched tensile meshes

Figure 5.17 shows the 2D axisymmetric meshes of ST and NT samples as well as the boundary conditions on a NT10 sample. Only one-fourth of each sample is meshed thanks to the symmetries. A 2D axisymmetric mesh is well adapted to these samples as the material undergoes isotropic plasticity. 8-node 3D hexahedral elements with 4 integration points (reduced integration) are used to mesh the sample. The mesh size is fixed to $100 \times 100\ \mu m^2$. All tensile simulations are displacement controlled. Boundary conditions are similar to the FNT sample shown above.

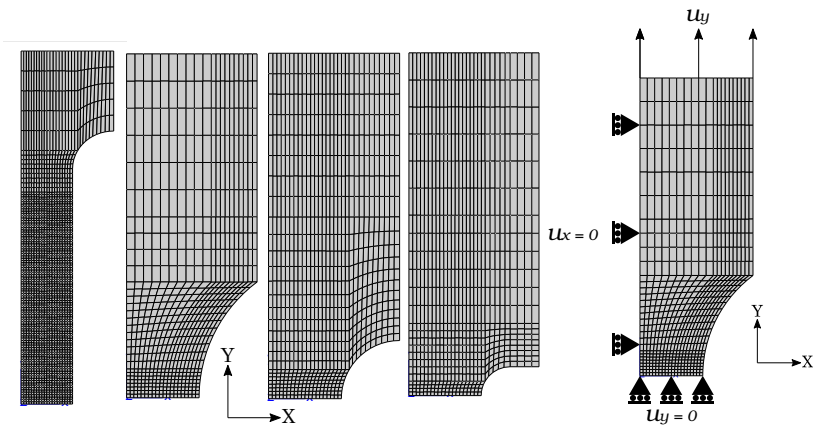

Figure 5.17: 2D axisymmetric meshes of ST and NT samples with the dimensions shown in fig. 5.3

Compact-tensions meshes

Figure 5.18 shows 4 CT meshes with different thicknesses. Figure 5.19 shows the boundary conditions applied on the studied CT samples. Only one-fourth of the CT sample is meshed thanks to the symmetries. To assure one of the symmetries, u_z is constrained for elements on the $u_z = 0$ plane (see fig. 5.19). 8-node 3D hexahedral elements with 8 integration points are used to mesh the sample. The mesh size is fixed to $100 \times 100 \times 100\ \mu m^3$. The used GTN model leads to material softening which results in strain and damage localization within one row of elements. As a result, the simulation results strongly depend on the mesh size. To overcome this issue, models integrating material internal lengths can be used (e. g. [Feld-Payet et al., 2011], [Mediavilla et al., 2006]). However, these models are still in an early development phase. The pragmatic solution chosen in this study is to fix a mesh size along the crack path [Liu et al., 1994; Rousselier, 1987]. The fixed mesh size controls the fracture energy in the case of mesh dependent simulations [Siegmund et al., 2000].

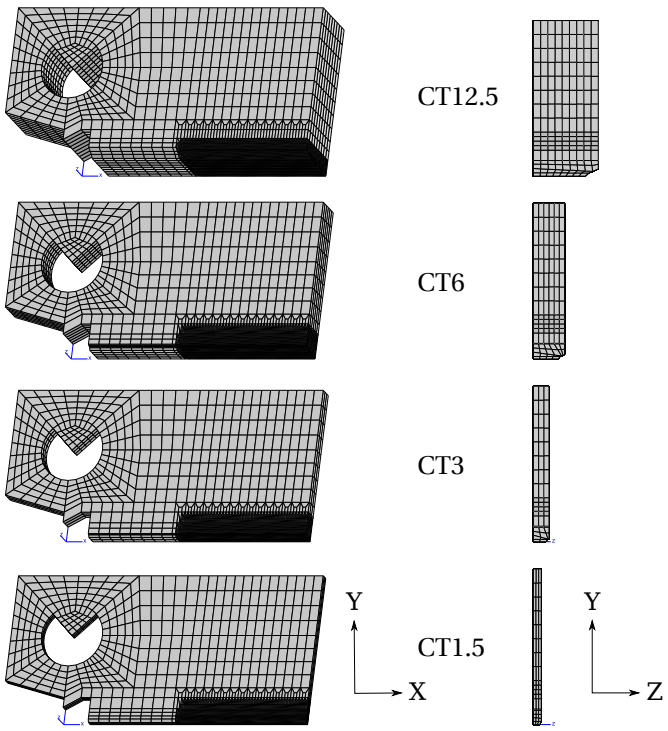

Figure 5.18: 3D meshes of the CT samples with the dimensions shown in fig. 5.3

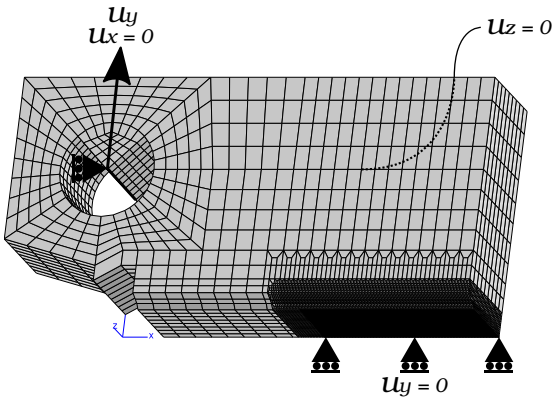

Figure 5.19: Boundary conditions applied to the CT samples used to simulate crack propagation

BIBLIOGRAPHY

ASTM-1820 (2017). *Standard Test Method for Measurement of Fracture Toughness*. Technical report. DOI: 10.1520/E1820-17 (see pp. 128, 129).

Asserin-Lebert, A. et al. (2005). 'Fracture of 6056 aluminum sheet materials: Effect of specimen thickness and hardening behavior on strain localization and toughness.' In: *Mater. Sci. Engng A* 395, pages 186–194 (see p. 120).

Babout, L. et al. (2004). 'Damage initiation in model metallic materials: X-ray tomography and modelling.' In: *Acta Mater.* 52.8, 2475–2487 (see p. 130).

Bai, Y. and T. Wierzbicki (2010). 'Application of extended Mohr-Coulomb criterion to ductile fracture.' In: *Int. J. Frac.* 161.1, 1–20 (see p. 123).

Bandstra, J. P. and D. A. Koss (2001). 'Modeling the ductile fracture process of void coalescence by void-sheet formation.' In: *Mater. Sci. Engng A* 319–321, pages 490–495 (see p. 121).

Bao, Y. and T. Wierzbicki (2004a). 'A comparative study on various ductile crack formation criteria.' In: *J. Engng Mater. Technol.* 126, pages 314–324 (see pp. 123, 124).

Bao, Y. and T. Wierzbicki (2004b). 'On fracture locus in the equivalent strain and stress triaxiality space.' In: *Int. J. Mech. Sci.* 46.1, pages 81–98 (see p. 119).

Barsoum, I. and J. Faleskog (2007). 'Rupture mechanisms in combined tension and shear — Experiments.' In: *Int. J. Solids Structures* 44.6, pages 1768–1786 (see p. 120).

Barsoum, I. and J. Faleskog (2011). 'Micromechanical analysis on the influence of the Lode parameter on void growth and coalescence.' In: *Int. J. Solids Structures* 48.6, pages 925–938. ISSN: 0020-7683. DOI: 10.1016/j.ijsolstr.2010.11.028 (see p. 145).

Benzerga, A. and J. Besson (2001). 'Plastic potentials for anisotropic porous solids.' In: *Eur. J. Mech./A* 20A.3, pages 397–434 (see p. 119).

Benzerga, A. and J.-B. Leblond (2010). 'Ductile Fracture by Void Growth to Coalescence.' In: *Advances in Applied Mechanics* 44, 169–305 (see pp. 120, 130).

Beremin, F. M. (1981). 'Cavity formation from inclusions in ductile fracture of A508 steel.' In: *Met. Trans.* 12A, pages 723–731 (see p. 139).

Besson, J. (2010). 'Continuum models of ductile fracture: a review.' In: *Int. J. Damage Mech.* 19, pages 3–52 (see pp. 120, 128).

Besson, J. and C. Guillemer-Neel (2003). 'An extension of the Green and Gurson models to kinematic hardening.' In: *Mech. Mater.* 35, pages 1–18 (see p. 119).

Besson, J. et al. (2001). 'Modeling of crack growth in round bars and plane strain specimens.' In: *Int. J. Solids Structures* 38.46–47, pages 8259–8284 (see p. 137).

Brocks, W. et al. (1995). 'Verification of the transferability of micromechanical parameters by cell model calculations with visco-plastic materials.' In: *Int. J. Plasticity* 11, pages 971–989 (see pp. 121, 143).

Broggiato, G. et al. (2007). 'Identification of Material Damage Model Parameters: an Inverse Approach Using Digital Image Processing.' In: *Meccanica* 42, pages 9–17. DOI: 10.1007/s11012-006-9019-5 (see p. 141).

Bron, F. et al. (2004). 'Ductile rupture in thin sheets of two grades of 2024 aluminum alloy.' In: *Mater. Sci. Engng A* 380, pages 356–364 (see p. 120).

Butcher, C. and Z. Chen (Apr. 2011). 'Characterizing void nucleation in a damage-based constitutive model using notched tensile sheet specimens.' In: *Theor. Appl. Fract. Mech.* 55, pages 140–147. DOI: 10.1016/j.tafmec.2011.04.004 (see pp. 120, 149).

Cadet, C. et al. (2021). 'Ductile fracture of materials with randomly distributed voids.' In: *Int. J. Frac.* 230, pages 1573–2673. DOI: 10.1007/s10704-021-00562-7 (see p. 143).

Cadet, C. et al. (Apr. 2022). 'Strain localization analysis in materials containing randomly distributed voids: Competition between extension and shear failure modes.' working paper or preprint (see p. 145).

Chu, C. and A. Needleman (1980). 'Void nucleation effects in biaxially stretched sheets.' In: *J. Engng Mater. Technol.* 102, pages 249–256 (see pp. 120, 149).

Doege, E. et al. (1995). 'Prediction of necking and wrinkling in sheet–metal forming.' In: *J. Mat. Proc. Tech.* 50, pages 197–206 (see p. 119).

Driemeier, L. et al. (2015). 'A bifailure specimen for accessing failure criteria performance.' In: *Int. J. Plasticity* 71, pages 62–86. ISSN: 0749-6419. DOI: 10.1016/j.ijplas.2015.02.013 (see p. 123).

Enakoutsa, K. (2013). 'Modeling ductile fracture in metals involving two populations of voids – influence of continuous nucleation of secondary voids upon growth and coalescence of primary voids.' In: *Mathematics and Mechanics of Solids* 18.3, pages 323–345. DOI: 10.1177/1081286512438883 (see p. 121).

Fabrègue, D. and T. Pardoen (2008). 'A constitutive model for elastoplastic solids containing primary and secondary voids.' In: *J. Mech. Phys. Solids* 56, pages 719–741 (see pp. 120, 121, 125).

Faleskog, J. and C. Shih (1997). 'Micromechanics of coalescence — I. Synergistic effects of elasticity, plastic yielding and multi–size–scale voids.' In: *J. Mech. Phys. Solids* 45.1, pages 21–50 (see p. 121).

Faleskog, J. et al. (1998). 'Cell model for nonlinear fracture analysis — I. Micromechanics calibration.' In: *Int. J. Frac.* 89, pages 355–373 (see p. 141).

Farahani, B. et al. (2017). 'A GTN Failure Analysis of an AA6061-T6 Bi-Failure Specimen.' In: *Procedia Structural Integrity* 5, pages 981–988. DOI: 10.1016/j.prostr.2017.07.147 (see p. 123).

Feld-Payet, S. et al. (2011). 'Finite element analysis of damage in ductile structures using a nonlocal model combined with a three-field formulation.' In: *Int. J. Damage Mech.* 20, pages 655–680 (see p. 153).

Frodal, B. et al. (2021). 'On the coupling of damage and single crystal plasticity for ductile polycrystalline materials.' In: *Int. J. Plasticity* 142, page 102996. ISSN: 0749-6419. DOI: 10.1016/j.ijplas.2021.102996 (see p. 124).

Frodal, B. et al. (2022). 'On fracture anisotropy in textured aluminium alloys.' In: *Int. J. Solids Structures* 244-245, page 111563. ISSN: 0020-7683. DOI: 10.1016/j.ijsolstr.2022.111563 (see p. 124).

Gao, X. and J. Kim (2006). 'Modeling of ductile fracture: Significance of void coalescence.' In: *Int. J. Solids Structures* 43.20, pages 6277–6293. DOI: 10.1016/j.ijsolstr.2005.08.008 (see pp. 121, 139).

Ghahremaninezhad, A. and K. Ravi-Chandar (2013). 'Ductile Failure Behavior of Polycrys-talline Al 6061-T6 Under Shear Dominant Loading.' In: *Int. J. Frac.* 180, 23–29. DOI: 10.1007/s10704-012-9793-0 (see pp. 120, 135).

Gilioli, A. et al. (2010). 'Calibration of a constitutive material model for Al 6061-T6 aluminium alloy.' In: (see p. 124).

Gilioli, A. et al. (2014). 'Numerical simulation of a fracture toughness test of an Al6061-T6 aluminium alloy using a ductile criterion.' In: *Mechanics Research Communications* 58, pages 2–9. DOI: 10.1016/j.mechrescom.2013.08.007 (see pp. 122, 123).

Gologanu, M. et al. (1993). 'Approximate models for ductile metals containing non–spherical voids — Case of axisymmetric prolate ellipsoidal cavities.' In: *J. Mech. Phys. Solids* 41.11, pages 1723–1754 (see p. 119).

Gologanu, M. et al. (1994). 'Approximate models for ductile metals containing non–spherical voids — case of axisymmetric oblate ellipsoidal cavities.' In: *J. Engng Mater. Technol.* 116, pages 290–297 (see p. 119).

Gologanu, M. et al. (1997). 'Recent extensions of Gurson's model for porous ductile metals.' In: *Continuum micromechanics, CISM Lectures series*. Edited by P. Suquet. Springer, New York, pages 61–130 (see pp. 119, 124).

Grange, M. et al. (2000). 'An anisotropic Gurson model to represent the ductile rupture of hydrided Zircaloy–4 sheets.' In: *Int. J. Frac.* 105.3, pages 273–293 (see p. 119).

Gurson, A. L. (1977). 'Continuum theory of ductile rupture by void nucleation and growth: Part I— Yield criteria and flow rules for porous ductile media.' In: *J. Engng Mater. Technol.* 99, pages 2–15 (see p. 135).

Hahn, G. and A. Rosenfield (1975). 'Metallurgical factors affecting fracture toughness of aluminum alloys.' In: *Met. Trans.* 6A.4, pages 653–668 (see p. 120).

Han, X. et al. (2013). 'A yield function for single crystals containing voids.' In: *Int. J. Solids Structures* 50, pages 2115–2131. DOI: 10.1016/j.ijsolstr.2013.02.005 (see p. 143).

Hancock, J. and A. Mackenzie (1976). 'Mechanisms of ductile failure in high-strength steels subjected to multi- axial stress states.' In: *J. Mech. Phys. Solids* 24, pages 147–160 (see p. 127).

Hannard, F. et al. (2016). 'Characterization and micromechanical modelling of microstructural heterogeneity effects on ductile fracture of 6xxx aluminium alloys.' In:

Acta Mater. 103, pages 558–572. DOI: 10.1016/j.actamat.2015.10.008 (see pp. 120, 123).

Hannard, F. et al. (2018). 'Quantitative assessment of the impact of second phase particle arrangement on damage and fracture anisotropy.' In: *Acta Mater.* 148.15, pages 456–466 (see p. 120).

Haynes, M. and R. Gangloff (1998). 'Temperature-dependent void-sheet fracture in Al-Cu-Mg-Ag-Zr.' In: *Metall. Mater. Trans. A* 29A, pages 1599–1613 (see p. 120).

He, Z. et al. (2021). 'An improved shear modified GTN model for ductile fracture of aluminium alloys under different stress states and its parameters identification.' In: *Int. J. Mech. Sci.* 192, page 106081. ISSN: 0020-7403. DOI: 10.1016/j.ijmecsci.2020.106081 (see pp. 119, 123, 128).

Huber, G. et al. (2005). 'Predictive model for void nucleation and void growth controlled ductility in quasi-eutectic cast aluminium alloys.' In: *Acta Mater.* 53.9, pages 2739–2749. ISSN: 1359-6454. DOI: 10.1016/j.actamat.2005.02.037 (see pp. 122, 124).

Jiang, W. et al. (2016). 'Modified GTN model for a broad range of stress states and application to ductile fracture.' In: *Eur. J. Mech./A* 57, pages 132–148. ISSN: 0997-7538. DOI: 10.1016/j.euromechsol.2015.12.009 (see p. 119).

Klocker, H. and V. Tvergaard (2003). 'Growth and coalescence of non-spherical voids in metals deformed at elevated temperature.' In: *Int. J. Mech. Sci.* 45, pages 1283–1308 (see p. 119).

Koplik, J. and A. Needleman (1988). 'Void growth and coalescence in porous plastic solids.' In: *Int. J. Solids Structures* 24.8, pages 835–853 (see pp. 143, 144).

Lassance, D. et al. (Jan. 2007). 'Micromechanics of room and high temperature fracture in 6xxx Al alloys.' In: *Progress in Materials Science* 52, pages 62–129. DOI: 10.1016/j.pmatsci.2006.06.001 (see pp. 120, 122, 124).

Leblond, J. et al. (1994). 'Exact results and approximate models for porous viscoplastic solids.' In: *Int. J. Plasticity* 10.3, pages 213–235 (see p. 119).

Leblond, J. et al. (1995). 'An improved Gurson–type model for hardenable ductile metals.' In: *Eur. J. Mech./A* 14A.4, pages 499–527 (see p. 119).

Lemaitre, J. and R. Desmorat (2005). *Engineering damage mechanics*. Springer (see p. 141).

Liao, K. et al. (1997). 'Approximate criteria for anisotropic porous ductile sheet metals.' In: *Mech. Mater.* 26, pages 213–226 (see p. 119).

Ling, C. et al. (2016). 'An elastoviscoplastic model for porous single crystals at finite strains and its assessment based on unit cell simulations.' In: *Int. J. Plasticity* 84, pages 58–87. DOI: 10.1016/j.ijplas.2016.05.001 (see p. 143).

Liu, G. et al. (2011). 'Coupling effect of primary voids and secondary voids on the ductile fracture of heat-treatable aluminum alloys.' In: *Mech. Mater.* 43, pages 556–566. DOI: 10.1016/J.MECHMAT.2011.06.014 (see p. 120).

Liu, Y. et al. (1994). 'Mesh–dependence and stress singularity in finite element analysis of creep crack growth by continuum damage mechanics approach.' In: *Eur. J. Mech./A* 13A.3, pages 395–417 (see p. 153).

Maire, E. et al. (2005). 'Damage initiation and growth in metals. Comparison between modelling and tomography experiments.' In: *J. Mech. Phys. Solids* 53, pages 2411–2434 (see pp. 120, 130).

Massalski, T. and H. Okamoto (1986). *Binary Alloy Phase Diagrams*. Volume 1. American Society for Metals (see p. 125).

Mc Clintock, F. A. (1968). 'A criterion for ductile fracture by the growth of holes.' In: *J. App. Mech.* 35, pages 363–371 (see p. 135).

Mear, M. and J. Hutchinson (1985). 'Influence of yield surface curvature on flow localization in dilatant plasticity.' In: *Mech. Mater.* 4, pages 395–407 (see p. 119).

Mediavilla, J. et al. (2006). 'Discrete crack modelling of ductile fracture driven by non-local softening plasticity.' In: *Int. J. Numer. Meth. Engng* 66.4, pages 661–688 (see p. 153).

Moran, B. et al. (1990). 'Formulation of implicit finite element methods for multiplicative finite deformation plasticity.' In: *Int. J. Numer. Meth. Engng* 29, pages 483–514 (see p. 119).

Morgeneyer, T. et al. (2008). 'Evolution of voids during ductile crack propagation in an aluminium alloy sheet toughness test studied by synchrotron radiation computed tomography.' In: *Acta Mater.* 56, pages 1671–1679 (see p. 120).

Morgeneyer, T. et al. (2009). 'Experimental and numerical analysis of toughness anisotropy in AA2139 Al alloy sheet.' In: *Acta Mater.* 57.13, pages 3902–3915 (see pp. 121, 139).

Nahshon, K. and J. Hutchinson (2008). 'Modification of the Gurson model for shear failure.' In: *Eur. J. Mech./A* 27A, pages 1–17 (see p. 119).

Needleman, A. (1987). 'A continuum model for void nucleation by inclusion debonding.' In: *J. Applied Mech.* 54, pages 525–531 (see p. 120).

Nguyen, H. et al. (2018). 'Ductile fracture prediction and forming assessment of AA6061-T6 aluminum alloy sheets.' In: *Int. J. Frac.* 209, pages 143–162. DOI: 10.1007/s10704-017-0249-4 (see pp. 122, 123, 128).

Nielsen, K. L. and V. Tvergaard (2009). 'Effect of a shear modified Gurson model on damage development in a FSW tensile specimen.' In: *Int. J. Solids Structures* 46.3-4, 587–601 (see p. 119).

Pardoen, T. and J. Hutchinson (2000). 'An extended model for void growth and coalescence.' In: *J. Mech. Phys. Solids* 48.12, pages 2467–2512 (see pp. 119, 120).

Perrin, G. and J.-B. Leblond (2000). 'Accelerated void growth in porous ductile solids containing two populations of cavities.' In: *Int. J. Plasticity* 16.1, pages 91–120 (see pp. 119, 121, 134, 138, 145).

Petit, T. et al. (2019). 'Effect of hardening on toughness captured by stress-based damage nucleation in 6061 aluminum alloy.' In: *Acta Mater.* 180, 349–365. DOI: 10.1016/j.actamat.2019.08.055 (see pp. 120–123, 125, 130, 139, 149).

Pineau, A. et al. (2016). 'Failure of metals I: Brittle and ductile fracture.' In: *Acta Mater.* 107, 424–483 (see p. 120).

Puttick, K. E. (1959). 'Ductile fracture in metals.' In: *The Philosophical Magazine: A Journal of Theoretical Experimental and Applied Physics* 4.44, pages 964–969. DOI: 10.1080/14786435908238272 (see p. 135).

Rice, J. R. and D. M. Tracey (1969). 'On the ductile enlargement of voids in triaxial stress fields.' In: *J. Mech. Phys. Solids* 17, pages 201–217 (see pp. 123, 135).

Rivalin, F. et al. (2000). 'Ductile tearing of pipeline-steel wide plates — I. Dynamic and quasi-static experiments.' In: *Eng. Fract. Mech.* 68.3, pages 329–345 (see p. 119).

Rousselier, G. (1987). 'Ductile fracture models and their potential in local approach of fracture.' In: *Nucl. Eng. Des.* 105, pages 97–111 (see p. 153).

Rousselier, G. (2001). 'Dissipation in porous metal plasticity and ductile fracture.' In: *J. Mech. Phys. Solids* 49, pages 1727–1746 (see p. 123).

Safdarian, R. (2018). 'Forming limit diagram prediction of 6061 aluminum by GTN damage model.' In: *Mechanics & Industry* 19.2, page 202. DOI: 10.1051/meca/2018006 (see p. 123).

Schöberl, J. (1997). 'NETGEN An advancing front 2D/3D-mesh generator based on abstract rules.' In: *Computing and Visualization in Science* 1, pages 41–52. DOI: 10.1007/S007910050004 (see p. 143).

Shen, Y. (Dec. 2012). 'Comportement et endommagement des alliages d'aluminium 6061-T6: approche micromécanique.' PhD thesis. Ecole Nationale Supérieure des Mines de Paris (see p. 125).

Shen, Y. et al. (2013). 'Three-dimensional quantitative in situ study of crack initiation and propagation in AA6061 aluminum alloy sheets via synchrotron laminography and finite-element simulations.' In: *Acta Mater.* 61, pages 2571–2582. DOI: 10.1016/j.actamat.2013.01.035 (see pp. 121, 122, 124, 130, 141).

Shokeir, Z. et al. (2022a). 'Analytical formula for optimum GTN q_1 and q_2 parameters.' In: *Int. J. Frac.* (see pp. 142, 143).

Shokeir, Z. et al. (2022b). 'Edge tracing technique to study post–necking behavior and failure in Al–alloys and anisotropic plasticity in line pipe steels.' In: *Fatigue and Fract. Engng Mater. Struct.*, pages 1–16. DOI: 10.1111/ffe.13754 (see pp. 122, 123, 126, 128, 137).

Siegmund, T. and W. Brocks (2000). 'A numerical study on the correlation between the work of separation and the dissipation rate in ductile fracture.' In: *Eng. Fract. Mech.* 67, pages 139–154 (see p. 153).

Simar, A. et al. (2010). 'Micro-mechanical modelling of ductile failure in 6005A aluminium using a physics based strain hardening law including stage IV.' In: *Eng.*

Fract. Mech. 77.13, pages 2491–2503. ISSN: 0013-7944. DOI: 10.1016/j.engfracmech.2010.06.008 (see p. 124).

Springmann, M. and M. Kuna (2006). 'Determination of Ductile Damage Parameters by Local Deformation Fields: Measurement and Simulation.' In: *Arch. of Appl. Mech.* DOI: 10.1007/s00419-006-0033-9 (see p. 141).

Tancogne-Dejean, T. et al. (2021). 'Ductile damage of AA2024-T3 under shear loading: Mechanism analysis through in-situ laminography.' In: *Acta Mater.* 205, page 116556. ISSN: 1359-6454. DOI: 10.1016/j.actamat.2020.116556 (see p. 120).

Tekoğlu, C. et al. (2015). 'On localization and void coalescence as a precursor to ductile fracture.' In: *Philosophical transactions of the Royal Society of London. A* 373. DOI: 10.1098/rsta.2014.0121 (see p. 128).

Totten, G. et al. (2018). 'Encyclopedia of Aluminum and Its Alloys, Two-Volume Set (Print).' In: 1st edition. Metals and Alloys Encyclopedia Collection. CRC Press. Chapter 6XXX Alloys: Chemical Composition and Heat Treatment, pages 1–15. ISBN: 1466510803, 9781466510807 (see p. 125).

Trejo-Navas, V. et al. (2018). 'Void growth and coalescence in a three-dimensional non-periodic void cluster.' In: *Int. J. Solids Structures* 139–140, pages 65–78. DOI: 10.1016/j.ijsolstr.2018.01.024 (see p. 120).

Tu, H. et al. (2019). '3D optical measurement and numerical simulation of the fracture behavior of Al6061 laser welded joints.' In: *Eng. Fract. Mech.* 206, pages 501–508. ISSN: 0013-7944. DOI: 10.1016/j.engfracmech.2018.12.005 (see pp. 122, 123).

Tu, H. et al. (2016). 'Simulation of the fracture behavior of Al6061 laser welded joints with the Rousselier model.' In: *Comput. Mat. Sci.* 116, pages 122–128. DOI: 10.1016/j.commatsci.2015.10.030 (see p. 123).

Tvergaard, V. (1981). 'Influence of voids on shear band instabilities under plane strain condition.' In: *Int. J. Frac.* 17.4, pages 389–407 (see p. 141).

Tvergaard, V. (1982). 'On the localization in ductile materials containing spherical voids.' In: *Int. J. Frac.* 18.4, pages 237–252 (see p. 141).

Tvergaard, V. (1990). 'Material failure by void growth to coalescence.' In: *Advances in Applied Mechanics* 27, pages 83–151 (see p. 119).

Tvergaard, V. (1998). 'Interaction of very small voids with larger voids.' In: *Int. J. Solids Structures* 30, pages 3989–4000. DOI: 10.1016/S0020-7683(97)00254-0 (see p. 121).

Tvergaard, V. (2008). 'Effect of T-stress on crack growth under mixed mode I–III loading.' In: *Int. J. Solids Structures* 45.18-19, pages 5181–5188 (see p. 120).

Tvergaard, V. (2009). 'Behaviour of voids in a shear field.' In: *Int. J. Frac.* 158, pages 41–49. DOI: 10.1007/s10704-009-9364-1 (see pp. 120, 138).

Tvergaard, V. and A. Needleman (1984). 'Analysis of the cup–cone fracture in a round tensile bar.' In: *Acta Metall.* 32, pages 157–169 (see pp. 137–139).

Ueda, T. et al. (2014). 'In situ laminography study of three-dimensional individual void shape evolution at crack initiation and comparison with Gurson–Tvergaard–Needleman-

type simulations.' In: *Acta Mater.* 78, pages 254–270. ISSN: 1359-6454. DOI: 10.1016/j.actamat.2014.06.029 (see pp. 120, 121, 134, 135, 138, 139, 150).

Yu, H. et al. (2014). 'Tensile fracture of ultrafine grained aluminum 6061 sheets by asymmetric cryorolling for microforming.' In: *Int. J. Damage Mech.* 23.8, pages 1077–1095. DOI: 10.1177/1056789514538083 (see p. 124).

Zhu, Y. and M. Engelhardt (2018). 'Prediction of ductile fracture for metal alloys using a shear modified void growth model.' In: *Eng. Fract. Mech.* 190, pages 491–513. ISSN: 0013-7944. DOI: 10.1016/j.engfracmech.2017.12.042 (see p. 123).

6

STRAIN HARDENING AND STRENGTH EFFECT ON THE FRACTURE BEHAVIOR OF THE 6061 ALUMINUM ALLOYS

RÉSUMÉ

Le premier objectif de cette étude est de décorréler l'effet du durcissement et de la chute de l'écrouissage sur la ténacité. Ceci est réalisé par des essais de ténacité sur cinq matériaux traités thermiquement. Un alliage 6061 subit un traitement de réchauffage, suivi d'une trempe et enfin d'un traitement de durcissement par vieillissement. Le temps de durcissement par vieillissement varie afin de produire cinq matériaux avec cinq niveaux de durcissement. Le deuxième objectif est de remettre en question le modèle d'endommagement GTN calibré dans chapter 5. Par conséquent, le deuxième objectif de ce chapitre est de répondre à la question suivante : le modèle GTN calibré dans chapter 5 est-il capable de modéliser la ténacité des matériaux à durcissement différent ? Les résultats par éléments finis présentés dans ce chapitre montrent que le modèle GTN calibré est capable de prédire l'endommagement dans des matériaux présentant différents niveaux de durcissement.

6.1 INTRODUCTION

The radiation damage discussed earlier (see chapter 2) leads to a rapid increase in the yield strength and a significant decrease in strain hardening capacity [Alexander, 1993; King et al., 1969; Weeks et al., 1993]. The third objective of this PhD thesis is to decorrelate the effect of strengthening and strain hardening drop on the overall fracture toughness. This can be done via an experimental investigation on irradiated samples. However, experiments on irradiated samples are expensive and time consuming. $6xxx$ aluminum alloys can be strengthened by other means than irradiation (e. g. work hardening or age hardening) [Mukhopadhyay, 2012].

In the current work, a 6061 aluminum alloy is age hardened to produce different yield strengths and strain hardening levels. At a constant age hardening temperature, the age hardening time results in microstructural changes [Develay, 1992]. The latter have a subsequent effect on the mechanical properties (i. e. strength and strain hardening capacity) [Kumar et al., 2022; Rady et al., 2019]. The heat treatment process that tailors the mechanical properties can be summarized in three consecutive steps:

1. Firstly, a reheat treatment is applied to the material. The temperature is raised to about 550°C for one hour in order to partially dissolve the micron-sized $\beta - Mg_2Si$ phase already found in the α-Al matrix. The reheat temperature should be high enough to allow the dissolution of $\beta - Mg_2Si$ without exceeding the solidus line temperature (593°C). Increasing the reheat temperature increases the amount of Mg an Si atoms available in the α-Al matrix. This results in a higher density regarding the strengthening phase nucleated during age hardening [Dorward et al., 1998]. The higher density of the strengthening phase leads to an increase in strength and fracture toughness [Kumar et al., 2022]. For instance, Dorward et al., 1998 observe an increase in the fracture toughness of a 6061 alloy when the reheat temperature is increased from 527 to 557°C. Furthermore, Ikei et al., 2000 observe an increase in the yield and ultimate tensile strengths of a 6061 alloy when the reheat temperature is increased from 530 to 560°C. Therefore, increasing the reheat temperature has a positive effect on the strength and fracture toughness.

2. Secondly, the alloy is quenched to trap the Mg and Si atoms in the solid solution $\alpha - Al$. The mechanical properties of the $6xxx$ alloy are sensitive to the quench rate [Kassner et al., 2011]. Steele et al., 2007 observe a decrease in the volume of fraction of micron-sized $\beta - Mg_2Si$ particles along the grain boundaries as the quench rate increases. The micron-sized $\beta - Mg_2Si$ particles fail during mechanical loading which creates micro-voids in the alloy and decreases the fracture toughness [Lassance et al., 2007; Maire et al., 2005; Petit et al., 2019; Shen et al., 2013]. Therefore, the quench rate must be controlled to avoid the precipitation of micron-sized $\beta - Mg_2Si$ that have a negative impact on mechanical properties.

3. Finally, the age hardening treatment is carried out to obtain the Mg_xSi_y strengthening phase. The latter precipitates according to the following sequence [Edwards et al., 1998; Lars et al., 2000]:

$$\alpha\text{−Al} \rightarrow GP \rightarrow \beta'' \rightarrow \beta' \rightarrow \beta(Mg_xSi_y) \tag{6.1}$$

   where α-Al is the solutionized solid solution, GP are the Guinier-Preston zones, β'' are β' are the strengthening nano-sized metastable phases, and $\beta(Mg_ySi_x)$ is the stable non-coherent phase. The precipitation process of the strengthening phases in 6061 alloys is more complicated than it seems and is extensively described in the literature [Edwards et al., 1998; Flament, 2015; Matsuda et al., 2000; Totten et al., 2018].

As discussed in the work of Develay, 1992, the yield and ultimate tensile strengths at a given age hardening temperature (e. g. 175°C) are expected to slightly increase at the beginning of the aging process: at 10 hours according to fig. 6.1. At the beginning

of the age hardening process, the alloy is rich in GP zones which result in a high ratio of tensile to yield strength (work hardening capacity) and high fracture toughness [Kaufman, 2000]. This temper is also called "under-aged". At $\sim$ 10 hours according to fig. 6.1, the alloy GP zones are replaced by β'' (see eq. (6.1)). The β'' precipitates provide the highest strength level. The fracture toughness is lower than the "under-aged" alloy. This temper is also called "peak-aged". Beyond 10 hours of age hardening, the β'' precipitate ripen and form $\beta(Mg_xSi_y)$ which have a lower strengthening effect. The hardening capacity and fracture toughness are lower than the "peak-aged" alloy [Dumont, 2001; Dumont et al., 2003]. This temper is also called "over-aged".

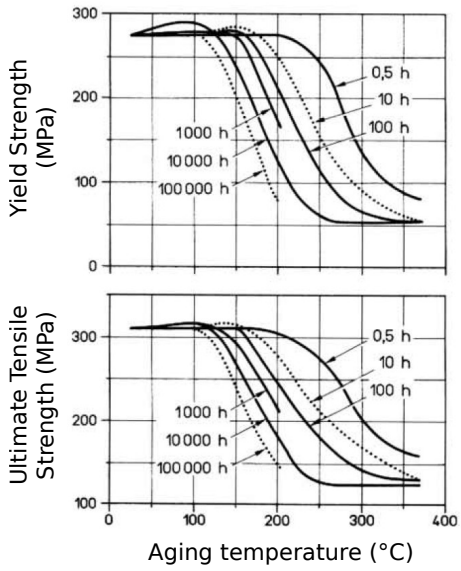

Figure 6.1: Effect of the age hardening temperature and time on the yield and ultimate tensile strengths respectively [Develay, 1992]

In this chapter, a 6061 alloy undergoes a reheat treatment, followed by a quench and finally an age hardening treatment. The age hardening time is varied to produce five materials with five strengthening levels. The first main objective of this study is to decorrelate the effect of strengthening and strain hardening drop on the overall fracture toughness. This is done via fracture toughness testing over the five heat treated materials. The second main objective is to challenge the GTN damage model calibrated in chapter 5. The latter is focused on identifying the GTN parameters over a 6061-T6 alloy which is not investigated in this chapter (see table 1.1). Therefore, the second objective of this chapter is to answer the following question: is the calibrated GTN model in chapter 5 capable of capturing the effect of hardening on the fracture toughness? Given the two identified objectives, this chapter is divided into the following sections:

- Section 6.2: presents the heat treatment applied to obtain the studied materials.
- Section 6.3: is divided into three parts. The first part presents the experimental setup and tested samples. The second and third parts illustrate the tensile and fracture toughness results respectively. This experimental study aims to decorrelate the effect of strengthening and strain hardening drop on the overall fracture toughness.
- Section 6.4: is divided into three parts. The first part explains the calibration of the plastic flow model for the studied materials. The second part recalls the GTN model and its parameters. The third part models all experiments carried out in section 6.3. This section aims to answer the question stated above (regarding the potentiality of the GTN model in capturing the effect of hardening on the fracture toughness).

6.2 STUDIED MATERIALS

Table 6.1 shows the chemical composition of the studied alloy. The as-received alloy (hereby referred to as T6 AR) is a T6 temper. The T6 AR is obtained by a 4-hour reheat treatment at 530°C followed by a 12-hour age hardening treatment at 175°C.

Table 6.1: Chemical composition by % wt. of the studied 6061 aluminum alloy

Mg	Si	Fe	Cu	Cr	Mn	Zn	Ti	Al
1.08	0.53	0.38	0.22	0.18	0.06	0.22	0.02	bal.

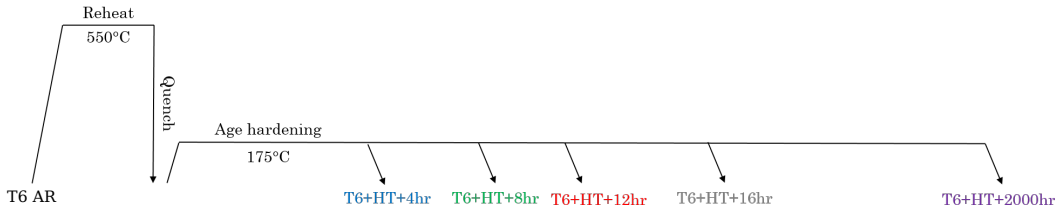

Figure 6.2: Heat treatment of the AA6061 leading to under-aged, peak-aged, and over-aged states. Before the reheat phase, the alloy is in a T6 state (aka peak-aged alloy). The age hardening time results in different microstructures leading to unlike mechanical properties

In order to obtain the materials required for this study, the T6 AR is reheated for 5 hours at 550°C then water quenched as shown in fig. 6.2. The age hardening is carried out at 175°C to produce different tempers named after their aging time as follows: "T6+HT+$x$hr", where HT corresponds to the reheat process at 550°C and x the aging

time in hours. The purpose of the different age hardening treatments is to obtain different strength and hardening levels. Therefore, the 5 materials obtained via age hardening as well as the as received material are listed below:

- T6 AR
- T6+HT+4hr
- T6+HT+8hr
- T6+HT+12hr
- T6+HT+16hr
- T6+HT+2000hr

It is important to note that the "T6+HT+$x$hr" material has a different chemical composition by %wt. than the 6061-T6-BE material studied in chapter 4 and chapter 5. The "T6+HT+$x$hr" has more than the double regarding %wt. of Fe (0.38 compared to 0.16 in the 6061-T6-BE material). This results a higher volume fraction of intermetallic particles as shown in fig. 6.3 (a). The latter reveal a SEM (back-scattered electrons) image of the microstructure of the "T6+HT+$x$hr" material and compares it to the microstructure of the 6061-T6-BE material in fig. 6.3 (b).

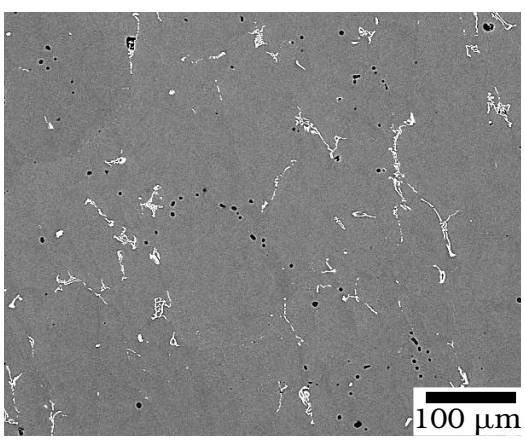

(a) 6061+HT+$x$hr studied in this chapter

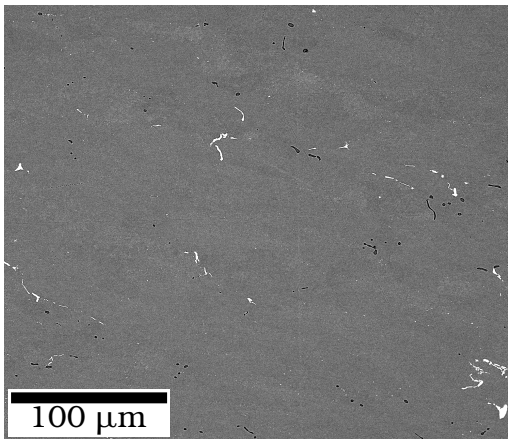

(b) 6061-T6-BE studied in chapter 4 and chapter 5

Figure 6.3: SEM (back-scattered electrons) image of the microstructure of: (a) 6061+HT+$x$hr studied in this chapter (courtesy of Petit et al., 2019) and (b) 6061-T6-BE studied in chapter 4 and chapter 5. The 6061+HT+$x$hr material has a higher wt% Fe which results in more intermetallic particles.

6.3 EXPERIMENTS

6.3.1 *Experimental setup and samples*

Tensile tests are carried out on simple tensile (ST) and notched tensile (NT) axisymmetric specimens that are shown in chapter 5. For a fixed minimum cross-section diameter (Φ_0), varying the initial notch curvature radius (R) increases the stress triaxiality level [Hancock et al., 1976]. The NT10, NT4 and NT2 have an initial R of 4, 1.6 and 0.8 mm respectively and an initial minimum cross-section diameter $\Phi_0 = 4$ mm. Given the initial R and Φ_0, each NT sample gets its name as follows: $\text{NT}_x = 10\,R\,/\,\Phi_0$, where x is the sample's name. Small 'v' notches are machined in the NT specimens beyond the notch area to easily attach an axial extensometer during the test (gauge length $L_0 = 10$ mm for all NT samples). The 'v' notches prevent the extensometer knives from sliding. Smooth tensile bars are machined following the ASTM–E8 standard [ASTM, 2015]. The reduced section in the ST sample is 20 mm long, the initial minimum cross-section diameter $\Phi_0 = 4$ mm and the extensometer gauge length $L_0 = 17.8$ mm.

All tensile tests are carried out at room temperature using a strain rate of about $5 \times 10^{-4}\ s^{-1}$. The Edge Tracing (ET) method is used to take images of the sample during the experiment and calculate the radial deformation. The ET method is detailed in previous work [Shokeir et al., 2022]. Table 6.2 shows the number of tested tensile samples for each of the studied materials. Some of the ST tests are carried out in the work of Petit et al., 2018. The latter have similar testing conditions (i. e. same temperature and strain rate) but do not use the ET method.

Fracture toughness tests are carried out on Compact-Tension (CT12.5) samples that are shown in chapter 5. CT samples are machined according to the ASTM E1820 standards [ASTM-1820, 2017]. The sample length $W = 25$ mm, while other dimensions are a function of the thickness B. The net thickness without the side grooves $B_n = 0.8\,B$ and the side groove depth is equal to $B/10$ mm. The side grooves machined on the crack propagation line facilitate a uniform crack propagation without deviation. The side grooves are machined at an angle of 45°. A pre-crack is introduced in all samples by fatigue loading on a hydraulic tensile machine. The frequency is maintained between 8 Hz and 12 Hz till the pre-crack a_0 length reaches 15 mm.

Table 6.2 shows the tested CT12.5 samples. The CT12.5 samples of the T6 AR and T6+HT+2000hr materials are tested in this study using an elastic–unloading procedure to obtain a J-resistance curve as described by ASTM E1820 standards [ASTM-1820, 2017]. Compliance is used to measure the crack size which is later confirmed by $post - mortem$ optical crack size measurements. A universal testing machine is used to perform the tests at a constant speed of ± 0.16 mm/min. A clip-on displacement gauge is used to control the speed and measure the Crack Mouth Opening Displacement (CMOD). The CT12.5 samples of the T6+HT+4hr, T6+HT+8hr, T6+HT+12hr and T6+HT+16hr are tested in the work of Petit et al., 2018. Three

out of four samples are tested using the elastic–unloading procedure as mentioned above. The remaining sample is tested under monotonic loading using a cross-head displacement control. The J-resistance curve of this sample is obtained using the Key-Curve method explained in the work of Petit et al., 2018.

Table 6.2: A total of 64 tested ST, NT10, NT4, NT2 and CT12.5 samples

SAMPLE	ST	NT10	NT4	NT2	CT12.5
T6 AR	3	-	-	-	2
T6+HT+4hr	$4^{\dagger}$	3	3	2	4^{*}
T6+HT+8hr	$4^{\dagger}$	-	-	-	4^{*}
T6+HT+12hr	$3^{\dagger}$	-	-	-	4^{*}
T6+HT+16hr	$3^{\dagger}$	2	2	2	3^{*}
T6+HT+2000hr	3	2	2	2	4

† Three out of four (or two out of three) samples are tested in the work of Petit et al., 2018 without the ET method. The remaining sample is tested in this work using the ET method.

* All samples are tested in the work of Petit et al., 2018. Three out of four (or two out of three) samples are tested using the elastic–unloading procedure. The remaining sample is tested under monotonic loading without elastic–unloading.

6.3.2 *Tensile results*

Figure 6.4 displays the tensile behavior of all six tested materials. In parallel, fig. 6.5 summarizes the tensile properties shown in fig. 6.4. Figure 6.4 shows a single tensile test for each material for the purpose of clarity. However, for each studied material, several tensile tests are carried out and are shown by circles in fig. 6.5. For each material, the tensile results are repeatable.

According to results in fig. 6.5, the yield and ultimate tensile strengths increase as the aging time increases up till 16hr. Beyond 16 hours of age hardening, the yield strength remains almost constant, while the ultimate tensile strength decreases. The hardening capacity (ultimate/yield strengths ratio) decreases as the aging time increases (even beyond 16 hours of age hardening).

The astonishing fact is that the over-aged alloy (T6+HT+2000hr) shows only a drop of 6 MPa and 18 MPa regarding the yield and ultimate tensile strengths respectively. On the other hand, when comparing the 10hr (peak-aged) and 1000hr (over-aged) in

fig. 6.1 [Develay, 1992], a $\sim$ 40 MPa and $\sim$ 50 MPa drop are observed regarding the yield and ultimate tensile strengths respectively.

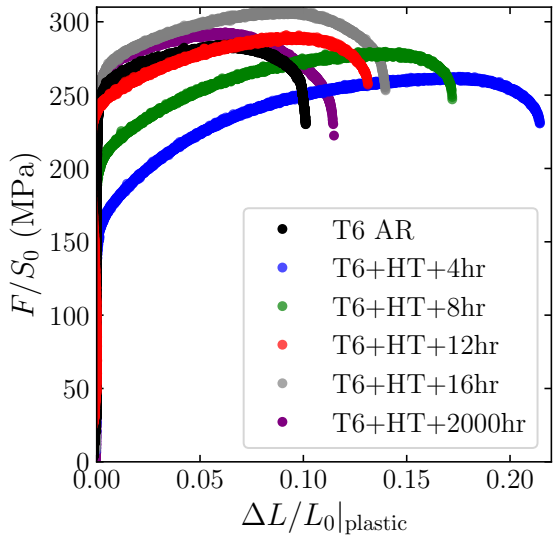

Figure 6.4: Nominal stress—plastic deformation curves of the 6 studied materials

In order to study the effect of the reheat temperature, the T6 AR can be systematically compared to the T6+HT+12hr since both materials undergo a 12-hour age hardening treatment at 175°C. The major difference between both materials is the reheat temperature (530°C and 550°C for the T6 AR and T6+HT+12hr respectively). The reheat temperature has an influence on the strengthening and the ductility at failure of the material.

To explain the effect of the reheat temperature on the strain at failure, one can recall the explanation stated earlier: the reheat temperature enhances the dissolution of micron-sized $\beta - Mg_2Si$ particles that initiate damage and dictate the fracture toughness [Lassance et al., 2007; Maire et al., 2005; Petit et al., 2019; Steele et al., 2007]. Therefore, it is expected that the T6 AR is less ductile than the T6+HT+12hr. Figure 6.5 illustrate that the uniform and total elongation % decrease as the aging time increases. The T6 AR has a lower uniform and total elongation % than the T6+HT+12hr which is obvious in fig. 6.4. The lower elongation % in the T6 AR confirms the fact that the reheat temperature has a direct impact on the ductility [Dorward et al., 1998]. As a matter of fact, the T6 AR has a lower hardening capacity than the T6+HT+12hr.

Unlike results in the work of Ikei et al., 2000, the yield strength does not increase as the reheat temperature increases. The T6 AR and T6+HT+12hr have a similar yield strength (see fig. 6.5). However, the T6 AR has a slightly lower ultimate tensile strength. The reheat temperature has an effect on the maximum tensile strength since the temperature determines the quantity of Mg and Si in solid solution for the precipitation of nano Mg_xSi_y phases. The T6 AR has a lower reheat temperature which

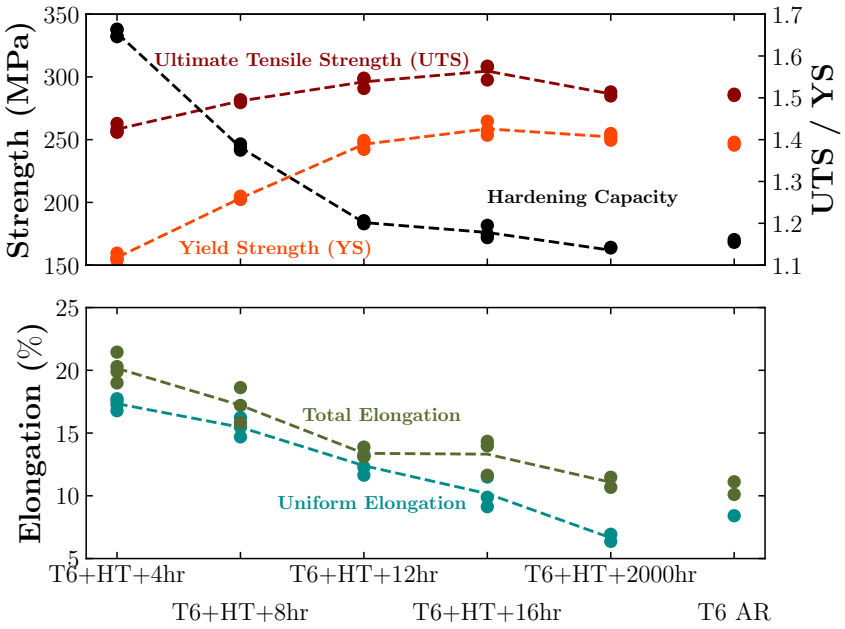

Figure 6.5: Evolution of the mechanical properties as a function of the aging time. The analyzed properties are: 0.2% yield strength (YS), ultimate tensile strength (UTS), hardening capacity (UTS/YS), uniform elongation % and total elongation %.

results in less nano Mg_xSi_y precipitates and a lower ultimate tensile strength as shown in fig. 6.5.

In order to study the effect of stress triaxiality on the strain at failure, tensile testing is extended to notched tensile (NT) samples. Figure 6.6 shows the nominal stress—radial deformation curves of ST, NT10, NT4 and NT2 samples of the three following materials: T6+HT+4hr, T6+HT+16hr, T6+HT+2000hr. The two remaining materials (T6+HT+8hr and T6+HT+12hr) are excluded from this NT study since they have intermediate hardening levels between the T6+HT+4hr and T6+HT+16hr. The ST test curves shown in fig. 6.6 are already plotted in fig. 6.4 using the longitudinal deformation ($\Delta L/L_0$) and not the radial deformation ($\Delta\Phi/\Phi_0$) as shown in fig. 6.6.

The strain at failure is highest in the T6+HT+4hr and lowest in the T6+HT+2000hr as observed in NT test results in fig. 6.6. Figure 6.7 shows, for the three studied materials, the critical strain which corresponds to the sharp load drop observed in fig. 6.6 (e. g. $\Delta\Phi/\Phi_0 = 0.10$ in the T6+HT+4hr NT4 sample). The critical strain drops as a function of the stress triaxiality. This is explained by the fact that void growth (i. e. damage) increases as the stress triaxiality increases [Barsoum et al., 2007; Benzerga et al., 2010; Besson, 2010]. The critical strain in the T6+HT+2000hr is slightly lower than the T6+HT+16hr as observed in fig. 6.7. The lower critical strain in the T6+HT+2000hr is related to the lower strain hardening capacity. Experimental results shown in fig. 6.6 are to be simulated in section 6.4 in order to fulfill the second main objective of this study.

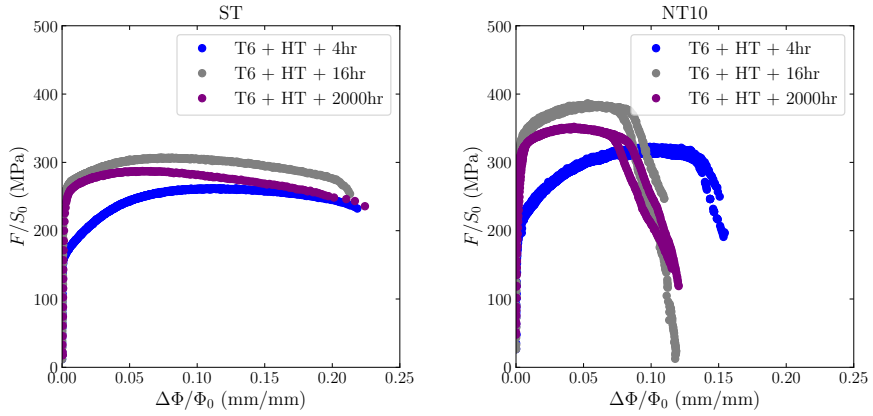

(a) ST samples

(b) NT10 samples

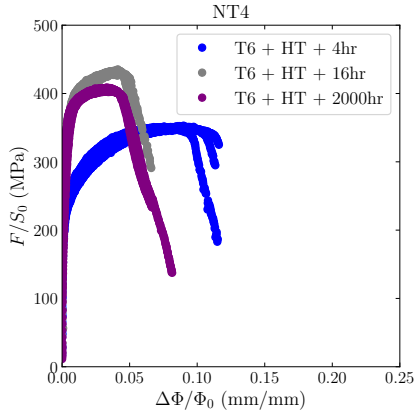

(a) NT4 samples

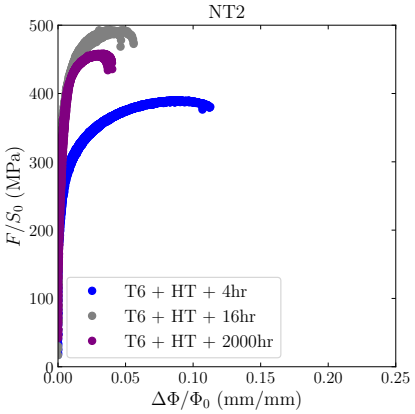

(b) NT2 samples

Figure 6.6: ST and NT nominal stress—radial deformation curves of three studied materials: T6+HT+4hr, T6+HT+16hr and T6+HT+2000hr

6.3.3 *Fracture toughness results*

Figure 6.8 displays the load—CMOD (Crack Mouth Opening Displacement) curves of the six studied materials. The elastic–unloading phases recorded during testing is removed in fig. 6.8 for the purpose of clarity. The test curves in fig. 6.8 are used to obtain the J-resistance curves which are shown in fig. 6.9 (as described by ASTM E1820 standards [ASTM-1820, 2017]). Figure 6.9 also shows the 0, 0.2 and 1 blunting lines for each material. The slope of each blunting line is a function of the material's yield (YS) and ultimate tensile (UTS) strengths (slope $= k\ (\mathrm{YS} + \mathrm{UTS})/2$, where $k = 2$). The curve intersection with the 0.2BL gives the $J_{0.2\mathrm{BL}}$, while the $\mathrm{d}J/\mathrm{da}$ is calculated as follows: $(J_{1\mathrm{BL}} - J_{0.2\mathrm{BL}})/0.8$ (i. e. no R-curve adjustment required). Both $J_{0.2\mathrm{BL}}$ and $\mathrm{d}J/\mathrm{da}$ decrease as the age hardening time increases as shown in fig. 6.10. The latter illustrates the drop in $J_{0.2\mathrm{BL}}$ as the aging time increases (i. e. ultimate tensile strength increases) till 304 MPa (16 hours of aging). Beyond 16 hours of aging, the ultimate strength drops while the $J_{0.2\mathrm{BL}}$ slightly re-increases. The error bars plotted in

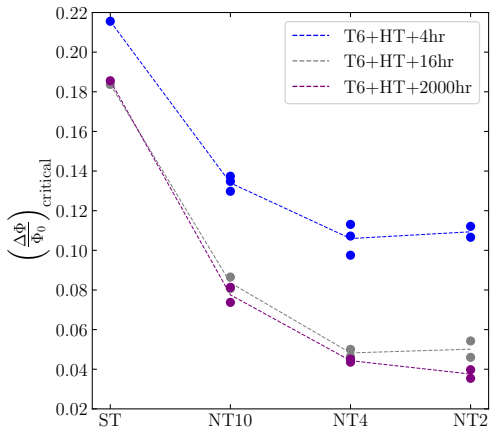

Figure 6.7: Critical strain in ST and NT samples of three studied materials. Critical strain corresponds to the sharp load drop observed in fig. 6.6.

fig. 6.11 correspond to the maximum and minimum $J_{0.2\text{BL}}$ values for each material. Furthermore, the T6 AR has a lower fracture toughness than the T6+HT+12hr.

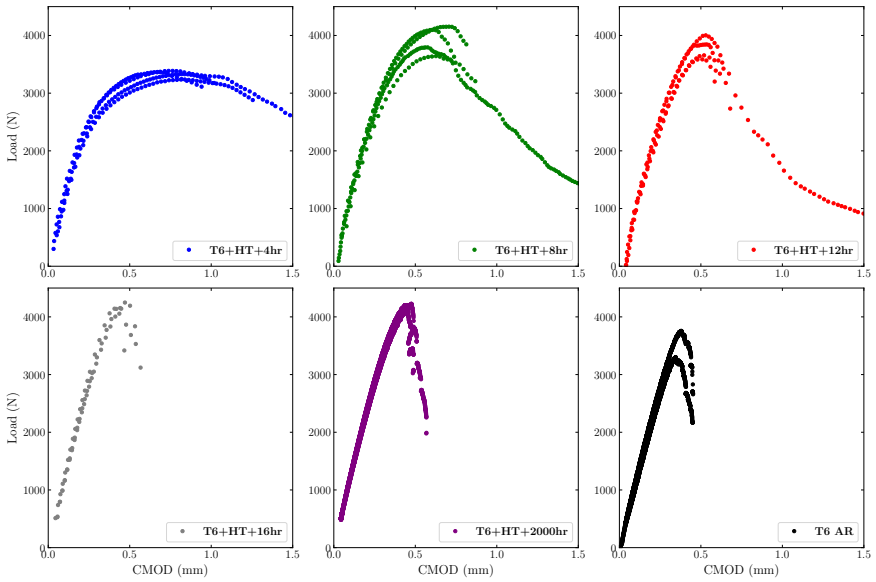

Figure 6.8: Load—CMOD of the six tested materials

Even though it is difficult to conclude that the over-aged regains it toughness, an explanation is given in the work of Dumont et al., 2003. The cited authors study the effect of the microstructure (i. e. heat treatment) on the mechanical properties (i. e. strength, hardening and fracture toughness) of a 7050 aluminum alloy. Dumont et al., 2003 observe similar results as shown in fig. 6.11. The toughness decreases as the hardening time (or yield strength) increases till the peak-aged material. After that, the fracture toughness slightly increases in the over-aged material. Dumont et al., 2003 explain that after the quench following the reheat process, micron-sized Mg_2Si particles form at grain boundaries. The areas surrounding the Mg_2Si particles contains

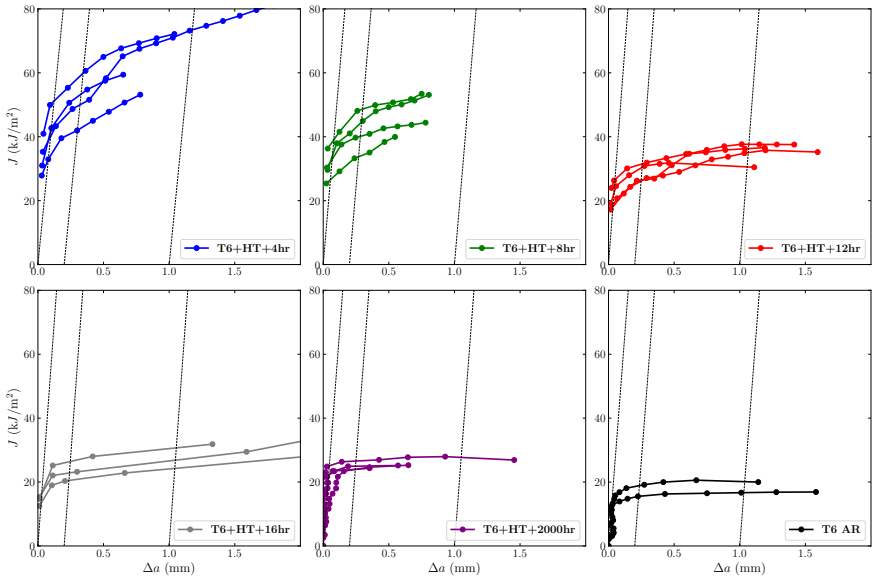

Figure 6.9: J-Δa curves of the six tested materials

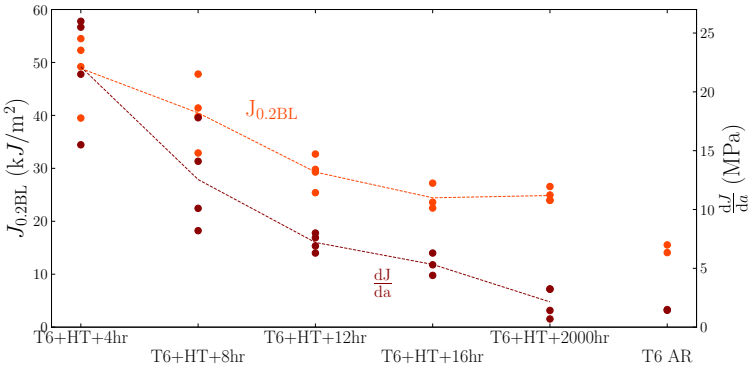

Figure 6.10: Evolution of the fracture toughness proprieties as a function of the age hardening time. The error bars plotted in fig. 6.11 correspond to the maximum and minimum $J_{0.2\text{BL}}$ values for each material.

a lower amount of Mg and Si in solid solution. Therefore, these areas are softer as they do not contain age hardening Mg_xSi_y precipitates and are called Precipitate-Free-Zones (PFZ). Dumont et al., 2003 explain that the over-aged material contains less PFZ which leads to a more homogeneous plastic flow inside the grain (due to less contrast in strength between the PFZ and precipitate-rich zones). Dumont et al., 2003 state that this fact leads to less plastic localization inside the grain which enhances the toughness.

At this stage, attempts can be made to decorrelate the effect of strengthening and strain hardening drop on the overall fracture toughness. The relative increase or decrease in mechanical properties (given T6+HT+16hr as the reference material) are highlighted in table 6.3. The T6+HT+4hr and T6+HT+2000hr gain 50% and 2% in $J_{0.2\text{BL}}$ respectively with respect to the T6+HT+16hr. Considering only the hardening capacity

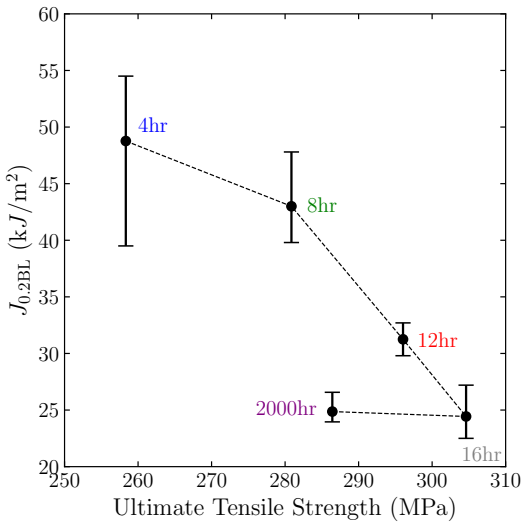

Figure 6.11: $J_{0.2\mathrm{BL}}$—ultimate tensile strength. The lowest and highest ultimate strengths correspond to the T6+HT+4hr and T6+HT+16hr respectively.

and $J_{0.2\mathrm{BL}}$, a gain of 40% in hardening leads to a gain of 50% in $J_{0.2\mathrm{BL}}$ (see T6+HT+4hr vs. T6+HT+16hrin table 6.3). However, a loss of 4% in hardening leads to a gain of 2% in $J_{0.2\mathrm{BL}}$ (see T6+HT+2000hr vs. T6+HT+16hrin table 6.3). Now considering the yield strength, a loss of 37% in yield strength results in a gain of 50% in $J_{0.2\mathrm{BL}}$. On the other hand, a loss of 2.5% in yield strength results in a gain of 2% in $J_{0.2\mathrm{BL}}$. In reality, both yield strength and hardening affect the overall fracture toughness. An increase in the yield strength and a decrease in hardening can lead to an increase or decrease in fracture toughness. This depends on the amount of increase in yield strength with respect to the amount of decrease in hardening. This also depends on underlying factors as the effect of decreasing the PFZs on the toughness as explained above.

Table 6.3: Relative increase or decrease in mechanical properties when comparing the under-aged (T6+HT+4hr), peak-aged (T6+HT+16hr) and over-aged (T6+HT+2000hr)

Materials	$J_{0.2\mathrm{BL}}$	**Yield strength**	**Ultimate tensile strength**	**Hardening capacity**
T6+HT+4hr vs. T6+HT+16hr	+50%	−37%	−15%	+40%
T6+HT+2000hr vs. T6+HT+16hr	+2%	−2.5%	−6%	−4%

6.4 FINITE ELEMENT SIMULATIONS

6.4.1 *Elastic–plastic flow*

The strain hardening model shown in eq. (6.2) is used to model the elastic–plastic behavior of the three studied materials. The flow stress (σ_F) depends on the accumulated plastic strain (p) and material parameters ($\sigma_0, A_1, b_1, A_2, b_2$) shown in table 6.4. The material's elastic limit is given by the σ_0 parameter.

$$\sigma_F(p) = \sigma_0 + \sum_{i=1}^{2} A_i \ (1 - \exp(-b_i \ p)) \tag{6.2}$$

Table 6.4: Strain hardening law parameters of the simulated materials

Material	σ_0	A_1	b_1	A_2	b_2
T6+HT+4hr	115 MPa	173 MPa	12.0	52 MPa	1554
T6+HT+8hr †	199 MPa	145 MPa	12.7	0 MPa	0
T6+HT+12hr †	237 MPa	114 MPa	14.3	0 MPa	0
T6+HT+16hr	236 MPa	127 MPa	6.8	42 MPa	250
T6+HT+2000hr	225 MPa	70 MPa	9.2	50 MPa	185

† There are no NT tests available regarding the T6+HT+8hr and T6+HT+12hr materials. The NT tests and the ET method are essential for determining the hardening parameters at large strains as it is done for the T6+HT+4hr, T6+HT+16hr and T6+HT+2000hr materials. Due to the lack of NT tests, the hardening parameters of the T6+HT+8hr and T6+HT+12hr materials are taken from the work of Petit et al., 2019. The cited authors calibrate the σ_0, A_1 and b_1 parameters using ST tests (without the ET method).

The hardening parameters shown in table 6.4 are fit over the ST and NT tensile tests previously shown in fig. 6.6 (except for the T6+HT+8hr and T6+HT+12hr materials due to lack of NT tests). Finite element simulations (without damage) are carried out to asses the parameters of the hardening model. The simulated results are compared with the stress—strain curves in fig. 6.12 (a) (till the onset of sharp load drop). An objective function is minimized to find the best set of parameters shown in table 6.4. This optimization method is explained in chapter 4. It assures that the plastic behavior is well modeled beyond the necking phase which is crucial when modeling damage at large strains. Chapter 5 illustrates the used FE meshes for all tensile samples.

6.4.2 *GTN model*

A brief presentation of the GTN model is provided in this section. More details regarding the model are provided in chapter 5.

Damage is incorporated in the GTN model via the porosity (f). The latter is expressed as the sum of increase in volume fraction due to void growth (f_g) and void nucleation (f_n) [Tvergaard et al., 1984]. The effective stress of the GTN model is implicitly defined as a function of the Cauchy stress tensor and the porosity as shown below:

$$\left(\frac{\sigma_{\text{eq}}}{\sigma_\star}\right)^2 + 2q_1 f_* \cosh\left(\frac{3}{2}q_2\frac{\sigma_m}{\sigma_\star}\right) - 1 - {q_1}^2 f_*^2 \equiv 0 \tag{6.3}$$

where σ_{eq} is the von Mises equivalent stress, and σ_m the mean stress. f_* is defined such that:

$$f_* = \begin{cases} f & \text{if } \Delta f_g < \Delta f_g\text{crit.} \\ f + \delta\ \langle \Delta f_g - \Delta f_{g\ \text{crit.}} \rangle & \text{otherwise} \end{cases} \tag{6.4}$$

where the "acceleration" factor $\delta > 0$ is a material parameter. Coalescence is triggered when the increase in void growth (Δf_g, where $\Delta f_g = f_g - f_0$) reaches the critical value Δf_gcrit. (f_0 is the initial porosity). The definition of f_* shown in eq. (6.4) is different from the model proposed by Tvergaard and Needleman [Tvergaard et al., 1984]. Section 5.3.2 explains the theory behind modifying the f_* original equations. The Δf_gcrit. depends on the stress triaxiality ($\sigma_m/\sigma_{\text{eq}}$) as follows:

$$\Delta f_g - \Delta f_{g\ \text{crit.}} = \alpha\ \exp\left(-\beta\ \frac{\sigma_m}{\sigma_{\text{eq}}}\right) + \gamma \tag{6.5}$$

where α, β and γ are material parameters. Equation (6.5) is used to account for void coalescence by void sheeting and its dependence on the stress state. This explains why the critical void growth porosity (onset of coalescence, $\Delta f_g - \Delta f_{g\ \text{crit.}}$) depends on the stress triaxiality ($\sigma_m/\sigma_{\text{eq}}$ in eq. (6.5)). Void coalescence through void sheeting takes place in materials with two populations of voids. Primary voids nucleated on micron-sized particles interact with voids nucleated on sub-micron particles. The latter stop the growth of primary voids and lead to void coalescence in a shear band (i. e. void sheet).

Void nucleation is modeled by the Beremin model [Beremin, 1981] which defines the stress inside the particle as the sum of the stress in the matrix and an additional stress transfer arising from the deformation mismatch between the particle and the

matrix. Particles are considered as brittle solids that fracture when the maximum principal stress in the particle reaches the nucleation critical stress:

$$\sigma_I^{\text{particle}} = \sigma_c \tag{6.6}$$

The maximum principal stress in the particle ($\sigma_I^{\text{particle}}$) can be expressed as proposed by Beremin [Beremin, 1981]:

$$\sigma_I^{\text{particle}} = \sigma_I^{\text{matrix}} + k_b \left(\sigma_{\text{eq}} - \sigma_0\right) \tag{6.7}$$

where σ_I^{matrix} is the maximum principal stress in the matrix, k_b is a geometrical factor that depends on the particle shape and orientation, σ_{eq} and σ_0 are the von Mises equivalent stress and yield stress respectively. The geometrical factor k_b is taken equal to 1 (assuming perfect spherical particles). The rate of increase in porosity due to void nucleation $\dot{f}_n$ can be expressed as a function of the plastic deformation increment ($\dot{p}$):

$$\dot{f}_n = A_n \, \dot{p} \tag{6.8}$$

where A_n is expressed as a function of the particle stress and the critical stress:

$$A_n = \begin{cases} a_n \left(\frac{\sigma_I^{\text{particle}}}{\sigma_c} - 1 \right) & \text{if } \sigma_I^{\text{particle}} > \sigma_c \text{ and } p \geq p_n \text{ and } f_n \leq f_n^{\max} \\ 0 & \text{otherwise} \end{cases} \tag{6.9}$$

where a_n is a material parameter, p_n is the strain nucleation threshold and $f_n^{\max}$ the maximum nucleation porosity. The latter is usually taken equal to the volume fraction of particles that drive void nucleation (i. e. intermetallic particles in the case of the 6061 aluminum alloy).

Table 6.5 displays the calibrated GTN parameters used to model the three studied materials. Void nucleation parameters (a_n, p_n and σ_c) are identified via *insitu* tensile testing in chapter 5. The latter also explains the calibration of void coalescence parameters via a novel cell model. Finally, void growth parameters (q_1 and q_2) are estimated via the universal analytical formula presented in chapter 3. As a reminder, η_{q1} and η_{q2} are parameters that account for the heterogeneous particle distribution and its effect on void growth.

All parameters in table 6.5 are identified in chapter 5 over another 6061-T6 alloy with a slightly different chemical composition (regarding Mg, Si and Fe). As a result, two material parameters in table 6.5 are modified. The first parameter is the f_0 which represents the initial void and Mg_2Si volume fraction. The second parameter is the $f_n^{\max}$ which represents the volume fraction of intermetallic particles. Figure 6.3 confirms

that the T6+HT+$x$hr material studied in this chapter is richer in intermetallic particles than the 6061-T6-BE material studied in chapter 5. Therefore, the volume fraction of constituent particles (Mg_2Si and Al(FeMn)Si) are measured on polished cross-sections (non-deformed area) of tensile samples to adjust f_0 and $f_n^{\max}$ respectively [Petit et al., 2019]. As explained in chapter 5, each of the q-parameters is multiplied by an η factor (*i.e.* η_{q1} q_1 and η_{q2} q_2) to account for the heterogeneous particle distribution in the studied 6061-T6 alloy and its effect on void growth. The studied T6+HT+$x$hr material in this chapter has a higher volume fraction of intermetallic particles and a less heterogeneous particle distribution. This means that the η_{q1} should be lower than the calibrated value found in chapter 5. Therefore, the η_{q1} parameter is to be calibrated over macroscopic tensile and fracture toughness curves presented in section 6.4.3.

Table 6.5: Calibrated GTN parameters for the three studied materials

Pre-existing voids and void nucleation					**Void growth**		**Void coalescence**				**Mesh size**
f_0	Void nucleation law				η_{q1}	η_{q2}	α	β	γ	δ	h
	$f_n^{\max}$	a_n	p_n	σ^{critical}							
%	%	-	%	MPa	-	-	-	-	-	-	μm
0.35	2.15	0.6	2.6	337	1.3	1.0	0.2	2.4	0.01	1.5	100

6.4.3 *Finite element results*

The aim of this section is to fulfill the second objective of this chapter: "is the calibrated GTN model in chapter 5 capable of capturing the effect of hardening on the fracture toughness?" Therefore, this section is divided into two parts. The first part is dedicated to simulating the tested NT samples over the T6+HT+4hr, T6+HT+16hr and T6+HT+2000hr materials. There are no NT tests available for the T6+HT+8hr and T6+HT+12hr materials. The second part is dedicated to simulating the fracture toughness of all T6+HT+$x$hr materials {T6+HT+4hr, T6+HT+8hr, T6+HT+12hr, T6+HT+16hr, T6+HT+4hr}.

Chapter 5 presents the 2D axisymmetric meshes of ST and NT samples. Only one-fourth of each sample is meshed thanks to the symmetries. 8-node 2D hexahedral elements with 4 integration points (reduced integration) are used to mesh the sample. The mesh size is fixed to 100×100 μm^2. All tensile simulations are displacement controlled. Chapter 5 also presents the CT12.5 3D mesh. Only one-fourth of the CT sample is meshed thanks to the symmetries. 8-node 3D hexahedral elements with 8 integration points are used to mesh the sample. The mesh size is fixed to $100 \times 100 \times 100$ μm^3. The used GTN model leads to material softening which results in strain and damage localization within one row of elements. As a result, the simulation results strongly depend on the mesh size. To overcome this issue, models integrating material internal lengths can be used (e. g. Feld-Payet et al., 2011, Mediavilla et al.,

2006). However, these models are still in the development phase. The pragmatic solution chosen in this study is to fix a mesh size along the crack path [Liu et al., 1994; Rousselier, 1987]. The fixed mesh size controls the fracture energy in the case of mesh dependent simulations [Siegmund et al., 2000].

Figure 6.12 displays the simulation results regarding the NT samples of the T6+HT+4hr, T6+HT+16hr and T6+HT+2000hr materials with the elastic–plastic model (a) and the GTN model (b). A good agreement is found between the experiment and model curves. The strain at failure is slightly overestimated in the NT10 and NT4 samples of the T6+HT+16hr. However, the strain at failure is correctly predicted for the NT2 sample of the T6+HT+16hr. The observed results are encouraging. Nevertheless, it is still not clear how the calibrated GTN model differentiates the strain at failure between the studied materials.

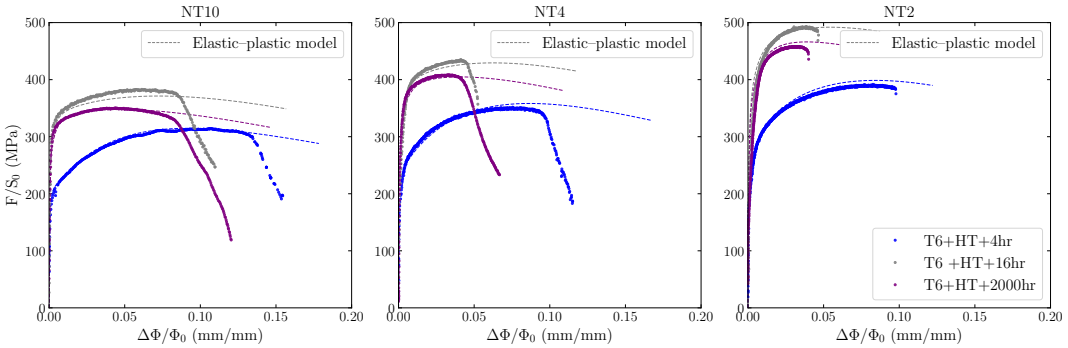

(a) Elastic–plastic FE simulations (without damage)

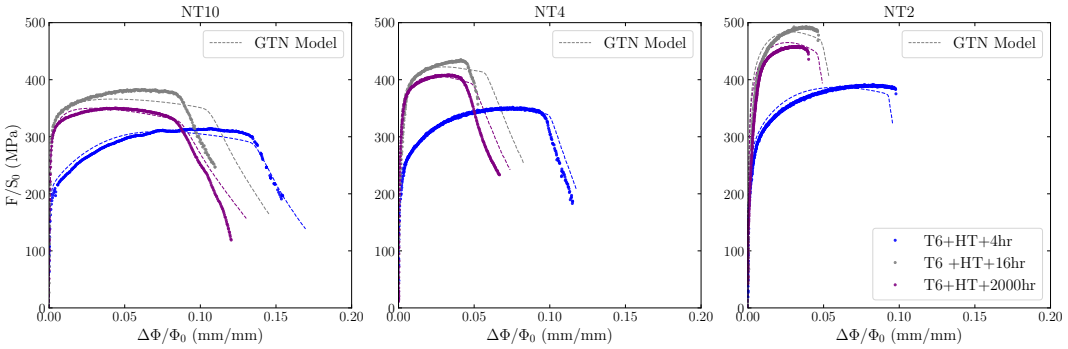

(b) GTN FE simulations

Figure 6.12: Simulated NT tests of three studied materials with a) the elastic–plastic model and b) the GTN model

In order to understand this issue, the CT12.5 samples are modeled and displayed in fig. 6.13. It appears that a good agreement is found between the experiments and the model for the three studied materials. Regarding the T6+HT+4hr material, the simulation is carried twice. The first simulation is performed using the q_1 and q_2

parameters of the T6+HT+4hr material (see q_1 and q_2 of T6+HT+4hrin fig. 6.13). The q_1 and q_2 parameters are a function of the plastic behavior as explained in chapter 3. The second simulation is performed using the q_1 and q_2 parameters of the T6+HT+16hr material (see q_1 and q_2 of T6+HT+16hrin fig. 6.13). As a result, the q_1 and q_2 parameters of the T6+HT+16hr overestimate damage as shown in fig. 6.13. This highlights the fact that the q-parameters that depend on the plastic behavior allow to differentiate between different hardening levels. At this point, the question stated earlier in this chapter can be answered: the GTN model calibrated in chapter 5 is able to capture the effect of hardening on the fracture toughness thanks to the q-parameters that relate hardening and strength to void growth.

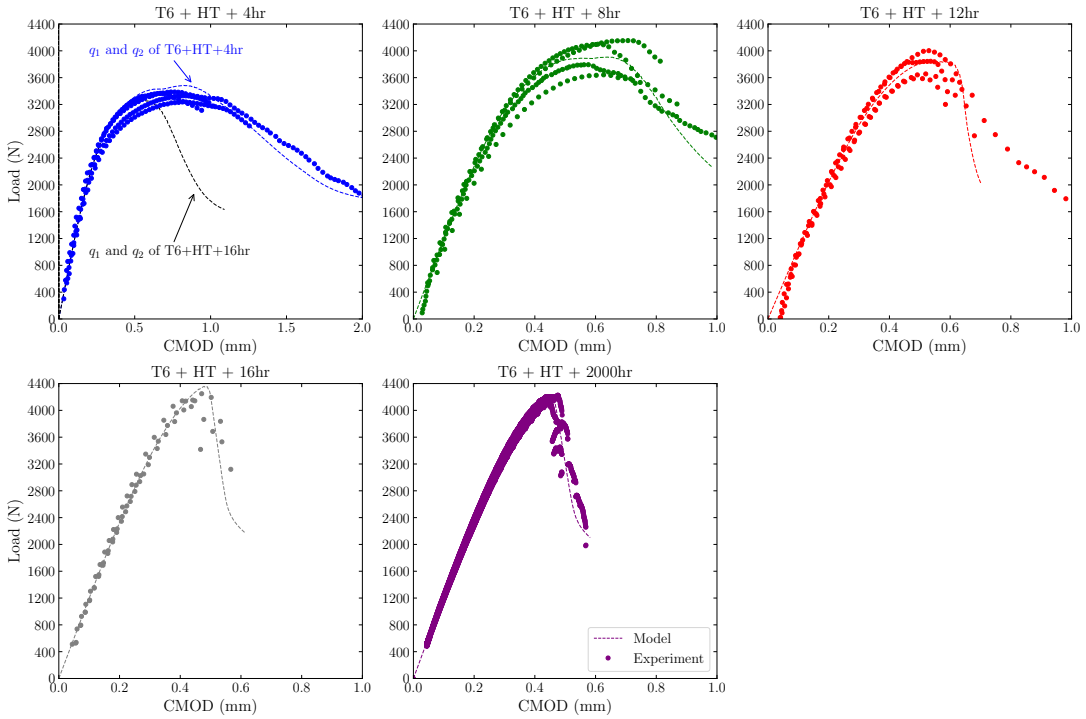

Figure 6.13: Simulated CT tests of three studied materials. The T6+HT+4hr is simulated once with the adequate q_1 and q_2 parameters and a second time with the q_1 and q_2 parameters of the T6+HT+16hr material.

A post-processing routine is applied to all FE simulations presented in fig. 6.13 to calculate the average crack length as a function of time. The average crack increment is equal to a single broken row of elements in the CT sample. A single broken row of elements is equal to at least half of the elements which must be broken (i. e. yield surface tends towards 0). Then, the analytical formulas of the ASTM-1820 standard are used to calculate the J as a function of the crack length Δa. The resulting J-Δa curves are plotted in fig. 6.14 and compared with the experimental curves already presented in fig. 6.9. A good agreement is found between experimental and FE simulation results.

The simulated $J_{0.2}$ values seem to be slightly higher than the experimental values (especially in the T6+HT+12hr and T6+HT+16hr materials). This is confirmed in fig. 6.15. The latter compares the experimental and simulated $J_{0.2}$ values for all age hardened materials. The simulated $J_{0.2}$ values are found above the average given by the dotted line in fig. 6.15. However, since the experimental dispersion is high, the simulated $J_{0.2}$ values are found between the maximum and minimum experimental $J_{0.2}$ values. Figure 6.16 compares the experimental and simulated $\mathrm{d}J/\mathrm{da}$ values for all age hardened materials. The simulated $\mathrm{d}J/\mathrm{da}$ values are found below the average for the T6+HT+12hr and T6+HT+16hr materials given by the dotted line in fig. 6.16. However, a good agreement between the simulated and experimental $\mathrm{d}J/\mathrm{da}$ values is found for all other materials. These results shown in fig. 6.13, fig. 6.15 and fig. 6.16 highlight the fact that the calibrated GTN model is capable of predicting the fracture toughness of materials with different hardening levels.

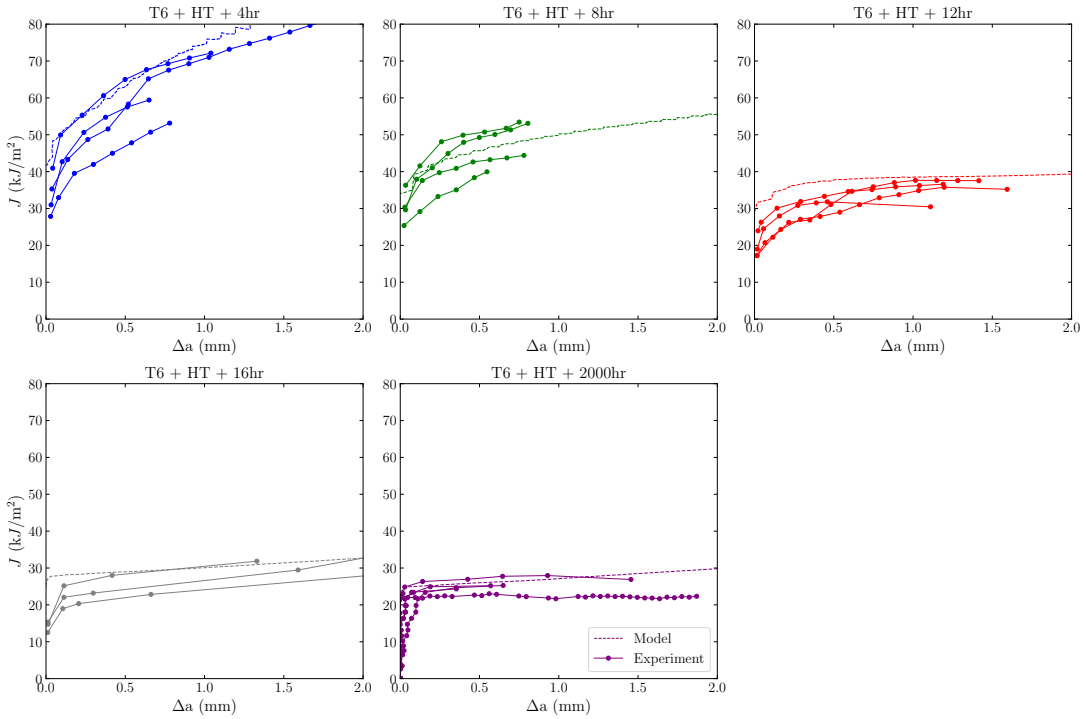

Figure 6.14: J-Δa simulated and experimental curves of the T6+HT+$x$hr tested materials

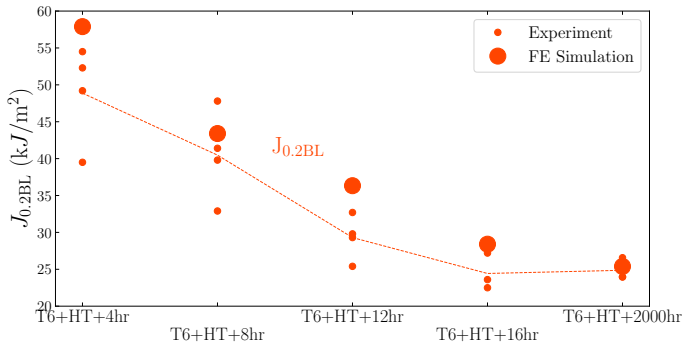

Figure 6.15: Evolution of the experimental versus simulated $J_{0.2}$ as a function of the age hardening time. Experimental values are also presented in fig. 6.10.

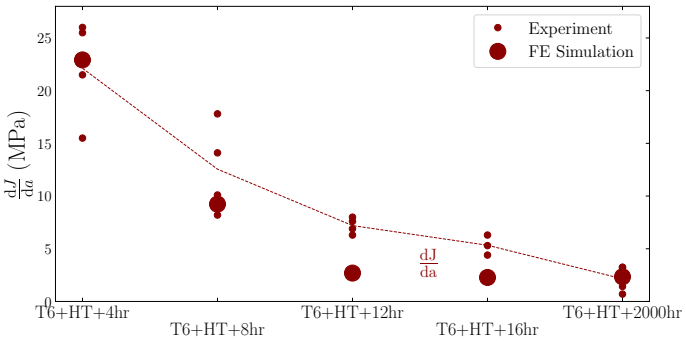

Figure 6.16: Evolution of the experimental versus simulated dJ/da as a function of the age hardening time. Experimental values are also presented in fig. 6.10.

6.5 CONCLUSION

To conclude, this chapter has two main objectives. The first objective is to decorrelate the effect of strengthening and strain hardening drop on the overall fracture toughness. The second objective is to understand if the calibrated GTN model in chapter 5 can predict damage in materials with different hardening levels. In order to fulfill these objectives, a 6061 alloy undergoes an age hardening treatment to produce different strengthening and hardening levels. Six materials are investigated in this study to understand the relation between strength, hardening and fracture toughness.

The experimental results obtained over the studied materials show that the fracture toughness varies accordingly: under-aged (T6+HT+4hr) $>$ over-aged (T6+HT+2000hr) $\geq$ peak-aged (T6+HT+16hr). There is not significant increase in the fracture toughness of the over-aged material (T6+HT+2000hr) with respect to the peak-aged one as discussed in the literature [Dumont et al., 2003]. Even though the under-aged material is less stronger, the hardening capacity is 40% higher in the under-aged with respect to the peak-aged. The surprising fact is that the over-aged material incurs a 4% loss in hardening with respect to the peak-aged material and yet, the over-aged material does

not undergo a drop in toughness with respect to the peak-aged material. Therefore, it is concluded that both strength and hardening have an unequal contribution regarding the overall fracture toughness. In order to understand the order of magnitude of fracture toughness increase/decrease with respect to yield strength and hardening, more materials should be studied. The 6061 alloy can be aged for more than 2000 hours to further decrease the yield strength and hardening capacity. In the future, such results can help confirm the unclear trend observed in the current study.

The finite element results in this chapter show that the calibrated GTN model is capable of predicting damage in materials with different hardening levels. In order to understand the key element that allows to differentiate between hardening levels, the q-parameters of the T6+HT+16hr material are used to simulate crack propagation in the T6+HT+4hr. As a result, void growth is highly overestimated. Therefore, it is concluded that the q-parameters that depend on the plastic behavior produce good estimations of void growth on the microscopic level. On the macroscopic level, a good agreement is found regarding the fracture toughness experiments and simulations.

BIBLIOGRAPHY

ASTM-1820 (2017). *Standard Test Method for Measurement of Fracture Toughness*. Technical report. DOI: 10.1520/E1820-17 (see pp. 168, 172).

ASTM (2015). *Designation: E8/E8M – 13a Standard Test Methods for Tension Testing of Metallic Materials 1*. Technical report. DOI: 10.1520/E0008_E0008M-13A (see p. 168).

Alexander, D. (1993). 'The Effect of Irradiation on the Mechanical Properties of 6061-T651 Aluminum.' In: *Effects of Radiation on Mater.*, pages 1151–1167. DOI: 10.2172/10162906 (see p. 163).

Barsoum, I. and J. Faleskog (2007). 'Rupture mechanisms in combined tension and shear — Experiments.' In: *Int. J. Solids Structures* 44.6, pages 1768–1786 (see p. 171).

Benzerga, A. and J.-B. Leblond (2010). 'Ductile Fracture by Void Growth to Coalescence.' In: *Advances in Applied Mechanics* 44, 169–305 (see p. 171).

Beremin, F. M. (1981). 'Cavity formation from inclusions in ductile fracture of A508 steel.' In: *Met. Trans.* 12A, pages 723–731 (see pp. 177, 178).

Besson, J. (2010). 'Continuum models of ductile fracture: a review.' In: *Int. J. Damage Mech.* 19, pages 3–52 (see p. 171).

Develay, R. (1992). 'Propriétés de l'aluminium et des alliages d'aluminium corroyés.' In: *Techniques de l'ingénieur Métaux et alliages non ferreux* TIB357DUO.m440 (see pp. 163–165, 170).

Dorward, R. and C. Bouvier (1998). 'A rationalization of factors affecting strength, ductility and toughness of AA6061-type AlMgSi(Cu) alloys.' In: *Mater. Sci. Engng A* 254.1, pages 33 –44. DOI: 10.1016/S0921-5093(98)00761-8 (see pp. 164, 170).

Dumont, D. (2001). 'Relations Microstructure / Ténacité dans les alliages aéronautiques de la série 7000.' PhD thesis. Institut National Polytechnique de Grenoble (see p. 165).

Dumont, D. et al. (2003). 'On the relationship between microstructure, strength and toughness in AA7050 aluminum alloy.' In: *Mater. Sci. Engng A* 356.1, pages 326–336. ISSN: 0921-5093. DOI: 10.1016/S0921-5093(03)00145-X (see pp. 165, 173, 174, 183).

Edwards, G. et al. (1998). 'The precipitation sequence in AlMgSi alloys.' In: *Acta Mater.* 46.11, pages 3893 –3904. DOI: 10.1016/S1359-6454(98)00059-7 (see p. 164).

Feld-Payet, S. et al. (2011). 'Finite element analysis of damage in ductile structures using a nonlocal model combined with a three-field formulation.' In: *Int. J. Damage Mech.* 20, pages 655–680 (see p. 179).

Flament, C. (2015). 'Etude des évolutions microstructurales sous irradiation de l'alliage d'aluminium 6061-T6.' PhD thesis. Université Grenoble Alpes (see p. 164).

Hancock, J. and A. Mackenzie (1976). 'Mechanisms of ductile failure in high-strength steels subjected to multi- axial stress states.' In: *J. Mech. Phys. Solids* 24, pages 147–160 (see p. 168).

Ikei, C. et al. (May 2000). 'The Effect of Processing Parameters on the Mechanical Properties and Distortion Behavior of 6061 and 7075 Aluminum Alloy Extrusions.' In: *Aluminium Alloys - Their Physical and Mechanical Properties*. Volume 331. Materials Science Forum. Trans Tech Publications Ltd, pages 663–668. DOI: 10.4028/www.scientific.net/MSF.331-337.663 (see pp. 164, 170).

Kassner, M. et al. (2011). 'A Study of the Quench Sensitivity of 6061-T6 and 6069-T6 Aluminum Alloys.' In: *J. of Metallurgy* 2011, pages 1687–9465. DOI: doi.org/10.1155/2011/747198 (see p. 164).

Kaufman, J. (2000). 'Introduction to Aluminum Alloys and Tempers.' In: ASM International. Chapter Understanding the Aluminum Temper Designation System, pages 39–67. ISBN: 9780871706898 (see p. 165).

King, R. et al. (1969). 'High-Neutron Fluence Damage in an Aluminum Alloy.' In: *J. Nuclear Materials* 35, pages 231–243 (see p. 163).

Kumar, N. et al. (2022). 'A Critical Review on Heat Treatment of Aluminium Alloys.' In: *Materials Today: Proceedings*. ISSN: 2214-7853. DOI: 10.1016/j.matpr.2021.12.586 (see pp. 163, 164).

Lars, L. and R. Nils (2000). 'Precipitation of dispersoids containing Mn and/or Cr in AlMgSi alloys.' In: *MSEA* 283, pages 144–152. DOI: 10.1016/S0921-5093(00)00734-6 (see p. 164).

Lassance, D. et al. (Jan. 2007). 'Micromechanics of room and high temperature fracture in 6xxx Al alloys.' In: *Progress in Materials Science* 52, pages 62–129. DOI: 10.1016/j.pmatsci.2006.06.001 (see pp. 164, 170).

Liu, Y. et al. (1994). 'Mesh–dependence and stress singularity in finite element analysis of creep crack growth by continuum damage mechanics approach.' In: *Eur. J. Mech./A* 13A.3, pages 395–417 (see p. 180).

Maire, E. et al. (2005). 'Damage initiation and growth in metals. Comparison between modelling and tomography experiments.' In: *J. Mech. Phys. Solids* 53, pages 2411–2434 (see pp. 164, 170).

Matsuda, K. et al. (2000). 'Precipitation sequence of various kinds of metastable phases in Al1.0mass% Mg2Sio.4mass% Si alloy.' In: *J. Mater. Sci.* 35, pages 179–189. DOI: 10.1023/A:1004769305736 (see p. 164).

Mediavilla, J. et al. (2006). 'Discrete crack modelling of ductile fracture driven by non-local softening plasticity.' In: *Int. J. Numer. Meth. Engng* 66.4, pages 661–688 (see p. 179).

Mukhopadhyay, P. (2012). 'Alloy Designation, Processing, and Use of AA6XXX Series Aluminium Alloys.' In: *ISRN Metallurgy* 2012. DOI: 10.5402/2012/165082 (see p. 163).

Petit, T. et al. (2018). 'Impact of machine stiffness on "pop-in" crack propagation instabilities.' In: *Eng. Fract. Mech.* 202, pages 405–422 (see pp. 168, 169).

Petit, T. et al. (2019). 'Effect of hardening on toughness captured by stress-based damage nucleation in 6061 aluminum alloy.' In: *Acta Mater.* 180, 349–365. DOI: 10.1016/j.actamat.2019.08.055 (see pp. 164, 167, 170, 176, 179).

Rady, M. et al. (Sept. 2019). 'Effect of Heat Treatment on Tensile Strength of Direct Recycled Aluminium Alloy (AA6061).' In: *Advanced Materials Science*. Volume 961. Materials Science Forum. Trans Tech Publications Ltd, pages 80–87. DOI: 10.4028/www.scientific.net/MSF.961.80 (see p. 163).

Rousselier, G. (1987). 'Ductile fracture models and their potential in local approach of fracture.' In: *Nucl. Eng. Des.* 105, pages 97–111 (see p. 180).

Shen, Y. et al. (2013). 'Three-dimensional quantitative in situ study of crack initiation and propagation in AA6061 aluminum alloy sheets via synchrotron laminography and finite-element simulations.' In: *Acta Mater.* 61, pages 2571–2582. DOI: 10.1016/j.actamat.2013.01.035 (see p. 164).

Shokeir, Z. et al. (2022). 'Edge tracing technique to study post–necking behavior and failure in Al–alloys and anisotropic plasticity in line pipe steels.' In: *Fatigue and Fract. Engng Mater. Struct.*, pages 1–16. DOI: 10.1111/ffe.13754 (see p. 168).

Siegmund, T. and W. Brocks (2000). 'A numerical study on the correlation between the work of separation and the dissipation rate in ductile fracture.' In: *Eng. Fract. Mech.* 67, pages 139–154 (see p. 180).

Steele, D. et al. (Jan. 2007). 'Quantification of grain boundary precipitation and the influence of quench rate in 6XXX aluminum alloys.' In: *Materials Characterization* 58, pages 40–45. DOI: 10.1016/j.matchar.2006.03.007 (see pp. 164, 170).

Totten, G. et al. (2018). 'Encyclopedia of Aluminum and Its Alloys, Two-Volume Set (Print).' In: 1st edition. Metals and Alloys Encyclopedia Collection. CRC Press. Chapter 6XXX Alloys: Chemical Composition and Heat Treatment, pages 1–15. ISBN: 1466510803, 9781466510807 (see p. 164).

Tvergaard, V. and A. Needleman (1984). 'Analysis of the cup–cone fracture in a round tensile bar.' In: *Acta Metall.* 32, pages 157–169 (see p. 177).

Weeks, J. et al. (1993). 'Effects of High Thermal Neutron Fluences on Type 6061 Aluminum.' In: *Effects of Radiation on Mater.*, pages 1168–1182 (see p. 163).

7

PHENOMENOLOGICAL APPROACH FOR MODELING THE RADIATION–INDUCED HARDENING IN 6061 ALUMINUM ALLOYS

RÉSUMÉ

Ce chapitre illustre la méthodologie de développement du modèle phénoménologique élastique-plastique utilisé pour exprimer l'écoulement plastique en fonction de la fluence thermique et de R_Φ. La première étape est liée à un travail de compilation exhaustive des données publiées concernant les essais de traction des éprouvettes 6061-T6 irradiées. Seuls des résultats de traction discrets (valeurs de la limite d'élasticité/résistance mécanique et pourcentage d'allongement) ont été trouvés dans la littérature. Les courbes de traction des éprouvettes irradiés sont absentes de la littérature. En conséquence, le processus d'ajustement d'une loi d'écoulement des contraintes est plus complexe. La deuxième étape est liée à la méthode d'ajustement de la loi d'écoulement des contraintes. Enfin, des simulations par éléments finis sont effectuées en utilisant le modèle développé pour simuler les résultats de traction de la littérature. Le résultat principal est que la loi d'écoulement plastique irradiée développée donne des prédictions précises du comportement élastique-plastique.

7.1 INTRODUCTION

Aluminum alloys are not the best candidates for power nuclear reactors (generating electricity), marine propulsion or high temperature heat process. However, they are identified as excellent candidates for nuclear research reactors NRR. In the latter, temperatures are relatively much lower than in the core of power nuclear reactors. The principal function of NRRs is to generate neutrons for multiple reasons as: production of medical and industrial isotopes, neutron scattering studies and study of radiation effects in candidate materials for power reactors. 80% of the heat in the nuclear core is generated in the fissile materials as a result of the fission reaction. The remaining 20% is in the non-fissile material bombarded by neutrons that generate heat [Farrell, 2012]. While heat is required in power reactors to generate electricity, it is a nuisance product in NRRs. The optimal material for core structural components is the fastest non-fissile material that could get rid of this generated heat. Therefore, aluminum

is the chosen material as it has greatly contributed to the success and longevity of nuclear research reactors [Farrell, 1995].

Aluminum as well as other metals get damaged when bombarded by neutrons produced from the nuclear fission reaction. Neutrons are classified according to their energy and can be fast (0.1-10 MeV), intermediate (10 eV-0.1 MeV) or thermal ($\sim$ 0.025 eV at 20°C) [Azevedo, 2011; Gittus, 1978; Little, 1976]. The damage caused in a 6061 aluminum alloy by neutrons of different energies is explained below:

- Fast neutrons cause damage in metals by displacing atoms in the lattice structure from their initial sites thus creating a disorder. This creates point defects (interstitials and vacancies), one-dimensional defects (dislocations), two-dimensional defects (dislocation loops), and three-dimensional defects (voids and solute rich clusters, precipitates). These defects (except point defects) are assumed to impede the dislocation gliding which hardens the material and decreases its ductility [Azevedo, 2011; Becquart et al., 2010; Little, 1976; Lucas, 1994; Nordlund et al., 2018].

- Thermal neutrons (E $\sim$ 0.025 eV) are responsible for the transmutation of aluminum atoms into silicon atoms as follows:

$$^{27}Al + n_{th} \rightarrow {}^{28}Al + \gamma\,;\ {}^{28}Al \rightarrow {}^{28}Si + e^{-} + \bar{\nu} \tag{7.1}$$

  Si is insoluble in Al below 350°C [Farrell, 2012; Farrell et al., 1970]. One study reported an increase of 7 wt% Si in an irradiated 6061 aluminum alloy at a thermal fluence (irradiation dose) of $341 \times 10^{21}\ n/cm^2$ [Farrell et al., 1979]. In $6xxx$ aluminum alloys, added Si slightly contributes to hardening by the ripening of Mg_2Si particles [Kolluri, 2016]. Excess Si at extremely high thermal fluences are believed to cause a dramatic drop in fracture toughness due to their precipitation at grain boundaries and the change of rupture mode [Alexander, 1999; Weeks et al., 1993].

- Intermediate neutrons are not considered in this study for the sake of simplicity. The considered fast and thermal neutron flux are given specific energy values: $E > 0.1$ MeV for fast neutrons and $E = 0.025$ eV for thermal neutrons. The reason behind the fixed energy values for each type of flux is to compare data from the literature review and to define the ratio of thermal to fast neutrons. This ratio is explained below from both theoretical and phenomenological point of views.

The hardening features explained above assumed no coupling between fast and thermal neutrons. The spectrum effect (i. e. ratio of thermal to fast fluence $R_\Phi = \frac{\Phi_{th}}{\Phi_f}$) is well explained in the literature [Alexander, 1993; Farrel, 2011]. Given two irradiated 6061-T6 alloys at two different R_Φ, the compared mechanical properties at the same thermal fluence are not the same. The alloy irradiated at a higher R_Φ has a lower

hardening level. The following section explains the spectral effect by investigating more closely the combined effect of the two types of neutrons.

7.2 RADIATION DAMAGE IN THE 6061-T6 ALUMINUM ALLOY

7.2.1 *Before irradiation*

The $6xxx$ series is an age hardening AlMgSi alloy widely used in fast neutron reactors. The state T6 refers to a reheat treatment followed by quenching then age hardening. This temper is known as the peak aging as the alloy exhibits the highest strength but a lower fracture toughness than the T4 temper [Develay, 1992; Kaufman, 2000]. The 6061-T6 is a multi-phase alloy of which the mechanical properties are determined by the microstructure and the morphology of its nanophases. During the age hardening process, the Mg_xSi_y strengthening phase nucleates. An optimal age hardening treatment leads to a highly dispersed needle-like coherent β'' phase as shown in fig. 7.1 (a). The β'' phase gives the maximum strengthening (peak-aged alloy) since the precipitates are coherent with the matrix in the direction parallel to the needles and semi coherent in the perpendicular direction [Dubost et al., 1991]. However, since the β'' is a metastable phase, it might be dissolved during irradiation by recoil dissolution [Was, 2017a].

7.2.2 *During and after irradiation*

The atom-fast neutron elastic interaction gives birth to a primary knock-on atom (PKA). The atom is displaced from its initial site and displaces more atoms as it travels in the lattice structure. This domino-like effect is known as the displacement cascade. The PKA terminates as an interstitial that created Frenkel defects (self-interstitial atoms and vacancy pairs) along its passage in the lattice structure. After the ballistic phase, the possible events taking place in a lattice structure are: migration, dissociation (emission of small defects resulting from bigger ones), aggregation of like defects, and annihilation between opposite defects [Becquart et al., 2010]. Figure 7.1 (e,f,g) show the principal defects created by the fast fluence Φ_f and their density as a function of the thermal fluence Φ_{th}. A low R_Φ is compared to a high R_Φ for the purpose of highlighting the spectrum effect on radiation damage. For the moment, the spectrum has no effect on the defects produced by fast neutrons: dislocation lines, loops and cavities. These defects reach a saturation level that depends on the material. The saturation Φ_f is about $\sim 2 \times 10^{26}\ n/m^2$ for steels irradiated at 603 K ($\sim 0.35 T_m$) [Was, 2017b]. Al alloys are expected to saturate at lower fluences due to the low effective displacement energy ($\sim$ 25 eV) compared to Fe ($\sim$ 40 eV) [Farrell, 2012].

The recoil dissolution of the β'' phase is assumed to saturate as well. There is no experimental observations in the literature concerning the evolution of this phase during irradiation. The current hypothesis of recoil dissolution is based on the metastability of the β'' phase and the phase stability under irradiation mechanisms [Was, 2017a].

The Si production is driven by the atom-thermal neutron interaction. Si is insoluble in Al below 350°C [Farrell, 2012; Farrell et al., 1970]. However, dissolved Mg in the Al matrix reacts with the produced Si to create Mg_2Si particles [Kolluri, 2016]. Figure 7.1 (c) shows the evolution of the precipitate size (r) as a function of Φ_{th}. Fast neutrons promote more transport of sputtered Si atoms to ripen precipitates. The comparison of two R_Φs is carried at a fixed Φ_{th}. A high R_Φ indicates a low Φ_f. Therefore, for the low R_Φ, the resulting precipitates are coarser (higher Φ_f). The precipitation density is related to the displacement of Si atoms and the available Mg in the matrix. Given a % wt. of available Mg, a low R_Φ favors the Si atoms transportation and the creation of larger precipitates leading to a lower precipitation density, fig. 7.1 (d). The precipitation rate is assumed to be bi-linear, fig. 7.1 (b). The Mg is not abundant in the Al matrix, which leads to a rapid precipitation rate in the offset irradiation phase till the available Mg is consumed. Beyond this, Si precipitates at grain boundaries at extremely high thermal fluences and is believed to cause a dramatic drop in fracture toughness [Alexander, 1999; Weeks et al., 1993].

Figure 7.1 (h, i) [Farrel, 2011] show the microstructures of an irradiated 6061-T6 alloy at a low and high R_Φ respectively. Figure 7.1 (h) shows relatively coarse precipitates due to the transportation of Si atoms promoted by fast neutrons as illustrated in fig. 7.1 (c). Coarser precipitates lead to a lower relative hardening level when compared to the high R_Φ. The latter results in the relatively finer precipitates shown in fig. 7.1 (i). It is important to note that the hardening level in aluminum alloys is principally affected by the irradiation spectrum rather than fast or thermal fluences separately. Si does not produce as much hardening as point defects. Shearing of soft Si amorphous particles produces low amounts of strain hardening [Kolluri, 2016]. It is concluded that the R_Φ controls the ripening of the Mg_2Si precipitates, which determines the degree of hardening.

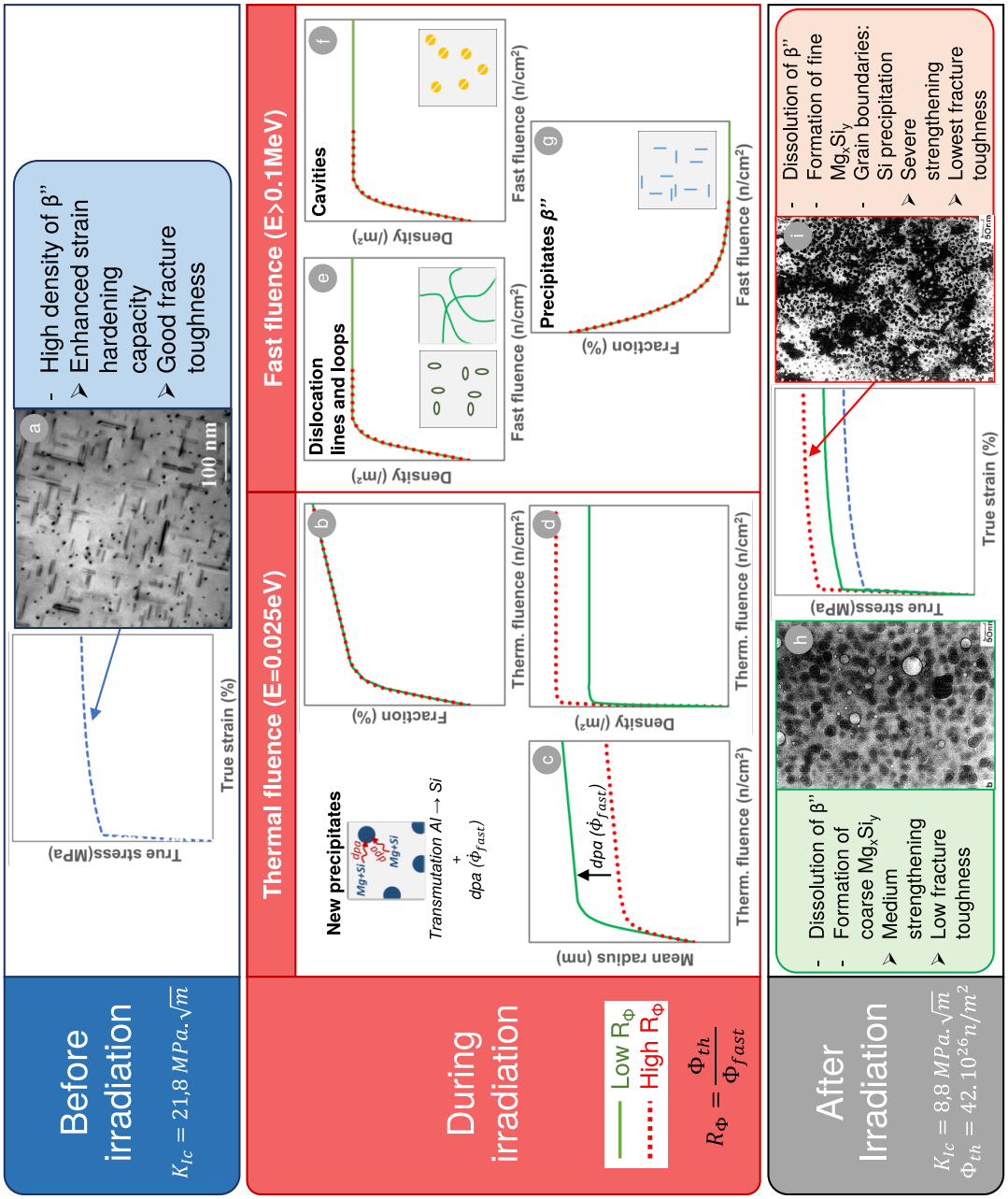

Figure 7.1: Diagram of irradiation hardening in 6xxx aluminum alloys

7.3 MODELING OF THE IRRADIATED PLASTIC FLOW

The objective of this section is to elaborate the two steps in the process of obtaining the phenomenological irradiated plastic flow law. The first step is related to an exhaustive review work that is carried out over published data regarding tensile testing of irradiated 6061-T6 samples. Only discrete tensile results (i. e. values of yield/ultimate tensile strengths and % elongation) are found in the literature. Tensile curves of irradiated samples are missing from the literature. Consequently, the process of fitting a stress flow law is more complex. The second step is related to the stress flow law fitting method.

7.3.1 *Tensile experimental results of irradiated samples*

Results of tensile testing conducted on irradiated 6061-T6 samples are collected from different sources in the literature. These sources published tested samples irradiated in either the HFIR (High Flux Isotope Reactor) or the HFBR (High Flux Beam Reactor). Both are NRR owned by The American Oak Ridge National Laboratory. Figure 7.2 shows the maximum Φ_{th}, Φ_f and the associated R_Φ for each of the tensile testing campaigns [Alexander, 1993, 1999; Farrell et al., 1979, 1975; King et al., 1972; Weeks et al., 1990, 1993]. In other words, the arrows of fig. 7.2 point out to the maximal Φ_{th} and Φ_f of the mostly irradiated specimens. This does not exclude the fact that other specimens at lower fluences are tested during the same campaign.

A total of 120 tensile tests on irradiated 6061 samples are compiled in the current study's database. A wide range of irradiation (50-95°C) and testing temperatures (25-75°C) are considered in the current study. Data is classified only according to the Φ_{th} and R_Φ. All other testing parameters are neglected for the purpose of substantiating a relation between the tensile behavior, Φ_{th} and R_Φ. Tensile testing campaigns are classified according to their R_Φ. Three classes of R_Φ are defined: low ($R_\Phi \leq 2$), medium ($5.4 \leq R_\Phi \leq 7.9$) and high ($R_\Phi = 21$). An inventory of irradiated tensile results is shown in table 7.2.

Results of all gathered tensile tests are scattered as shown in fig. 7.3. The tests are segmented by their R_Φ. The variation observed in the experimental data is due to the differences in alloy composition, irradiation temperature, testing temperature and conditions. The variation is particularly high regarding the total elongation %. Consequently, the total elongation % is excluded during the elaboration of the irradiated plastic flow law. Very few insufficient data points are found in the literature regarding the high R_Φ. This is why their tendencies are excluded from fig. 7.3.

Figure 7.3 show that the 0.2% yield (R_{YS}) and ultimate tensile (R_{UTS}) stresses increase rapidly at the first phase of irradiation and then continue to increase at a lower rate. The uniform (E_U), total (E_T) elongation as well as the strain hardening capacity

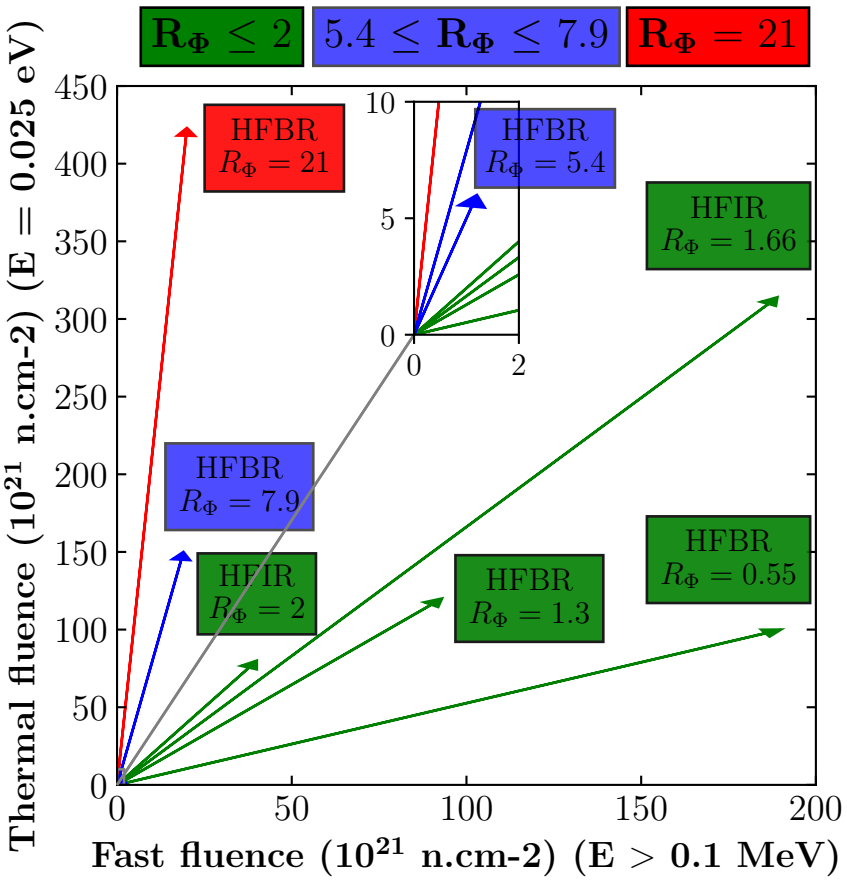

Figure 7.2: Maximum thermal and fast fluence as well as their ratio (R_Φ) for each of the tensile testing campaigns issued from the irradiated samples in NRR: HFIR (High Flux Isotope Reactor) and the HFBR (High Flux Beam Reactor) [Alexander, 1993, 1999; Farrell et al., 1979, 1975; King et al., 1972; Weeks et al., 1990, 1993]

($\frac{R_{UTS}}{R_{YS}}$) drop rapidly at the initial irradiation phase and then decrease gradually. The plotted fits makes it easier to remark the evolution of each tensile property. Figure 7.4 shows the evolution of the ratio of ultimate tensile stress to 0.2% yield stress as a function of thermal fluence. The strain hardening capacity drops significantly for the medium R_Φ which needs to be confirmed by obtaining more experimental data at high thermal fluences.

The fits shown in fig. 7.3 and fig. 7.4 are obtained by a power law described in eq. (7.2) which accounts for the thermal fluence:

$$\begin{aligned} R_{YS}\left(\Phi_{th}\right) &= R_0^{YS} + R_1^{YS} * \left(\Phi_{th}\right)^k \\ R_{UTS}\left(\Phi_{th}\right) &= R_0^{UTS} + R_1^{UTS} * \left(\Phi_{th}\right)^m \\ E_U\left(\Phi_{th}\right) &= E_0^U - E_1^U * \left(\Phi_{th}\right)^n \\ E_T\left(\Phi_{th}\right) &= E_0^T - E_1^T * \left(\Phi_{th}\right)^j \\ \frac{R_{UTS}}{R_{YS}}\left(\Phi_{th}\right) &= \left(\frac{R_{UTS}}{R_{YS}}\right)_0 - \left(\frac{R_{UTS}}{R_{YS}}\right)_1 * \left(\Phi_{th}\right)^a \end{aligned} \tag{7.2}$$

Henceforth, only values of (R^{YS}, R^{UTS}, E^{UE}) are considered for the fitting process of the irradiated plastic flow law. The offset values (R_0^{YS}, R_0^{UTS}, E_0^{UE}) are taken as the average of all unirradiated tensile tests. The bases (R_1^{YS}, R_1^{UTS}, E_1^{UE}) and the exponents (k, m, n) are the unknowns. Given the fact that there is less data for high Φ_{th}, a weighted factor is given to every batch of tests on a range of 50 n.cm^{-2}. This weight is defined as the inverse of the number of tests available for a given increment of 50 n.cm^{-2} of Φ_{th}. Therefore, the few available tests at high Φ_{th} count as more valuable data in the least squares method used to obtain the fits.

At this stage, the evolution of each tensile property is described by a continuous scalar function with a set of three parameters that depend on R_Φ and Φ_{th}. This allows to extrapolate non-tested fluences.

7.3.2 *Irradiated plastic flow law*

In order to model the irradiated plastic flow, the plastic law shown in eq. (7.3) is chosen to simplify the problem to a classical isotropic hardening case. σ_Φ is the flow stress which depends on the thermal fluence.

$$f\left(\underline{\sigma}, R_\Phi, \Phi_{th}\right) = J(\underline{\sigma}) - \sigma_\Phi \tag{7.3}$$

The flow stress is described by eq. (7.4) which depends intrinsically on R_Φ and Φ_{th}. $\sigma_{\Phi\,0}$, $\sigma_{\Phi\,s}$ and p_0 are the three unknowns that guarantee the relation between the plastic behavior, thermal fluence and R_Φ. Therefore, the next step is to define the evolution of each of three unknowns as a function of R_Φ and Φ_{th}.

$$\sigma_\Phi\left(p\right) = \sigma_{\Phi\,0} + \left(\sigma_{\Phi\,s} - \sigma_{\Phi\,0}\right)\left(1 - e^{-\frac{p}{p_0}}\right) \tag{7.4}$$

Three equations are needed to solve for the three unknowns: $\sigma_{\Phi\,0}$, $\sigma_{\Phi\,s}$ and p_0. The equations are written as shown in eq. (7.6). In the first two equations, the true stress and strain were substituted in eq. (7.4). The two known states are:

1. The engineering stress corresponding to a 0.2% of engineering strain. Both are converted to be expressed as true stress and true strain: ($R_{YS}(1 + 0.002)$, $ln(1 + 0.002)$).

2. The maximum engineering stress corresponding to a % of uniform elongation. Both are converted to be expressed as true stress and true strain: $(R_{UTS}(1+E_U),\ ln(1+E_U))$.

The third equation is obtained by the Considère tensile instability criterion defined as [Considère, 1885]:

$$\frac{d\sigma}{d\varepsilon}\left(ln(1+E_U)\right) = \sigma\left(ln(1+E_U)\right) \tag{7.5}$$

$$\begin{aligned}
\sigma_\Phi(ln(1+0.002)) &= R_{YS}(1+0.002)\\
\sigma_\Phi(ln(1+E_U)) &= R_{UTS}(1+E_U)\\
\sigma_\Phi\left(ln(1+E_U)\right) &= \frac{d\sigma_\Phi}{dp}\left(ln(1+E_U)\right)
\end{aligned} \tag{7.6}$$

The set of three equations with three unknowns is solved over a range of given Φ_{th}. A range of Φ_{th} between 0 and $500\times10^{21}\ n/cm^2$ is chosen for $R_\Phi \leq 2$ since enough experimental data is available for high fluences. A range of Φ_{th} between 0 and $200\times10^{21}\ n/cm^2$ is chosen for $5.4 \leq Rphi \leq 7.9$ since less experimental data is available for high fluences. For each Φ_{th}, a set of R_{YS}, R_{UTS}, E_U is obtained by using eq. (7.2), then substituted in eq. (7.6) to obtain a triplet of $\sigma_{\Phi\,0}$, $\sigma_{\Phi\,s}$ and p_0 to be used in the irradiated plastic flow law in eq. (7.4).

Three equations are used to fit the evolution of each of $\sigma_{\Phi\,0}$, $\sigma_{\Phi\,s}$ and p_0 respectively as a function of Φ_{th} as shown in fig. 7.5 and eq. (7.7). For simplicity, $\sigma_{\Phi\,0}$ and $\sigma_{\Phi\,s}$ are hereby noted σ_0 and σ_s respectively:

$$\begin{aligned}
\sigma_0(\Phi_{th}) &= (\sigma_0)_0 + (\sigma_0)_1 * (\Phi_{th})^q\\
\sigma_s(\Phi_{th}) &= (\sigma_s)_0 + (\sigma_s)_1 * (\Phi_{th})^r\\
p_0(\Phi_{th}) &= a(\Phi_{th}) + b(\Phi_{th})^2 + c(\Phi_{th})^3 + d(\Phi_{th})^4 + e(\Phi_{th})^5 + f
\end{aligned} \tag{7.7}$$

The coefficients of eq. (7.7) are noted in table 7.1 and used to plot the evolution of σ_0, σ_s and p_0 for 2 ranges of R_Φ in fig. 7.5. σ_0 and σ_s have the same magnitude and units as R_{YS} and R_{UTS} respectively. However, p_0 cannot be compared to E_U as p_0 is not a strain measurement. p_0 is a parameter which describes the rate at which $\sigma_\Phi\,(p)$ tends to $\sigma|_{\varepsilon_\infty}$ (i. e. true stress when true strain tends to ∞).

7.3.3 *Verification of the developed irradiated plastic flow law*

The aim of this section is to verify that the developed irradiated plastic flow law results in accurate predictions of the elastic–plastic behavior. Therefore, two checks are carried out in this section.

Table 7.1: Parameters used to simulate the elastic–plastic behavior of an irradiated 6061-T6. Given R_Φ and Φ_{th}, a triplet of $\sigma_{\Phi\,0}$, $\sigma_{\Phi\,s}$ and p_0 are obtained to use eq. (7.4)

	$\boldsymbol{\sigma_0} = (\sigma_0)_0 + (\sigma_0)_1 * (\Phi_{th})^q$			$\boldsymbol{\sigma_s} = (\sigma_s)_0 + (\sigma_s)_1 * (\Phi_{th})^r$		
	$(\sigma_0)_0$	$(\sigma_0)_1$	q	$(\sigma_s)_0$	$(\sigma_s)_1$	r
$R_\Phi \leq 2$	270	21.76	0.37	339	17.00	0.38
$5.4 \leq R_\Phi \leq 7.9$		24	0.44		17.61	0.46

	$\boldsymbol{p_0} = a(\Phi_{th}) + b(\Phi_{th})^2 + c(\Phi_{th})^3 + d(\Phi_{th})^4 + e(\Phi_{th})^5 + f$					
	a	b	c	d	e	f
$R_\Phi \leq 2$	5.94×10^{-5}	-5.94×10^{-7}	2.71×10^{-9}	-5.55×10^{-12}	4.56×10^{-15}	3.54×10^{-02}
$5.4 \leq R_\Phi \leq 7.9$	-3.80×10^{-4}	5.57×10^{-6}	-3.49×10^{-8}	7.95×10^{-11}	0	2.37×10^{-02}

The first check aims to verify that eq. (7.4) results in the expected global trends: increase in strength and decrease in hardening capacity as a function of Φ_{th} (for both ranges of R_Φ). Figure 7.6 shows the evolution of real stress as a function of the plastic deformation using the parameters σ_0, σ_s and p_0 of four chosen thermal fluences: 0, 10, 50 and $100 \times 10^{21}\ n/cm^2$. As expected, the true yield stress and the $\sigma|_{\varepsilon_\infty}$ increase as the Φ_{th} increases while the hardening capacity decreases. Moreover, for a given Φ_{th} (except $\Phi_{th} = 0$), the higher the R_Φ, the higher the irradiation hardening level.

The second check aims to verify if the irradiated plastic predicts the irradiated tensile properties in the literature. In order to do so, finite element simulations are carried out using the flow rule in eq. (7.4) to simulate a simple tensile sample. The finite element mesh and the boundary conditions are illustrated in chapter 5. The same exact simulation is repeated over a given range of Φ_{th} (between 0 and $500 \times 10^{21}\ n/cm^2$ for $R_\Phi \leq 2$ and between 0 and $100 \times 10^{21}\ n/cm^2$ for $5.4 \leq R_\Phi \leq 7.9$) in order to plot the results shown in fig. 7.7. The latter also shows the experimental data regarding the 0.2% yield (R_{YS}), ultimate tensile (R_{UTS}) stresses and the uniform elongation (E_U). These experiments regarding ($R_\Phi \leq 2$) are already presented in fig. 7.3. The simulation results indicate a high level of confidence in the developed phenomenological irradiated plastic flow rule.

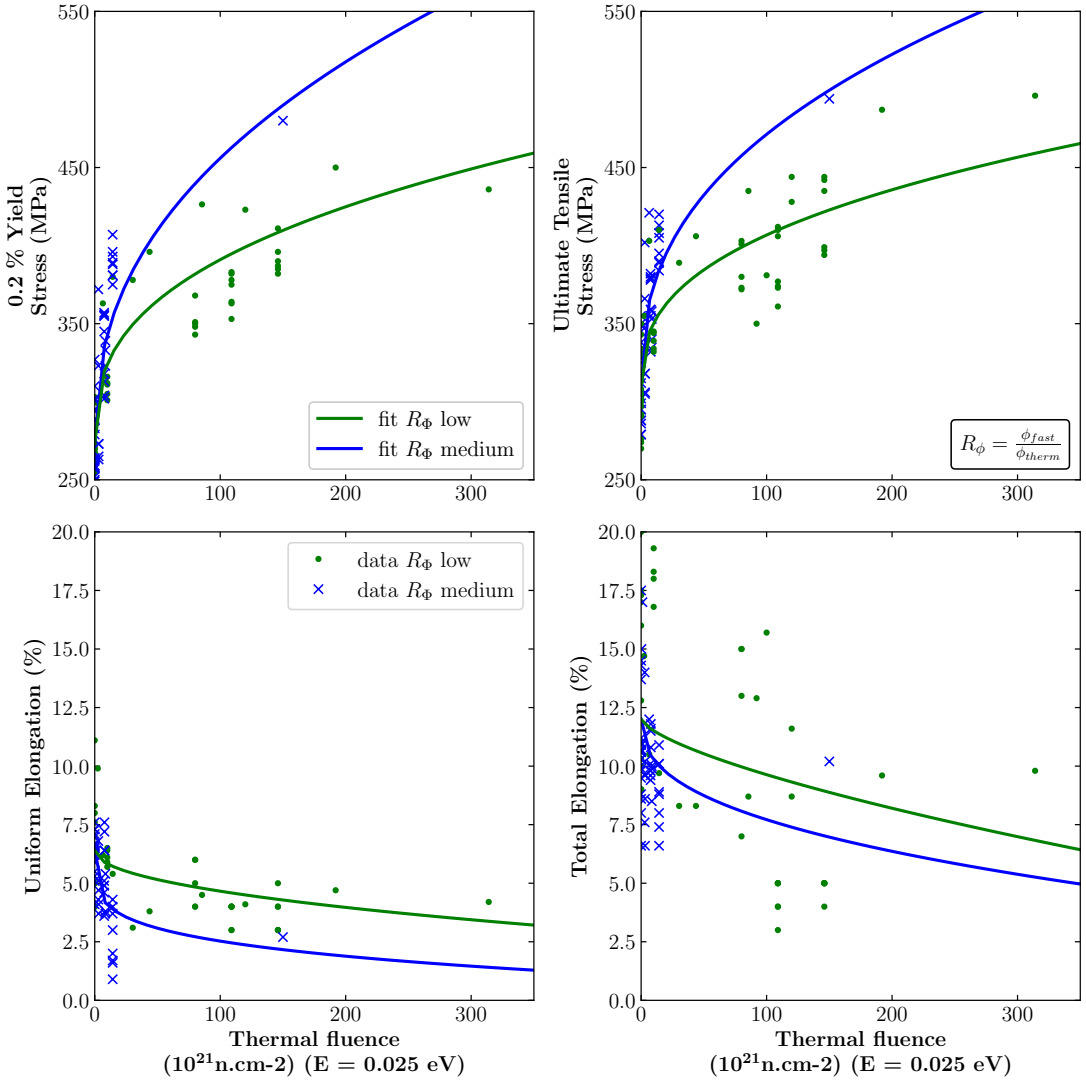

Figure 7.3: Scattered data of tensile tests from the literature and the corresponding fit describing the evolution of each tensile property as a function of the thermal fluence [Alexander, 1993, 1999; Farrell et al., 1979, 1975; King et al., 1972; Weeks et al., 1990, 1993]

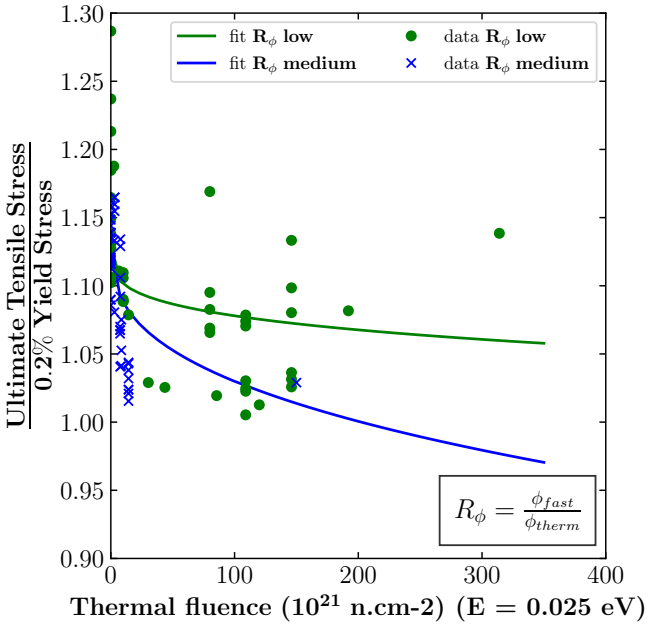

Figure 7.4: Strain hardening capacity evolution as a function of thermal fluence [Alexander, 1993, 1999; Farrell et al., 1979, 1975; King et al., 1972; Weeks et al., 1990, 1993]

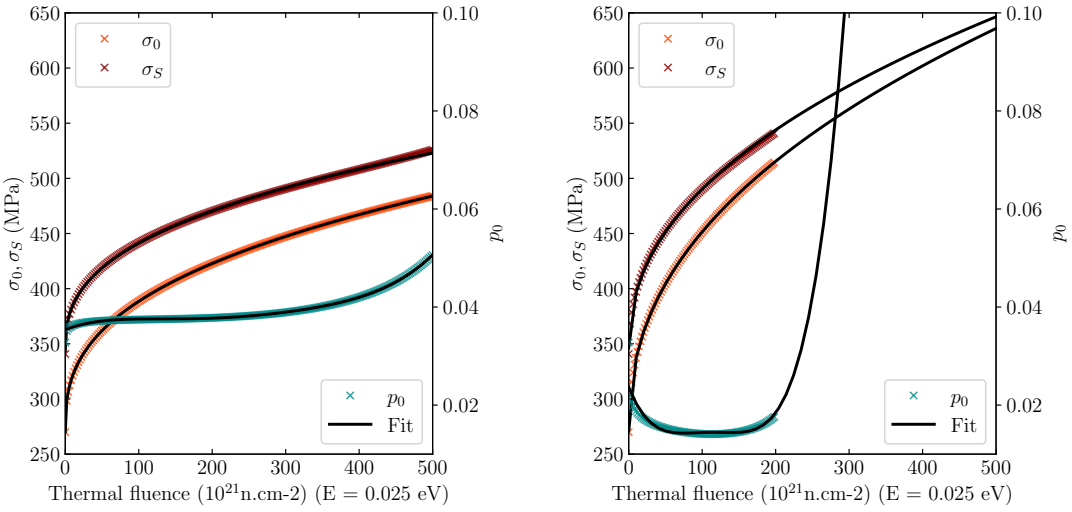

(a) $R_\Phi \leq 2$ (b) $5.4 \leq R_\Phi \leq 7.9$

Figure 7.5: Evolution of σ_0, σ_s and p_0 as a function of Φ_{th}. Values are obtained by solving eq. (7.6).

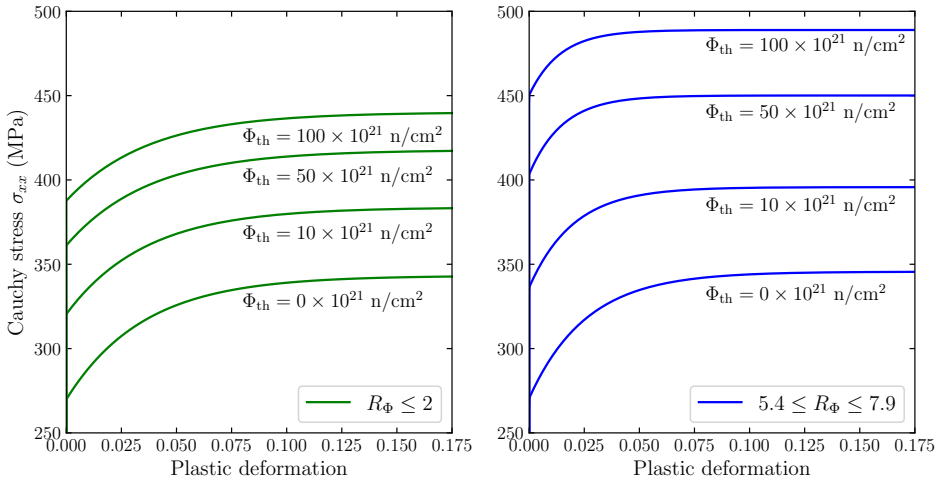

Figure 7.6: Analytical solution of eq. (7.4) given the parameters from eq. (7.7) for four chosen Φ_{th} and two studied ratios of thermal to fast fluence ($R_\Phi = \Phi_{th}/\Phi_f$)

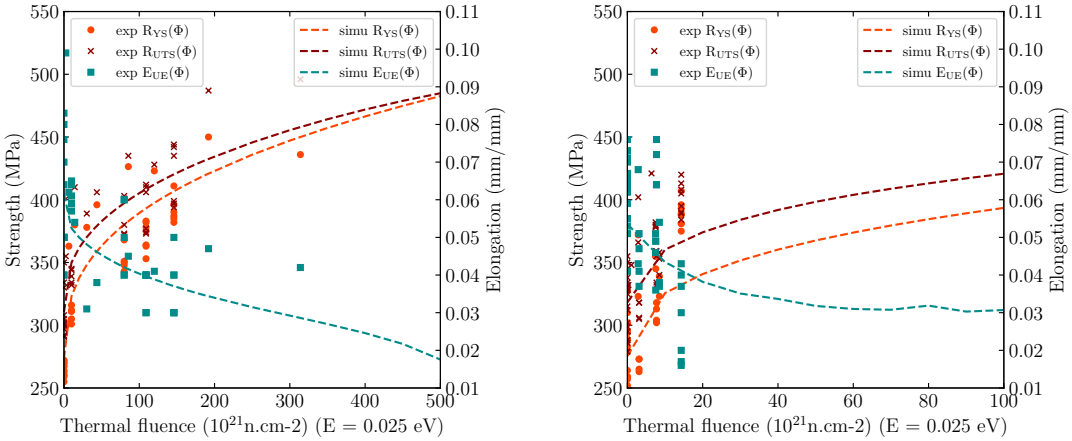

(a) $R_\Phi \leq 2$ (b) $5.4 \leq R_\Phi \leq 7.9$

Figure 7.7: Evolution of the three parameters of the irradiation plastic flow law: ($\sigma_{\Phi\,0}$, $\sigma_{\Phi\,s}$ and p_0) as a function of Φ_{th}. The experimental data is converted to true stresses and scattered in the figure. The simulated trends are obtained by FE simulations carried out every $\Phi_{th} = 10 \times 10^{21}$ over the studied range.

7.4 CONCLUSION

To conclude, neutron radiation has a significant effect on the strength and ductility of the 6061 aluminum alloy. 120 tensile tests on irradiated 6061 samples are compiled from the literature to be analyzed and to develop the irradiated plastic flow model. The compiled data show that the average yield strength, ultimate strength and % uniform elongation of the unirradiated alloy is 273 MPa, 310 MPa and 6.4% respectively. The increase/decrease in these tensile properties depends on the R_Φ. For instance, at $\Phi_{th} = 100 \times 10^{21}\ n/cm^2$ and $R_\Phi \leq 2$, the increase in yield and ultimate strength is 43% and 31% respectively while the decrease in the % uniform elongation is 28%. However, at $\Phi_{th} = 100 \times 10^{21}\ n/cm^2$ and $5.4 \leq R_\Phi \leq 7.9$, an increase of 67% and 52% is observed in the yield and ultimate strengths respectively while a decrease of 61% is observed regarding the % uniform elongation.

The stress—strain curves of the 120 tensile tests are missing in the literature. Only discrete tensile results (i. e. values of yield/ultimate tensile strengths and % elongation) are found in the literature. Consequently, the process of fitting a stress flow law is more complex and is explained above in details. The outcome model is shown in Equation (7.4) which is used to model the elastic–plastic behavior of the irradiated 6061-T6. For a given simulation, the R_Φ and Φ_{th} are known. Equation (7.4) is used to calculate the flow stress as a function of the plastic deformation. Equation (7.4) requires three entry parameters: σ_0, σ_s and p_0. Therefore, the following steps are followed:

1. R_Φ is used to choose the set of parameters from table 7.1 needed for eq. (7.7).
2. Φ_{th} is injected in eq. (7.7) to obtain a triplet of σ_0, σ_s and p_0.
3. $\sigma_{\Phi\,0}$, $\sigma_{\Phi\,s}$ and p_0 are then replaced in eq. (7.4) to estimate the plastic flow.

A check is carried out to verify that the irradiated plastic flow model predicts the tensile properties found in the literature. The model results in good agreement with experimental results which confirms that it can be used later to simulate the fracture toughness of the irradiated material.

APPENDIX

Table 7.2 shows an inventory of irradiated tensile results in the literature. The irradiated plastic flow developed in this chapter is based on these results. Due to the lack of tensile stress—strain curves in the literature, the yield strength (R_{YS}), ultimate tensile strength (R_{UTS}) and the uniform elongation % (E_U) in table 7.2 are used to calibrate the parameters of the irradiated plastic flow as explained above. Some data is missing in some articles as the R_{YS} and R_{UTS} in the work of Weeks et al., 1990, 1993.

Table 7.2: Inventory of irradiated tensile results in the literature. The yield and ultimate tensile strengths are noted R_{YS} and R_{UTS} respectively. The uniform and total elongation % are noted E_U and E_T respectively.

Reference	Φ_{th} (n.cm^{-2})	Test temp.(°C)	R_{YS} (MPa)	R_{UTS} (MPa)	E_U (%)	E_T (%)
[Weeks et al., 1990] $R_\Phi = 5.4$	0	23	-	334, 350, 330	-	17.5, 11.0, 10.3
	2.70×10^{20}	23	-	332	-	15.0
	1.07×10^{21}	23	-	348	-	17.0
	6.40×10^{21}	23	-	421	-	12.0
[Alexander, 1993, 1999] $R_\Phi = 2$	0	26	270, 255, 261, 267, 268, 260	301, 297, 300, 302, 305, 308	7.0, 8.0, 8.3, 6.4, -, -	20.0, 17.0, 20.7, 17.3, -, -
	1×10^{22}	26	311, 312, 301, 316, 305	339, 345, 334, 344, 332	6.5, 6.4, 5.7, 6.1, 5.9	20.3, 18.3, 18.0, 16.8, 19.3
	8×10^{22}	26	343, 368, 348, 351, 350	401, 403, 372, 380, 373	4.0, 5.0, 4.0, 6.0, 6.0	-, 15.0, 7.0, 13.0, 15.0
[Weeks et al., 1990] $R_\Phi = 0.55$	9.20×10^{22}	23	-	350	-	12.9
	1.00×10^{23}	23	-	381	-	15.7
[Weeks et al., 1990] $R_\Phi = 1.3$	1.20×10^{23}	23	-	428	-	11.6
[Weeks et al., 1990] $R_\Phi = 7.9$	1.50×10^{23}	23	-	494	-	10.2
[Farrell et al., 1979] $R_\Phi = 2$	0	23	248, 303	313, 343	7.6, 11.1	12.8, 16.0
	2.43×10^{21}	23	299	355	9.9	14.7

Reference	Φ_{th} (n.cm^{-2})	Test temp.(°C)	R_{YS} (MPa)	R_{UTS} (MPa)	E_U (%)	E_T (%)
	6.47×10^{21}	23	363	403	6.2	10.5
	1.43×10^{22}	23	380	410	5.4	9.7
	3.03×10^{22}	23	378	389	3.1	8.3
	4.37×10^{22}	23	396	406	3.8	8.3
	8.55×10^{22}	23	426	435	4.5	8.7
	1.20×10^{23}	23	423	444	4.1	8.7
	1.92×10^{23}	23	450	487	4.7	9.6
	3.14×10^{23}	23	436	496	4.2	9.8
[Weeks et al., 1993] $R_\Phi = 21$	0	23	-	326, 346	-	11.2, 10.6
	4.70×10^{22}	23	-	423	-	17.0
	1.71×10^{23}	23	-	560	-	8.4
	3.21×10^{23}	23	-	590	-	8.8
	4.23×10^{23}	23	-	670	-	7.1

BIBLIOGRAPHY

Alexander, D. (1993). 'The Effect of Irradiation on the Mechanical Properties of 6061-T651 Aluminum.' In: *Effects of Radiation on Mater.*, pages 1151–1167. DOI: 10.2172/10162906 (see pp. 189, 193, 194, 198, 199, 202).

Alexander, D. (1999). 'The Effect of Irradiation on the Mechanical Properties of 6061-T651 Aluminum Base Metal and Weldments.' In: *Effects of Radiation on Mater.*, pages 1027–1044. DOI: 10.1520/STP13918S (see pp. 189, 191, 193, 194, 198, 199, 202).

Azevedo, C. (2011). 'A review on neutron-irradiation-induced hardening of metallic components.' In: *Eng. Fail. Anal.* 18.8, pages 1921 –1942. ISSN: 1350-6307. DOI: 10.1016/j.engfailanal.2011.06.008 (see p. 189).

Becquart, C. et al. (2010). 'Modeling the long-term evolution of the primary damage in ferritic alloys using coarse-grained methods.' In: *Journal of Nuclear Materials* 406.1, pages 39 –54. DOI: 10.1016/j.jnucmat.2010.05.019 (see pp. 189, 190).

Considère, A. (1885). 'Mémoire sur l'emploi du fer et de l'acier dans les constructions.' In: *Annales des ponts et chaussées*, pages 574–775 (see p. 196).

Develay, R. (1992). 'Propriétés de l'aluminium et des alliages d'aluminium corroyés.' In: *Techniques de l'ingénieur Métaux et alliages non ferreux* TIB357DUO.m440 (see p. 190).

Dubost, B. and P. Sainfort (1991). 'Durcissement par précipitation des alliages d'aluminium.' In: *Techniques de l'ingénieur Méthodes de caractérisation et d'analyse des métaux et alliages* TIB532DUO.m240 (see p. 190).

Farrel, K. (2011). 'A Spectral Effect on Phase Evolution in Neutron-Irradiated Aluminum?' In: *MRS Proceedings*. Volume 373. DOI: 10.1557/PROC-373-165 (see pp. 189, 191).

Farrell, K. (1995). 'Assessement of aluminum structural materials for service within the ANS reflector vessel.' In: DOI: 10.2172/201578 (see p. 189).

Farrell, K. (2012). 'Performance of Aluminum in Research Reactors.' In: *Comprehensive Nuclear Materials*, 147–175. DOI: 10.1016/B978-0-08-056033-5.00113-0 (see pp. 188–191).

Farrell, K. and R. King (1979). 'Tensile Properties of Neutron-Irradiated 6061 Aluminum Alloy in Annealed and Precipitation-Hardened Conditions.' In: *Effects of Radiation on Mater.*, pages 440–449. DOI: 10.1520/STP38180S (see pp. 189, 193, 194, 198, 199, 202).

Farrell, K. and A. Richt (1975). 'Postirradiation properties of the 6061-T6 aluminum High Flux Isotope Reactor hydraulic tube.' In: *American Society for Testing and Materials, Special Technical Publication*, pages 311–325. DOI: 10.1520/STP33695S (see pp. 193, 194, 198, 199).

Farrell, K. et al. (1970). 'Transmutation-produced silicon precipitates in irradiated aluminum.' In: *Metallography* 3.3, pages 275 –284. DOI: 10.1016/0026-0800(70)90015-7 (see pp. 189, 191).

Gittus, J. (1978). *Irradiation effects in crystalline solids*. United Kingdom: Applied Science Publishers. ISBN: 0 85334 778 6 (see p. 189).

Kaufman, J. (2000). 'Introduction to Aluminum Alloys and Tempers.' In: ASM International. Chapter Understanding the Aluminum Temper Designation System, pages 39–67. ISBN: 9780871706898 (see p. 190).

King, R. et al. (1972). 'Neutron irradiation damage in a precipitation-hardened aluminum alloy.' In: *Symposium on the effects of radiation on structural materials*. Volume 14 (see pp. 193, 194, 198, 199).

Kolluri, M. (2016). 'Neutron Irradiation Effects in 5xxx and 6xxx Series Aluminum Alloys: A Literature Review.' In: *Radiation Effects in Mat.*, pages 393–411. DOI: 10.5772/63294 (see pp. 189, 191).

Little, E. A. (1976). 'Neutron-irradiation hardening in irons and ferritic steels.' In: *Int. Mater. Rev.* 21.1, pages 25–60. DOI: 10.1179/imtr.1976.21.1.25 (see p. 189).

Lucas, G. (1994). 'Effects of radiation on the mechanical properties of structural materials.' In: *J. Nuclear Materials* 216, pages 322 –325. DOI: 10.1016/0022-3115(94)90018-3 (see p. 189).

Nordlund, K. et al. (2018). 'Primary radiation damage: A review of current understanding and models.' In: *J. Nuclear Materials* 512, pages 450 –479. DOI: 10.1016/j.jnucmat.2018.10.027 (see p. 189).

Was, G. (2017a). 'Fundamentals of Radiation Materials Science.' In: Springer-Verlag New York. Chapter 9, pages 485–584. DOI: 10.1007/978-1-4939-3438-6 (see pp. 190, 191).

Was, G. (2017b). 'Fundamentals of Radiation Materials Science.' In: Springer-Verlag New York. Chapter 2, pages 3–76. DOI: 10.1007/978-1-4939-3438-6 (see p. 190).

Weeks, J. et al. (1990). 'Effects of High Thermal and High Fast Fluences on the Mechanical Properties of Type 6061 Aluminum on the HFBR.' In: *Effects of Radiation on Mater.* 2, pages 441–452 (see pp. 193, 194, 198, 199, 201, 202).

Weeks, J. et al. (1993). 'Effects of High Thermal Neutron Fluences on Type 6061 Aluminum.' In: *Effects of Radiation on Mater.*, pages 1168–1182 (see pp. 189, 191, 193, 194, 198, 199, 201, 203).

8

NEUTRON RADIATION EFFECT ON THE FRACTURE BEHAVIOR OF THE 6061 ALUMINUM ALLOY

RÉSUMÉ

Ce chapitre est le résultat final des chapitres précédents. Le modèle d'endommagement calibré est couplé avec la loi d'écoulement élastique-plastique phénoménologique pour simuler la ténacité de l'alliage 6061-T6 irradié. Compte tenu de l'objectif identifié, ce chapitre est divisé en deux sections. La première section présente les résultats expérimentaux des éprouvettes de traction irradiés (testées au CEA) ainsi que les résultats de ténacité publiés dans la littérature. La deuxième section couvre les simulations par éléments finis effectuées sur des éprouvettes de traction et de CT pour prédire la ténacité du matériau irradié.

Très peu de données concernant la ténacité du matériau irradié sont publiées dans la littérature. Les données sont compilées et analysées de manière approfondie. Deux tendances opposées sont observées. Premièrement, une stabilité de la ténacité en fonction de la fluence thermique. Deuxièmement, une chute de la ténacité lorsque la fluence thermique augmente. Deux hypothèses sont formulées pour expliquer les tendances mentionnées ci-dessus. La première hypothèse explique la première tendance (ténacité stable). On suppose que l'augmentation de la limite d'élasticité après irradiation compense la diminution du durcissement, ce qui entraîne une stabilité de la ténacité. La deuxième hypothèse explique la deuxième tendance (baisse de la ténacité). Il est supposé, sur la base de quelques preuves expérimentales dans la littérature, que le Si transmuté précipite aux joints de grains, ce qui fragilise le matériau et peut conduire à une séparation intergranulaire.

La première hypothèse est confirmée par la simulation de la ténacité à la rupture d'éprouvettes Le modèle d'endommagement calibré dans chapter 5 est utilisé sans changement. Les résultats de la simulation FE confirment que la ténacité à la rupture ne diminue pas après irradiation. La deuxième hypothèse est mise en oeuvre en modifiant les paramètres d'endommagement utilisés dans la simulation de la ténacité des éprouvettes CT12.5. La porosité critique qui définit le début de la coalescence est diminuée en fonction du Φ_{th}. Le taux de croissance de la porosité entre le début de la coalescence et la rupture du matériau est augmenté en fonction de Φ_{th}. Ces deux modifications sont basées sur les très rares preuves expérimentales de la littérature concernant l'effet de fragilisation du Si transmuté. À ce stade, il est difficile de confirmer quelle tendance observée représente le cas réel. La réalité peut être plus complexe qu'elle n'est supposée dans cette thèse. Cela signifie qu'une ténacité stable

ou une baisse de celle-ci pourrait dépendre des conditions d'irradiation (R_Φ, Φ_{th} et température) mais aussi de la composition chimique de l'alliage d'aluminium. Cependant, étant donné le peu de données concernant la ténacité à la rupture et l'analyse de cette thèse, on peut conclure que la ténacité à la rupture n'est pas beaucoup affectée par l'irradiation. On peut observer une diminution de la ténacité à la rupture qui dépend des conditions d'irradiation et du matériau.

8.1 INTRODUCTION

The evolution of fracture toughness as a function of the radiation dose in the 6061 aluminum alloy is discussed earlier in chapter 2. Two opposite trends are observed. The first trend is a stable fracture toughness as a function of the radiation dose. The second trend is a drop in fracture toughness of the irradiated material. In addition, there are two main conclusions that can be drawn based on the presented fracture toughness results. Firstly, very few results are found in the literature. This makes it difficult to validate the first or second trend. Secondly, some important factors (non-exhaustive list) affect the accuracy of fracture toughness results and must be considered: thermal fluence (Φ_{th}), spectrum ($R_\Phi = \Phi_{th}/\Phi_f$), irradiation temperature, specimen type, machining, and testing conditions (i. e. machining carried out before or after irradiation). The ASTM 1820 standard [ASTM-1820, 2017] define the specimens used for fracture toughness measurement: Single Edge Bending, Compact Tension (CT) and Disk Compact Tension. Such specimens are designed for crack propagation which is used to estimate the resistance to crack initiation and the tearing modulus (i. e. resistance to crack propagation). Other specimens (e. g. Impact specimens) can be used to estimate the resilience but could not provide the tearing modulus. Therefore, specimens listed in the ASTM 1820 standard are generally preferred to study fracture toughness. Taking these factors into consideration, data in the literature regarding the fracture toughness of the irradiated 6061 aluminum alloy are commented below:

- Weeks et al., 1993: study 6061-T6 miniature 3 mm thick notched Charpy impact specimens machined from irradiated CRDF tubes (i. e. control rod drive follower tubes, irradiation temperature = 50°C) found in the HFBR at Brookhaven National Laboratory, USA. Specimens are cut from areas of the tube where the thermal fluence is estimated to be $\Phi_{th} = 420 \times 10^{21}\ n/cm^2$ and the fast fluence to be $\Phi_f = 20 \times 10^{21}\ n/cm^2$ ($E > 0.1$ MeV). Impact testing is carried out in a hot cell (a chamber dedicated to irradiated material testing) using the ASTM E23 standard and a Tinius Olsen impact tester (designed for testing plastics and adapted for aluminum alloys). Results from this study cannot be compared to

other data in the literature since the thermal fluence and R_Φ are significantly high (i. e. R_Φ 10 times higher than the two studies discussed below). Moreover, results regarding the unirradiated samples cannot be compared to other studies discussed below since the tested specimens are different and not mentioned in the ASTM 1820 standard.

- Alexander, 1999: study 6061-T651 Compact-Tension (CT) specimens which are machined prior to irradiation. Afterwards, CT specimens are irradiated in HFIR at Oak Ridge National Laboratory (ORNL), USA. The thermal fluence is estimated to be $\Phi_{th} = 10$ and 80×10^{21} n/cm^2 and the fast fluence to be $\Phi_f = 5$ and 40×10^{21} n/cm^2 ($E > 0.1$ MeV) for two batches of irradiated samples respectively. 16 CT samples are inserted in a capsule which holds them end-to-end. Narrow channels in each capsule allows the reactor's cooling water to pass over the samples to maintain the required temperature (95°C). The flux gradient in the capsule is calculated over the length. This leads to an accurate estimation of the irradiation dose received by each tested sample. A good degree of confidence is attributed to the results from this study for two reasons. First, CT samples are machined prior to irradiation which makes it easier to machine the desired sample geometry. Second, the carried tests follow the ASTM 1820 standard regarding the sample geometry and fracture toughness measurements.

- Source 2002: is a study that is the courtesy of CEA. Fracture toughness tests are carried out on pre-cracked bending samples that are machined from an extracted neutron-irradiated tube. The chemical composition of the tested alloy is not in the tolerances of the 6061 aluminum alloy's composition.

Based on the above facts, it can be highlighted that a good degree of confidence can be attributed to the work of Alexander, 1999 as samples are machined prior to irradiation, monitored during irradiation (regarding the local thermal fluence, Φ_{th}) and tested according to the ASTM 1820 standard. However, this data is insufficient to conclude the fracture toughness of the irradiated 6061 aluminum alloy. This explains the aim of this chapter: Modeling the fracture toughness of the irradiated 6061 aluminum alloy. This chapter is the final outcome of the above chapters. The calibrated damage model illustrated in chapter 5 is coupled with the phenomenological irradiated plastic flow law (chapter 7) to simulate the fracture toughness of the irradiated 6061-T6 alloy. Given the identified objective, this chapter is divided into the following sections:

- Section 8.2: is divided into two parts. The first part presents the experimental results of the recently irradiated tensile samples. The latter have a low radiation dose when compared to highly irradiated samples in the literature (see chapter 7). The second part presents the available fracture toughness results.

- Section 8.3: covers the finite element simulations carried out over tensile and CT samples discussed in section 8.2. The calibrated damage model used in

this chapter is already presented in chapter 5. The latter also shows the finite element meshes as well as the boundary conditions. Finally, the irradiated plastic flow model accounting for radiation-induced hardening is already explained in chapter 7.

8.2 EXPERIMENTAL DATA

8.2.1 *Notched tensile testing on irradiated material*

In this section, tensile testing results on Notched Tensile (NT) samples are presented (see chapter 4 for the geometry of NT samples). Unirradiated NT samples are already discussed in chapter 5. These results are used in this chapter to compare with the irradiated material. The latter has a similar chemical composition and heat treatment process as the 6061-T6 aluminum alloy studied in chapter 5. Irradiated samples are irradiated in Osiris at CEA, France. The average thermal fluence of the irradiated samples is estimated to be $\Phi_{th} = 6.7 \times 10^{21}\ n/cm^2$ (relatively low dose). Table 8.1 shows the exact thermal fluence of all the tested samples. The ratio of thermal to fast neutron flux is estimated as $R_\Phi = 5$.

Table 8.1: Thermal fluence of tested NT and ST samples

SAMPLE ID	SAMPLE TYPE	Φ_{th} ($\times 10^{21}\ n/cm^2$)
L89	NT10	6.63
L90		6.53
L91		6.68
L85	NT4	6.77
L86		6.95
L87		6.78
L88	NT2	6.62
L83		6.96

Irradiated samples are tested in a hot cell as shown in fig. 8.1. Hot cells are chambers which are designed under extreme security conditions to manipulate irradiated materials. The studied specimens have a minimal diameter Φ_0 of 4 mm and a notch curvature radius R_0 equal to 4, 1.6 and 0.8 mm (respectively corresponding to NT10, NT4 and NT2 specimens). All NT quasi-static tests are carried out at room temperature using a strain rate of about $5 \times 10^{-4}\ s^{-1}$. Images of the sample are taken during the test to calculate the radial deformation using the Edge Tracing technique presented in chapter 4.

Figure 8.1: Example of hot cells (a chamber dedicated for irradiated material testing)

Figure 8.2 shows the nominal stress—radial deformation curves of the irradiated and unirradiated materials. As expected, the irradiated material has a higher strength and lower ductility. The sharp load drop is achieved in the irradiated NT10 samples by decreasing the strain rate to 5×10^{-6} s^{-1} after the maximum load is reached. The aim is to reduce the machine displacement rate (i. e. strain rate) when a crack is initiated in the sample's center due to the higher stress triaxiality [Tekoğlu et al., 2015]. The strain localization in the damaged area leads to a higher local strain rate which might lead to an unstable failure (without having a stable load drop phase) if the machine displacement rate is not decreased. However, it is difficult to obtain the load sharp drop in irradiated NT4 samples as the crack propagation is more rapid after irradiation [Alexander, 1999]. As for NT2 samples, it is difficult to achieve a controlled load drop in both the unirradiated and irradiated materials. This load drop is beneficial for evaluating the model predictions in section 8.3.

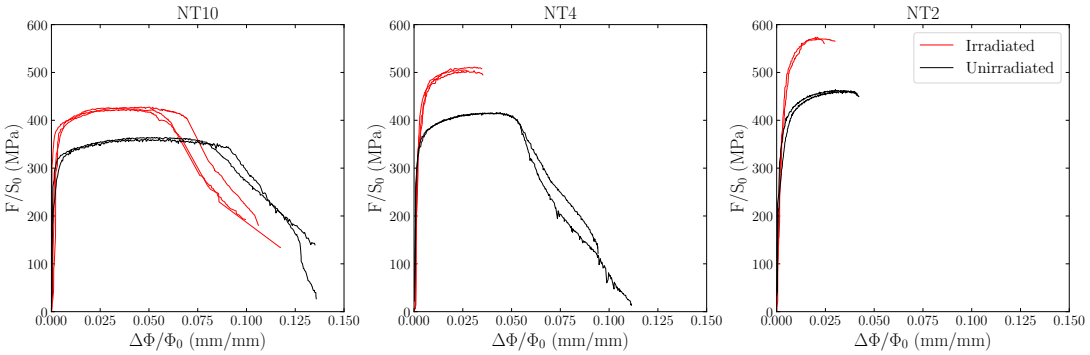

Figure 8.2: Nominal stress—radial deformation curves of irradiated and unirradiated NT10, N4 and NT2 samples. Thermal fluence of irradiated sample is estimated to be $\Phi_{th} = 6.7 \times 10^{21}\ n/cm^2$.

The presented tensile results in fig. 8.2 are used to assess the radiation-induced hardening which is developed in chapter 7. The NT test results are also used in

section 8.3 to see if the damage model can predict the strain at failure of the mildly irradiated material.

8.2.2 *Fracture toughness results*

Figure 8.4 shows a compilation of all available data in the literature regarding the fracture toughness of the irradiated 6061-T6 aluminum alloy. As mentioned earlier, results in the study of Weeks et al., 1993 cannot be compared to other work due to the different specimen type (which makes the unirradiated K_{Jc} value lower than other studies) and the excessively high spectrum ($R_\Phi = 21$, compared to $R_\Phi = 2$ in both other studies). A high degree of confidence is attributed to results in the work of Alexander, 1999 as the tested CT specimens are machined before irradiation according to the ASTM 1820 standard. Results in the work of [Source 2022] are obtained using bending specimens which might lead to the higher K_{Jc} in the unirradiated material. Furthermore, the chemical composition of the aluminum alloy tested in [Source 2022] is slightly different from a typical 6061 aluminum alloy.

Considering results in the work of Alexander, 1999 and [Source 2002], two hypothesis can be formulated in order to explain the opposite trends regarding fracture toughness versus thermal fluence:

1. Fracture toughness of the 6061 aluminum alloy is not affected by irradiation. This hypothesis is driven by a mechanics-based brainstorming approach.

   After irradiation, the yield strength increases and the strain hardening capacity decreases. An increase in the former improves fracture toughness while a decrease in the latter deteriorates fracture toughness. Therefore, the stable fracture toughness as a function of Φ_{th} (observed in fig. 8.4, Alexander, 1999 and Petit et al., 2022) can be explained by a competition between the increase in yield strength and the decrease in hardening which results in a stable fracture toughness. On one hand, results in chapter 6 show that the yield strength has a first order effect on fracture toughness as the relative increase obtained via neutron radiation or age hardening is significant. On the other hand, the relative decrease in hardening obtained via neutron radiation is less significant. This can be observed in fig. 7.3 which illustrates the continuous increase in yield strength as a function of Φ_{th}. However, fig. 7.4 shows that the hardening capacity decreases in the early stage of irradiation and then reaches a plateau [1].

   In addition to the changes in yield strength and hardening, it is assumed that the micron-sized constituent particles are not affected by neutron radiation

1 Tested samples in the work of Alexander, 1999 are irradiated at a spectrum $R_\Phi = 2$. Therefore, one must analyze R_Φ low in fig. 7.3 and fig. 7.4. Tested samples in the work of Petit et al., 2022 are irradiated at $R_\Phi = 5$ and show the same trend as in the work of Alexander, 1999. However, the Φ_{th} in the work of Petit et al., 2022 is lower.

(Hypothesis 1 in chapter 1). This assumption is important when building a hypothesis to understand the stable fracture toughness in the work of Alexander, 1999.

2. Fracture toughness of the 6061 aluminum alloy decreases as a function of Φ_{th}. This hypothesis is driven by a metallurgy-based brainstorming approach.

   The added silicon by transmutation creates Si-rich amorphous particles that precipitate at grain boundaries. The Si-rich particles are observed on fracture surfaces in the work of Weeks et al., 1993. The cited authors link the drop in fracture toughness to two aspects: the precipitation of Si-rich particles at grain boundaries and the fine nano Mg_xSi_y precipitates that replaced the original coarser Mg_xSi_y nano precipitates created during age hardening. The new Mg_xSi_y is finer in the work of Weeks et al., 1993 since the R_Φ is extremely high ($R_\Phi = 21$ versus $R_\Phi = 2$ in the work of Alexander, 1999 and [Source 2002] respectively). A high R_Φ leads to less point defects which limits the diffusion of silicon atoms. Consequently, the nano precipitates are fine. However, a low R_Φ leads to more points defects and more diffusion of transmuted silicon atoms which ripens the new nano Mg_xSi_y precipitates. This explanation is based on the study of Farrel, 2011 which focuses on the effect of R_Φ on the size and density of the new nano Mg_xSi_y precipitates. Nonetheless, the approach based on the size and density of new nano Mg_xSi_y precipitates is not pertinent at this point since the samples in the work of Alexander, 1999 and [Source 2002] are irradiated at the same spectrum ($R_\Phi = 2$). Yet, the fracture toughness stays stable in the work of Alexander, 1999 and drops in the work of [Source 2002].

   Therefore, the only explanation behind the drop in fracture toughness in the work of [Source 2002] observed in fig. 8.4 is the amorphous Si-rich particles that precipitate at grain boundaries and lead to an intergranular separation (see flakes of Si-rich phase at the grain boundaries in fig. 8.3). Another important factor to highlight is that the local thermal fluence of the irradiated CT samples is monitored during the irradiation program in the work of Alexander, 1999. On the other hand, the bending samples in the work of [Source 2002] are machined post-irradiation from an irradiated tube. The local thermal fluence is taken as an average of the measured Φ_{th} over sections in the tube. This issue questions the accuracy of the thermal fluence value of irradiated samples [Source 2002] in fig. 8.4 ($\Phi_{th} = 155 \times 10^{21}\ n/cm^2$). Is the real thermal fluence in the tested samples higher or lower than the average value taken over sections in the irradiated tube? In addition, there are no tested samples between the unirradiated ($\Phi_{th} = 0$) and irradiated ($\Phi_{th} = 155 \times 10^{21}\ n/cm^2$) samples in the work of [Source 2002]. Does the fracture toughness drop continuously as Φ_{th} increases (as shown by dashed lines in fig. 8.4, [Source 2002]) or is it stable till a critical Φ_{th} after which

toughness decreases? The lack of data makes it difficult to answer the above questions.

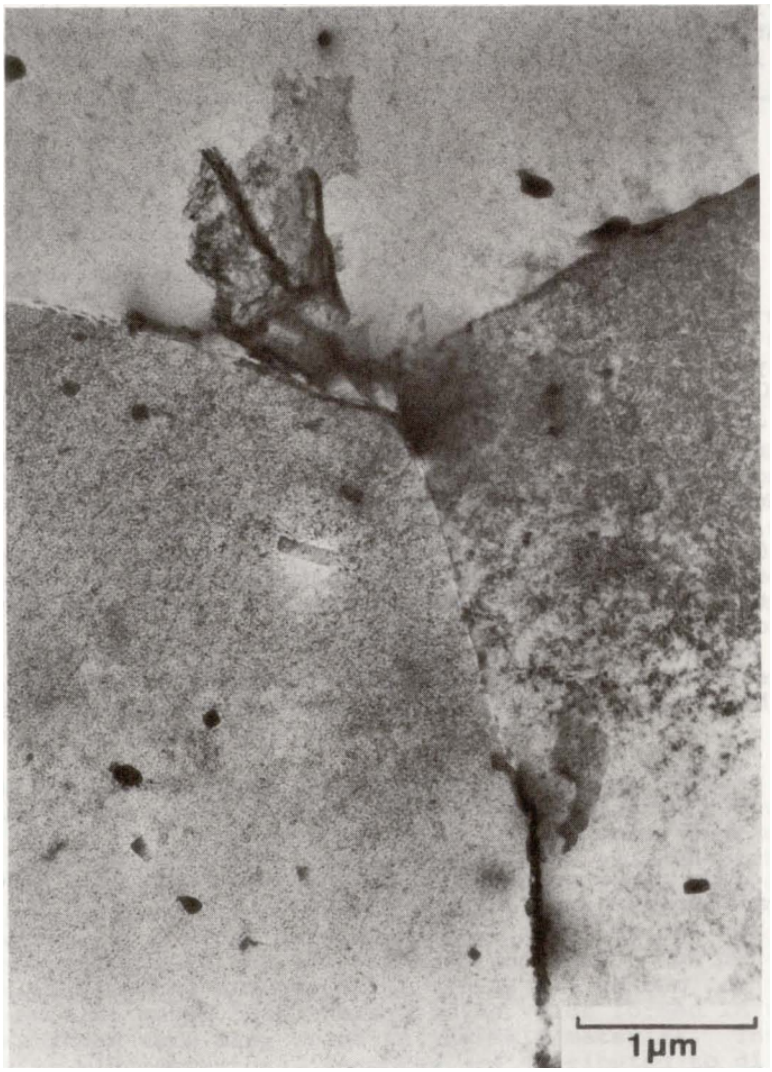

Figure 8.3: Irradiated sample in the work of Weeks et al., 1993 showing large flakes of Si-rich phase at the grain boundaries of a 6061 alloy

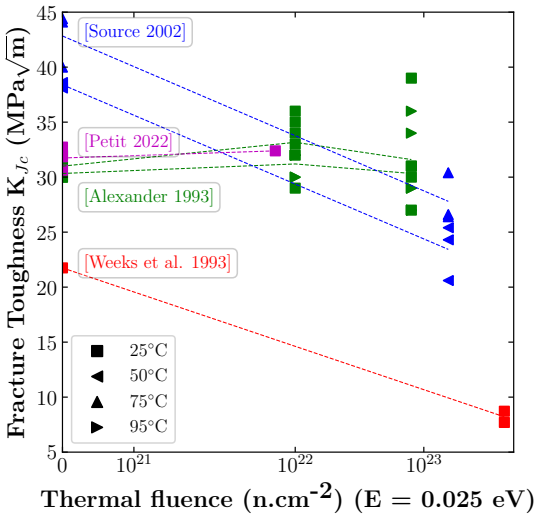

Figure 8.4: Fracture toughness (K_{Jc}) results of irradiated 6061-T6 samples tested at different temperatures (25-95°C). Samples are irradiated in the HFIR ($R_\Phi = 2$) [Alexander, 1993], HFBR ($R_\Phi = 21$) [Weeks et al., 1993] and Osiris ($R_\Phi = 5$) [Petit et al., 2022]. [Source 2002] is unpublished research.

8.3 MODELING THE FRACTURE TOUGHNESS OF THE IRRADIATED MATERIAL

In this section, finite element simulations are carried out to test the developed model over tensile and fracture toughness results presented above. Tensile and CT finite element meshes as well as boundary conditions are explained in chapter 5. The latter illustrates the damage model and its parameters. The calibration of the damage model is carried out over an unirradiated 6061-T6 aluminum alloy. Based on hypothesis 1 in chapter 1, micron-sized constituent particles that cause damage (through void nucleation, growth and coalescence) are not affected by neutron radiation. Therefore, the damage model calibrated in chapter 5 is used to model damage in the irradiated material. The radiation-induced hardening is taken into account via the irradiated plastic flow model explained in chapter 7. Therefore, the outcome model of this PhD thesis is a combination of the irradiated plastic flow and the calibrated GTN damage model.

8.3.1 *Irradiated plastic flow & GTN parameters*

The irradiated plastic flow developed in chapter 7 is expressed as follows:

$$\sigma_{\Phi F}(p) = \sigma_{\Phi 0} + (\sigma_{\Phi s} - \sigma_{\Phi 0})\left(1 - e^{-\frac{p}{p_0}}\right) \tag{8.1}$$

where $\sigma_{\Phi F}$ is the irradiated flow stress, p the plastic deformation and $\sigma_{\Phi 0}$, $\sigma_{\Phi s}$, p_0 are material parameters that depend on the thermal fluence. Equation (8.1) can be simplified as follows:

$$\sigma_{\Phi F}(p) = \sigma_{\Phi 0} + A \ (1 - \exp(-b\ p)) \tag{8.2}$$

This simplification replaces $(\sigma_{\Phi s} - \sigma_{\Phi 0})$ by A and $1/p_0$ by b. Thus, eq. (8.2) can be expressed in the same way as in chapter 5. Table 8.2 lists the material parameters of the unirradiated and 5 irradiated materials. The highly irradiated material ($\Phi_{th} = 400 \times 10^{21}\ n/cm^2$) corresponds to the high radiation dose in fig. 8.4.

Table 8.2: Irradiated plastic flow law parameters. $p_{\text{Considère}}$ is the plastic deformation ($p_{\text{Considère}}$) at which the maximum engineering stress is reached. $p_{\text{Considère}}$ is estimated by the Considère instability criterion [Considère, 1885]. A higher $p_{\text{Considère}}$ translates a higher hardening capacity.

Φ_{th}	$\sigma_{\Phi 0}$	A	b	$p_{\text{Considère}}$
$0 \times 10^{21}\ n/cm^2$	270 MPa	74 MPa	28.7	0.065
$10 \times 10^{21}\ n/cm^2$	320 MPa	64 MPa	27.9	0.056
$50 \times 10^{21}\ n/cm^2$	361 MPa	57 MPa	26.8	0.049
$100 \times 10^{21}\ n/cm^2$	389 MPa	53 MPa	26.7	0.045
$200 \times 10^{21}\ n/cm^2$	422 MPa	48 MPa	26.4	0.039
$400 \times 10^{21}\ n/cm^2$	467 MPa	41 MPa	23.8	0.030

Figure 8.5 shows the irradiated plastic flow of the studied materials listed in table 8.2. As explained earlier, neutron radiation increases the yield strength and decreases the strain hardening capacity. This is clearly observed in fig. 8.5. Table 8.2 also notes $p_{\text{Considère}}$ which is the plastic deformation ($p_{\text{Considère}}$) at which the maximum engineering stress is reached. $p_{\text{Considère}}$ is estimated by the Considère instability criterion [Considère, 1885]. A higher $p_{\text{Considère}}$ in fig. 8.5 translates a higher hardening capacity.

Table 8.3 shows the GTN parameters already calibrated in chapter 5 and used as is in this chapter. As a reminder, void growth is described by the universal analytical formula proposed in chapter 3. This formula is a function of the elastic–plastic behavior which depends on the thermal fluence. Therefore, void growth is influenced by Φ_{th}.

8.3.2 *Modeling of the tensile behavior*

Figure 8.6 shows the FE simulation results in the tested NT unirradiated and irradiated samples. The unirradiated 6061-T6 aluminum samples are modeled in chapter 5 and

Table 8.3: Calibrated GTN parameters in chapter 5

Pre-existing voids and void nucleation					**Void growth**		**Void coalescence**				**Mesh size**
f_0	Void nucleation law				η_{q1}	η_{q2}	α	β	γ	δ	h
	$f_n^{\max}$	a_n	p_n	σ^{critical}							
%	%	-	%	MPa	-	-	-	-	-	-	μm
0.44	1.2	0.6	2.6	337	1.8	1.0	0.2	2.4	0.01	1.5	100

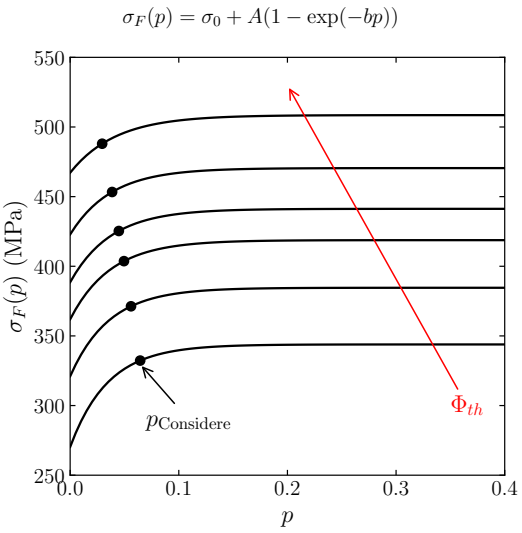

Figure 8.5: Irradiated flow stress versus plastic deformation using eq. (8.2) for 1 unirradiated and 5 irradiated 6061-T6 aluminum alloys: $0, 10, 50, 100, 200$ and $400 \times 10^{21}\ n/cm^2$.

plotted in fig. 8.6 for comparison. A good agreement is found between experiments and FE simulations in the NT10 and NT4 samples. However, the model slightly overestimates the strain at failure in the irradiated NT2 samples. This is explained by the fact that the stress triaxiality is high in the NT2 sample which leads to a rapid crack propagation and an unstable failure. On the other hand, the crack propagation can be controlled at lower stress triaxiality as shown in the NT10 and NT4 samples. Furthermore, Alexander, 1999 states that the resistance to crack initiation is not affected by neutron radiation while the resistance to crack propagation (i. e. tearing modulus) decreases after irradiation. The current model indirectly accounts for the resistance to crack initiation via the radiation-induced hardening effect. However, the damage parameters are not modified to decrease the resistance to crack propagation after irradiation. This can explain the overestimated strain at failure in the irradiated NT2 sample.

This analysis allows to test the model over mildly irradiated samples ($\Phi_{th} = 6.7 \times 10^{21}\ n/cm^2$) and low/intermediate stress triaxiality (0.8—2). Observations show that the strain at failure is fairly predicted in all samples (with a higher strain at failure

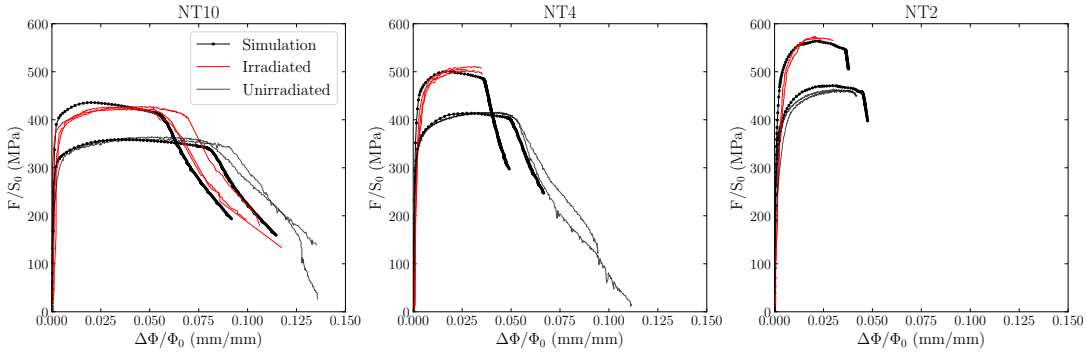

Figure 8.6: FE simulation curves of tensile tests presented in fig. 8.2. $\Phi_{th} = 6.7 \times 10^{21}\ n/cm^2$.

in the NT2 sample). This verification allows to use the model over highly irradiated CT specimens in the following section.

8.3.3 *Modeling of the fracture toughness*

The fracture toughness modeling section is divided into three parts. The first part is dedicated to modeling an irradiated CT sample tested in the work of Petit, 2018 at a low thermal fluence ($\Phi_{th} = 6.91 \times 10^{21}\ n/cm^2$ and $R_\Phi = 5$). The second part is dedicated to modeling the stable K_{Jc} values found in the work of Alexander, 1993, 1999 and Petit et al., 2022. The third part is dedicated to modeling the drop in K_{Jc} observed in the work of Source [2002].

8.3.3.1 *Modeling of the Load—Crack Mouth Opening Displacement curve*

Figure 8.7 shows the experimental Load—Crack Mouth Opening Displacement (CMOD) curve of the tested CT sample in the work of Petit, 2018. A FE simulation is carried out to test the PhD model on a CT sample with a higher stress triaxiality (compared to NT samples presented earlier). Given the $R_\Phi = 5$ and $\Phi_{th} = 6.91 \times 10^{21}\ n/cm^2$, the hardening parameters are as follows: $\sigma_{\Phi\,0} = 315$ MPa, $A = 65$ MPa, and $b = 28.1$. The GTN parameters shown in table 8.3 are used as is (except for the f_0 parameter). The initial pores and Mg_2Si volume fraction of the tested material is slightly lower than the material studied in chapter 5. Therefore, a $f_0 = 0.3\%$ is used to simulate the sample shown in fig. 8.7. As observed, the model results in a higher absolute maximum load which might overestimate the resistance to crack initiation. However, once the crack propagates and the macroscopic load drops, a good agreement is found between experimental and simulated curves in fig. 8.7. It is difficult to conclude if the difference between the experimental and simulated maximum load is due to an experimental or a model issue. More experiments are

needed to confirm if the model needs to be adapted. Therefore, at this stage, the model can be used as it is for the second part of this section.

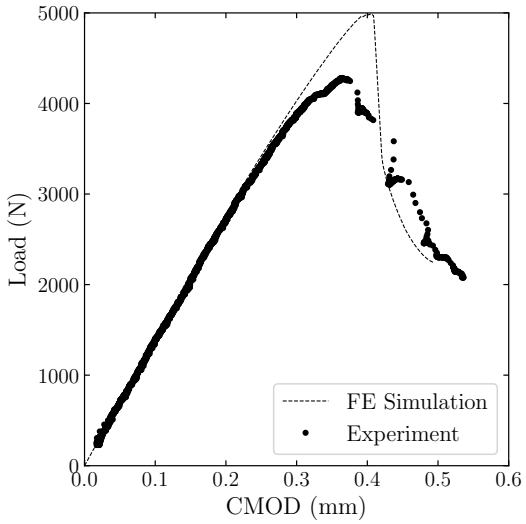

Figure 8.7: Load—Crack Mouth Opening Displacement (CMOD) curves of the tested CT sample in the work of Petit, 2018 ($\Phi_{th} = 6.91 \times 10^{21}\ n/cm^2$ and $R_\Phi = 5$)

8.3.3.2 *Modeling of the stable fracture toughness*

As explained above, the aim of this part is to model the stable K_{Jc} values found in the work of Alexander, 1993, 1999 and Petit et al., 2022. Fracture toughness FE simulations are carried out on CT12.5 samples. For each simulation, the K_{Jc} is measured to estimate the resistance to crack initiation as follows:

$$K_{Jc} = \sqrt{\frac{J_{0.2\text{BL}}\, E}{1-\nu^2}} \tag{8.3}$$

where $J_{0.2\text{BL}}$ is the J-value measured at the intersection with the 0.2 mm blunting line, E Young's modulus and ν Poisson coefficient. The slope the 0.2 mm blunting line is a function of the material's yield (YS) and ultimate tensile (UTS) strengths (slope $= k\,(\text{YS}+\text{UTS})/2$, where $k = 2$). In order to obtain the $J_{0.2\text{BL}}$ from the simulated CT12.5 samples, a post-processing routine calculates the average crack length as a function of time. Then, the analytical formulas of the ASTM-1820 standard are used to calculate the J as a function of the crack length Δa. As a reminder, the analytical formulas of the ASTM-1820 standard are also used to calculate the fracture toughness in the work of Alexander, 1999.

Figure 8.8 (a) and (b) show the Load—CMOD and J—Δa curves respectively of the simulated CT12.5 samples using the GTN parameters in table 8.3. For the sake of clarity in fig. 8.8, $\Phi_{th} = 100$ and $200 \times 10^{21}\ n/cm^2$ are not shown. It is observed in fig. 8.8 (a) that the unirradiated sample ($\Phi_{th} = 0$) has a lower maximum load

capacity and a steeper load drop than the irradiated samples. This is translated by a flat J—Δa curve in fig. 8.8 (b) (see $\Phi_{th} = 0$). The $J_{0.2}$ values seem to be slightly decreasing at low Φ_{th} (between $\Phi_{th} = 0$ and $10 \times 10^{21}\ n/cm^2$) and increasing once again at $\Phi_{th} > 50 \times 10^{21}\ n/cm^2$. A slight drop of 4% in $J_{0.2\text{BL}}$ (between $\Phi_{th} = 0$ and $10 \times 10^{21}\ n/cm^2$) is attributed to the sudden drop in hardening capacity. The drop of the latter is observed in tensile results in the literature (see fig. 7.4). The slight increase of fracture toughness at $\Phi_{th} > 50 \times 10^{21}\ n/cm^2$ is attributed to the increase in yield and tensile strengths while the hardening capacity drop saturates at high radiation doses. The saturation of hardening capacity drop is observed in fig. 7.4, while the continuous increase in strength is observed in fig. 7.3. Regardless of the re-increase in fracture toughness, the $J_{0.2\text{BL}}$ value at $\Phi_{th} = 400 \times 10^{21}\ n/cm^2$ is 0.7% lower than at $\Phi_{th} = 0$. This indicates a stable resistance to crack initiation which confirms the discussion in the work of Alexander, 1999. There are no experimental load—CMOD curves in the literature to compare with the results in fig. 8.8. Therefore, the next step is to analyze the K_{Jc} values to compare them with the literature results.

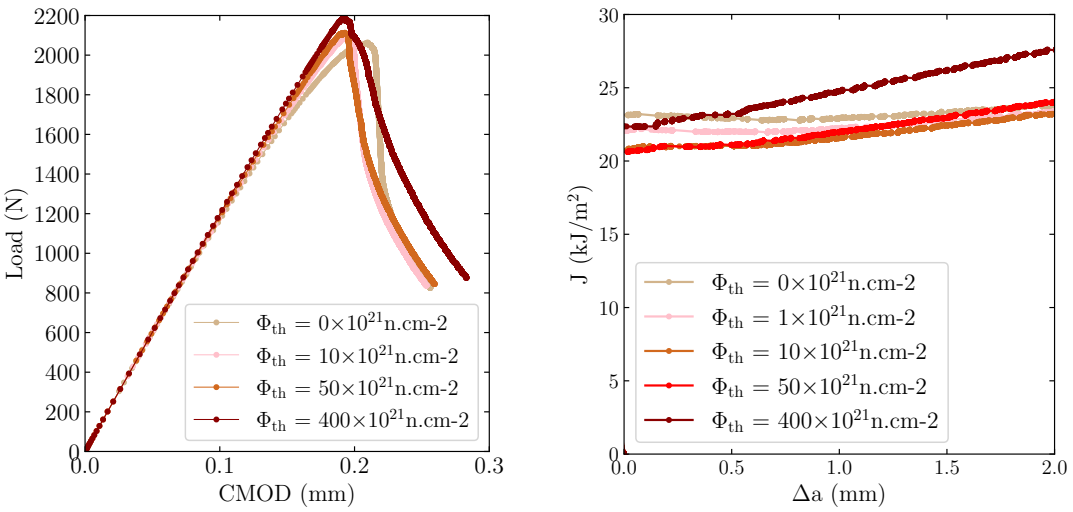

(a) Load—Crack Mouth Opening Displacement (CMOD)

(b) J—Δa curves

Figure 8.8: (a) Load—CMOD and (b) J—Δa curves of the simulated CT12.5 samples using the GTN parameters in table 8.3.

Figure 8.9 shows the fracture toughness (K_{Jc} values) of the simulated CT12.5 samples using the damage model and parameters calibrated in chapter 5. The damage parameters are not changed for the reason mentioned above: intermetallic particles that damage the alloy via void nucleation, growth and coalescence are not affected by neutron radiation (i. e. particle size, density and morphology). As explained earlier, the simulated fracture toughness is almost stable as a function of the thermal fluence.

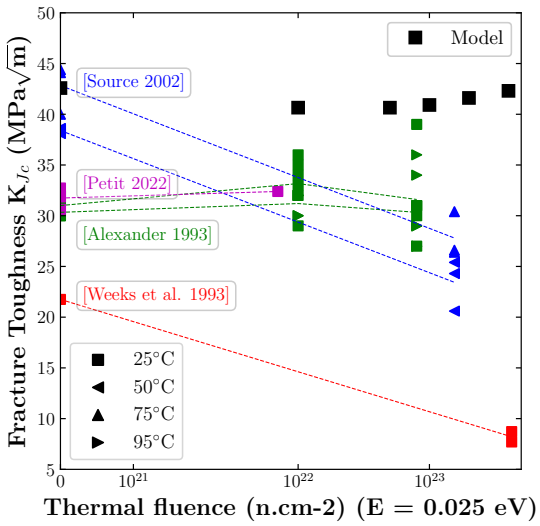

Figure 8.9: Simulated fracture toughness of the irradiated CT12.5 samples compared to the results from the literature when the damage parameters calibrated in chapter 5 are used as is.

In order to understand the slight increase in fracture toughness observed at $\Phi_{th} > 50 \times 10^{21}\ n/cm^2$, a single element in the center and at the edge of the CT sample at 1 mm from the crack tip are analyzed during the simulations (see fig. 8.10 (a)). As observed in fig. 8.10 (b), the maximum "Gurson stress triaxiality" in P1 drops as the thermal fluence increases. The "Gurson stress triaxiality" remains constant in P2 as a function of the thermal fluence. The "Gurson stress triaxiality" is defined as $\sigma_m/\sigma_\star$ where σ_m is the mean stress and $\sigma_\star$ the effective stress. Usually the stress triaxiality is defined as $\sigma_m/\sigma_{\text{eq}}$ where σ_{eq} is the equivalent stress (e. g. von Mises stress). However, the Gurson stress triaxiality is directly related to the porosity (see eq. (A.6)). This means that an increase in the Gurson stress triaxiality leads to an increase in void growth. Therefore, the maximum Gurson stress triaxiality is plotted as a function of the thermal fluence in fig. 8.10 (b) to highlight the fact that the simulated void growth decreases in the irradiated material. This observations is nontrivial. As the GTN stress triaxiality decreases, void growth decreases and the resistance to crack initiation increases at high radiation doses. This phenomenon explains the increase in $dJda$ (slope in fig. 8.8 (b)) at high radiation doses. However, the calibrated damage model in chapter 5 is capable of predicting stable K_{Jc} values as observed in the work of Alexander, 1999.

8.3.3.3 *Modeling of the drop in fracture toughness*

The aim of this part is to model the drop in K_{Jc} observed in the work of Source [2002]. A hypothesis is made in section 8.2.2 in order to explain the drop in fracture toughness observed in the work of Source [2002]. This hypothesis is driven by the fact that the added Si precipitates on grain boundaries lead to a fragilisation effect. As discussed

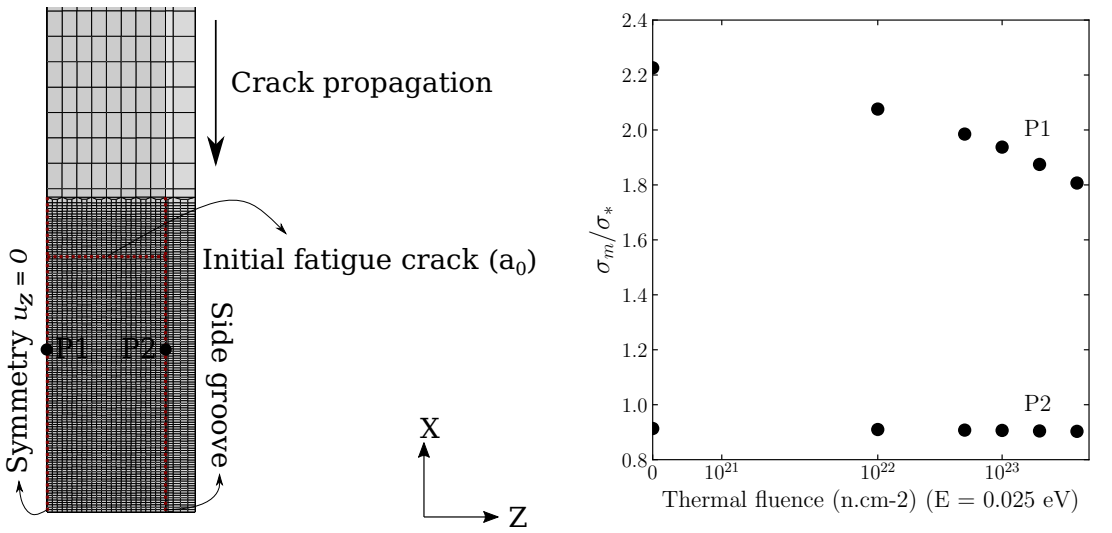

(a) P1, P2: analyzed FE elements (b) Max. Gurson stress triaxiality = $\sigma_m/\sigma_\star$

Figure 8.10: (a) Analyzed FE elements in the center and at the edge of the CT sample at 1 mm from the crack tip, (b) drop of Gurson stress triaxiality ($\sigma_m/\sigma_\star$) as a function of the thermal fluence at P1 in CT12.5 samples simulated in fig. 8.9 (a).

by Weeks et al., 1993, amorphous Si that precipitate at grain boundaries can lead to an intergranular separation. One way to account for this phenomenon is to add a void nucleation law which predicts nucleation over transmuted Si particles. However, no sufficient evidence of void nucleation over amorphous Si particles is found in the work of Weeks et al., 1993. Figure 8.3 shows the Si particles at grain boundaries, but no void nucleation is observed. Therefore, another way to account for this phenomenon is to relate the coalescence phase in the GTN model to the thermal fluence. One can assume that as the thermal fluence increases, more transmuted Si create precipitates at grain boundaries which leads to an intergranular separation and accelerates void coalescence.

The void coalescence model developed in chapter 5 relates the critical porosity ($\Delta f_{g\ \text{crit.}}$) to the stress triaxiality ($\sigma_m/\sigma_{\text{eq}}$). In order to link $\Delta f_{g\ \text{crit.}}$ to the thermal fluence, it can be assumed that the drop in hardening capacity leads to a decrease in the critical porosity. This is confirmed by results in fig. 8.11. The latter shows the $\Delta f_{g\ \text{crit.}}$ as a function of stress triaxiality for different hardening levels. The $\Delta f_{g\ \text{crit.}}$ is evaluated via FE simulations over the cell model with a secondary population of voids (see chapter 5). Each point in fig. 8.11 represents a single FE simulation at a constant stress triaxiality and a given hardening behavior. The analyzed hardening behaviors are presented in chapter 3. Even though fig. 8.11 covers a wide range of hardening capacity ($p_{\text{Considère}}$), the unirradiated material has a $p_{\text{Considère}} = 0.065$ while the highly irradiated material ($400 \times 10^{21}\ n/cm^2$) has a $p_{\text{Considère}} = 0.030$ (see

table 8.2). Therefore, the high $p_{\text{Considère}}$ values in fig. 8.11 are not interesting for this study. However, these high $p_{\text{Considère}}$ values confirm the trend that increasing the hardening capacity retards the onset of void coalescence.

Using the results in fig. 8.11, the parameters $\{\alpha, \beta, \gamma\}$ that define the onset of void coalescence can be related to the hardening capacity. This can be done by interpolating between $p_{\text{Considère}} = 0.060$ and $p_{\text{Considère}} = 0.020$ in fig. 8.11. Consequently, fig. 8.12 (a) shows the evolution of $\Delta f_{g\ \text{crit.}}$ as a function of Φ_{th}.

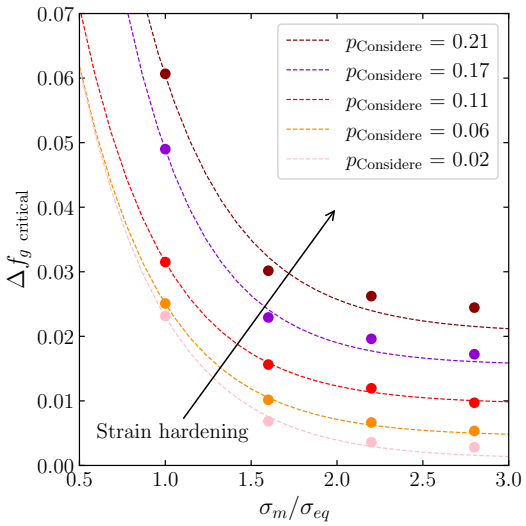

Figure 8.11: Critical porosity at onset of coalescence over a range of stress triaxiality ($0.8 < T < 2.8$) and for different hardening behaviors. The cell model is explained in chapter 5. The critical porosity decreases as the hardening capacity decreases.

Since the $\Delta f_{g\ \text{crit.}}$ only defines the onset of coalescence, another parameter in the GTN model must be changed to accelerate the coalescence once it is triggered. The aim of this acceleration is to predict the fragilisation due to transmuted Si at grain boundaries. In the GTN model, once coalescence is triggered, the porosity growth is accelerated by a δ factor till material failure is reached. The δ is calibrated to be equal to 1.5 in chapter 5. In this part of the current section, δ increases as a function of the Φ_{th}. There is no sufficient experimental evidence to calibrate the increase in δ as a function of the Φ_{th}. Therefore, it is assumed that the δ factor increases as follows:

$$\delta(\Phi_{th}) = \delta_0 + \delta_1 \Phi_{th}^n \tag{8.4}$$

where $\delta_0 = 1.5$, $\delta_1 = 0.1$ and $n = 0.5$. The parameters δ_1 and n are not calibrated based on experimental evidence. However, they are found by trial and error through testing their influence on the K_{Jc} values.

Therefore, by decreasing the critical porosity ($\Delta f_{g\ \text{crit.}}$) and accelerating the void growth after coalescence (via the δ factor), it is assumed that the transmuted Si

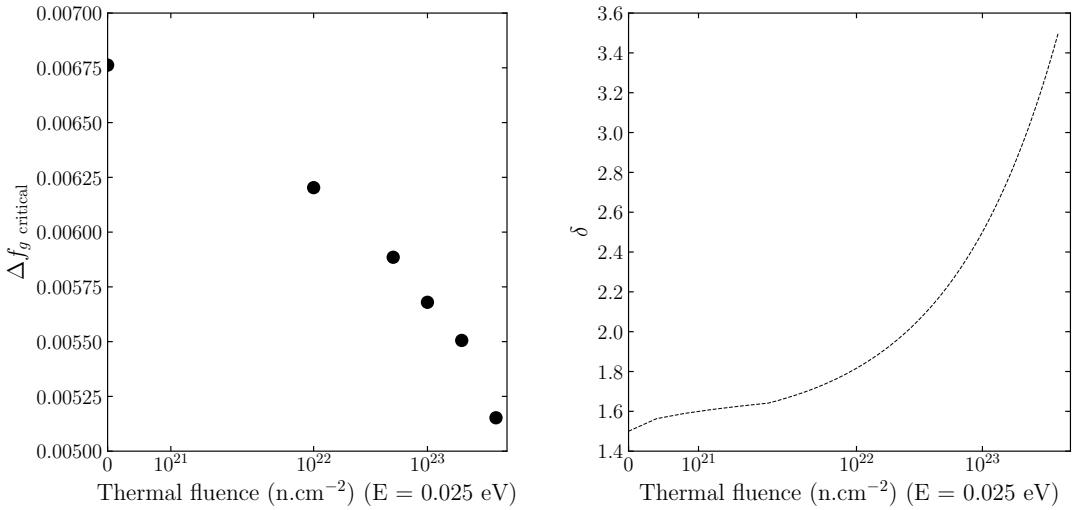

(a) Critical porosity versus Φ_{th}

(b) δ versus Φ_{th}

Figure 8.12: (a) Decrease of critical porosity (estimated at P1 shown in fig. 8.10 (a)) as a function of the thermal fluence. (b) Increase of the δ as a function of the thermal fluence. The critical porosity defines the onset of coalescence while δ defines the acceleration of the porosity growth when coalescence is triggered. It is assumed that the transmuted Si precipitate at grain boundaries which decreases Δf_gcrit. and increases δ. The following $\Delta f_{g\ \text{crit.}}$ and δ are used to simulate the fracture toughness in fig. 8.9 (b).

leads to a fragilizing effect. The critical porosity values and the increase in δ as a function of Φ_{th} shown in fig. 8.12 (a) and (b) respectively are used to model the CT samples in fig. 8.13. Figure 8.13 (a) and (b) show the Load—CMOD and J—Δa curves respectively of the simulated CT12.5 samples using the modified GTN parameters. Due to numerical convergence issues, the load drop phase is difficult to achieve at high thermal fluences (see $\Phi_{th} = 50$ and $400 \times 10^{21}\ n/cm^2$ in fig. 8.13). The increased δ parameter significantly accelerates void growth at high Φ_{th} which leads to a numerical instability. When comparing fig. 8.13 (a) to fig. 8.8 (a), it is observed that the resistance to crack initiation (i. e. onset of load drop) decreases as Φ_{th} increases when the GTN parameters are modified. Figure 8.13 (b) shows a decrease in $J_{0.2\text{BL}}$ as a function of Φ_{th}. A drop of 21% in $J_{0.2\text{BL}}$ is observed between $\Phi_{th} = 0$ and $400 \times 10^{21}\ n/cm^2$.

Figure 8.14 shows the K_{Jc} values of the CT samples simulated with the modified GTN parameters. The drop in the simulated K_{Jc} values is lower than the drop in experimental values in the literature. In order to obtain the same drop in K_{Jc} values, the δ parameter should be increased which is tested in this work. Unfortunately, the extremely high δ values lead to numerical divergence of all simulated CT samples with $\Phi_{th} > 0$. The only experimental evidence to validate the assumptions regarding the modified GTN parameters is found in the work of Weeks et al., 1993 where Si

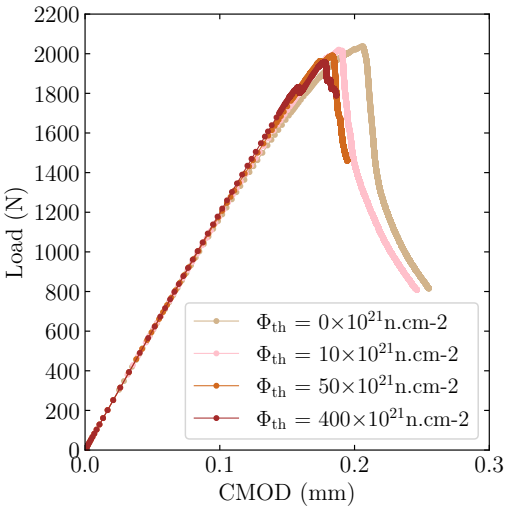

(a) Load—Crack Mouth Opening Displacement (CMOD)

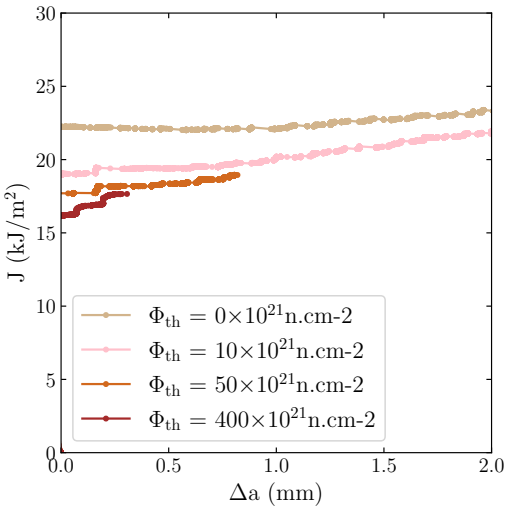

(b) J—Δa curves

Figure 8.13: (a) Load—CMOD and (b) J—Δa curves of the simulated CT12.5 samples using the modified GTN parameters explained in fig. 8.12

is found at grain boundaries and an intergranular separation is observed. However, the Φ_{th} and R_Φ in the work of Weeks et al., 1993 are extremely high when compared to [Source 2002] ($R_\Phi = 21$ and $R_\Phi = 2$ for [Weeks et al., 1993] and [Source 2002] respectively). The assumptions made allow to observe a drop in the simulated fracture toughness as shown in fig. 8.14. Therefore, the drop in fracture toughness observed in the work of [Source 2002] can be simulated by applying an accelerated coalescence in the irradiated material. The only drawback behind these assumptions is the lack of experimental evidence to calibrate the coalescence parameters as a function of the radiation dose.

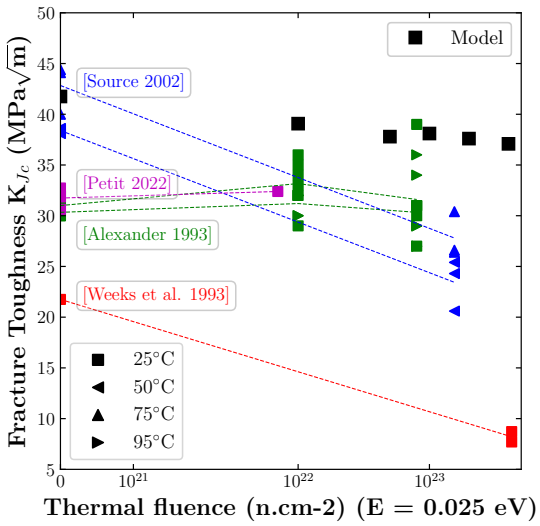

Figure 8.14: Simulated fracture toughness of the irradiated CT12.5 samples compared to results from the literature when the damage parameters are modified to model the drop in fracture toughness. Modified parameters are explained in fig. 8.12.

8.4 CONCLUSION

To conclude, this chapter is the final outcome of this Phd thesis. A damage model is developed in chapter 3 and chapter 5 over the unirradiated material. An irradiated plastic flow model is developed in chapter 7. The irradiated plastic flow model is combined with the calibrated damage model to simulate the irradiated samples. However, the latter are very limited. A few mildly irradiated NT samples are tested and presented in this chapter. A very few irradiated fracture toughness samples are published in the literature. The data in the latter are compiled and analyzed thoroughly. Two opposite trends are observed. Firstly, a stable fracture toughness as a function of the thermal fluence. Secondly, a drop in the fracture toughness as the thermal fluence increases.

Two hypotheses are made to explain the above mentioned trends. The first hypothesis explains the first trend (stable fracture toughness). It is assumed that the increase in yield strength after irradiation compensates the decrease in hardening which results in a stable fracture toughness. The second hypothesis explains the second trend (drop in the fracture toughness). It is assumed, based on a few experimental evidence in the literature, that the transmuted Si precipitate at grain boundaries which fragilizes the material and can lead to intergranular separation.

The first hypothesis is confirmed by simulating the fracture toughness of CT12.5 samples. The damage model calibrated in chapter 5 is used with no change. The FE simulation results confirm that the fracture toughness does not drop after irradiation. However, a surprising fact is observed. A slight increase in the simulated fracture toughness at extremely high doses is observed. This is explained by the decrease in

the stress triaxiality at high doses. Since damage in the GTN damage model depends on the stress triaxiality, decreasing the latter decreases damage and increases the resistance to crack initiation and propagation. Therefore, there might be a missing element in the damage model that prevents an increase in the fracture toughness at high doses. This could be introduced in the model by assuming a lower resistance to crack initiation at high doses.

The second hypothesis is confirmed by modifying the damage parameters used in simulating the fracture toughness of CT12.5 samples. The critical porosity which defines the onset of coalescence is decreased as a function of Φ_{th}. The rate of porosity growth between the onset of coalescence and material failure is increased as a function of Φ_{th}. These two modifications are based on the very few experimental evidence in the literature regarding the fragilizing effect of the transmuted Si. However, the experimental data are insufficient to properly calibrate the coalescence parameters. When the coalescence parameters are modified, a drop in the simulated fracture toughness is observed which confirms the second observed trend.

At this stage, it is difficult to confirm which observed trend represents the real case. The reality can be more complex than it is supposed in this thesis. This means that a stable fracture toughness or a drop in the latter might depend on the irradiation conditions (R_Φ, Φ_{th} and temperature) but also on the chemical composition of the aluminum alloy. There is no doubt concerning the strengthening effect of neutron radiation. Enough data in the literature confirm an increase in the yield strength and a decrease in strain hardening during irradiation. However, given the few data regarding the fracture toughness and the analysis in this PhD thesis, it can be concluded that the fracture toughness is not much affected by neutron radiation. A decrease in fracture toughness can be observed which depends on the irradiation conditions and the material.

BIBLIOGRAPHY

ASTM-1820 (2017). *Standard Test Method for Measurement of Fracture Toughness*. Technical report. DOI: 10.1520/E1820-17 (see p. 207).

Alexander, D. (1993). 'The Effect of Irradiation on the Mechanical Properties of 6061-T651 Aluminum.' In: *Effects of Radiation on Mater.*, pages 1151–1167. DOI: 10.2172/10162906 (see pp. 214, 217, 218).

Alexander, D. (1999). 'The Effect of Irradiation on the Mechanical Properties of 6061-T651 Aluminum Base Metal and Weldments.' In: *Effects of Radiation on Mater.*, pages 1027–1044. DOI: 10.1520/STP13918S (see pp. 208, 210–212, 216–220).

Considère, A. (1885). 'Mémoire sur l'emploi du fer et de l'acier dans les constructions.' In: *Annales des ponts et chaussées*, pages 574–775 (see p. 215).

Farrel, K. (2011). 'A Spectral Effect on Phase Evolution in Neutron-Irradiated Aluminum?' In: *MRS Proceedings*. Volume 373. DOI: 10.1557/PROC-373-165 (see p. 212).

Petit, T. (2018). 'Compréhension et modélisation d'essais de ténacité avec pop-in: application á l'aluminium 6061-T6 et influence de l'irradiation neutronique.' PhD thesis. Ecole Nationale Supérieure des Mines de Paris (see pp. 217, 218).

Petit, T. et al. (2022). 'Neutron irradiation and heat treatment effects on pop-in crack propagation instabilities in a 6061 aluminium alloy.' In: *J. Nuclear Materials*, page 153909. DOI: 10.1016/j.jnucmat.2022.153909 (see pp. 211, 214, 217, 218).

Tekoğlu, C. et al. (2015). 'On localization and void coalescence as a precursor to ductile fracture.' In: *Philosophical transactions of the Royal Society of London. A* 373. DOI: 10.1098/rsta.2014.0121 (see p. 210).

Weeks, J. et al. (1993). 'Effects of High Thermal Neutron Fluences on Type 6061 Aluminum.' In: *Effects of Radiation on Mater.*, pages 1168–1182 (see pp. 207, 211–214, 221, 223, 224).

9

CONCLUSIONS AND PROSPECTS

RÉSUMÉ

Cette thèse porte sur la modélisation de la ténacité de l'alliage d'aluminium 6061-T6 irradié dans le réacteur nucléaire de recherche Jules Horowitz. Le CEA doit garantir la ténacité de l'assemblage caisson-cœur présenté dans chapter 1. Il y a deux raisons principales à cette approche de modélisation. La première est que le CEA ne dispose pas d'éprouvettes fortement irradiés pour tester le comportement du matériau irradié. La seconde est que très peu de données dans la littérature étudient la ténacité du matériau irradié. En conséquence, cette thèse est conçue pour développer un modèle basé sur la physique qui prédit l'endommagement dans les alliages d'aluminium 6061 non irradiés et irradiés. Pour plus de détails, cette thèse s'articule autour de trois objectifs qui sont expliqués dans la section chapter 1.

Le modèle développé dans chapter 5 est basé sur des preuves expérimentales (*insitu* et *post mortem*). Chaque partie du modèle est évaluée séparément pour s'assurer qu'elle prédit les phénomènes expérimentaux. Ensuite, l'ensemble du modèle GTN (nucléation de cavités basée sur les déformations et les contraintes, formule analytique de croissance de cavités de q_1 et q_2 et approche modifiée de $f_\star$ pour la coalescence par la formation de voidsheeting) est évalué en simulant différents essais de traction et de ténacité. Les résultats macroscopiques expérimentaux et simulés sont en bon accord. Par conséquent, Objective 1 est atteint avec des résultats satisfaisants. Certains aspects du modèle peuvent être améliorés et sont expliqués dans la section 9.2.

Objective 2 est réalisée via le modèle développé dans chapter 7. Pour rappel, l'objectif principal de cette thèse est de modéliser la ténacité de l'alliage irradié. En conséquence, le modèle d'écoulement plastique irradié doit être couplé avec le modèle d'endommagement dans le dernier chapitre de cette thèse. Cette question est discutée ci-dessous.

En résumé, l'analyse dans chapter 6 montre que le durcissement et l'écrouissage ont respectivement un effet de premier et de second ordre sur la ténacité de l'alliage d'aluminium étudié. Cela pourrait être dû à l'augmentation relative élevée du durcissement et à la diminution relative limitée de l'écrouissage obtenues par traitement thermique. Un matériau plus vieilli avec une capacité d'écrouissage plus faibles est intéressant pour des travaux futurs afin de tirer des conclusions claires concernant l'effet du durcissement et de la baisse de l'écrouissage sur la ténacité. Le fait intéressant est que le modèle d'endommagement est utilisé pour simuler la propagation de fissure dans les matériaux traités thermiquement et que de bonnes prédictions sont

obtenues. Cela signifie que le modèle d'endommagement peut être utilisé pour simuler la propagation des fissures dans les matériaux irradiés avec différents comportements de durcissement.

Dans l'ensemble, chapter 8 répond à l'objectif principal de cette thèse de doctorat. Le modèle de la thèse prédit une baisse de la déformation à rupture après irradiation et aucun changement dans la ténacité. Compte tenu du peu de données dans la littérature, on peut conclure que le modèle de la thèse produit de bons résultats lorsqu'il est comparé aux données expérimentales dans le travail de Alexander, 1993, 1999. Néanmoins, davantage de données expérimentales sont nécessaires pour confirmer la stabilité de la ténacité après irradiation. Si ce fait est confirmé, le modèle de la thèse peut être utilisé pour prédire la ténacité à des doses très élevées. Ces résultats sont intéressants lorsqu'il s'agit de décider si la durée de vie de JHR peut être prolongée au-delà des très hautes doses. Si les données expérimentales supplémentaires désapprouvent le fait que la ténacité est stable après irradiation, le modèle de la thèse doit être adapté pour prendre en considération les éléments sous-jacents comme le rôle des précipités de Si amorphe sur les joints de grains. Une façon de prendre en compte ce phénomène est de lier la coalescence des vides au Φ_{th} comme montré dans chapter 8.

This PhD thesis deals with modeling the fracture toughness of the irradiated aluminum 6061-T6 alloy in the Jules Horowitz nuclear research reactor. The CEA must guarantee the toughness of the vessel discussed in chapter 1. The results obtained via this model are analyzed to understand how the radiation damage affects the fracture toughness of the aluminum 6061-T6 alloy. There are two main reasons behind this approach of modeling. The first one is that the CEA does not have any highly irradiated samples in order to test the behavior of the irradiated material. The second one is that very few data in the literature investigates the toughness of the irradiated material. The results in the literature show two opposite trends. The first trend is a stable fracture toughness as a function of the radiation dose. The second trend is a drop in fracture toughness of the irradiated material. Therefore, this PhD thesis is designed to develop a physics-based model that predicts damage in unirradiated and irradiated 6061 aluminum alloys. In more details, this PhD deals with three objectives which are explained in chapter 1. The current chapter is divided into two sections. The following section concludes on how this PhD help achieve the objectives listed in chapter 1. The second section gives some prospects and scientific insights for the future.

9.1 CONCLUSIONS

Chapter 3, chapter 4 and chapter 5 study damage in the unirradiated material in the purpose of achieving Objective 1. The latter aims to understand the micro damage mechanisms (i. e. void nucleation, growth and coalescence) under different stress triaxiality levels via experimental observations in order to model these phenomena. The main conclusions are summarized as follows:

1. As discussed in the work of Hannard et al., 2016; Petit et al., 2019; Shen et al., 2013, void nucleation takes place over micron-sized particles in the 6061 alloy. There are two types of particles: large Mg_2Si and intermetallics elongated along grain boundaries. The *insitu* tensile test carried out in chapter 5 confirms that Mg_2Si particles fail at an early stage and can be considered as pre-existing voids as suggested by Maire et al., 2005. However, intermetallic particles require more accumulated strain and high stresses inside the particle to fail. In this work, *insitu* experimental evidence prove that a quasi-linear relationship can be established between the number of intermetallic particles that fail and strain. Nonetheless, there are various models in the literature which assume more complex void nucleation dynamics.

   For instance, Shen, 2012 use the Chu and Needleman nucleation model [Chu et al., 1980] which is based on a Gaussian distribution to describe nucleation as a function of strain. Huber et al., 2005 use a sixth order polynomial function to model void nucleation as a function of plastic strain in AlSiMg aluminum alloys. Petit et al., 2019 use a second order polynomial function to model void nucleation as a function of the maximum principal stress in a 6061 aluminum alloy. Although, the cited authors obtain satisfying results, void nucleation can be modeled by a first order linear function which results in good predictions when compared to nucleation experimental results (see chapter 5). Another issue is the choice between strain– and stress–based nucleation models. It is well known that strain–based models underestimate void nucleation [Butcher et al., 2011]. A mix of strain– and stress–based nucleation model is used in this work to model nucleation. This allows to account for the stress effect on nucleation while avoiding numerical difficulties as the nucleation model is expressed as a function of the incremental plastic strain and not the incremental stress (the latter can fluctuate and lead to divergence issues). In other words, an increase in plastic strain is required to obtain void nucleation. However, the nucleation rate is still driven by the stress state.

2. It is well established since the work of Mc Clintock, 1968 and Rice et al., 1969 that voids grow under plastic strain. Later, Faleskog et al., 1998 develop a calibration method for the q-parameters of the GTN model. This method is based on the unit cell model. A series of unit cell finite element simulations are

carried out to cover a wide range of stress triaxiality. Then, a single element with the GTN behavior is used to calibrate the q_1 and q_2 parameters such that the single element and unit cell have the same behavior. The drawback of this calibration method is that it is time consuming since it should be carried out whenever the material changes (i. e. elastic–plastic behavior changes). Chapter 3 discusses an analytical formula that gives calibrated q_1 and q_2 parameters as a function of the hardening in the material. The analytical formula is inspired by the calibration method of Faleskog et al., 1998. A wide number of unit cell simulations are carried out with different hardening, initial porosity and stress triaxiality. Then, coefficients of the analytical formula are calibrated over the wide number of simulations. This guarantees that the analytical formula gives optimum q_1 and q_2 parameters for low, medium and high hardening materials. The analytical formula results in good predictions and it is easy to implement in a finite element code which makes it usable in future work.

3. Void coalescence through void sheeting is an unanswered question in the literature. On one hand, authors like Ueda et al., 2014, Shen et al., 2013 and Petit et al., 2019 observe secondary voids over fracture surfaces (i. e. voids which are smaller in size than primary voids nucleated on micron-sized particles). On the other hand, it is difficult to model the role of secondary voids in the process of ductile failure as it is highly improbable to observe void nucleation and growth over sub-micron particles [Perrin et al., 2000]. For instance, no secondary voids are observed during *insitu* tensile testing in chapter 5 (even at high magnifications). However, evidence of void coalescence over sub-micron particles is observed in chapter 5 over polished surfaces of tested CT samples. The main challenge is to properly simulate this phenomenon without having enough *insitu* data as it is the case for void nucleation over intermetallic particles.

   There are three approaches in the literature to take into account the void sheeting through void coalescence. The first one is developed in the work of Perrin et al., 2000 and is based on modifying the constitutive Gurson equations to incorporate a second variable related to the secondary porosity (i. e. f_2). The drawback of this approach is that it accounts for secondary voids only in the growth phase (i. e. no void nucleation nor coalescence over secondary voids and therefore, no interaction between primary and secondary voids). The second approach is presented in the work of Ueda et al., 2014 and is based on adding a secondary nucleation law that accounts for the secondary voids. The main drawback of this approach is that it overestimates void growth in the simulated material. The third approach is detailed in the work of Gao et al., 2006 and is based on reducing the critical porosity (f_c parameter in the GTN model) to accelerate the onset of coalescence. Although this approach does not account for void nucleation

over secondary voids, it takes into account the interaction between primary and secondary voids. Secondary voids grow during damage till they interrupt the primary void growth as primary voids are linked by the smaller voids in the inter–void ligament. By decreasing the critical porosity in the GTN model, the primary void growth is interrupted and the coalescence phase is activated at a lower strain. However, the approach presented by Gao et al., 2006 assumes that the critical porosity includes the porosity increase due to nucleation and the porosity increase due to growth. In fact, an increase in primary nucleation porosity is not related to the secondary voids and its effect on void coalescence. Nucleated voids must grow before interacting with secondary voids. Therefore, in this work the $f_\star$ coalescence approach developed by Tvergaard and Needleman Tvergaard et al., 1984 is modified to relate the onset of void coalescence to porosity increase due to growth of primary voids. Then, a cell model is developed in chapter 5 to investigate the effect of secondary voids on the onset of coalescence (i. e. interaction between primary and secondary voids in the inter–void ligament). It is observed that the critical porosity decreases as the stress triaxiality increases. Therefore, a fit is carried out over the cell model results to relate the critical porosity to the stress triaxiality in the modified $f_\star$ coalescence approach. The advantage of this approach that it takes into account the interaction between primary and secondary void growth. The secondary voids interrupt the growth of primary voids as expected. However, it is assumed that secondary voids are nucleated or pre-existing in the material. There is no criterion for the nucleation of secondary voids. This matter can be discussed in future work.

The developed model in chapter 5 is based on experimental (*insitu* and *post mortem*) evidence. Each part of the model is evaluated separately as explained above to make sure it predicts the experimental phenomena. Then, the whole GTN model (i. e. linear strain– and stress–based void nucleation, analytical q_1 and q_2 void growth formula and modified $f_\star$ approach for coalescence by void sheeting) is evaluated by simulating different tensile and toughness tests. The macroscopic experimental and simulated results are in good agreement. As a result, Objective 1 is achieved with satisfying results. There are some aspects that can be improved in the model and that are explained in section 9.2.

Chapter 7 develops an irradiated plastic flow model in the purpose of achieving Objective 2. The main conclusion is summarized as follows:

4. A total of 120 tensile tests on irradiated 6061 samples are compiled from the literature to be used in developing a phenomenological model. Available articles in the literature confirm that neutron radiation increases the yield and ultimate tensile strengths, and decreases the uniform and total % elongation. In addition, very few stress—strain tensile curves are published. Therefore, the available trends in mechanical properties (yield and ultimate strengths as well as uniform

% elongation) are used to develop the irradiated plastic flow model. The latter is tested using finite element simulations to make sure that it results in good predictions. Simulation results are compared to the compiled experimental data. The same calibration and testing methods are carried out over two neutron spectrum ($R_\Phi = \Phi_{th}/\Phi_f$). Therefore, the developed irradiated plastic flow can be used to predict the elastic–plastic behavior of irradiated 6061 aluminum alloys over a certain range of Φ_{th} and R_Φ.

To conclude, Objective 2 is achieved via the developed model in chapter 7. As a reminder, the main objective of this PhD is to model the fracture toughness of the irradiated alloy. Therefore, the irradiated plastic flow model is to be coupled with the damage model in the final chapter of this thesis. This matter is discussed below.

Chapter 6 investigates several heat treated aluminum 6061 materials with different hardening behaviors in the purpose of achieving Objective 3. The age hardening heat treatment modifies the nano Mg_xSi_y precipitation which results in different mechanical properties. Increasing the age hardening time increases the yield and ultimate strengths and decreases the hardening capacity (as neutron irradiation) till a certain limit in time. The material with the highest strength is referred to as "peak-aged". After the critical age hardening time, the strength drops again [Develay, 1992] ("over-aged material"). The main conclusions are summarized as follows:

5. In this study, it is found that there is no significant drop in the strength of the over-aged material as reported in the literature [Develay, 1992] (compared to the peak-aged material). However, a drop in hardening capacity and a slight increase in fracture toughness are observed. From a macroscopic point of view, the drop in hardening capacity is explained by the fact that the ultimate tensile strength slightly decreases while the yield strength remains almost constant. From a nano precipitation point of view, it is well known that the β' Mg_xSi_y nano precipitates (supposedly found in the over-aged material) have a lower strengthening effect than the β'' Mg_xSi_y nano precipitates in the peak-aged material [Flament, 2015]. Since the β' Mg_xSi_y nano precipitates decrease the hardening capacity, this results in a smaller plastic zone near the crack tip which decreases the fracture toughness (following the Irwin relation which relates the radius of the plastic zone at the crack tip with the yield strength (YS) and stress intensity factor (K_I) in mode I under plane deformation conditions). Another explanation to the slight increase in fracture toughness of the over-aged material is found in the work of Dumont et al., 2003. The latter states that after the quench following the reheat process, micron-sized Mg_2Si particles precipitate at grain boundaries. The zones surrounding the Mg_2Si particles contain a lower amount of Mg and Si in solid solution. Therefore, these zones are softer as they do not contain nano Mg_xSi_y precipitates and are called Precipitate-Free-Zone (PFZ). Dumont et al., 2003 explain that the over-aged material has less PFZ which leads to a

homogeneous plastic flow inside the grain due to the lower contrast in strength between the PFZ and precipitate-rich zones. This fact leads to a lower plastic localization inside the grain which slightly enhances the fracture toughness of the over-aged material.

6. The different hardening materials obtained in chapter 6 are also used to test the damage model explained earlier. As mentioned above, the damage model is tested over a wide range of stress triaxialities. Although this result is encouraging, the main objective is to simulate fracture toughness of the irradiated material. The latter has a different hardening behavior when compared to the unirradiated one. The increase in strength and decrease in hardening that are provoked by neutron irradiation are artificially obtained in the heat treated materials in chapter 6. Therefore, testing the model over the heat treated 6061 materials is crucial for this study. If the model results in good predictions over the different hardening materials, it is still essential to understand the main driver in the model which allows to obtain these results. It is observed in chapter 6 that tensile and fracture toughness tests are well simulated by using the model equations and parameters from chapter 5. It is also found that the main driver in the model to simulate different hardening materials is the q-parameters' analytical formula that depend on the material's plastic behavior. To illustrate, when a single set of fixed q-parameters are used to model the under-aged and peak-aged materials, the simulated crack propagation results are incorrect. However, using the analytical q-parameters formula from chapter 3, good predictions are achieved over the under-aged, peak-aged and over-aged materials.

To sum up, the analysis in chapter 6 shows that the strength and hardening have respectively a first and second order effect on the fracture toughness of the studied aluminum alloy. This might be due to the high relative increase in strength and limited relative decrease in hardening obtained via heat treatment. A more over-aged material with a lower strength and hardening is interesting for future work to draw clear conclusions regarding the effect of strengthening and strain hardening drop on the overall fracture toughness. Moreover, some prospects regarding this study are proposed in section 9.2. The interesting fact is that the damage model is used to simulate crack propagation in the heat treated materials and good predictions are achieved. This connotes that the damage model can be used to simulate crack propagation in irradiated materials with different hardening behaviors.

Chapter 8 is focused on the fracture behavior of the irradiated material in the purpose of achieving the main objective of this PhD. The irradiated plastic flow model calibrated in chapter 7 is coupled with the GTN model developed in chapter 5 to study fracture in irradiated materials. The main conclusions are summarized as follows:

7. The strain at failure in irradiated notched tensile samples is well estimated using the PhD model (i. e. irradiated plastic flow model + damage GTN model).

The radiation dose (Φ_{th}) of the tested tensile samples is relatively low when compared to the dose of the tested samples in the literature. Yet, this step is compulsory to make sure the model gives fair macroscopic stress—strain results at low radiation doses.

8. Fracture toughness results found in the literature are thoroughly analyzed. The main criteria considered when comparing results are: thermal fluence (Φ_{th}), spectrum ($R_\Phi = \Phi_{th}/\Phi_f$), specimen type and machining conditions (i. e. machining carried out before or after irradiation). Results with the highest degree of confidence (i. e. samples machined before irradiation according to the ASTM 1820 standards and radiation dose monitored during the irradiation campaign) are published in the work of Alexander, 1993, 1999. The cited author do not observe a drop in fracture toughness after irradiation. This can be explained from a macro and microscopic point of view. From a microscopic point of view, the age hardening Mg_xSi_y nano precipitates are dissolved and replaced by new nano precipitates that have a higher strengthening effect. From a macroscopic point of view, the new nano precipitates decrease the hardening capacity but this is compensated by the increase in strength. As a result, the fracture toughness remains constant. Other fracture toughness results which are courtesy of the CEA are discussed in chapter 8. These samples are not machined prior irradiation and the radiation dose is not monitored during the irradiation campaign. In addition, the chemical composition of the tested material is slightly different from the typical aluminum 6061 alloy. Thus, a lower degree of confidence is attributed to these results. A decrease in fracture toughness is observed in the irradiated samples. The explanation behind this drop might be due to a heterogeneous precipitation of Si particles over grain boundaries that fragilize the alloy [Weeks et al., 1993]. Up till now, no trends are observed in the literature regarding the fracture toughness of the irradiated 6061 aluminum alloy. Even though Alexander, 1993, 1999 report a stable toughness as a function of Φ_{th}, the results are very few and do not allow to make conclusions.

9. The fracture toughness is simulated using the PhD model over a wide range of Φ_{th} ($0 — 400 \times 10^{21}\ n/cm^2$). By applying the damage model with the parameters calibrated over the unirradiated material in chapter 5, a hypothesis is made (see Hypothesis 1 in chapter 1): "Mg_2Si and intermetallic particles are not impacted by neutron radiation". At this stage, it is difficult to test this hypothesis since it requires an investigation on the particles in the irradiated material. That being said, using the damage model with the parameters calibrated in chapter 5 results in a stable fracture toughness as a function of Φ_{th} as observed in the work of Alexander, 1993, 1999. At high doses ($\Phi_{th} > 100 \times 10^{21}\ n/cm^2$), a slight increase in the simulated fracture toughness is observed. This nontrivial matter is investigated and it is found that, for a given CT sample, the GTN

stress triaxiality ($\sigma_m/\sigma_\star$) decreases at high doses. As the GTN stress triaxiality decreases, void growth decreases and the resistance to crack initiation increases at high radiation doses. This phenomenon explains the increase in fracture toughness at high radiation doses. Since a fracture toughness drop is observed in some of the experimental results, the damage model is modified to predict this drop. The latter is simulated by linking void coalescence to Φ_{th}. Thus, the onset of void coalescence is decreased as the radiation dose increases. This results in an equivalent drop in fracture toughness as the experimental results. However, the link between onset of void coalescence and the radiation dose is not calibrated over experimental data.

All in all, chapter 8 addresses the main objective of this PhD thesis. The PhD model predicts a drop in strain at failure after irradiation and no change in fracture toughness. Given the few data in the literature, it can be concluded that the PhD model produces good results when compared to the experimental data in the work of Alexander, 1993, 1999. Nonetheless, more experimental data is needed to confirm the stable fracture toughness after irradiation. If this fact is confirmed, the PhD model can be used to predict the toughness at very high doses. Such results are interesting when it comes to deciding whether the lifespan of the JHR can be extended beyond very high doses or not. If the additional experimental data disapprove the fact that the fracture toughness is stable after irradiation, the PhD model needs to be adapted to take into consideration the underlying elements as the role of amorphous Si precipitates over grain boundaries. One way of taking this phenomenon into account is by linking void coalescence to Φ_{th} as mentioned above.

9.2 PROSPECTS

Some of the above discussed aspects can be improved or further investigated in the future. The prospects proposed in this section can be divided into two parts. The first part deals with future experimental work while the second part deals with modifications in the PhD model.

From an experimental point of view, three issues can be further investigated. Firstly, coalescence through void sheeting can be studied via X-ray tomography *insitu* tests. Void nucleation over sub-micron particles require very high magnifications that cannot yet be achieved in 2022. However, it would be interesting to confirm the role of secondary voids in ductile damage. The main questions to answer are: do secondary voids create thin bands that interrupt growth of primary voids? (see fig. 9.1) If the dispersoid particles that give birth to secondary voids are present, does this increase the strain at failure? These questions can help confirm once and for all that the secondary voids have a predominant role in ductile damage.

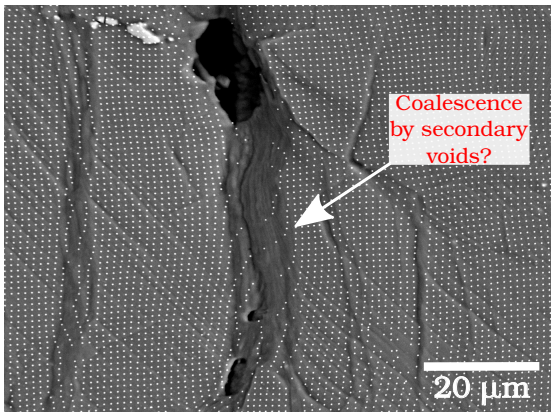

Figure 9.1: One of the questions that need to be answered in future work: do secondary voids create thin bands that interrupt growth of primary voids?

Secondly, the nano precipitation in the over-aged material in chapter 6 can be investigated to understand their role in the slight increase in toughness. Some explanations are given in section 9.1. However, these explanations can be confirmed by experimental evidence. The main questions to answer are: what is the morphology and structure of the nano precipitates in the over-aged material compared to the peak-aged one? Are there less PFZ in the over-aged material as claimed by Dumont et al., 2003? These questions can clarify the ambiguity regarding the relationship between the microstructural changes after heat treatment and the slight increase in fracture toughness.

Thirdly and lastly, more experimental data regarding the toughness of the irradiated 6061 aluminum alloy is needed to confirm or disapprove the stable fracture toughness observed in the work of Alexander, 1993, 1999. For the moment, this prospect is highly ambitious since it takes several years to obtain highly irradiated samples. However, testing intermediate doses can help draw preliminary conclusions along the way.

From a model point of view, two facts need to be taken into consideration in the future. The first one is the void shape. It is found in chapter 5 that nucleated voids results from the cracking of intermetallic particles which result in prolate voids. The latter can decrease the inter–void distance and lead to a higher local damage compared to spherical voids. This issue is neglected in the current GTN model which assumes that all voids are spherical. It is known from unit cell simulations with prolate voids that the void shape affects the onset of coalescence since the ligament distance is decreased [Benzerga et al., 2016]. The question to be answered is: how to account for prolate voids nucleated over intermetallic particles in the 6061 aluminum alloy and how do they affect the fracture toughness of the material? The second fact to be taken into consideration is the relation between the stress and void growth. The GTN model presumes that the mean stress drives the porosity increase. However, the mean stress has a lower effect over the growth of a prolate void than the axial stress (assuming the

prolate void is perpendicular to the axial stress). Therefore, it would be interesting to dig into both facts and understand if a better model can be obtained.

BIBLIOGRAPHY

Alexander, D. (1993). 'The Effect of Irradiation on the Mechanical Properties of 6061-T651 Aluminum.' In: *Effects of Radiation on Mater.*, pages 1151–1167. DOI: 10.2172/10162906 (see pp. 229, 235–237).

Alexander, D. (1999). 'The Effect of Irradiation on the Mechanical Properties of 6061-T651 Aluminum Base Metal and Weldments.' In: *Effects of Radiation on Mater.*, pages 1027–1044. DOI: 10.1520/STP13918S (see pp. 229, 235–237).

Benzerga, A. et al. (2016). 'Ductile Failure Modeling.' In: *Int. J. Frac.* 201, pages 29–80. DOI: 10.1007/s10704-016-0142-6 (see p. 237).

Butcher, C. and Z. Chen (Apr. 2011). 'Characterizing void nucleation in a damage-based constitutive model using notched tensile sheet specimens.' In: *Theor. Appl. Fract. Mech.* 55, pages 140–147. DOI: 10.1016/j.tafmec.2011.04.004 (see p. 230).

Chu, C. and A. Needleman (1980). 'Void nucleation effects in biaxially stretched sheets.' In: *J. Engng Mater. Technol.* 102, pages 249–256 (see p. 230).

Develay, R. (1992). 'Propriétés de l'aluminium et des alliages d'aluminium corroyés.' In: *Techniques de l'ingénieur Métaux et alliages non ferreux* TIB357DUO.m440 (see p. 233).

Dumont, D. et al. (2003). 'On the relationship between microstructure, strength and toughness in AA7050 aluminum alloy.' In: *Mater. Sci. Engng A* 356.1, pages 326–336. ISSN: 0921-5093. DOI: 10.1016/S0921-5093(03)00145-X (see pp. 233, 237).

Faleskog, J. et al. (1998). 'Cell model for nonlinear fracture analysis — I. Micromechanics calibration.' In: *Int. J. Frac.* 89, pages 355–373 (see pp. 230, 231).

Flament, C. (2015). 'Etude des évolutions microstructurales sous irradiation de l'alliage d'aluminium 6061-T6.' PhD thesis. Université Grenoble Alpes (see p. 233).

Gao, X. and J. Kim (2006). 'Modeling of ductile fracture: Significance of void coalescence.' In: *Int. J. Solids Structures* 43.20, pages 6277–6293. DOI: 10.1016/j.ijsolstr.2005.08.008 (see pp. 231, 232).

Hannard, F. et al. (2016). 'Characterization and micromechanical modelling of microstructural heterogeneity effects on ductile fracture of 6xxx aluminium alloys.' In: *Acta Mater.* 103, pages 558–572. DOI: 10.1016/j.actamat.2015.10.008 (see p. 230).

Huber, G. et al. (2005). 'Predictive model for void nucleation and void growth controlled ductility in quasi-eutectic cast aluminium alloys.' In: *Acta Mater.* 53.9, pages 2739–2749. ISSN: 1359-6454. DOI: 10.1016/j.actamat.2005.02.037 (see p. 230).

Maire, E. et al. (2005). 'Damage initiation and growth in metals. Comparison between modelling and tomography experiments.' In: *J. Mech. Phys. Solids* 53, pages 2411–2434 (see p. 230).

Mc Clintock, F. A. (1968). 'A criterion for ductile fracture by the growth of holes.' In: *J. App. Mech.* 35, pages 363–371 (see p. 230).

Perrin, G. and J.-B. Leblond (2000). 'Accelerated void growth in porous ductile solids containing two populations of cavities.' In: *Int. J. Plasticity* 16.1, pages 91–120 (see p. 231).

Petit, T. et al. (2019). 'Effect of hardening on toughness captured by stress-based damage nucleation in 6061 aluminum alloy.' In: *Acta Mater.* 180, 349–365. DOI: 10.1016/j.actamat.2019.08.055 (see pp. 230, 231).

Rice, J. R. and D. M. Tracey (1969). 'On the ductile enlargement of voids in triaxial stress fields.' In: *J. Mech. Phys. Solids* 17, pages 201–217 (see p. 230).

Shen, Y. (Dec. 2012). 'Comportement et endommagement des alliages d'aluminium 6061-T6: approche micromécanique.' PhD thesis. Ecole Nationale Supérieure des Mines de Paris (see p. 230).

Shen, Y. et al. (2013). 'Three-dimensional quantitative in situ study of crack initiation and propagation in AA6061 aluminum alloy sheets via synchrotron laminography and finite-element simulations.' In: *Acta Mater.* 61, pages 2571–2582. DOI: 10.1016/j.actamat.2013.01.035 (see pp. 230, 231).

Tvergaard, V. and A. Needleman (1984). 'Analysis of the cup–cone fracture in a round tensile bar.' In: *Acta Metall.* 32, pages 157–169 (see p. 232).

Ueda, T. et al. (2014). 'In situ laminography study of three-dimensional individual void shape evolution at crack initiation and comparison with Gurson–Tvergaard–Needleman-type simulations.' In: *Acta Mater.* 78, pages 254–270. ISSN: 1359-6454. DOI: 10.1016/j.actamat.2014.06.029 (see p. 231).

Weeks, J. et al. (1993). 'Effects of High Thermal Neutron Fluences on Type 6061 Aluminum.' In: *Effects of Radiation on Mater.*, pages 1168–1182 (see p. 235).

APPENDIX A

A.1 POROUS PLASTIC MODELS

A.1.1 *Porosity evolution in porous plastic models*

A porous plastic model is generally defined by a stress criterion $\sigma_\star$ which explicitly depends on the Cauchy stress tensor $(\underline{\sigma})$ and the porosity (f):

$$\sigma_\star = \phi(\underline{\sigma}, f) \tag{A.1}$$

The porous plastic models available in the literature consider the plastic flow in two ways. The first method does not take into account the porosity in the expression of the flow rule:

$$\underline{\dot{\varepsilon}}^p = \dot{p}\frac{\partial \sigma_\star}{\partial \underline{\sigma}} \tag{A.2}$$

This class of models encompasses the work of Ponte-Castaneda [PonteCastañeda, 1991], and the work of Rousselier [Rousselier et al., 1989]. In the second method, the flow rule is affected by a correction factor $(1-f)$ [Berdin et al., 2004]:

$$\underline{\dot{\varepsilon}}^p = (1-f)\,\dot{p}\,\frac{\partial \sigma_\star}{\partial \underline{\sigma}} \tag{A.3}$$

where p is the equivalent plastic strain in the matrix. The term $(1-f)$ comes from the definition of p as the equivalent plastic strain in the matrix through the modeling of hardening:

$$\underline{\sigma} : \underline{\dot{\varepsilon}}^p \Rightarrow \dot{\lambda}\underline{\sigma} : \frac{\partial \sigma_\star}{\partial \underline{\sigma}} = \dot{\lambda}\sigma_\star = (1-f)R(p)\dot{p} \Rightarrow \dot{\lambda} = (1-f)\dot{p} \tag{A.4}$$

The evolution of the porosity is composed of two terms: one due to plastic flow and another one due to void nucleation $f_n^i dp$:

$$\dot{f} = (1-f)\mathrm{tr}(\underline{\dot{\varepsilon}}^p) + \sum_j f_n^j \dot{p} \tag{A.5}$$

The first term describes the matrix incompressiblility given the assumption that the change of volume associated due to the elastic dilatation is negligible.

Different stress criteria can be derived in that manner. A few stress criteria are explained below.

A.1.2 *Gurson-Tvergaard-Needleman stress criterion*

$$S = \left(\frac{\sigma_{vM}}{\sigma_\star}\right)^2 + 2q_1 f_\star \cosh\left(\frac{3}{2}q_2\frac{\sigma_m}{\sigma_\star}\right) - 1 - q_1^2 f_\star^2 = 0 \tag{A.6}$$

where $\sigma^\star$ is implicitly given, σ_{eq} is the von Mises equivalent stress, and σ_m the mean stress. $f_\star$ is defined such that:

$$f_\star = \begin{cases} \delta f & \text{if } f < f_c \\ f_c + \delta(f - f_c) & \text{otherwise} \end{cases} \tag{A.7}$$

with δ the acceleration factor:

$$\delta = \begin{cases} 1 & \text{si } f < f_c \\ \dfrac{1}{q_1} - f_c & \\ \dfrac{}{f_r - f_c} & \text{otherwise} \end{cases} \tag{A.8}$$

The parameters of the model are:

$$\{q_1, q_2, f_c, f_r\}$$

For $\{q_1, q_2, f_c, f_r\} = \{1, 1, +\infty, -\}$, Gurson-Tvergaard-Needleman model reduces to the Gurson model [Gurson, 1977] which has no free parameters.

Since $\sigma_\star$ is implicitly defined through $S(\underline{\sigma}, \sigma_\star, f) = 0$, the first and second order derivatives of the function S are required to compute the first and second order derivatives of $\sigma_\star$:

$$S = A\frac{\sigma_1}{\sigma_\star} + B\cosh\left(\frac{C\sigma_2}{\sigma^\star}\right) + D = 0 \tag{A.9}$$

The parameters $\{A, B, C, D\}$ are user-defined functions of the porosity. The parameters $\{\sigma_1, \sigma_2\}$ are user-defined functions of the stress tensor.

The parameters of the model are therefore:

$$\left\{\sigma_1, \sigma_2, A, B, C, B, \frac{\partial A}{\partial f}, \frac{\partial B}{\partial f}, \frac{\partial C}{\partial f}, \frac{\partial D}{\partial f}, \frac{\partial \sigma_1}{\partial \underline{\sigma}}, \frac{\partial \sigma_2}{\partial \underline{\sigma}}, \frac{\partial^2 \sigma_1}{\partial \underline{\sigma}^2}, \frac{\partial^2 \sigma_2}{\partial \underline{\sigma}^2}\right\}$$

The first and second order derivatives of the function S are computed as given below:

$$\begin{aligned}
\frac{\partial S}{\partial \sigma_\star} &= -2A\frac{\sigma_1^2}{\sigma_\star^3} - \frac{BC\sigma_2}{\sigma_\star^2}\sinh\left(C\frac{\sigma_2}{\sigma_\star}\right)\\
\frac{\partial S}{\partial B} &= \cosh\left(C\frac{\sigma_2}{\sigma_\star}\right)\\
\frac{\partial S}{\partial \sigma_1} &= 2A\frac{\sigma_1}{\sigma_\star^2}\\
\frac{\partial S}{\partial C} &= \frac{B\sigma_2}{\sigma_\star}\sinh\left(C\frac{\sigma_2}{\sigma_\star}\right)\\
\frac{\partial S}{\partial \sigma_2} &= \frac{BC}{\sigma_\star}\sinh\left(C\frac{\sigma_2}{\sigma_\star}\right)\\
\frac{\partial S}{\partial D} &= 1\\
\frac{\partial S}{\partial A} &= \frac{\sigma_1^2}{\sigma_\star^2}
\end{aligned}$$

$$\begin{aligned}
\frac{\partial^2 S}{\partial \sigma_1^2} &= \frac{2A}{\sigma_\star^2}\\
\frac{\partial^2 S}{\partial \sigma_\star \partial A} &= -2\frac{\sigma_1^2}{\sigma_\star^3}\\
\frac{\partial^2 S}{\partial \sigma_2^2} &= B\left(\frac{C}{\sigma_\star}\right)^2\cosh\left(C\frac{\sigma_2}{\sigma_\star}\right)\\
\frac{\partial^2 S}{\partial \sigma_\star \partial B} &= -\frac{C\sigma_2}{\sigma_\star^2}\sinh\left(C\frac{\sigma_2}{\sigma_\star}\right)\\
\frac{\partial^2 S}{\partial \sigma_1 \partial A} &= 2\frac{\sigma_1}{\sigma_\star^2}\\
\frac{\partial^2 S}{\partial \sigma_\star \partial C} &= -\frac{B\sigma_2}{\sigma_\star^2}\sinh\left(C\frac{\sigma_2}{\sigma_\star}\right) - \frac{BC\sigma_2^2}{\sigma_\star^3}\cosh\left(C\frac{\sigma_2}{\sigma_\star}\right)\\
\frac{\partial^2 S}{\partial \sigma_1 \partial B} &= 0\\
\frac{\partial^2 S}{\partial \sigma_\star \partial D} &= 0\\
\frac{\partial^2 S}{\partial \sigma_1 \partial C} &= 0\\
\frac{\partial^2 S}{\partial \sigma_\star \partial \sigma_1} &= -\frac{4A\sigma_1}{\sigma_\star^3}\\
\frac{\partial^2 S}{\partial \sigma_1 \partial D} &= 0
\end{aligned}$$

$$\frac{\partial^2 S}{\partial \sigma_\star \partial \sigma_2} = -\frac{BC}{\sigma_\star^2}\sinh\left(C\frac{\sigma_2}{\sigma_\star}\right) - \frac{BC^2\sigma_2}{\sigma_\star^3}\cosh\left(C\frac{\sigma_2}{\sigma_\star}\right)$$
$$\frac{\partial^2 S}{\partial \sigma_2 \partial A} = 0$$
$$\frac{\partial^2 S}{\partial \sigma_2 \partial B} = \frac{C}{\sigma_\star}\sinh\left(C\frac{\sigma_2}{\sigma_\star}\right)$$
$$\frac{\partial^2 S}{\partial \sigma_2 \partial C} = \frac{B}{\sigma_\star}\sinh\left(C\frac{\sigma_2}{\sigma_\star}\right) + B\sigma_2\frac{C}{\sigma_\star^2}\cosh\left(C\frac{\sigma_2}{\sigma_\star}\right)$$
$$\frac{\partial^2 S}{\partial \sigma_2 \partial D} = 0$$

The first and second order derivatives of $\sigma_\star$ are:

$$\frac{\partial \sigma_\star}{\partial \underline{\sigma}} = -\left(\frac{\partial S}{\partial \sigma_\star}\right)^{-1}\frac{\partial S}{\partial \underline{\sigma}} = -\left(\frac{\partial S}{\partial \sigma_\star}\right)^{-1}\left[\frac{\partial S}{\partial \sigma_1}\frac{\partial \sigma_1}{\partial \underline{\sigma}} + \frac{\partial S}{\partial \sigma_2}\frac{\partial \sigma_2}{\partial \underline{\sigma}}\right]$$
$$\frac{\partial \sigma_\star}{\partial f} = -\left(\frac{\partial S}{\partial \sigma_\star}\right)^{-1}\frac{\partial S}{\partial f} = -\left(\frac{\partial S}{\partial \sigma_\star}\right)^{-1}\left[\frac{\partial S}{\partial A}\frac{\partial A}{\partial f} + \frac{\partial S}{\partial B}\frac{\partial B}{\partial f} + \frac{\partial S}{\partial C}\frac{\partial C}{\partial f} + \frac{\partial S}{\partial D}\frac{\partial D}{\partial f}\right]$$

$$\begin{aligned}\frac{\partial^2 S}{\partial \sigma_1 \partial f} &= \frac{\partial}{\partial \sigma_1}\left(\frac{\partial S}{\partial A}\frac{\partial A}{\partial f} + \frac{\partial S}{\partial B}\frac{\partial B}{\partial f} + \frac{\partial S}{\partial C}\frac{\partial C}{\partial f} + \frac{\partial S}{\partial D}\frac{\partial D}{\partial f}\right)\\ &= \frac{\partial^2 S}{\partial A \partial \sigma_1}\frac{\partial A}{\partial f} + \frac{\partial^2 S}{\partial B \partial \sigma_1}\frac{\partial B}{\partial f} + \frac{\partial^2 S}{\partial C \partial \sigma_1}\frac{\partial C}{\partial f} + \frac{\partial^2 S}{\partial D \partial \sigma_1}\frac{\partial D}{\partial f}\end{aligned}$$
$$\begin{aligned}\frac{\partial^2 S}{\partial \sigma_2 \partial f} &= \frac{\partial}{\partial \sigma_2}\left(\frac{\partial S}{\partial A}\frac{\partial A}{\partial f} + \frac{\partial S}{\partial B}\frac{\partial B}{\partial f} + \frac{\partial S}{\partial C}\frac{\partial C}{\partial f} + \frac{\partial S}{\partial D}\frac{\partial D}{\partial f}\right)\\ &= \frac{\partial^2 S}{\partial A \partial \sigma_2}\frac{\partial A}{\partial f} + \frac{\partial^2 S}{\partial B \partial \sigma_2}\frac{\partial B}{\partial f} + \frac{\partial^2 S}{\partial C \partial \sigma_2}\frac{\partial C}{\partial f} + \frac{\partial^2 S}{\partial D \partial \sigma_2}\frac{\partial D}{\partial f}\end{aligned}$$
$$\begin{aligned}\frac{\partial^2 S}{\partial \sigma_\star \partial f} &= \frac{\partial}{\partial \sigma_\star}\left(\frac{\partial S}{\partial A}\frac{\partial A}{\partial f} + \frac{\partial S}{\partial B}\frac{\partial B}{\partial f} + \frac{\partial S}{\partial C}\frac{\partial C}{\partial f} + \frac{\partial S}{\partial D}\frac{\partial D}{\partial f}\right)\\ &= \frac{\partial^2 S}{\partial A \partial \sigma_\star}\frac{\partial A}{\partial f} + \frac{\partial^2 S}{\partial B \partial \sigma_\star}\frac{\partial B}{\partial f} + \frac{\partial^2 S}{\partial C \partial \sigma_\star}\frac{\partial C}{\partial f} + \frac{\partial^2 S}{\partial D \partial \sigma_\star}\frac{\partial D}{\partial f}\end{aligned}$$
$$\begin{aligned}\frac{\partial^2 S}{\partial \underline{\sigma} \partial \sigma_\star} &= \frac{\partial}{\partial \sigma_\star}\left(\frac{\partial S}{\partial \sigma_1}\frac{\partial \sigma_1}{\partial \underline{\sigma}} + \frac{\partial S}{\partial \sigma_2}\frac{\partial \sigma_2}{\partial \underline{\sigma}}\right)\\ &= \frac{\partial^2 S}{\partial \sigma_1 \partial \sigma_\star}\frac{\partial \sigma_1}{\partial \underline{\sigma}} + \frac{\partial^2 S}{\partial \sigma_2 \partial \sigma_\star}\frac{\partial \sigma_2}{\partial \underline{\sigma}}\end{aligned}$$

$$\frac{\partial^2\sigma_\star}{\partial\underline{\sigma}\partial f} = -\left(\frac{\partial S}{\partial\sigma_\star}\right)^{-1}\left[\frac{\partial^2 S}{\partial\sigma_1\partial f}\frac{\partial\sigma_1}{\partial\underline{\sigma}} + \frac{\partial^2 S}{\partial\sigma_2\partial f}\frac{\partial\sigma_2}{\partial\underline{\sigma}}\right] + \frac{\partial^2 S}{\partial\sigma_\star\partial f}\left(\frac{\partial S}{\partial\sigma_\star}\right)^{-2}\left[\frac{\partial S}{\partial\sigma_1}\frac{\partial\sigma_1}{\partial\underline{\sigma}} + \frac{\partial S}{\partial\sigma_2}\frac{\partial\sigma_2}{\partial\underline{\sigma}}\right]$$

$$\frac{\partial^2\sigma_\star}{\partial\underline{\sigma}^2} = -\left(\frac{\partial S}{\partial\sigma_\star}\right)^{-1}\left[\frac{\partial S}{\partial\sigma_1}\frac{\partial^2\sigma_1}{\partial\underline{\sigma}^2} + \frac{\partial S}{\partial\sigma_2}\frac{\partial^2\sigma_2}{\partial\underline{\sigma}^2} + \frac{\partial^2 S}{\partial\sigma_1^2}\left(\frac{\partial\sigma_1}{\partial\underline{\sigma}}\right)^2 + \frac{\partial^2 S}{\partial\sigma_2^2}\left(\frac{\partial\sigma_2}{\partial\underline{\sigma}}\right)^2\right] + \left(\frac{\partial^2 S}{\partial\sigma_\star\partial\sigma_1}\frac{\partial\sigma_1}{\partial\underline{\sigma}} + \frac{\partial^2 S}{\partial\sigma_\star\partial\sigma_2}\frac{\partial\sigma_2}{\partial\underline{\sigma}}\right)\left(\frac{\partial S}{\partial\sigma_\star}\right)^{-2}\left[\frac{\partial S}{\partial\sigma_1}\frac{\partial\sigma_1}{\partial\underline{\sigma}} + \frac{\partial S}{\partial\sigma_2}\frac{\partial\sigma_2}{\partial\underline{\sigma}}\right]$$

This generic way of expressing the stress criterion can be used to write porous models that account for plastic anisotropy and void shape effect (e. g. [Benzerga et al., 2001; Madou et al., 2012; Morin et al., 2017; Paux et al., 2015]).

A.1.3 *Generic Thomason stress criterion*

$$\sigma_\star = A\sigma_I \tag{A.10}$$

where σ_I is the maximal principal stress. The parameter A is a material parameter that can be linked to the porosity through an auxiliary state variable.

The Thomason model can be written as follows:

$$A^{-1} = (1-\chi^2)\left[0.1\left(\frac{\chi^{-1}-1}{W}\right)^2 + 1.2\sqrt{\chi^{-1}}\right] \quad \text{with} \quad \chi = \left(\frac{6f\lambda}{\pi W}\right)^{1/3} \tag{A.11}$$

The evolution of the void aspect ratio W and cell aspect ratio λ are defined as follows:

$$\dot{W} = \frac{9\lambda}{4W}\left(1 - \frac{2}{\pi\chi^2}\right)\dot{\varepsilon}^p_{eq} \tag{A.12}$$

$$\dot{\lambda} = \lambda\dot{\varepsilon}_{II} \tag{A.13}$$

A.1.4 *Nucleation terms*

Different nucleation terms are available in the literature and are explained below. Multiple nucleation terms can be used simultaneously.

A.1.4.1 *Chu-Needleman strain based nucleation law [Chu et al., 1980]*

$$f_n = \frac{f_N}{s_N\sqrt{2\pi}}\exp\left(-\frac{1}{2}\left(\frac{p-\epsilon_N}{s_N}\right)^2\right) \tag{A.14}$$

where $\{f_N, s_N, \epsilon_N\}$ are material parameters and p is the matrix equivalent plastic strain.

A.1.4.2 *Chu-Needleman stress-based nucleation law [Chu et al., 1980]*

$$f_n = \frac{f_N}{s_N\sqrt{2\pi}} \exp\left(-\frac{1}{2}\left(\frac{\sigma_I - \sigma_N}{s_N}\right)^2\right) \tag{A.15}$$

where $\{f_N, s_N, \sigma_N\}$ are material parameters and σ_I the maximal positive principal stress.

A.1.4.3 *Power strain-based nucleation law*

$$f_n = f_N \left\langle \frac{p}{\epsilon_N} - 1 \right\rangle^m \quad \text{if } p \leq p_{max} \text{ and } \int f_n dp \leq f_{\text{nuc}}^{max} \tag{A.16}$$

where $\{f_N, m, \epsilon_N, p_{max}, f_{\text{nuc}}^{max}\}$ are material parameters and p is the matrix equivalent plastic strain.

A.1.4.4 *Power stress-based nucleation law*

$$f_n = f_N \left\langle \frac{\sigma_I}{\sigma_N} - 1 \right\rangle^m \quad \text{if } \sigma_I \leq \sigma_I^{max} \text{ and } \int f_n dp \leq f_{\text{nuc}}^{max} \tag{A.17}$$

where $\{f_N, m, \sigma_N, \sigma_I^{max}, f_{\text{nuc}}^{max}\}$ are material parameters and σ_I the maximal positive principal stress.

A.1.5 *Implicit schemes*

This section is devoted to the presentation of two implicit schemes that may be used to integrate the constitutive equations presented above.

A.1.5.1 *Standard implicit scheme*

Assuming a single porous stress criterion, the constitutive equations lead to the following system to be solved for an elastic-plastic flow:

$$\begin{aligned} \underline{\varepsilon}^{\text{el}} + \underline{\dot{\varepsilon}}^{\text{p}} - \underline{\varepsilon}^{\text{to}} &= 0 \\ \sigma_\star - R(p) &= 0 \\ \dot{f} - (1-f)\text{tr}(\underline{\dot{\varepsilon}}^{\text{p}}) - \sum_j f_n^j \dot{p} &= 0 \end{aligned} \tag{A.18}$$

A semi-implicit method is used to solve these equations according to the variables $\{\Delta\underline{\varepsilon}^{\text{el}}, \Delta p, \Delta f\}$

$$\mathcal{R}\Big(\Delta\underline{\varepsilon}^{\text{el}}, \Delta p, \Delta f\Big) = 0$$

where the residual $\mathcal{R}$ can be decomposed into blocks:

$$\begin{aligned}
\mathcal{R}_{\Delta \underline{\varepsilon}^{\mathrm{el}}} &= \Delta \underline{\varepsilon}^{\mathrm{el}} + (1 - f|_{t+\theta\Delta t})\Delta p \left.\frac{\partial \sigma_\star}{\partial \underline{\sigma}}\right|_{t+\theta\Delta t} - \Delta \underline{\epsilon}_{to} = 0 \\
\mathcal{R}_{\Delta p} &= \sigma_\star - R(p|_{t+\theta\Delta t}) = 0 \\
\mathcal{R}_{\Delta f} &= \Delta f - (1 - f|_{t+\theta\Delta t})^2 \Delta p \,\mathrm{tr}\left(\left.\frac{\partial \sigma_\star}{\partial \underline{\sigma}}\right|_{t+\theta\Delta t}\right) - \sum_j \left. f_n^j \right|_{t+\theta\Delta t} \Delta p = 0
\end{aligned} \tag{A.19}$$

Solving this system using a Newton-Raphson algorithm requires computing the Jacobian matrix:

$$J = \begin{pmatrix}
\dfrac{\partial \mathcal{R}_{\Delta \underline{\varepsilon}^{\mathrm{el}}}}{\partial \Delta \underline{\varepsilon}^{\mathrm{el}}} & \dfrac{\partial \mathcal{R}_{\Delta \underline{\varepsilon}^{\mathrm{el}}}}{\partial \Delta p} & \dfrac{\partial \mathcal{R}_{\Delta \underline{\varepsilon}^{\mathrm{el}}}}{\partial \Delta f} \\
\dfrac{\partial \mathcal{R}_{\Delta p}}{\partial \Delta \underline{\varepsilon}^{\mathrm{el}}} & \dfrac{\partial \mathcal{R}_{\Delta p}}{\partial \Delta p} & \dfrac{\partial \mathcal{R}_{\Delta p}}{\partial \Delta f} \\
\dfrac{\partial \mathcal{R}_{\Delta f}}{\partial \Delta \underline{\varepsilon}^{\mathrm{el}}} & \dfrac{\partial \mathcal{R}_{\Delta f}}{\partial \Delta p} & \dfrac{\partial \mathcal{R}_{\Delta f}}{\partial \Delta f}
\end{pmatrix}$$

where the different terms can be written as:

$$\begin{aligned}
\frac{\partial \mathcal{R}_{\Delta \underline{\varepsilon}^{\mathrm{el}}}}{\partial \Delta \underline{\varepsilon}^{\mathrm{el}}} &= \underline{\underline{\mathbf{I}}} + \theta \Delta p \left(1 - f|_{t+\theta\Delta t}\right) \left.\frac{\partial^2 \sigma_\star}{\partial \underline{\sigma}^2}\right|_{t+\theta\Delta t} : \left.\underline{\underline{\mathbf{D}}}\right|_{t+\theta\Delta t} \\
\frac{\partial \mathcal{R}_{\Delta \underline{\varepsilon}^{\mathrm{el}}}}{\partial \Delta p} &= \left(1 - f|_{t+\theta\Delta t}\right) \left.\frac{\partial \sigma_\star}{\partial \underline{\sigma}}\right|_{t+\theta\Delta t} \\
\frac{\partial \mathcal{R}_{\Delta \underline{\varepsilon}^{\mathrm{el}}}}{\partial \Delta f} &= \theta \Delta p \left(\left(1 - f|_{t+\theta\Delta t}\right) \left.\frac{\partial^2 \sigma_\star}{\partial \underline{\sigma} \partial f}\right|_{t+\theta\Delta t} - \left.\frac{\partial \sigma_\star}{\partial \underline{\sigma}}\right|_{t+\theta\Delta t} \right) \\
\frac{\partial \mathcal{R}_{\Delta p}}{\partial \Delta \underline{\varepsilon}^{\mathrm{el}}} &= \theta \left.\frac{\partial \sigma_\star}{\partial \underline{\sigma}}\right|_{t+\theta\Delta t} : \left.\underline{\underline{\mathbf{D}}}\right|_{t+\theta\Delta t} \\
\frac{\partial \mathcal{R}_{\Delta p}}{\partial \Delta p} &= -\theta \frac{dR(p)}{dp} \\
\frac{\partial \mathcal{R}_{\Delta p}}{\partial \Delta f} &= \theta \left.\frac{\partial \sigma_\star}{\partial f}\right|_{t+\theta\Delta t} \\
\frac{\partial \mathcal{R}_{\Delta f}}{\partial \Delta \underline{\varepsilon}^{\mathrm{el}}} &= -\theta \,\Delta p \left(1 - f|_{t+\theta\Delta t}\right)^2 \left(\left.\frac{\partial^2 \sigma_\star}{\partial \underline{\sigma}^2}\right|_{t+\theta\Delta t} : \left.\underline{\underline{\mathbf{D}}}\right|_{t+\theta\Delta t} \right) : \underline{I} - \theta \Delta p \sum_j \left.\frac{\partial f_n^j}{\partial \underline{\sigma}}\right|_{t+\theta\Delta t} : \left.\underline{\underline{\mathbf{D}}}\right|_{t+\theta\Delta t} \\
\frac{\partial \mathcal{R}_{\Delta f}}{\partial \Delta p} &= -\left(1 - f|_{t+\theta\Delta t}\right)^2 \left.\frac{\partial \sigma_\star}{\partial \underline{\sigma}}\right|_{t+\theta\Delta t} : \underline{I} - \theta \Delta p \sum_j \left.\frac{\partial f_n^j}{\partial p}\right|_{t+\theta\Delta t} - \sum_j \left. f_n^j \right|_{t+\theta\Delta t} \\
\frac{\partial \mathcal{R}_{\Delta f}}{\partial \Delta f} &= 1 - \theta \,\Delta p \left(1 - f|_{t+\theta\Delta t}\right) \left(-2 \left.\frac{\partial \sigma_\star}{\partial \underline{\sigma}} + \left(1 - f|_{t+\theta\Delta t}\right) \frac{\partial^2 \sigma_\star}{\partial \underline{\sigma} \partial f}\right) \underline{I} - \theta \Delta p \sum_j \left.\frac{\partial f_n^j}{\partial f}\right|_{t+\theta\Delta t}
\end{aligned} \tag{A.20}$$

Therefore, a porous model requires the following expressions:

$$\left\{ \sigma_\star, \frac{\partial \sigma_\star}{\partial \underline{\sigma}}, \frac{\partial \sigma_\star}{\partial \partial f}, \frac{\partial^2 \sigma_\star}{\partial \underline{\sigma}^2}, \frac{\partial^2 \sigma_\star}{\partial \underline{\sigma} \partial f} \right\}$$

as well as the following expressions for each nucleation mechanism:

$$\left\{ f_n^i, \frac{\partial f_n^i}{\partial \underline{\sigma}}, \frac{\partial f_n^i}{\partial p}, \frac{\partial f_n^i}{\partial f} \right\}$$

These expressions are detailed below for some stress criteria and nucleation formulas.

The Newton-Raphson algorithm may not succeed to find the solution of the non-linear system of equations, especially when the time step leads to a significant porosity increase.

Moreover, the porosity evolution leads to specific issues such as:

- Phenomenological laws describing void nucleation may have a threshold to be activated or inhibited.
- Material failure usually happens when the porosity reaches a critical value corresponding to the collapse of the yield surface. Detection of material failure is difficult when the equations governing the porosity evolution are included in the implicit system to be solved. For example, the estimates of the solution may exceed the critical value during the iterations while the solution of the implicit scheme may be below this critical value.

A.1.5.2 *A staggered approach*

As the main issues associated with the standard implicit scheme are associated with the porosity evolution, this section proposes a staggered approach where the porosity evolution and the evolution of other state variables (i. e. the elastic strain $\underline{\varepsilon}^{\text{el}}$ and the equivalent plastic strain p) are decoupled. A fixed point algorithm is used to ensure that the increments $\left\{ \Delta \underline{\varepsilon}^{\text{el}}, \Delta p, \Delta f \right\}$ satisfy the implicit System A.19.

Reduced implicit system:

Let i be the current step of the fixed point algorithm. The increment estimates of the elastic strain and the equivalent plastic strain at the next iterations, denoted respectively $\Delta \underline{\varepsilon}^{\text{el}}_{(i+1)}$ and $\Delta p_{(i+1)}$ satisfy a reduced implicit system:

$$\begin{aligned} \mathcal{R}_{\Delta \underline{\varepsilon}^{\text{el}}} = \Delta \underline{\varepsilon}^{\text{el}}_{(i+1)} + \left(1 - f_{(i)}\right) \Delta p_{(i+1)} \frac{\partial \sigma_\star}{\partial \underline{\sigma}} \left(\underline{\varepsilon}^{\text{el}}_{(i+1)}, f_{(i)} \right) - \Delta \underline{\epsilon}_{to} = 0 \\ \mathcal{R}_{\Delta p} = \sigma_\star \left(\underline{\varepsilon}^{\text{el}}_{(i+1)}, f_{(i)} \right) - R(p_{(i+1)}) = 0 \end{aligned} \tag{A.21}$$

where:

- $\underline{\varepsilon}^{\text{el}}_{(i+1)} = \underline{\varepsilon}^{\text{el}}\big|_t + \theta \, \Delta \underline{\varepsilon}^{\text{el}}_{(i+1)}$
- $p_{(i+1)} = p|_t + \theta \, \Delta p_{(i+1)}$

- $f_{(i)} = f|_t + \theta \, \Delta f_{(i)}$

The Implicit System above is solved using a standard Newton-Raphson method with the reduced Jacobian matrix:

$$\begin{bmatrix} \dfrac{\partial \mathcal{R}_{\Delta \underline{\varepsilon}^{\mathrm{el}}}}{\partial \Delta \underline{\varepsilon}^{\mathrm{el}}} & \dfrac{\partial \mathcal{R}_{\Delta \underline{\varepsilon}^{\mathrm{el}}}}{\partial \Delta p} \\ \dfrac{\partial \mathcal{R}_{\Delta p}}{\partial \Delta \underline{\varepsilon}^{\mathrm{el}}} & \dfrac{\partial \mathcal{R}_{\Delta p}}{\partial \Delta p} \end{bmatrix}$$

In practice, for numerical reasons, the full Implicit System A.19 is still solved, but the implicit equation related to the porosity evolution is modified as follows:

$$\mathcal{R}_{\Delta f} = \Delta f - \Delta f_{(i)} \tag{A.22}$$

Iterative determination of the porosity increment

Putting the constraints on the porosity evolution aside, the porosity is determined in an iterative manner as follows:

$$\Delta f^{(uc)}_{(i+1)} = \left(1 - f_{(i)}\right)^2 \Delta p_{(i+1)} \, \mathrm{tr}\left(\frac{\partial \sigma_\star}{\partial \underline{\sigma}}\left(\underline{\varepsilon}^{\mathrm{el}}_{(i+1)}, f_{(i)}\right)\right) - \textstyle\sum_j f^j_n\left(\underline{\varepsilon}^{\mathrm{el}}_{(i+1)}, p_{(i+1)}, f_{(i)}\right) \Delta p_{(i+1)} = 0 \tag{A.23}$$

Here the $^{(uc)}$ superscript means "uncorrected". Corrections to $\Delta f^{(uc)}_{(i+1)}$ are introduced in the next paragraphs to deal with thresholds in nucleation laws and detection of material failure.

Thresholds in nucleation laws

Let:

- $\Delta f^{j,(uc)}_n\Big|_{(i+1)} = f^j_n\left(\underline{\varepsilon}^{\mathrm{el}}_{(i+1)}, p_{(i+1)}, f_{(i)}\right) \Delta p_{(i+1)}$ be the uncorrected contribution of the j^{th} nucleation law to the porosity evolution.
- $f^j_n\Big|_t$ be the value of the nucleated porosity due to this void nucleation law at the beginning of the time step.
- $f^{j,\max}_n$ be the threshold of this nucleation law, i. e. the maximal value of the nucleated porosity due to this law.

$f^{j,\max}_n - f^j_n\Big|_t$ is the maximum allowed increase in porosity for this nucleation law.
The corrected contribution is defined $\Delta f^j_n\Big|_{(i+1)}$ as follows:

$$\Delta f^j_n\Big|_{(i+1)} = \min\left(\Delta f^{j,(uc)}_n\Big|_{(i+1)}, f^{j,\max}_n - f^j_n\Big|_t\right) \tag{A.24}$$

Treatment of material failure

To avoid the introduction of other notations, $\Delta f^{(uc)}_{(i+1)}$ is still used even though corrections related to thresholds in nucleations laws may have been taken into account at this stage.

If $f|_t + \Delta f^{(uc)}_{(i+1)}$ is greater than the critical porosity denoted $\alpha_1 f_r$, a dichotomic approach is used:

$$\Delta f_{(i+1)} = \frac{1}{2}\Big(f + \Delta f_{(i)} + \alpha_1 f_r\Big) - f|_t; \tag{A.25}$$

This approach allows the porosity to approach the critical porosity smoothly.

The α_1 factor is a user defined parameter, chosen by default as 98.5 %. The reason for not allowing the porosity be closer to f_r is that the implicit System becomes very difficult to solve as the be yield surfaces collapses.

Stopping criteria

The iterations are stopped when the porosity becomes stationary, i. e. when:

$$\left|\Delta f^{(uc)}_{(i+1)} - \Delta f_{(i)}\right| < \varepsilon_f \tag{A.26}$$

where the value of ε_f is a user defined value (by default, a stringent value of 10^{-10} is used).

Detection of the material failure (post-processing)

Once the stopping Condition above is satisfied, the material failure is detected when the final porosity is higher than a given threshold $\alpha_2 f_r$, where α_2 is a user defined constant chosen equal to 98 % by default.

When the material failure is detected, the value of the auxiliary state variable *broken* is set to one.

A.1.6 *Derivatives of stress criteria*

A.1.6.1 *Derivatives of the Gurson-Tvergaard-Needleman stress criterion*

$$
\begin{aligned}
\frac{\partial S}{\partial \sigma_\star} &= -2\frac{\sigma_{vM}^2}{\sigma_\star^3} - \frac{3q_1q_2f_\star\sigma_m}{\sigma_\star^2}\sinh\left(\frac{3}{2}q_2\frac{\sigma_m}{\sigma_\star}\right)\\
\frac{\partial S}{\partial \underline{\sigma}} &= 3\frac{\underline{s}}{\sigma_\star^2} + \frac{q_1q_2f_\star}{\sigma_\star}\sinh\left(\frac{3}{2}q_2\frac{\sigma_m}{\sigma_\star}\right)\underline{I}\\
\frac{\partial S}{\partial f} &= 2q_1\delta\cosh\left(\frac{3}{2}q_2\frac{\sigma_m}{\sigma_\star}\right) - 2q_3\delta f_\star\\
\frac{\partial^2 S}{\partial \underline{\sigma}^2} &= \frac{2}{\sigma_\star^2}\underline{\underline{\underline{\underline{\mathbf{M}}}}} + \frac{q_1\, q_2^2\, f_\star}{2\sigma_\star^2}\cosh\left(\frac{3}{2}q_2\frac{\sigma_m}{\sigma_\star}\right)\underline{I}\otimes\underline{I}\\
\frac{\partial^2 S}{\partial \underline{\sigma}\partial \sigma_\star} &= -\frac{6\underline{s}}{\sigma_\star^3} - \frac{q_1\, q_2\, f_\star}{\sigma_\star^2}\sinh\left(\frac{3}{2}q_2\frac{\sigma_m}{\sigma_\star}\right)\underline{I} - \frac{3\, q_1\, q_2^2\, f_\star\, \sigma_m}{2\,\sigma_\star^3}\cosh\left(\frac{3}{2}q_2\frac{\sigma_m}{\sigma_\star}\right)\underline{I}\\
\frac{\partial^2 S}{\partial \underline{\sigma}\partial f} &= \frac{q_1\, q_2\, \delta}{\sigma_\star}\sinh\left(\frac{3}{2}q_2\frac{\sigma_m}{\sigma_\star}\right)\underline{I}\\
\frac{\partial^2 S}{\partial \sigma_\star\partial f} &= -\frac{3\, q_1\, q_2\, \delta\, \sigma_m}{\sigma_\star^2}\sinh\left(\frac{3}{2}q_2\frac{\sigma_m}{\sigma_\star}\right)\\
\frac{\partial^2 S}{\partial \sigma_\star^2} &= 6\frac{\sigma_{vM}^2}{\sigma_\star^4} + \frac{6q_1q_2f_\star\sigma_m}{\sigma_\star^3}\sinh\left(\frac{3}{2}q_2\frac{\sigma_m}{\sigma_\star}\right) + \frac{9q_1q_2^2f_\star\sigma_m^2}{2\sigma_\star^4}\cosh\left(\frac{3}{2}q_2\frac{\sigma_m}{\sigma_\star}\right)
\end{aligned}
\tag{A.27}
$$

The first and second order derivatives of $\sigma_\star$ are:

$$
\begin{aligned}
\frac{\partial \sigma_\star}{\partial \underline{\sigma}} &= -\left(\frac{\partial S}{\partial \sigma_\star}\right)^{-1}\frac{\partial S}{\partial \underline{\sigma}}\\
\frac{\partial \sigma_\star}{\partial f} &= -\left(\frac{\partial S}{\partial \sigma_\star}\right)^{-1}\frac{\partial S}{\partial f}\\
\frac{\partial^2 \sigma_\star}{\partial \underline{\sigma}^2} &= -\left(\frac{\partial S}{\partial \sigma_\star}\right)^{-1}\left(\frac{\partial^2 S}{\partial \underline{\sigma}^2} + \frac{\partial^2 S}{\partial \underline{\sigma}\partial \sigma_\star}\otimes\frac{\partial \sigma_\star}{\partial \underline{\sigma}}\right) + \left(\frac{\partial S}{\partial \sigma_\star}\right)^{-2}\left(\frac{\partial S}{\partial \underline{\sigma}}\right)\otimes\left(\frac{\partial^2 S}{\partial \underline{\sigma}\partial \sigma_\star} + \frac{\partial^2 S}{\partial \sigma_\star^2}\frac{\partial \sigma_\star}{\partial \underline{\sigma}}\right)\\
\frac{\partial^2 \sigma_\star}{\partial \underline{\sigma}\partial f} &= -\left(\frac{\partial S}{\partial \sigma_\star}\right)^{-1}\left(\frac{\partial^2 S}{\partial \underline{\sigma}\partial f} + \frac{\partial^2 S}{\partial f\partial \sigma_\star}\frac{\partial \sigma_\star}{\partial \underline{\sigma}}\right) + \left(\frac{\partial S}{\partial \sigma_\star}\right)^{-2}\left(\frac{\partial^2 S}{\partial \underline{\sigma}\partial \sigma_\star} + \frac{\partial^2 S}{\partial \sigma_\star^2}\frac{\partial \sigma_\star}{\partial \underline{\sigma}}\right)\left(\frac{\partial S}{\partial f}\right)
\end{aligned}
\tag{A.28}
$$

A.1.6.2 *Derivatives of the Generic Thomason stress criterion*

The first and second order derivatives of $\sigma_\star$ are Bertram, 2012:

$$\frac{\partial \sigma_\star}{\partial \underline{\sigma}} = Ae_I \otimes e_I$$
$$\frac{\partial \sigma_\star}{\partial f} = 0$$
$$\frac{\partial^2 \sigma_\star}{\partial \underline{\sigma}^2} = A\Big((\sigma_I - \sigma_{II})^{-1} e_I \otimes e_{II} \otimes e_I \otimes e_{II} + e_{II} \otimes e_I \otimes e_{II} \otimes e_I\Big)$$
$$+ A\Big((\sigma_I - \sigma_{III})^{-1} e_I \otimes e_{III} \otimes e_I \otimes e_{III} + e_{III} \otimes e_I \otimes e_{III} \otimes e_I\Big)$$
$$\frac{\partial^2 \sigma_\star}{\partial \underline{\sigma} \partial f} = \underline{0}$$

where $\{e_I, e_{II}, e_{III}\}$ are the eigenvectors associated with the eigenvalues of the stress tensor $\{\sigma_I, \sigma_{II}, \sigma_{III}\}$.

A.1.7 *Derivatives of nucleation laws*

A.1.7.1 *Chu-Needleman strain-based nucleation law derivatives*

$$\frac{\partial A_n}{\partial \underline{\sigma}} = \underline{0}$$
$$\frac{\partial A_n}{\partial p} = -\frac{f_N}{s_N^2\sqrt{2\pi}} \left(\frac{p - \epsilon_N}{s_N}\right) \exp\left(-\frac{1}{2}\left(\frac{p - \epsilon_N}{s_N}\right)^2\right)$$
$$\frac{\partial A_n}{\partial f} = 0$$

A.1.7.2 *Chu-Needleman stress-based nucleation law derivatives*

$$\frac{\partial A_n}{\partial \underline{\sigma}} = -\frac{f_N}{s_N^2\sqrt{2\pi}} \left(\frac{\sigma_I - \sigma_N}{s_N}\right) \exp\left(-\frac{1}{2}\left(\frac{\sigma_I - \sigma_N}{s_N}\right)^2\right) e_I \otimes e_I$$

$$\frac{\partial A_n}{\partial p} = 0$$

$$\frac{\partial A_n}{\partial f} = 0$$

A.1.7.3 *Power strain-based nucleation law derivatives*

$$\frac{\partial A_n}{\partial \underline{\sigma}} = \underline{0}$$
$$\frac{\partial A_n}{\partial p} = \frac{m f_N}{\epsilon_N} \left\langle \frac{p}{\epsilon_N} - 1 \right\rangle^{m-1}$$
$$\frac{\partial A_n}{\partial f} = 0$$

A.1.7.4 *Power stress-based nucleation law derivatives*

$$\frac{\partial A_n}{\partial \underline{\sigma}} = \frac{m f_N}{\sigma_N} \left\langle \frac{\sigma_I}{\sigma_N} - 1 \right\rangle^{m-1} e_I \otimes e_I$$

$$\frac{\partial A_n}{\partial p} = 0$$

$$\frac{\partial A_n}{\partial f} = 0$$

B

APPENDIX B

The aim of this appendix is to extend the analysis of the *insitu* tensile test carried out in chapter 5 via advanced experimental techniques: nano gold monomers and Digital Image Correlation (DIC). These techniques can be applied to other materials to investigate other issues than the void nucleation studied in chapter 5.

B.1 ELECTRON BEAM LITHOGRAPHY

A 2D array of gold monomers (1×1 mm^2) is deposited via electron beam lithography to be able to obtain strain maps via DIC (see Marae-Djouda et al., 2017 for more details about the electron beam lithography process). Figure B.1 shows the 2D array occupying half of the notch. The studied regions of interest (ROI) are already discussed in chapter 5. During testing, the ROI 1 allows to analyze a large area while ROIs (2, 3, 4, 5, 6, 7) are used to focus on Al(FeMn)Si and Mg_2Si particles to study void nucleation. Micro-indentations are used to envelop the studied zones and make it easier to spot the zones during testing. Figure B.1 shows ROI 5 as well as a zoom on a single gold monomer (∼229 nm diameter).

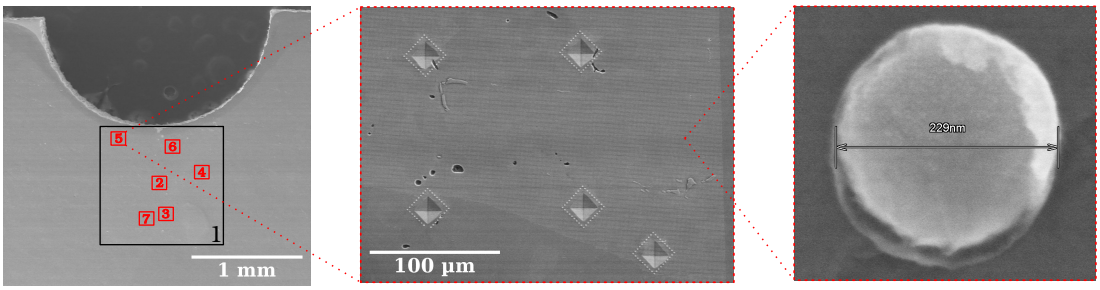

Figure B.1: From left to right: ROIs (from 1 to 7) in the tested FNT sample, zoom in ROI 5, a single gold monomer with a ∼229 nm diameter.

Figure B.2 shows images taken at 0, 8.18 and 21.6% of longitudinal deformation ($\Delta l / l_0$) in ROIs 1, 4 and 2. ROI 1 gives an overall estimation of the strain and reveals the band in which the plastic strain is localized before final rupture at $\Delta l / l_0 = 21.6\%$. ROI 4 is near the shown band which explains the rough torn surface at $\Delta l / l_0 = 21.6\%$ when compared to ROI 2 at the same deformation level. Such an observation indicates that the local strain is heterogeneous due to the damage taking place beneath the surface.

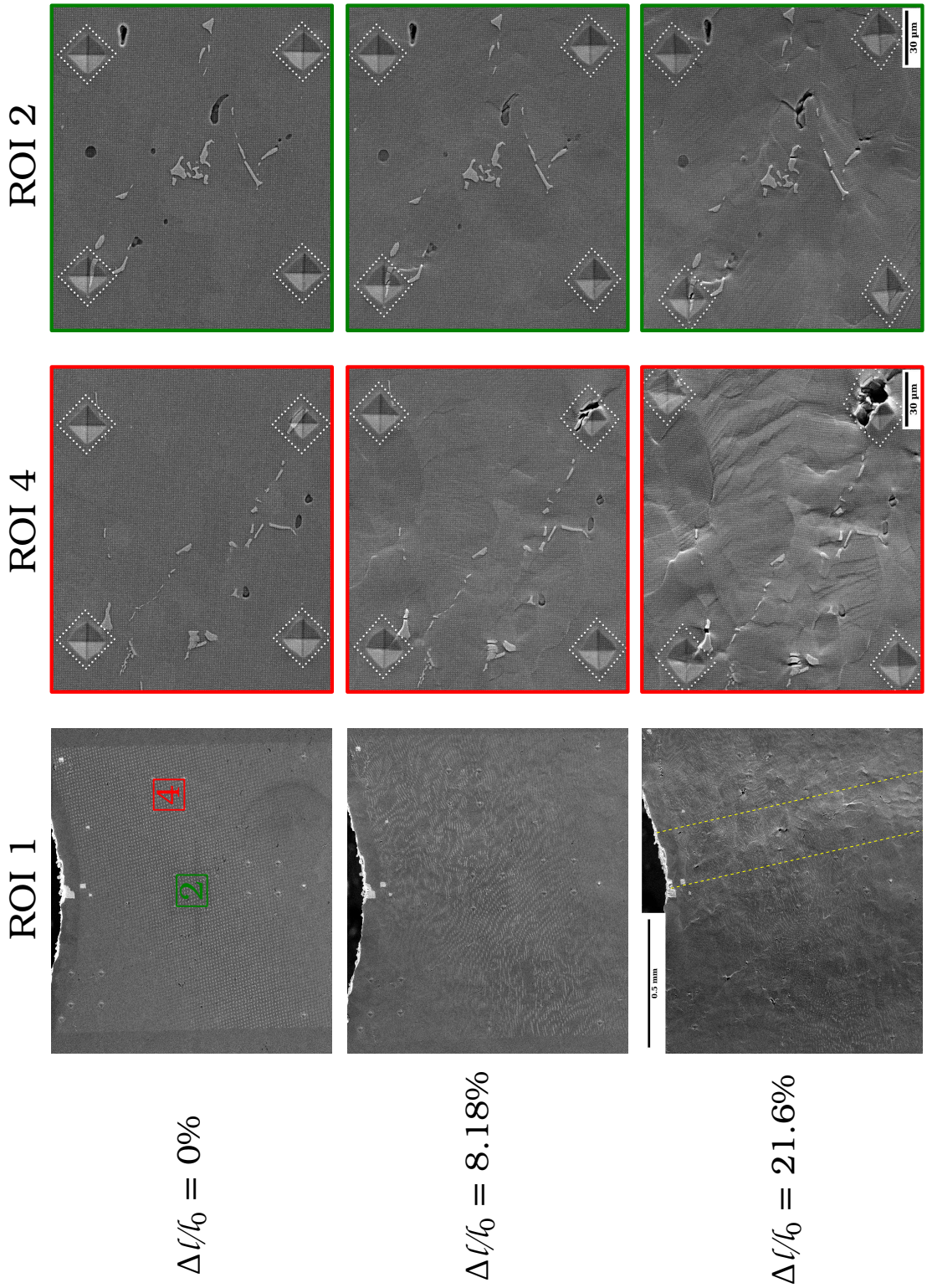

Figure B.2: ROIs 1, 4 and 2 at 0, 8.1 and 21.6% longitudinal deformation. ROI 2 is halfway between the sample's center and edge. Shaded lines in ROI 1 at $\Delta l/l_0 = 21.6\%$ show the plastic strain localization.

B.2 EXPERIMENTAL VERSUS SIMULATED STRAIN MAPS

B.2.1 *Digital Image Correlation*

Figure B.3 shows the strain maps (ε_{xx}) resulting from the DIC carried out in ROIs 2, 3, 4, 5, 6 and 7. The DIC is done via the Vic 2D software [1]. A subset of 57 and a step size of 13 are used to obtain the shown strain maps. The error related to the DIC strain estimation to be $\pm 0.11\%$. This error is estimated by analyzing the difference in strain between two similar static images. For all ROIs, the images size is 18×15 mm^2 with 4096×3536 pixels. A selected area in each ROI is used for the DIC analysis. ROIs 4 and 6 show the highest local strain levels. It is explained above that ROI 4 is near the localization band in which failure takes place. In addition, the ROI 6 is near the notch's edge which explains the high level of deformation. The following objective is to compare the measured strains to the finite element simulations.

B.2.2 *Finite Element Simulations*

Chapter 5 details the finite element mesh, boundary conditions and .

ROIs 2, 3, 4, 5, 6 and 7 are located in the mesh and highlighted as shown in chapter 5. Deformation in these elements is calculated and compared to the experimental deformation levels. The latter is estimated in each zone as $\Delta l / l_0$, given $l_0 = 100$ μm to be consistent with the mesh size. Figure B.4 illustrates the comparison between the experimental and simulated deformation levels in the 6 studied ROIs. The main observations are as follows:

1. ROIs 2, 3 and 7 are located near the sample's center where as the experimental $\Delta l / l_0$ is below the FE calculated values. ROIs 5 and 6 are near the notch's edge, while the calculated deformation is in good agreement with the experimental values. The deformation gradient between the center and the notch's edge is not astonishing.

2. However, the difference between the maximum experimental deformation values in ROIs 3 and 7 indicate that there is a deformation heterogeneity even between two zones that are located next to each other. Higher strain in ROI 3 with respect to ROI 7 may be explained by the local microplasticity effects related to local crystallography and microstructural details [Bugat et al., 1999].

3. Finally, the difference between the FE and experimental results in ROIs 2, 3 and 7 can be explained by the fact that these zones are in the sample's center and far from the localization band shown in fig. B.2 at $\Delta l / l_0 = 21.6\%$ in ROI

1 Vic 2D software used for digital image correlation: https://correlatedsolutions.eu/software/vic-software/

1. The parameters of the plastic flow model shown in chapter 5 are optimized on the macroscopic deformation of smooth round and notched tensile tests as explained above. In this case, the deformation heterogeneity observed between ROIs 3 and 7 cannot be predicted by the elastic–plastic model which provides an average deformation. In order to confirm this remark, two analyses are carried out.

The first analysis is shown in fig. B.5. As ROI 6 is located at the end the localization band shown in fig. B.2 at $\Delta l/l_0 = 21.6\%$ in ROI 1, it is expected that the deformation level would be higher in ROI 6. Figure B.5 confirms that the local deformation (ε_{xx}) in ROI 6 reaches 75% which is significantly higher than the estimated experimental $\Delta l/l_0$ in ROI 6 in fig. B.4. As a reminder, the latter shows the experimental $\Delta l/l_0$ using a gauge length $l_0 = 100\mu$m. This leads to lower strain values than what is revealed in fig. B.5 due to to the deformation heterogeneity.

The second analysis is shown in fig. B.6. The local deformation $\Delta l/l_0$ is estimated inside a zoomed area in the localization band shown in fig. B.2 at $\Delta l/l_0 = 21.6\%$ in ROI 1. As expected, the local deformation in this localization band is higher than the FE calculated values ("Model" in fig. B.6). It is challenging to obtain strain maps via DIC in the zoomed area shown in fig. B.6. Therefore, $\Delta l/l_0$ measurements are carried out using the displacement of a group of pixels.

The above presented comparisons between the local experimental and calculated FE deformation levels indicate that the isotropic hardening elastic–plastic model cannot predict the deformation heterogeneity observed when comparing two zones located near one another (e. g.ROIs 3 and 7). This should have consequences on nucleation criteria with a strain threshold.

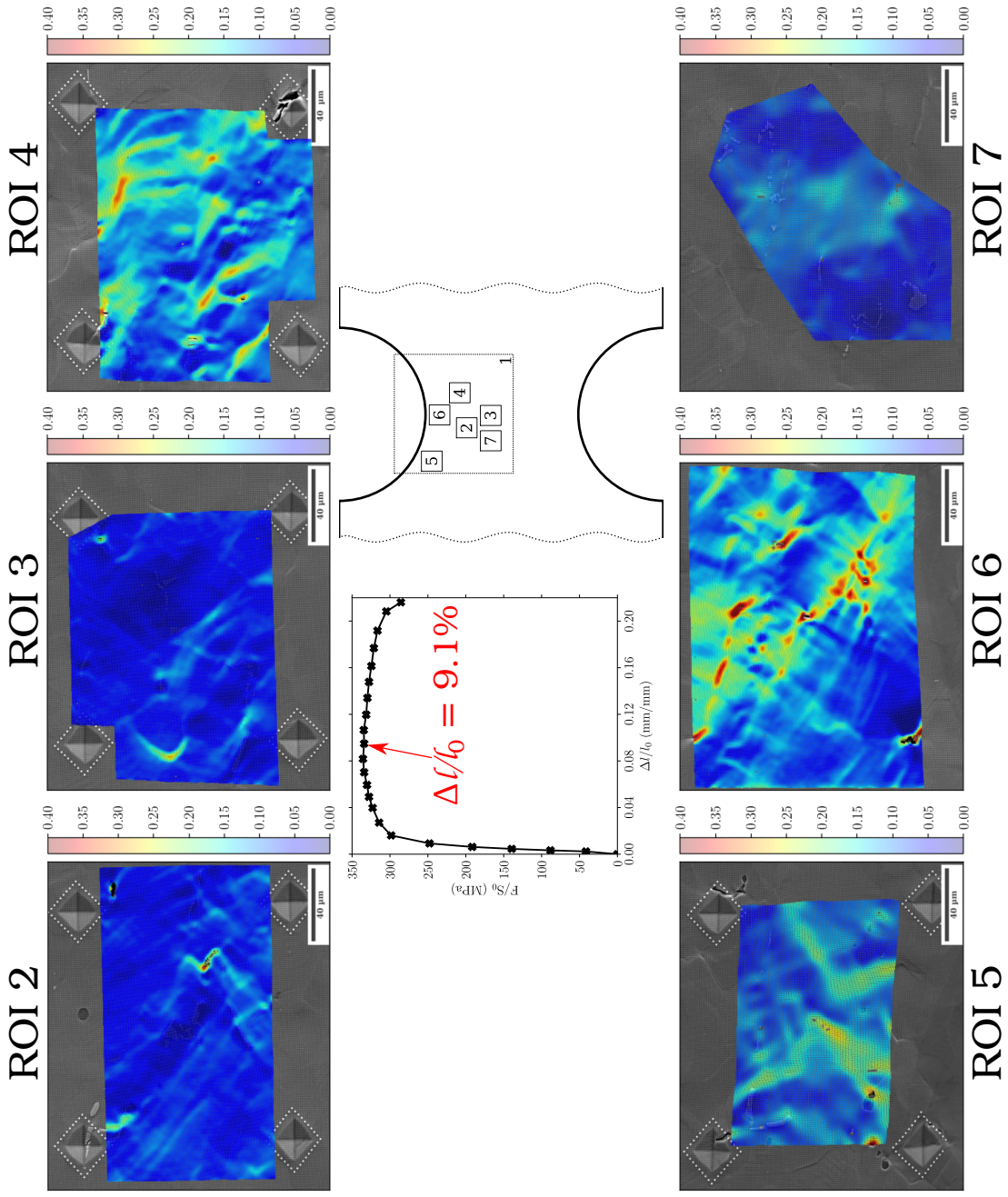

Figure B.3: Strain maps (ε_{xx}) in ROIs 2, 3, 4, 5, 6 and 7 at a longitudinal deformation of 9.1%. ROIs 4 and 6 show the highest strain as ROI 4 is near the localization band discussed in Figure B.2 while ROI 6 is near the sample's edge.

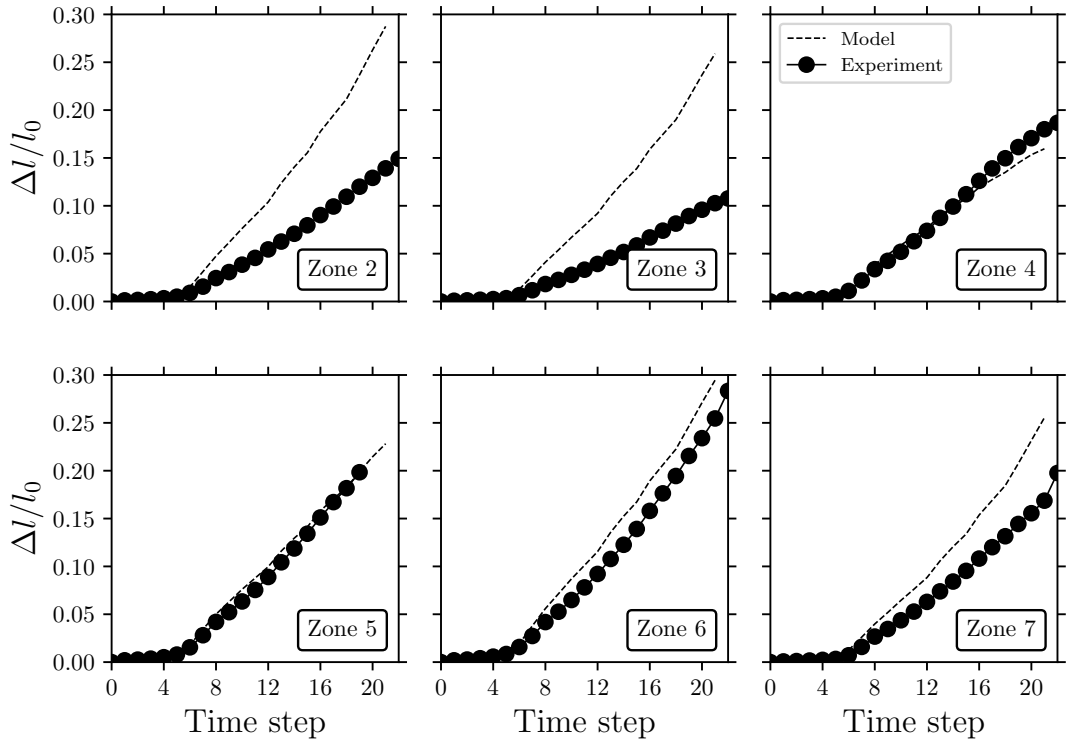

Figure B.4: Experimental and simulated deformation levels. Experimental deformation is estimated in each zone as $\Delta l/l_0$ with $l_0 = 100$ μm in order to compare with FE results where the mesh size in the xy plane = 100×100 μm^2.

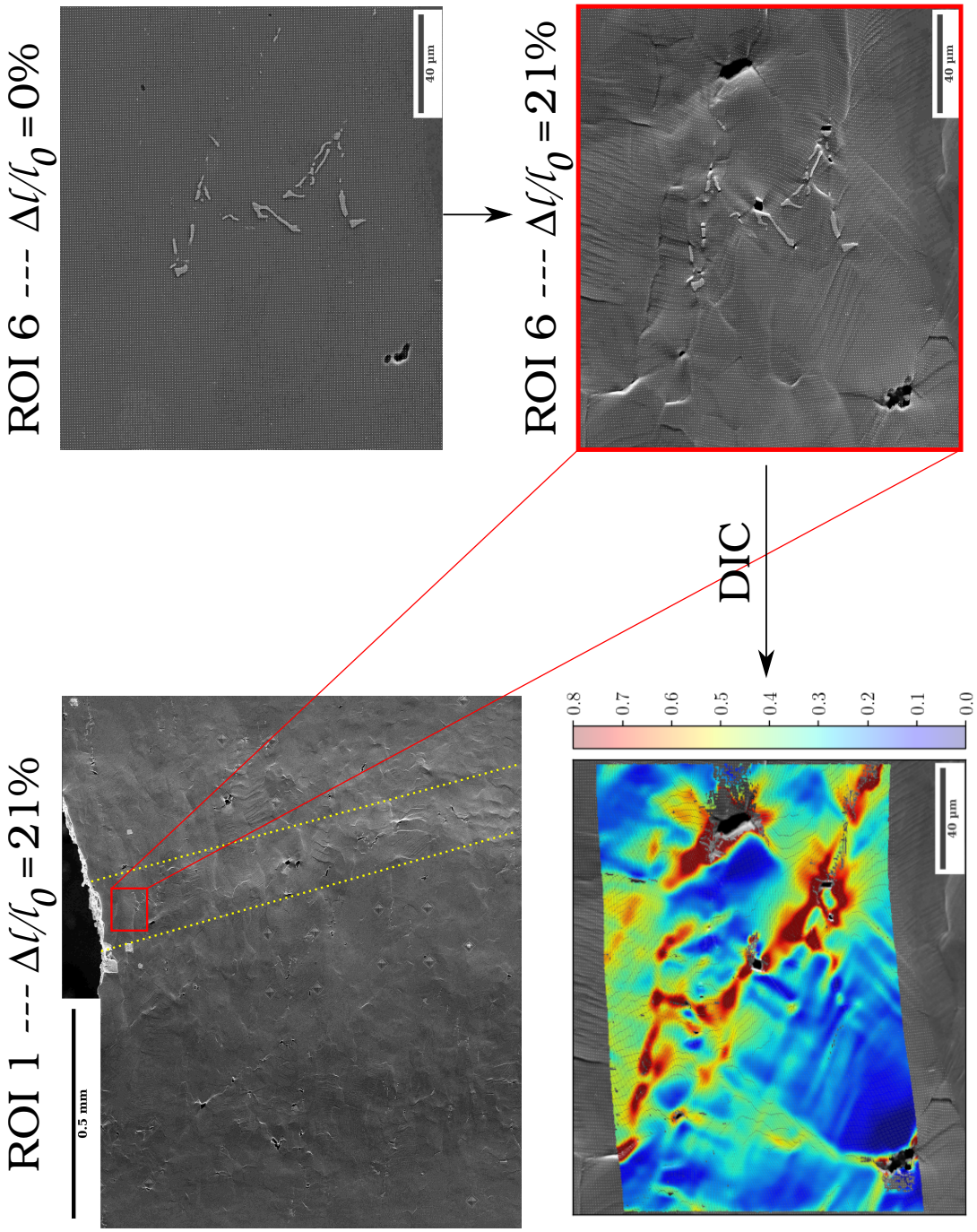

Figure B.5: *Upper left:* ROI 1 at $\Delta l/l_0 = 21\%$ showing ROI 6 (red rectangle) which is located near the edge and inside the localization band. *Upper right:* ROI 6 at $\Delta l/l_0 = 0\%$. *Lower right:* ROI 6 at $\Delta l/l_0 = 21\%$. *Lower left:* Strain maps of RO6 1 at $\Delta l/l_0 = 21\%$

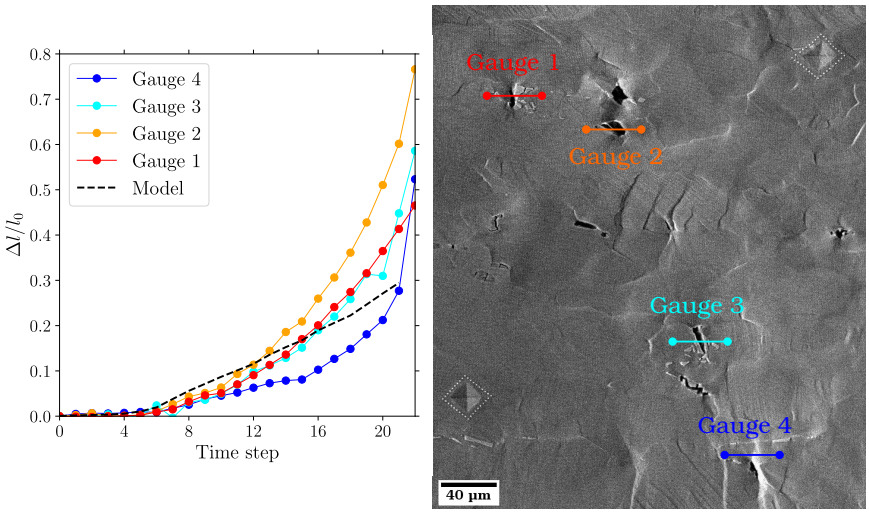

Figure B.6: Analysis of the local deformation inside the strain localization band shown in fig. B.2 in ROI 1 at $\Delta l/l_0 = 21.6\%$ and comparison with the FE calculated deformation ("model") in ROI 6

C

APPENDIX C

The aim of this appendix is to investigate X-ray tomography scans of interrupted tensile tests discussed in chapter 5. Damage is initiated in the center of the interrupted samples. A macro crack propagates from the center towards the surface of the samples. The objective is to quantify this damage.

C.1 X-RAY TOMOGRAPHY SCANS

The tested ST and NT samples in chapter 5 are scanned in a laboratory General Electric (GE) Phoenix v/tome/x m device using a microfocus tube used at an accelerating voltage of 220 kV and a 4000×4000 detector used in 2×2 binning mode. The detector is equipped with a lateral shift actuator that allows to randomly move the detector in the transverse direction between each projection, effectively spreading and practically eliminating ring artifacts. All samples are scanned at a voxel size of $\sim 2.5\ \mu m^3$ which helps reveal relatively large voids. Small nucleated voids or cracks in Al(FeMn)Si cannot be captured at this resolution.

An undamaged ST sample is scanned in addition to the tested samples for the sake of comparison. The scanned volumes are as listed below:

- ST → 1574×1589×1499 voxels
- NT10 → 1999×1999×1501 voxels
- NT4 → 2000×2000×850 voxels
- NT2 → 1999×2000×585 voxels
- Undamage ST → 1699×1694×1500 voxels

The scanned volumes are reconstructed using the GE proprietary software. The same reconstruction parameters are used for all samples, including software beam hardening correction, sample movement and illumination correction. Post-processing is carried out using a Python script in the following order:

1. The 3D reconstructed raw volume is loaded as shown in 2D slices in the x-y and x-z planes in fig. C.1 (example on the NT10 sample). The raw volume is then filtered by a non-local image denoising method [Buades et al., 2011] to get rid of the ring artifacts and other image noise.

2. The sample's mask is obtained as shown in fig. C.1 using a 3D convex hull method [Chazelle, 1993]. The mask is useful for defining the sample's borders and separate it from the surroundings.

3. Since the sample contains a macroscopic crack, the latter must be discarded when defining the sample's volume. Therefore, the crack is excluded from the initially obtained mask. This is done by labeling objects and excluding the connected object with a large volume. At this point, the mask is free from the crack and the remaining volume is realistic (see Mask–crack in fig. C.1).

4. To finish with the volume segmentation, the pores in the matrix are segmented using a combination of morphological operations to obtain a 3D volume with white pixels representing the voids as shown in fig. C.1.

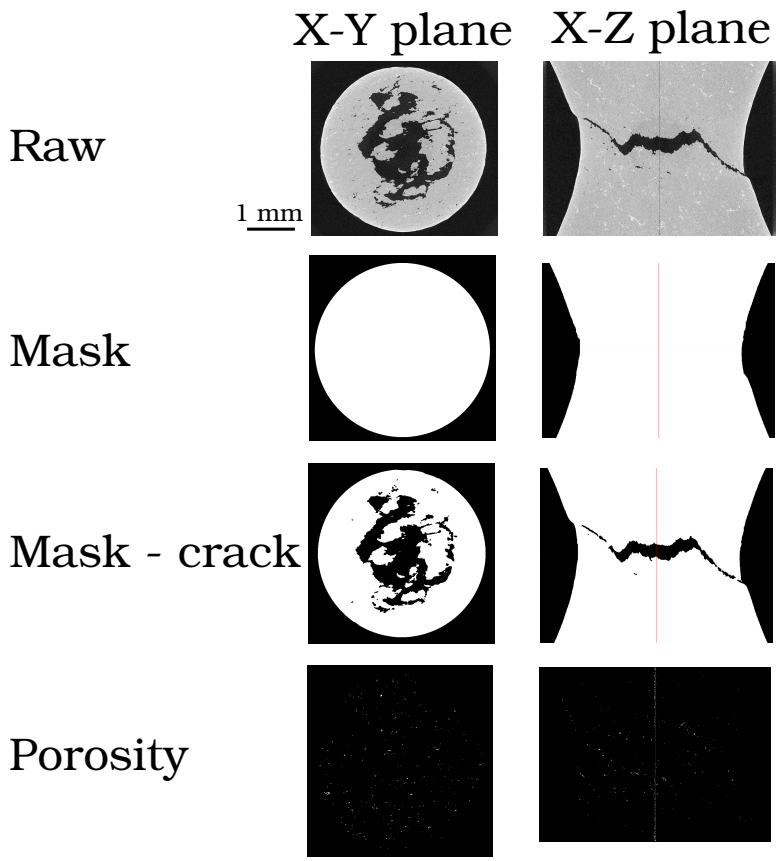

Figure C.1: X-ray tomography scan post-processing carried on ST and NT samples. An example is shown on a NT10 sample illustrating the 4 steps: loading raw volume & filtering, obtaining the mask, extracting the crack from the mask (mask–crack) and finally the porosity segmentation. Each step results in a 3D binary volume except for the first step with a 8bit gray level 3D volume.

C.2 QUANTITATIVE ANALYSIS OF VOID GROWTH

Once the mask–crack and porosity 3D binary volumes are obtained, a counting method is developed to estimate the porosity volume fraction in the sample. Since the mask–crack is a 3D binary volume, white pixels represent the metallic matrix, while

black pixels define the surroundings or the crack. The same goes for the porosity 3D volume in which white pixels represent the pores and black pixels define the rest. In each of the mask–crack and porosity 3D binary volumes, a cylinder with a diameter equivalent to 90% of the minimum cross-section diameter (Φ_{min}) is considered for analysis as shown in fig. C.2. The porosity volume fraction is obtained in the following order:

1. Starting at the Φ_{min}, a certain height dz is defined. The analyzed cylinder is divided into a certain number of disks with a height of dz each. Each disk in the sample's upper half is coupled with the corresponding disk from the lower half (e. g. 1 with 1′ as shown in fig. C.2).

2. For each two coupled disks (e. g. 1 with 1′), a certain thickness $d\Phi$ is defined, see fig. C.2. The disks are divided into a certain number of rings with a thickness of $d\Phi$ each. The total number of rings in a disk can be noted as: $N = 0.9\Phi_{min} \,/\, d\Phi$.

3. In each ring, the white pixels in the mask–crack and porosity volumes are counted respectively. Then, to estimate the porosity in a given disk (f_z), the sum of white porosity pixels is divided by the sum of white pixels in the mask–crack volume:

$$f_z = \sum_{dz=1}^{2} \sum_{d\Phi=1}^{N} \left(\frac{\text{porosity white pixels}_{d\Phi}}{\text{mask–crack white pixels}_{d\Phi}} \right)_{dz}$$

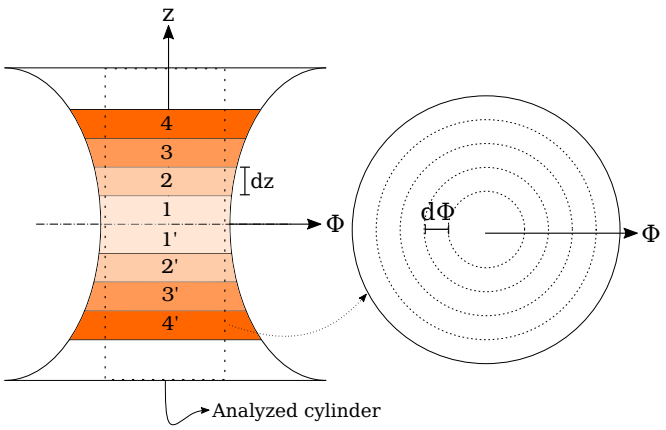

Figure C.2: Counting method applied on ST and NT X-ray post-processed tomography scans to calculate the porosity volume fraction and quantify void growth

The above explained post-processing and counting methods are applied to all scanned samples. Figure C.3 (a) shows x-z views of all tested samples with the inner crack. The NT10 contains a crack that is open up to the surface while the NT2 contains the smallest crack. The red line in fig. C.3 (a) represents the Φ_{min}.

Figure C.3 (b) illustrates the evolution of void growth along the ST sample's diameter. As the stress triaxiality is higher in the sample's center, one expects that the void growth is higher in the center and lower towards the sample's edges. However, fig. C.3

(b) shows that void growth in the center is similar to the void growth at the sample's edges. This indicates that void nucleation takes place along the sample's diameter and not preferably in the center. This confirms as well the fact that damage in the 6061-T6 aluminum alloy is "nucleation controlled" and not "void controlled". The latter refers to alloys that undergo significant amount of void growth. In the case of a "void controlled", void growth should be higher in the sample's center unlike fig. C.3 (b). The same porosity evolution along the diameter is observed for the NT samples. The porosity volume fraction displayed in fig. C.3 must not be used to calibrate damage model parameters since voids with a size inferior to the scan resolution ($\sim 2.5\ \mu m^3$ voxel size) are not counted.

Figure C.3 (c) displays the porosity volume fraction in all scanned samples along the longitudinal axis (loading axis). The curve of each sample starts beyond the crack (e. g. $z > 0.26$ mm in the NT10 sample). Since the NT10 and NT4 samples contain a wide open crack, the highest porosity level is lower than in the NT2 and ST samples. Regardless of the absolute maximum porosity value, one can tell that void growth drops dramatically at 1.26, 1.1 and 0.58 mm for the NT10, NT4 and NT2 samples respectively. The undeformed notch height is 3.6, 1.6 and 0.8 mm for the NT10, NT4 and NT2 samples respectively. This means large voids (superior to the scan resolution) are located in 35, 69, 72% of the notch's heigh in the NT10, NT4 and NT2 samples respectively.

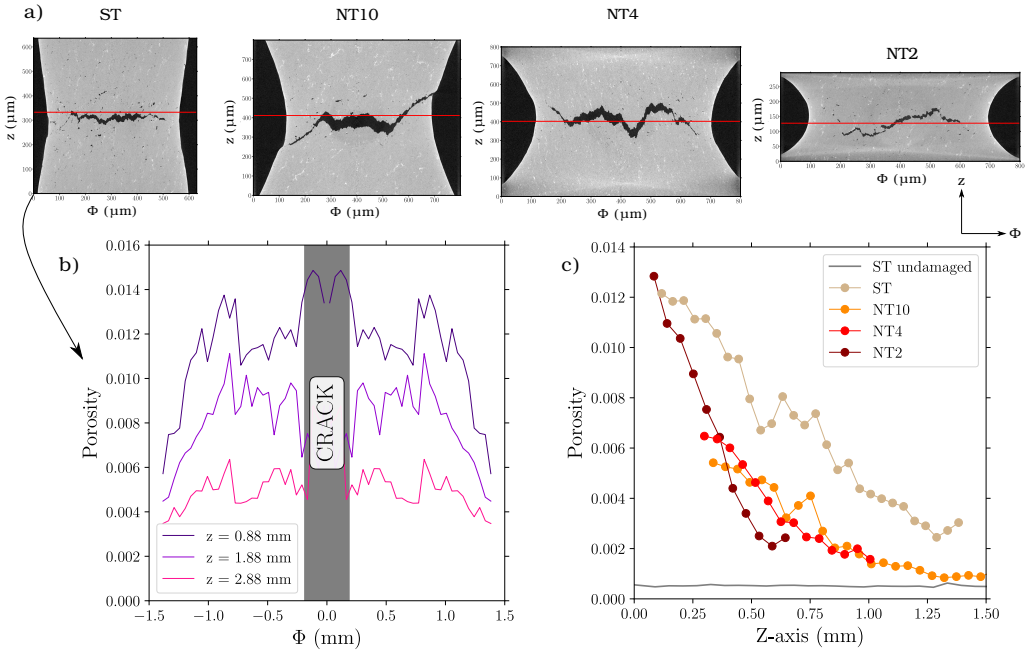

Figure C.3: a) x-z plane view of the tested scanned samples showing the inner crack that developed by coalescence of micro-voids, b) porosity evolution along the ST sample's diameter showing the void growth is similar between the center ($\Phi = 0$) and the edge ($\Phi > 1$), c) void growth in the samples' z-axis.

Figure C.4 displays the porosity as a function of the plastic deformation calculated in chapter 5 using elastic–plastic FE simulations. The void growth rate as a function of the plastic deformation can be used to asses the response of a damage model. The normalized porosity values in fig. C.4 can be compared to the model's normalized porosity to asses the α or q_i parameters in the Rice & Tracey or Gurson model respectively.

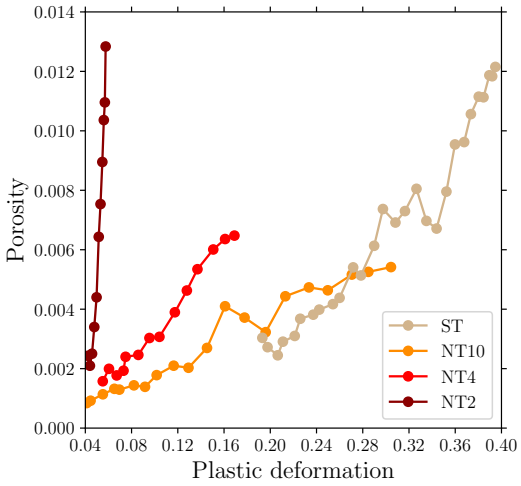

Figure C.4: Void growth in the ST and NT samples as a function of the FE calculated plastic deformation

BIBLIOGRAPHY

Benzerga, A. and J. Besson (2001). 'Plastic potentials for anisotropic porous solids.' In: *Eur. J. Mech./A* 20A.3, pages 397–434 (see p. 245).

Berdin, C. et al. (2004). *Local approach to fracture*. Presses de l'Ecole des Mines (Paris) (see p. 241).

Bertram, A. (2012). 'Elasticity and Plasticity of Large Deformations.' In: Springer, Heidelberg. Chapter 1, pages 3–90. DOI: 10.1007/978-3-642-24615-9 (see p. 251).

Buades, A. et al. (2011). 'Non-Local Means Denoising.' In: *IPOL J. Image Processing Online*, pages 208 –212. DOI: 10.5201/ipol.2011.bcm_nlm (see p. 262).

Bugat, S. et al. (1999). 'Micromechanical modeling of the behavior of duplex stainless steels.' In: *Comput. Mat. Sci.* 16.1–4, pages 158–166 (see p. 256).

Chazelle, B. (1993). 'An optimal convex hull algorithm in any fixed dimension.' In: *Discrete & Computational Geometry* 10, pages 377–409. DOI: 10.1007/BF02573985 (see p. 262).

Chu, C. and A. Needleman (1980). 'Void nucleation effects in biaxially stretched sheets.' In: *J. Engng Mater. Technol.* 102, pages 249–256 (see pp. 245, 246).

Gurson, A. L. (1977). 'Continuum theory of ductile rupture by void nucleation and growth: Part I— Yield criteria and flow rules for porous ductile media.' In: *J. Engng Mater. Technol.* 99, pages 2–15 (see p. 242).

Madou, K. and J. Leblond (2012). 'A Gurson-type criterion for porous solids containing arbitrary ellipsoidal voids — I: Limit-analysis of some representative cell.' In: *J. Mech. Phys. Solids* 60, pages 1020–1036 (see p. 245).

Marae-Djouda, J. et al. (2017). 'Angular plasmon response of gold nanoparticles arrays: approaching the Rayleigh limit.' In: *Nanophotonics* 6.1, pages 279–288. DOI: 10.1515/nanoph-2016-0112 (see p. 254).

Morin, L. et al. (2017). 'A Gurson-type layer model for ductile porous solids with isotropic and kinematic hardening.' In: *Int. J. Solids Structures* 118, 167–178 (see p. 245).

Paux, J. et al. (2015). 'An approximate yield criterion for porous single crystals.' In: *Eur. J. Mech./A* 51, pages 1–10 (see p. 245).

PonteCastañeda, P. (1991). 'The effective mechanical properties of nonlinear isotropic composites.' In: *J. Mech. Phys. Solids* 39.1, pages 45 –71. DOI: 10.1016/0022-5096(91)90030-R (see p. 241).

Rousselier, G. et al. (1989). 'Non–Linear Fracture Mechanics, ASTM STP 995.' In: volume II. Chapter A methodology for ductile fracture analysis based on damage mechanics: an illustration of a local approach of fracture, pages 332–354 (see p. 241).

RÉSUMÉ

L'alliage d'aluminium 6061-T6 est utilisé pour la fabrication de la cuve de réacteurs nucléaires de recherche. L'irradiation provoque des modifications microstructurales qui durcissent le matériau (augmentations de 45 et 60% de la limite d'élasticité et de la résistance mécanique) et détériorent sa ductilité (diminution de 9 à 15% de l'allongement à rupture). Malgré ces évolutions du comportement élastoplastique, il n'est pas prouvé dans la littérature que la ténacité de l'alliage irradié diminue, et quelques résultats montrent même qu'elle n'est pas affectée. Des investigations concernant l'influence de l'irradiation sur la rupture ductile de l'alliage sont donc nécessaires. L'objectif principal de cette thèse est ainsi de développer un modèle physique permettant de prédire la ténacité de l'alliage d'aluminium 6061-T6 irradié. Les mécanismes d'endommagement ductile sont investigués par une approche couplée expérimental – numérique : (i) La germination est étudiée via des coupes polies et des essais de traction in situ réalisés sur éprouvettes entaillés ; (ii) Des simulations par éléments finis de cellules unitaires permettent de quantifier la croissance ; (iii) En considérant deux populations de vides, ces simulations permettent également d'analyser la coalescence. Parallèlement, le durcissement et la chute d'écrouissage sont étudiés sur un aluminium 6061 modèle ayant subi différents traitements thermiques, afin de pouvoir décorréler leurs effets sur la ténacité : en appliquant le modèle précédemment développé, les propagations de fissure dans des éprouvettes CT sont correctement reproduites. En supposant que l'irradiation n'affecte pas les particules responsables de l'endommagement, le modèle non irradié est ensuite appliqué à l'état irradié, en le couplant à un modèle phénoménologique élastoplastique irradié, développé grâce à la base de données collectée dans la littérature. Des éprouvettes de traction et de ténacité irradiées sont testées dans des cellules blindées afin de valider définitivement le modèle de la thèse. Outre les différentes contributions apportées à la thématique de la modélisation de la rupture ductile, la principale conclusion est que la ténacité de l'alliage d'aluminium 6061-T6 reste constante en fonction de la dose d'irradiation.

MOTS CLÉS

Rupture ductile, Aluminium, Irradiation aux neutrons, Ténacité, Éléments finis

ABSTRACT

The 6061-T6 aluminum alloy is used for the fabrication of pressure vessels in nuclear research reactor. Neutron radiation causes microstructural changes that harden the material (45 and 60% increase in the yield and mechanical strengths respectively) and deteriorate its ductility (drop from 9 to 15% in the total elongation). Despite these changes in the elastic–plastic behavior, there is no evidence in the literature that the toughness of the irradiated alloy decreases, and some results even show that toughness is not affected. Therefore, investigating the influence of neutron radiation on the ductile failure of the alloy is necessary. The main objective of this thesis is to develop a physics-based model to predict the toughness of irradiated 6061-T6 aluminum alloy. The ductile damage mechanisms are investigated via a coupled experimental–numerical approach: (i) Void nucleation is studied via polished sections and in situ tensile tests performed on notched specimens; (ii) Finite element simulations of unit cells allow to quantify void growth; (iii) By considering two void populations, these simulations also allow to analyze void coalescence. In parallel, strain hardening drop is studied on a model 6061 aluminum having undergone different heat treatments, in order to be able to decorrelate its effect on toughness: by applying the previously developed model, crack propagations in CT specimens are correctly reproduced. Assuming that irradiation does not affect the particles responsible for the damage, the developed model is then applied to the irradiated material, by coupling it to an irradiated elastic–plastic phenomenological model, developed thanks to the database collected in the literature. Irradiated tensile and toughness specimens are tested in hot cells in order to definitively validate the PhD model. In addition to the various contributions brought to the topic of the modeling of the ductile failure, the main conclusion is that the toughness of the 6061-T6 aluminum alloy remains constant as a function of the irradiation dose.

KEYWORDS

Ductile failure, Aluminum, Neutron radiation, Fracture toughness, Finite element